UAB

Universitat Autònoma de Barcelona

Green synthesis of coordination polymers using supercritical carbon dioxide

Núria Portolés Gil

Green synthesis of coordination polymers using supercritical carbon dioxide

Núria Portolés Gil

Doctoral Thesis

Ph.D. in Chemistry

Supervisor: Prof. Concepción Domingo Pascual

Supervisor: Dra. Ana M. López Periago

Supervisor and tutor: Dr. José A. Ayllón Esteve

Departament de Química-Facultat de Ciències

2019

Thesis presented to aspire to the Doctorate in Chemistry degree by

Núria Portolés Gil

Supervisor:
Prof. Concepción Domingo Pascual

Supervisor and tutor:
Dr. José A. Ayllón Esteve

Supervisor:
Dra. Ana M. López Periago

Bellaterra, September 20, 2019

Abstract

Recently, the research in coordination polymers (CPs) and porous metal-organic frameworks (MOFs) has raised a large interest, since these materials are considered potential candidates for numerous applications, including drug delivery, catalysis, gas separation and storage. Generally, these materials are synthetized using toxic organic solvents and high temperatures. Therefore, the development of sustainable synthetic approaches becomes necessary to speed up the industrial expansion of these products. The main aim of this work is to synthetize CPs using a green technology based on supercritical carbon dioxide ($scCO_2$) solvent. To date, the use of $scCO_2$ in the field of CPs and MOFs has been mainly limited to the post-synthetic activation or cleaning steps. The use of $scCO_2$ can go further, including the synthesis of these materials. Hence, the main objective of this work is to demonstrate this possibility, stablishing a synthetic protocol.

In order to achieve the main aim, a new methodology has been developed to explore the synthesis of new single and mixed-metal CPs with different dimensionalities. CPs have been obtained by reacting a metallic complex and an organic linker in $scCO_2$. Fluorinated organometallic complexes (i.e., hexafluoroacetylacetonate) and N-donor organic linkers have been selected taking into account their significant solubility in $scCO_2$. Alternatives for systems involving metal complexes with low solubility have been also developed, based on the use of ancillary ligands for the metal. Linear bipyridyl and trigonal polypyridyl connectors have also been used. The growing interest in the synthesis of these CPs based on N-donor organic linkers is related to their core's planar geometry, ideally suited to generate highly symmetrical structures. Most importantly, the green character of the synthesis allows to consider its use for the synthesis of biocompatible materials. Therefore, as a proof of concept the use of bio-linkers, e.g., curcumin and ferulic acid, for 2D and 3D bioMOFs synthesis has been explored.

In short, along the different Chapters the viability of the easy, fast and eco-friendly synthesis of CPs and MOFs using $scCO_2$ has been demonstrated. Using diverse metal nodes and linkers, 17 new CPs have been crystallized in this solvent, most of them elucidated crystallographically. The way in which synthetic obstacles in $scCO_2$, such as low solubility of reagents or fast precipitation of kinetic phases are overcome, has been described along the different Chapters. Applications in gas adsorption, magnetism and drug delivery have also been presented.

Resum

Recentment l'interès per la investigació en polímers de coordinació (CPs) i en xarxes metal·lorgàniques (MOFs) ha crescut degut al potencial d'aquests materials per nombroses aplicacions com per exemple, l'alliberació controlada de fàrmacs, la catàlisi i l'emmagatzematge i la separació de gasos. Generalment aquests materials són sintetitzats utilitzant dissolvents orgànics tòxics i altes temperatures. Per aquest motiu, és necessari desenvolupar rutes sintètiques més sostenibles per accelerar l'expansió industrial d'aquests productes. L'objectiu principal del treball és sintetitzar CPs utilitzant tecnologies sostenibles basades en l'ús del diòxid de carboni supercrític (scCO$_2$) com a dissolvent. Fins avui, la utilització d'aquest dissolvent en l'àrea dels CPs i MOfs ha estat restringida a etàpes d'activació o neteja post-sintètica. No obstant l'ús de scCO$_2$ pot anar més enllà i pot ser utilitzat també com a solvent en la síntesi d'aquest materials. Per tant, l'objectiu principal d'aquesta tesi és demostrar aquesta possibilitat, establir un protocol sintètic.

Per tal d'aconseguir aquest objectiu, s'ha desenvolupat una nova metodologia per explorar la síntesis de nous polímers de coordinació homometal·lics o heterometal·lics de diferents dimensionalitats. Els CPs s'han obtingut mitjançant la reacció de complexos metàl·lics insaturat i els lligands orgànics en scCO$_2$. S'han seleccionat diferents complexes organometàl·lics fluorats i lligands orgànics N-donadors tenint en compte la seva solubilitat en scCO$_2$. Pels sistemes on s'utilitzen complexos metàl·lics amb baixa solubilitat, s'ha desenvolupat una alternativa basada en la utilització de lligands auxiliars pel metall. També s'han utilitzat connectors tipus bipiridina lineals o polipiridina trigonals. L'interès en la utilització d'aquests N-donadors per la síntesi de CPs està relacionat amb la geometria plana del nucli, que és ideal per generar estructures molt simètriques. Degut al caràcter sostenible de la síntesi s'ha considerat també el seu ús per la síntesi de materials biocompatibles. Per aquest motiu, com a prova de concepte, s'han utilitzat els productes naturals curcumina i àcid ferúlic com a lligands biocompatibles per la síntesi de bioMOFs de dos i de tres dimensions.

En resum, al llarg dels diferents capítols de la tesis es demostra la viabilitat de la utilització del scCO$_2$ per la síntesis de CPs i MOFs. S'ha aconseguit cristal·litzar 17 nous CPs i la majoria s'han pogut resoldre cristal·logràficament. A través dels diversos capítols es descriu la manera de superar els obstacles sintètics trobats al emprar scCO$_2$ com a solvent, tals com la baixa solubilitat dels reactius o la ràpida precipitació de les fases cinètiques. També són presentades aplicacions en adsorció de gasos, magnetisme i alliberació controlada de fàrmacs.

IV

Outline

This thesis describes the synthesis of coordination polymers (CPs) and metal-organic frameworks (MOFs) using a green methodology based on supercritical carbon dioxide (scCO$_2$). The thesis consists of 8 different Chapters, in which Chapters 1 and 3 gives a general introduction and the description of the experimental methods, respectively; Chapters 2 and 8 summarizes de thesis objectives and conclusions, respectively; and Chapters 3 to 7 are the thesis core describing results and discussion of the different addressed areas.

Chapter 1 gives a general introduction of the two main areas of concern in the thesis: CPs or MOFs and scCO$_2$ technology. It starts with a brief description of CPs and MOFs, including their properties, the most common synthetic methods and applications. Next, the properties and most important uses of scCO$_2$ are described with special emphasis on its suitability as a sustainable solvent for the synthesis of new materials. At the end of the Chapter, the motivation of this work is justified based on the analysis of the state of the art found for the use of scCO$_2$ in the area of CPs and MOFs.

Chapter 2 describes the objectives of this thesis.

Chapter 3 gives a general description of the used high-pressure equipment in scCO$_2$ technology. Equipment parts are shown and defined. The used methodology for the synthesis of CPs and MOFs is fully detailed. Moreover, used characterization techniques are briefly described at the end of this Chapter.

Chapter 4 addresses the drawbacks of the low solubility of most metal complexes in scCO$_2$ for the synthesis of CPs. A new synthetic approach based on the modulation of the solubility of the starting materials that possess low solubility in the medium based on temperature, use of co-solvent or ancillary ligands is presented. The same bipyridine derivative linkers that present good solubility are used for the different metals. This Chapter is based on the results of two published articles:

Portolés-Gil, N.; Parra-Aliana, R.; Álvarez-Larena, Á.; Domingo, C.; Ayllón, J. A.; López-Periago, A. Bottom-up approach for the preparation of hybrid nanosheets based on coordination polymers made of metal-diethyloxaloacetate complexes linked by 4,4′-bipyridine. *CrystEngComm,* **2017**, 19 (34), 4972-4982.
DOI: 10.1039/c7ce00909g

Portolés-Gil, N.; Gowing, S.; Vallcorba, O.; Domingo, C.; López-Periago, A. M.; Ayllón, J.A. Supercritical CO_2 utilization for the crystallization of 2D metal-organic frameworks using *tert*-butylpyridine additive. *Journal of CO₂ Utilization*, **2018**, 24, 444-453.

DOI: 10.1016/j.jcou.2018.02.004

Chapter 5 presents the one-pot synthesis of mixed-metal CPs based on bipyridine organic linkers using exclusively pure scCO₂ as a solvent. The mixed-metal obtained products involve Zn(II) and Co(II) metal-nodes. Therefore, the fascinating magnetic properties of these compounds have been studying, showing a behavior of single metal magnet for the CPs involving Co(II).

Chapter 6 extends the use of scCO₂ in CPs and MOFs synthesis to a more complex organic linker; i.e., a substituted 1,3,5-triazine (3-tpt). The use of three different polarity solvents (scCO₂, EtOH and $CHCl_3$) allows the crystallization of five new Cu(II) compounds involving this organic linker. This study demonstrates that the structural richness of coordination polymers is not only attained through the selection of the metal node and linker, but also by the synthetic conditions while keeping the reagents untouched. Moreover, a reversible phase transition has been observed with unprecedented control of the 3-tpt conformation.

Chapter 7 introduces the use of the scCO₂ green methodology for the synthesis of bioMOFs involving natural bio-active molecules as the organic linker. In particular, the synthesis of curcumin and ferulic bioMOFs is investigated. For curcumin, the obtained bio-MOF is a new compound from which the crystal structure was solved using an original methodology based on transmission electron diffraction. This Chapter is based on two published article:

Portolés-Gil, N.; Lanza, A.; Aliaga-Alcalde, N.; Ayllón, J. A.; Gemmi, M.; Mugnaioli, E.; López-Periago, A. M.; Domingo, C. Crystalline curcumin bioMOF obtained by precipitation in supercritical CO_2 and structural determination by electron diffraction tomography. *ACS Sustainable Chemistry & Engineering*. **2018**, 69, 12309-12319.

DOI: 10.1021/acssuschemeng.8b02738

López-Periago, A. M.; Portoles-Gil, N.; López-Domínguez, P.; Fraile, J.; Saurina, J.; Aliaga-Alcalde, N.; Tobias, G.; Ayllón, J. A.; Domingo, C. Metal-organic frameworks precipitated by reactive crystallization in supercritical CO_2. *Crystal Growth & Design.* **2017**, 17 (5), 2864-2872.

DOI: 10.1021/acs.cgd.7b00378

Chapter 8 summarizes the general conclusions of the main findings of this thesis, providing the answer to the questions raised in initial project thesis. Moreover, possible research lines opened for a future work are pointed out.

VIII

Acronyms

Alternating current	AC
Aerosol solvent extraction system	ASES
Attenuated total reflection	ATR
Barrett, Joyner and Halenda	BJH
Brunauer, Emmett, and Teller	BET
Cambridge crystallographic data center	CCDC
Coordination polymer	CPs
Critical pressure	Pc
Critical temperature	Tc
Direct current	DC
Electron diffraction tomography	EDT
Elemental analysis	E.A.
Energy-dispersive X-ray spectroscopy	EDS
Environmental, health and safety	EHS
European medicines evaluation agency	EMEA
Food and drug administration	FDA
Fourier transform	FT
Gas anti-solvent	GAS
Generally regarded as safe	GRAS
Inductively coupled plasma mass spectrometry	ICP-MS
Infrared spectroscopy	IR
Kramers doublets	KD
Magnetic resonance imaging	MRI
Magnetic susceptibility	χ
Materials of institute of Lavoisier	MIL
Materials science and powder diffraction	MSPD
Metal-biomolecule framework	bioMOFs
Metal-organic frameworks	MOFs
Molecular formula	MF
Nuclear magnetic resonance spectroscopy	NMR
Particles from gas-saturated solutions	PGSS®
Post-synthetic modification	PSM
Powder X-rays diffraction	PXRD
Rapid expansion of supercritical solutions	RESS
Scanning electron microscopy	SEM
Secondary building units	SBUs
Semicontinuous compressed fluid anti solvent	PCA
Single crystal X-ray diffraction	SCXRD

Acknowledgments

This thesis could not have been done alone, and for that reason I would like to thank all the people involved in some way during these four years towards the development of this project.

In first place I would like to thank Prof. Concepción Domingo, Dr. Ana M. López-Periago and José A. Ayllón, my thesis directors. I would like to express my gratitude for giving me the opportunity to develop this thesis and for guiding me during the process. Thank you for giving me the possibility to increase my knowledge, develop new skills and allow me to attend seminaries, conferences and specific courses.

This work would not have been possible without the collaboration of other researchers and experts. I would like to thank Dr. Arianna Lanza, Dr. Mauro Gemmi and Dr. Enrico Mugnaioli from CNI@NEST in Italy for the resolution of structures by EDT. Also Dr. Ángel, Álverez-Larena from the XRD department at UAB and Dr. Eduardo Solano from ALBA synchrotron. I am deeply grateful to Dr. Oriol Vallcorba for solving the major part of the structures, for shearing his knowledge in XRD techniques and answering all my questions. Dr. Gregorio Marbán from INCAR-CSIC, Spain for the XPS measurements and finally Dr. Sílvia Gómez, Dr. Eliseo Ruiz and Núria Clos for the magnetic measurements and theoretical calculations. Moreover, I would like to thank Dr. José Giner Planas and Dr. Núria Aliaga-Alcalde for their involvement, collaboration and for trusting me. I am grateful to Ricard Parra for preparing some of the starting materials and I would like to mention Sara Growing and Albert Rosado, that have invested their time in some of the experiments of my thesis. Thank you for your enthusiasm. I could not forget to express my gratitude to the technicians and researchers in the ICMAB and other institutes, ICN2 INCAR, London Metropolitan University and UAB that have performed some of the measurements for the characterization

of the new compounds. I would especially like to thank Julio Fraile also member of the group, for sharing his knowledge in N_2 adsorption and always being there to help with the reactors.

During these years in the group of SFFM I have shared laboratory with other students that have provided a pleasant work environment. I would really like to thank Alex Borrás for all these years, and for always being there to help me with the reactors, with computer issues and for being the photographer of the laboratory. I would particularly like to thank Laura Rodriguez for always being ready to help me, ask about my thesis and give me ideas. We have share a lot of hours learning new things together and long discussions about science and other topics. Thank you for your energy. I am pleased because during these four years I have had the opportunity to share laboratory with different students and I have had the opportunity to learn something from all them: Miguel, Fran, Pedro, Janos, Maria, Alba, Martí, Kenia, Llorenç, Dr. Amirali Yadzi and Márta.

I would like to acknowledge the ICMAB staff with whom I have share space during these years. I am also very grateful to all the people from other groups that I have met which I have share lunches or talks in the corridor during these four years. It was time for disconnection, laughter and sharing laboratory problems and advice. Thank you for being there: Sandra, Eulàlia, Júlia, Sole, Dani, Teresa, Ona, Raquel, Joseline, Josh, Jesse, Raúl, Ezhil and Amanda.

I also feel blessed for having had the opportunity to know other researchers and students in the courses and conferences. I have learned a lot, and I would like to thank the ones that still keep in contact with me and give me advice. I would like to express my gratitude Dr. Darren Bradshaw and his group for giving me the opportunity to visit his laboratory in the University of Southampton. Furthermore, I want to thank Selina Denuault and Dr. Guy Denuault for welcome me.

Més enllà de la ciència, no puc deixar de donar les gràcies a persones que també m'han ajudat durant aquests quatre anys. Voldria agrair a les meves amigues que s'han preocupat, m'han animat i han intentat que desconnectés durant aquests quatre anys. Amigues que malgrat no ser científics, en interessar-se, ara poden explicar què és un fluid supercrític. Algunes inclús vivint lluny han estat a prop i m'han ajudat, donat suport i s'han ofert a donar-me consell. No puc acabar els agraïments sense fer menció a la meva família. Han estat les persones més importants durant aquests quatre anys. Especialment els meus pares i el meu germà, són els que em van animar a fer la tesis, els que no m'han deixat rendir i m'han recolzat en tot moment. Si no fos per ells, avui no estaria escrivint aquests agraïments i entregant la tesis.

Table of contents

CHAPTER-1

General introduction

CHAPTER 1 is divided in three main sections. The first part focuses on the description of coordination polymers and metal-organic frameworks, their synthetic methodologies and main applications. The second part, introduces the most important features related to supercritical fluids technology and, specifically, to supercritical CO_2. Finally, the third part describes the motivation towards the connection between these two areas, supercritical CO_2 and coordination polymers in this project thesis.

1.1. Introduction to coordination polymers and metal-organic frameworks

1.1.1. Coordination polymers and metal organic frameworks

Coordination polymers (CPs) and metal-organic frameworks (MOFs) are hybrid structures containing metal cation centers bonded to organic linkers. In these compounds, the repeated units are coordination complexes. These entities are extended infinitely into one, two or three dimensions (1D, 2D or 3D) through covalent metal-linker bonds of different strength (Fig. 1.1).
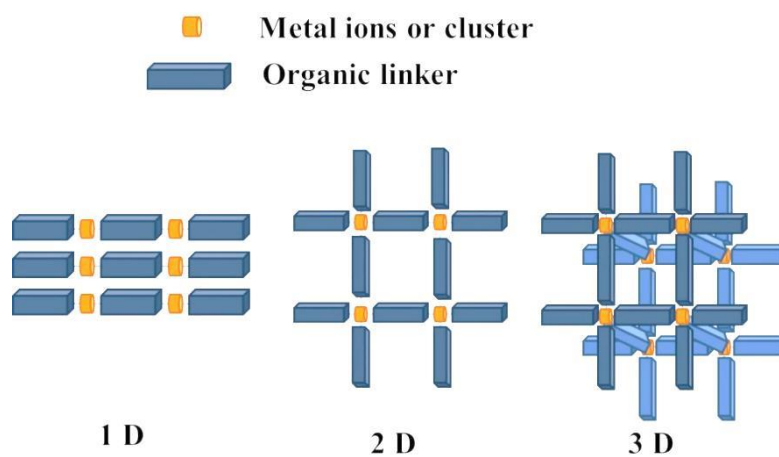
Figure 1.1. Scheme of the different dimensionalities in CPs.

The first use of the term "coordination polymer" can be traced to Bailar in 1964.[1] However, it is generally recognized that the Prussian blue pigment, reported by Diesbach earlier in the 18th century is the first known CP.[2] Nevertheless, the field did not begin to grow until the 90s, thanks to the contributions of the teams of Robson[3] and Kitagawa.[4,5] The term "metal-organic framework" was popularized by the team of Yaghi in 1995,[6] and it has been further defined preferentially to coordination networks with voids.[7] It is also generally considered a subclass of CPs. Both concepts, CPs and MOFs, have expanded rapidly during the last 20 years. A search in the web of science (WOS) data base for the concepts: *coordination polymer* OR metal-organic framework** performed in May 2019 provide 118,953 results (Fig. 1.2).
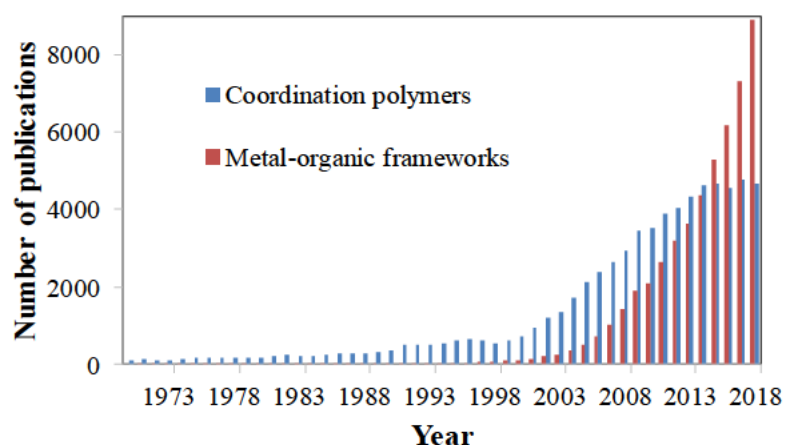
Figure 1.2. Number of publications per year in CPs and MOFs (source WOS).

Both terms, CP and MOF, have been developed from researchers of different areas. Indeed, the inorganic solid state community employs preferentially the term ''metal-organic framework'', whereas ''coordination polymer'' is the name mainly used by coordination chemists. In 2013, the IUPAC performed a provisional recommendation to unify the nomenclature, suggesting that MOFs are CPs with an open framework containing potential voids.[8] However, the indistinct use of both terms, CP and MOF, can be often found in the literature.[4] The dimensionality has also been proposed to differentiate CPs (1D and 2D) and MOFs (3D).[9]

1.1.1.1. Design and synthesis

The high interest of these materials relays in the versatility of the design and synthesis, which allows the preparation of an extensive variety of hybrid compounds with different structures and properties, just by choosing the desired metal ions and organic linkers. These multiple combinations generate a large number of possible CPs. In fact, in 2016 (last actualization), there were 80,000 synthetized structures identified in the Cambridge Crystallographic Data Center (CCDC).[10]

Linkers

In principle, any type of organic molecule with two or more coordinating positions may be self-assembled to metal centers to form polymeric structures.[11] The variety of organic linkers and the type of geometrical connection with the metal center would define the topology, the structure and porosity of the CPs. Organic linkers can have linear, trigonal, square-planar and tetrahedral geometry, among others.[12] Commonly, multidentate organic molecules containing oxygen or nitrogen donors are used as linkers. Some examples are shown in Fig. 1.3.
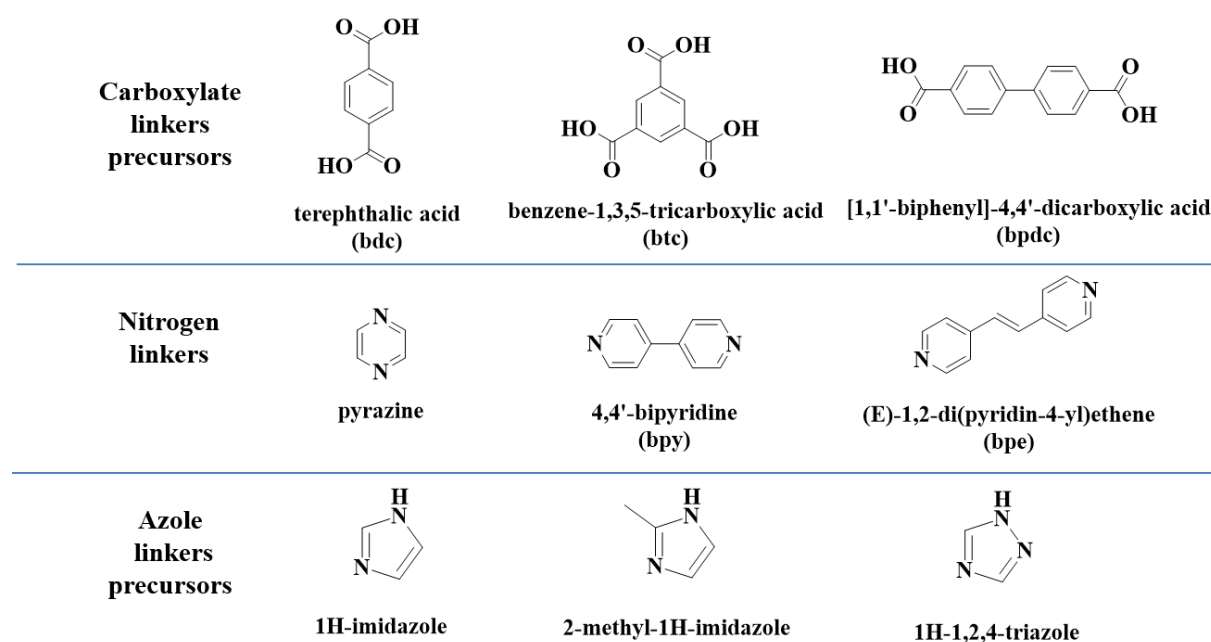
Figure 1.3. Representation of common organic linkers precursors used in CPs synthesis.

In MOFs design, the organic linker is synthesized and/or modified to adapt the structure to the desired porosity, pore size and functionality.[13] In this respect, Yaghi *et al.* introduced the isoreticular synthetic strategy, in which tuning the linker length, while maintaining the same coordination group and geometry, leads to an increase in the surface area of the MOF.[14,15] However, in some cases, by extending the length of the linkers interpenetration is favored, thus the porosity is not increased.[16,17]

In this work, four different bipyridine derivatives were chosen to perform the synthesis of most of the precipitated CPs (Fig. 1.4). These N-donor organic linkers have been extensively studied to construct stable CPs containing nitrogen-metal bonds.[18] Many of them possess good solubility in supercritical CO_2, which is the main solvent used for synthesis in this work. As an extension to the bidentate donors, trigonal polypyridyl connectors, of the type 2,4,6-tris(n-pyridyl)-1,3,5-triazine have also been used. The n-tpt molecule is considered a remarkable building block in supramolecular chemistry, since it can support different types of interactions, from covalent bonding to π-stacking.[19] The growing interest in the synthesis of MOFs containing n-tpt units is related to its core's planar geometry ideally suited to generate highly symmetrical structures. In addition, the use of a bio-linkers such as curcumin or ferulic acid has also been investigated for bioMOFs synthesis.

Chapter 4, 5	4,4'-bipyridine (bpy); (E)-1,2-di(pyridin-4-yl)ethene (bpe); 1,3-di(pyridin-4-yl)propane (bpp); 1,4-bis(pyridin-4-ylmethyl)benzene (bpymb)
Chapter 6	2,4,6-tris(3-pyridyl)-1,3,5-triazine (3-tpt)
Chapter 7	(*E*)-3-(4-hydroxy-3-methoxyphenyl)acrylic acid Ferulic Acid (FA); (1*E*,6*E*)-1,7-bis(4-hydroxy-3-methoxyphenyl)hepta-1,6-diene-3,5-dione Curcumin (CCM)
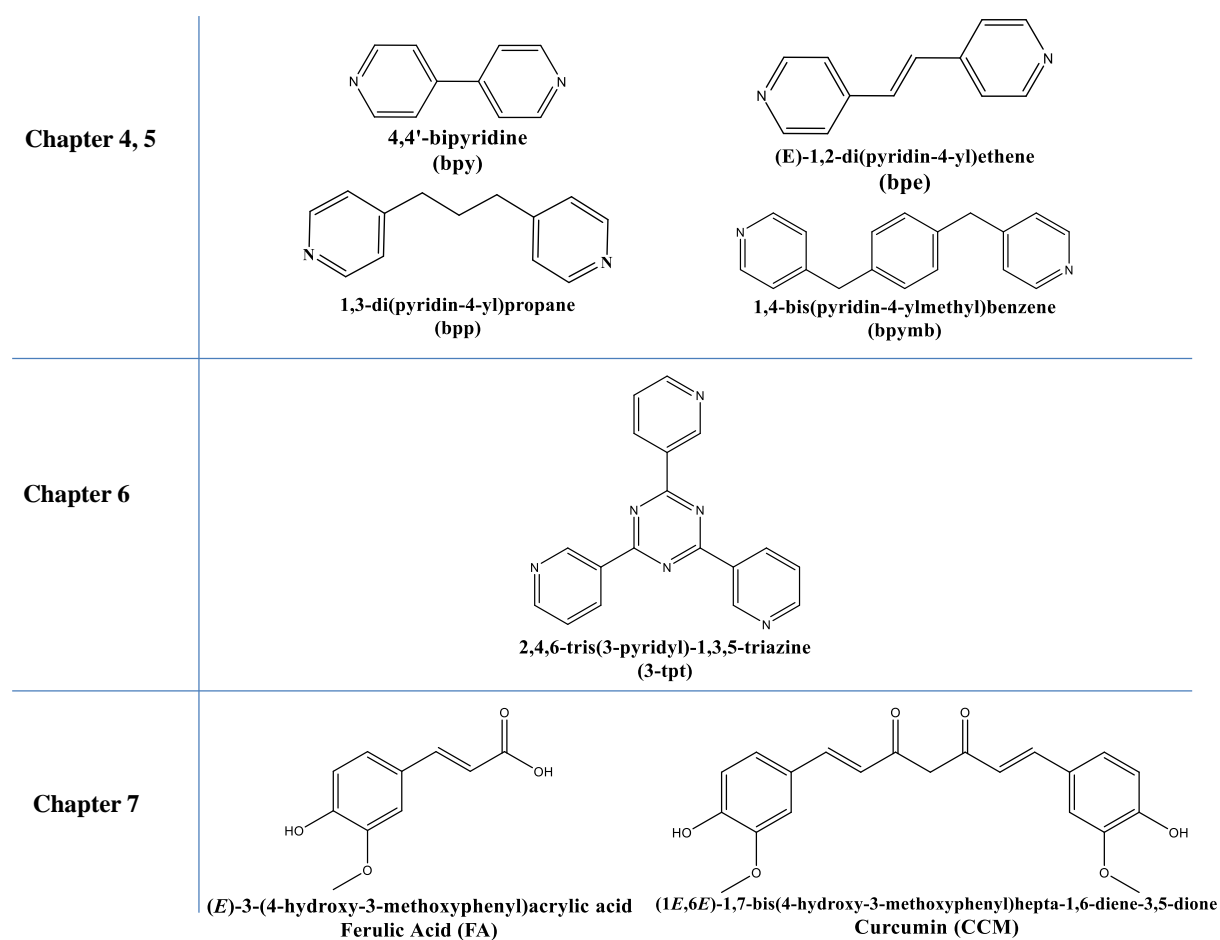
Figure 1.4. Used linkers in this thesis, indicating also the Chapter in which the results obtained with the reagent are described.

Metal complex

Choosing the appropriate linker is important, but basic properties of CPs also depend on metal centers acting as connectors between linkers. Transition metal ions are often used as versatile connectors. In those metals, coordination numbers can range from two to seven depending on the metal and its oxidation state.[12] Alkali metals and alkaline earth metals are also often used for MOFs construction too.[20] The alkali and alkaline-earth elements, e.g., Li or Mg, can be used to synthesize lightweight frameworks. Bonding between alkaline earth metal centers and linkers is mainly ionic in nature, making more difficult the prediction and control over coordination geometry. In recent years, lanthanide MOFs have been developed on the base of their interesting luminescent properties and intriguing topologies.[21]

For transition metals, the number and orientation of binding sites in the metal center mark various possible geometries, schematized in Fig. 1.5.[12] The extended structures can also be constructed by stitching together inorganic polynuclear clusters, known as secondary building

units (SBUs), and organic linkers. The SBUs are finite units with points of extension (points at which they are joined to the linkers) forming a well-defined polyhedral shapes. Common metal-containing SBUs are metal-oxygen clusters (oxoclusters).

Number of functional sites (metal complexes)	Common described geometries	
2	M M	Angular or Linear
3	M M	T- or Y-shaped
4	M M	Tetrahedral or Square-planar
5	M M	Square-pyramidal, or Trigonal-bipyramidal,
6	M	Octahedral
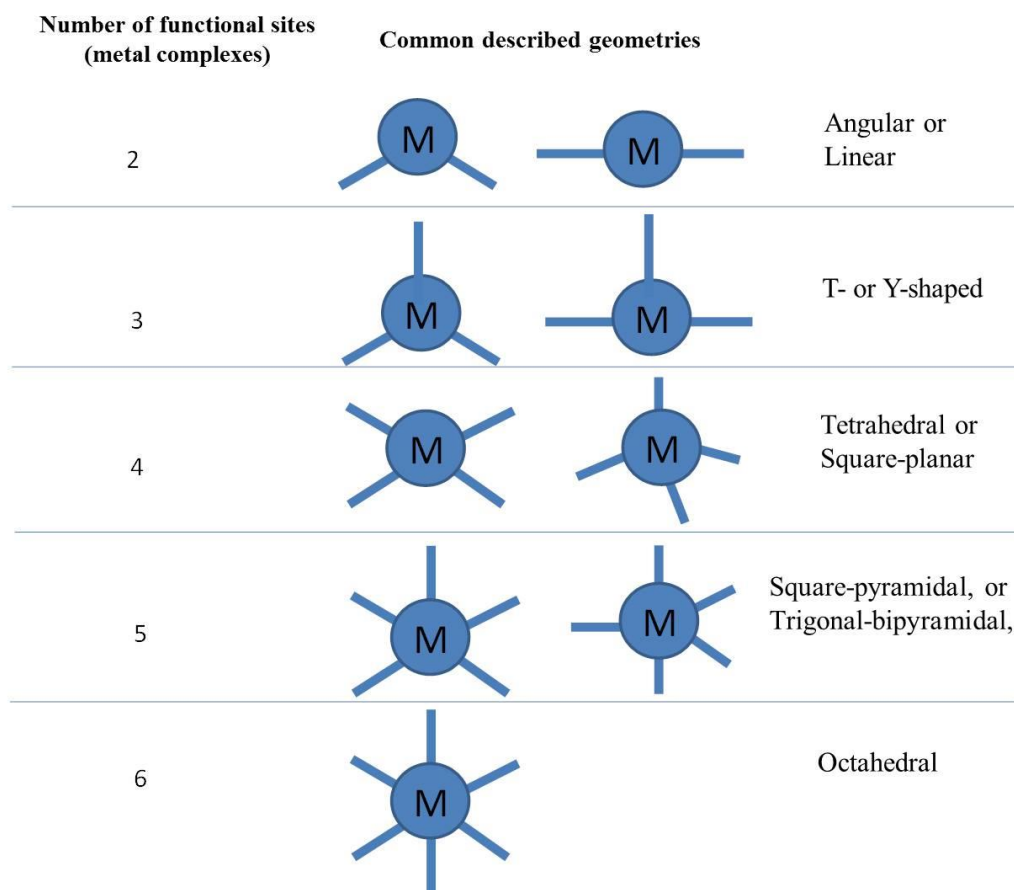
Figure 1.5. Typical coordination geometries described for metal centers.[12]

This thesis focus on the development of CPs involving mainly two transition metals, Cu(II) and Zn(II). Metallic complexes were selected taking into account their solubility in scCO$_2$. Hence, neutral and fluorinated compounds were chosen as ligands for the metal, specifically acetylacetonate, trifluoroacetylacetonate and hexafluoroacetylacetonate.[22,23] Moreover, Cu(II) and Zn(II) are transition metals more abundant, less toxic and less expensive than other metals like lanthanides used in coordination polymers. Co(II) was also selected to prepare CPs with magnetic properties. Fig. 1.6 shows a geometrical representation of the combination between the linkers and the metal complexes used in this thesis.

Metal complex	Connectivity	Organic linker	Connectivity	CP dimensionality
$[M(deox)_2(H_2O)_x]$ *Ch. 4*	(diagram)	bpy	(diagram)	1D
$M(tfa)_2$ *Ch. 4*	(diagram)	bpy, bpe, bpp	(diagram)	2D
$M(hfa)_2$ *Ch. 5*	(diagram)	bpymb	(diagram)	1D
$Cu(hfa)_2$ *Ch. 6*	(diagram)	3-tpt	(diagram)	1D
$Zn(acac)_2$ *Ch. 7*	(diagram)	CCM, FA	(diagram)	2D 3D

Figure 1.6. Schematic representation of the possible geometrical combinations between metal complexes and linkers used in this thesis.

1.1.1.2. Classification

CPs are first classified in non-porous and porous frameworks. All of them can be categorized based on the spatial dimension: 1D chains, 2D layers or 3D structures.[12,24] For porous MOFs, Kitagawa *et al*. proposed an alternative classification based on compound robustness (Fig. 1.7):[12]

i)   1ˢᵗ Generation MOFs are microporous frameworks sustained by guest molecules, which undergo an irreversible collapse once the guest is removed.[25]

ii)   2ⁿᵈ Generation MOFs have stable and robust frameworks characterized by permanent porosity, stable after guest removal.[25]

iii)   3ʳᵈ Generation MOFs are stable porous compounds that have flexible frameworks with a dynamic behavior in response to a particular external stimuli, such as adsorption/desorption of guest molecules.[26]

iv)   4ᵗʰ generation of MOFs are products that can maintain underlying topology and structural integrity towards various post-modification proccesses.[27]
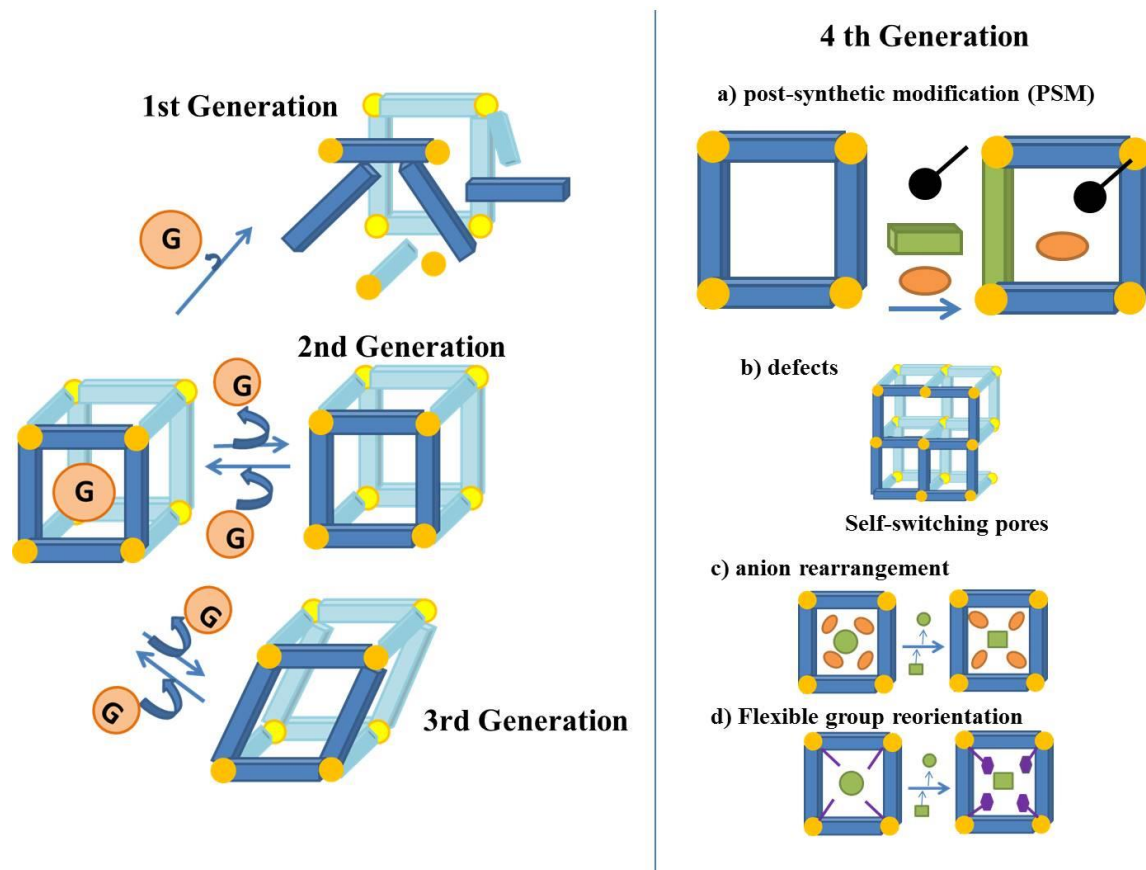
Figure 1.7. Classification of porous CPs based on the robustness. In 1st, 2nd and 3th generation, G represents the guest molecules and the effect on the material after their removal. In the 4th generation MOFs, the changes are provoked by post-synthetic modification, defects or by rearrangements by external stimuli like the interchange of a gest molecule.[27]

Table 1.1. Classification of the CPs obtained in this thesis and their structural porosity.

Ch.	Metal complex	Geometry	Organic linker	Geometry	CPs classification
4	[M(deox)$_2$(H$_2$O)$_x$]	Octahedral	bpy	linear	1D non-porous
4	M(tfa)$_2$	Octahedral	bpy, bpe or bpp	linear	2D non-porous
5	Zn(acac)$_2$	Trigonal, tethaedral or bipyramidal	CCM FA	T-shape Angular	2D 2nd generation 3D 2nd generation
6	Cu(hfa)$_2$	Octahedral or bipyramidal	3-tpt	trigonal	1D non-porous, 1D 2nd generation 1D 3rd generation
7	M(hfa)$_2$	Octahedral	bpymb	lineal	1D non-porous

1.1.1.3. Physicochemical characteristics

Ideally and historically, CPs have been regarded as robust crystalline structures, with high thermal and chemical stability, reflecting the strong coordination bonds, such as metal-oxygen or metal-nitrogen. Moreover, short aromatic and hydrogen bonding interactions participate in the development of the macrostructure.[28] Some reported CPs have been found stable even up to 772 K.[15] However, not all the CPs have these ideal properties. The first family of reported stable MOFs was the one composed by zeolitic imidazolate frameworks. From them, ZIF-8 has been one of the most studied. It is constructed by linking each Zn(II) cation to four imizadolate rings (Fig. 1.8).[29] Another well-known MOF with high thermal stability is UiO-66, which is made up of oxoclusters of Zr(IV) [$Zr_6O_4(OH)_4$] and 1,4-benzodicarboxylic acid struts.[30]

MOF-5	$Zn_4O(bdc)_3$, bdc=1,4-benzodicarboxylate	
MOF-177	$Zn_4O(btb)_2$, btb= benzene-1,3,5-tribenzoate	
UiO-66	$Zr_6O_4(OH)_4(bdc)_6$ bdc=1,4-benzodicarboxylic	
HKUST-1	$Cu_3(btc)_2$ btc = 1,3,5-benzene tricarboxylate	
ZIF-8	$Zn-(MeIm)_2$ MeIm = 2-methylimidazole	
MIL-101	$Cr_3(O)(bdc)_3(F)(H_2O)_2$ bdc= benzene-1,3-dicarboxylate terephthalate	
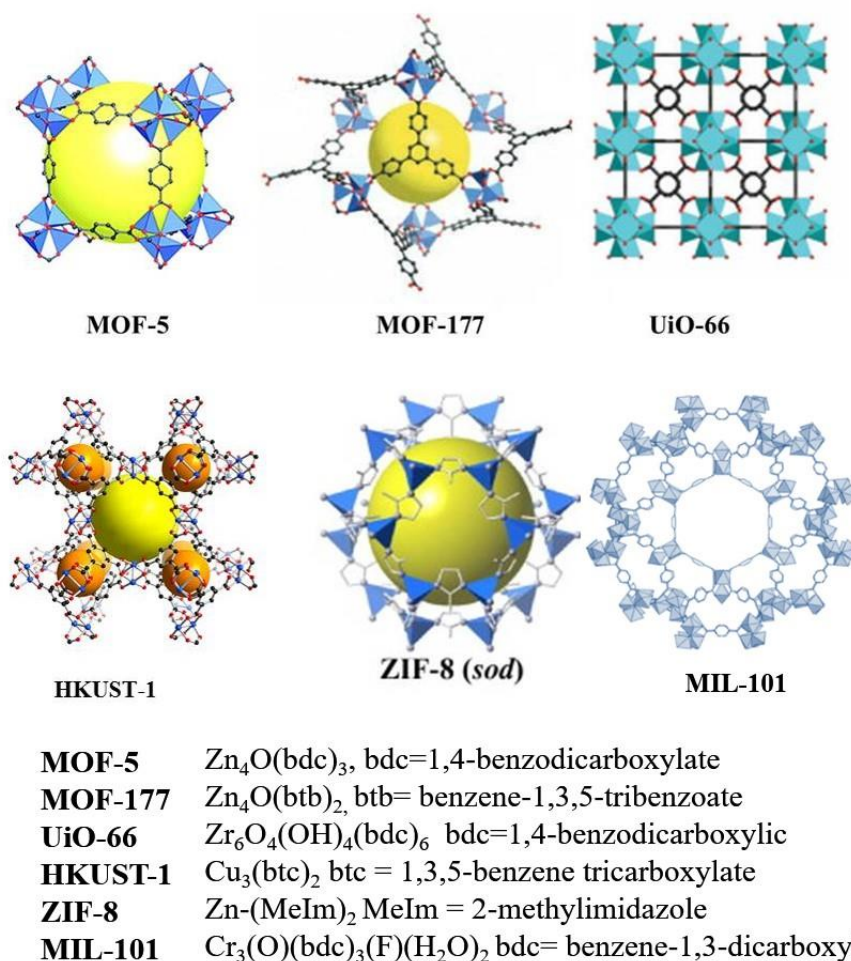
Figure 1.8. Schematic representation of the structures of several widely investigated MOFs: MOF-5,[31] MOF-177,[32] UiO-66,[33] HKUST-1[32] and ZIF-8.[34]

Some of the most interesting characteristic of MOFs are their high porosity and surface area and the tunable control of the pore size. MOFs possessing porosities higher than 50 v% and surface areas reaching values of more than 7,000 $m^2 \cdot g^{-1}$ have been described.[35] These textural values are higher than the ones obtained for other traditional porous materials, such as zeolites and activated carbons.[28] However, some of these highly porous MOFs have low stability, so they are not useful for many applications. Nowadays, chemical and thermal stability, recyclability and kinetics of adsorption-desorption are properties that are increasingly attracting attention.

1.1.2. Applications

Some of the most relevant applications of CPs are shown in this section, divided between those for porous and non-porous compounds. It should be pointed out that most of the described applications are for porous CPs (Fig 1.9). The particular properties of those MOFs, such as large surface area, pore size control, variable structure and possibility of post-functionalization, result in a large number of potential uses in different fields. For non-porous CPs the potential applications are less numerous. Some of the applications of porous CPs, such as catalysis or drug release, can also be achieved with non-porous materials. Moreover, they are proposed for other applications based on different physical properties like magnetism, luminescence, conductivity, etc. (Fig. 1.10).

1.1.2.1. Applications of porous CPs (MOFs)

Gas adsorption

Gas separation and gas storage are two of the applications of porous MOFs that has been deeply studied. Indeed, in the chemical industry there is a large interest in the partitioning of compounds with similar size and properties, e.g., separation of CO_2 from air or from methane and oxygen from nitrogen, or fractionation of light hydrocarbons, such as olefins and paraffins or linear and branched isomers.[36] All these separations are often difficult and energy consuming by using conventional molecular sieves.[37] MOFs are potential candidates to achieve this objective efficiently due to the possibility of pore size control, which allows separations by molecular size. Moreover, MOFs have been proposed in applications of gas storage. In fact, a large number of studies deal with the sorption of CO_2 by developing different strategies to increase the uptake, like introduction of amino functional groups, pore size control and addition of specific metal cations.[38] For example, MOF-177 (Fig. 1.8) is a

material described to have a very high CO_2 adsorption capacity (33.5 mmol·g^{-1} at ambient temperature and 3.5 MPa).[39,32] However, it is worth to mention that for CO_2 capture applications, the sustainability of processes using MOFs, constituted by expensive metals and linkers, would be difficult to justify.

MOFs have also been proposed for hydrogen and methane adsorption and storage. These gases have been considered for a long time promising alternative sources of energy for vehicles; however, the main challenge is still in increasing the safety of the storing.[37] The first study of hydrogen adsorption was performed with MOF-5 (Fig. 1.8) in 2003 by Trickett *et al*.[40] MOF-5 displayed a H_2 uptake of 5 wt% at 77 K and 9 MPa.[31] Another well-known MOF proposed for this application is UiO-66 (Fig. 1.8), which exhibits a H_2 uptake of 4.2 wt% at 77 K and 6 MPa.[41] A strategy explored to increase the H_2 storage capacity is reducing the pore size by embedding in the structure coordinative unsaturated metal centers.[37] Methane safe storage systems can significantly facilitate the implementation of natural gas fuel vehicles.[42] Indeed, HKUST-1 (Fig. 1.8) has demonstrated to be a potential effective candidate for this application, since it exhibits exceptionally high volumetric methane uptake at ambient temperature, exceeding that of any material reported to data.[43] From a collaboration between the team of Yaghi and the BASF company, the application of this MOFs in tanks of methane-powered vehicles has being explored and it is currently close to commercialization.[44] A double or even triple amount of natural gas can be safely stored in a tank containing HKUST-1 than in an empty tank.[45] Since 2013, the system has being tested in a fleet of demonstration vehicles. Although society is not currently in favor of methane fuels, indications are that this technology is getting very close to the market.[46]

Controlled drug release

Recently, MOFs have attracted attention for different applications in biomedicine, such as therapy through controlled drug release and diagnosis by imaging. Some important requirements are biocompatibility and low toxicity. For drug delivery applications, the encapsulation of active compounds inside the pore voids of MOFs was the first described process.[47] The objective is to control the administration rate of the therapeutic drug in the body to enhance efficacy and to reduce side effects.[48] For these systems, the drug release would be a function of the chemical interaction stablished between the drug and the framework and the degradation rate of the MOF by body fluids. The first family of MOFs used for drug delivery was the MIL (Materials of Institute of Lavoisier) series, designed by

Ferey *et al.* in 2005.[49] These MOFs are synthetized from trivalent cations, such as V(III), Cr(III) and Fe(III), linked by carboxylate anions. The series has been extended with p-elements, such as Al(III), Ga(III) or In(III).[50] They have a bimodal distribution of pore size, including micropores (4-10 Å) and mesopores (25-34 Å) and surface area values of 3,100-5,000 $m^2 \cdot g^{-1}$.[47] The MIL-101(Cr) ($[Cr_3O(bdc)_3F(H_2O)_2]_n$) and the MIL-100(M) ($[M_3O(OH)(H_2O)_2(btc)_2 \cdot nH_2O$, where M=Al(III) or Fe(III)) have been studied for the delivery of ibuprofen.[48] The biocompatible MIL-100(Fe) has been further impregnated with anticancer and antiviral drugs.[51]

Catalysis

The use of MOFs has also been proposed in catalysis, thanks to the presence of active metal sites in the porous structure protected from degradation by the organic framework.[52] The crystalline framework also improves the steric selectivity due to the fixed size and shape of the pores. Fujita *et al.* in 1994 reported for the first time the use of a CP as a catalyst.[53] The material was composed of Cd(II) and 4,4-bipyridyl, and was used to catalyse the reaction of cyanosilyation of aldehydes.[54] Other examples involve the use of MIL-101(Cr) that after removing the coordinated H_2O exhibits open metal sites.[55] A new trend in catalysis is the use of mixed-metal MOFs.[52] The presence of more than one metal with different catalytic activity allows performing more than one reaction at the same time. One example is the MFM-300 with a mixture of Ga(III) and Fe(III) ($[Ga_{1.87}Fe_{0.13}OH)_2(H_4L)]$ where H_4L is biphenyl-3,3′,5,5′-tetracarboxylic acid). The use of this catalyst for the ring opening of styrene oxide showed a complete conversion to 2-methoxy-2-phenylethano, while only 40% was attained with the monometallic MOF of Ga(III).[56,57] Also, Cu(II) and Mg(II) MOFs ($[CuMg(pdc)_2(H_2O)_4] \cdot 2H_2O]_n$ where pdc is pyridine-2,5-dicarboxylic acid) have been used to sequentially catalyze two kinds of reactions: olefin to its epoxide followed by epoxide ring opening.[58] Active sites for catalysis can also be generated in the organic linker by the incorporation of pyridyl, amine or amino groups.[59] For instance, Jiang *et al.* reported a sulfonic acid functionalized MIL-101 with excellent catalytic performance in the ring opening of styrene oxide.[59,60] The catalytic activity can also be increased by impregnating the MOF with nanoparticles.[59] One reported example is the addition of nanoparticles of palladium into the pores of IRMOF-3 ($[Zn_4O(abdc)_3]$, where abdc is 2-amino-1,4-benzenedicarboxylate).[61,62]
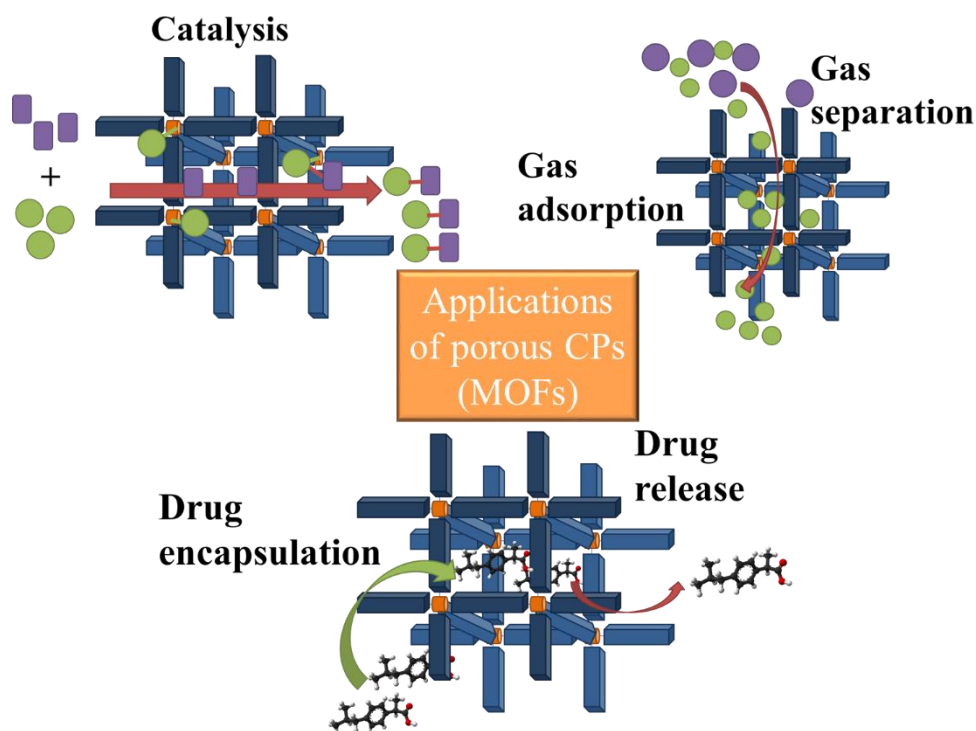
Figure 1.9. Schematic representation of common applications of porous CPs (MOFs).

1.1.2.2. Applications of non-porous CPs

Porous carbons

The synthesis of nanoporous carbons from non-porous CPs has been performed by thermal conversion.[63] These nanoporous carbon materials have gained much attention owing to their high surface area, narrow pore size distribution, and good thermal and chemical stability. These characteristics allow porous carbon to be utilized for a large variety of applications, such as adsorbents, catalyst supports, electrode materials, and so on. Although porous carbons can be also prepared from porous CPs, the surface area is enhanced by using non-porous CPs in the pyrolisis.[64,65] Besides, non-porous CPs have also been used as templates to construct aerogels.[66]

Drug delivery (bioMOFs)

In the drug delivery field, a different novel approach is to construct the MOF using bioactive compounds as linkers, thus developing the family of bioMOFs. In this case, the linker is the therapeutic agent, which is released to the body by the degradation of the MOF. To present a biomedical effect, bioMOFs do not need to have pores for drug adsorption. Miller *et al.* in 2010 described the first active bioMOF, based on nicotinic acid as the linker and Fe(III) as the

metal center.[67] Currently, a large number of different bioMOFs is being developed based on endogenous molecules or active ingredients as building blocks, thus overcoming the toxicity issue.[68] There are a wide variety of active ingredients that may act as constitutive organic linkers on the rational design of bioMOFs, including amino acids, peptides, proteins, nucleobases, saccharides, porphyrins, or even commercial drugs.

Diagnosis by magnetic resonance imaging

Recently, CPs are generating considerable attention for biomedical imaging applications, such as contrast agents for magnetic resonance imaging (MRI). For this application, the CPs do not need to be porous, but of nanometric size. Indeed, nonporous compounds would have a high specific magnetic density for contrast enhancement. Gd(II) and Fe(III)-containing CPs have been proposed for this application.[69] These CPs have diagnostic applications as MRI contrast agents either as a T_1 or T_2 or combined T_1 and T_2. The size dependent quantum effects of the CPs play an important role in developing CP-based MRI contrast agents. If the sizes of CPs can be scaled down to the size of nanomaterials, it may help to control the toxicity, systemic circulation in blood, and may allow a facile endocytosis by the living animals or plant cells without causing any significant cytotoxicity.

Magnetsim

Electronic properties, i.e., magnetic, electrical or optical properties, can also be introduced into CPs by adequately choosing the functional nodes, the organic linkers and the way in which they are connected in the solid. As CPs are built up with metal centers, magnetism is an interesting property to be explored.[70] Among these materials, depending on the magnetic dimensionality within and between the two constituent sublattices (the extended framework and the building units), CPs exhibiting cooperative properties (e.g., magnetic ordering or cooperative spin crossover) and CPs exhibiting molecular properties (e.g., single-molecule magnetism) can be distinguished. The main focus of research in the field of molecular magnetism has been on the design of high curie temperature magnets, materials exhibiting spontaneous magnetization above room temperature, or at least above liquid nitrogen. These materials are highly desirable in magnetism since they can compete with the traditional inorganic magnets, showing at the same time superior properties from the point of view of their chemical adaptability and their structural and electronic versatilities. Most of the studies have been performed in CPs in which the coordination framework is magnetic. In these

materials, a rational chemical design has been crucial for the appearance of new properties and for controlling the effects of different stimuli on the magnetic properties. Cu(II), Ni(II) and Co(II) metals are often used as metal nodes for this application.[71,72]

Sensors

Lanthanide CPs have been studied for luminescence properties due to their higher thermal stability than the pure organic linker and, moreover, for the effect of the metal in the emission wavelength.[73,74] They are used as luminescent sensors.[21] CPs based on d^{10} metal centers have shown high luminescence properties and they have been utilized as luminescent probes for the detection of nitroaromatic compounds and metal ions. On the other hand, selective and sensitive detection of a trace amount of metal ions (Fe(III), Al(III), Pb(II), Hg(II), Cu(II), etc.) with luminescent coordination polymers has received great attention due to the fact that some metal ions have important effects in biological systems and are also environmentally toxic to human life.
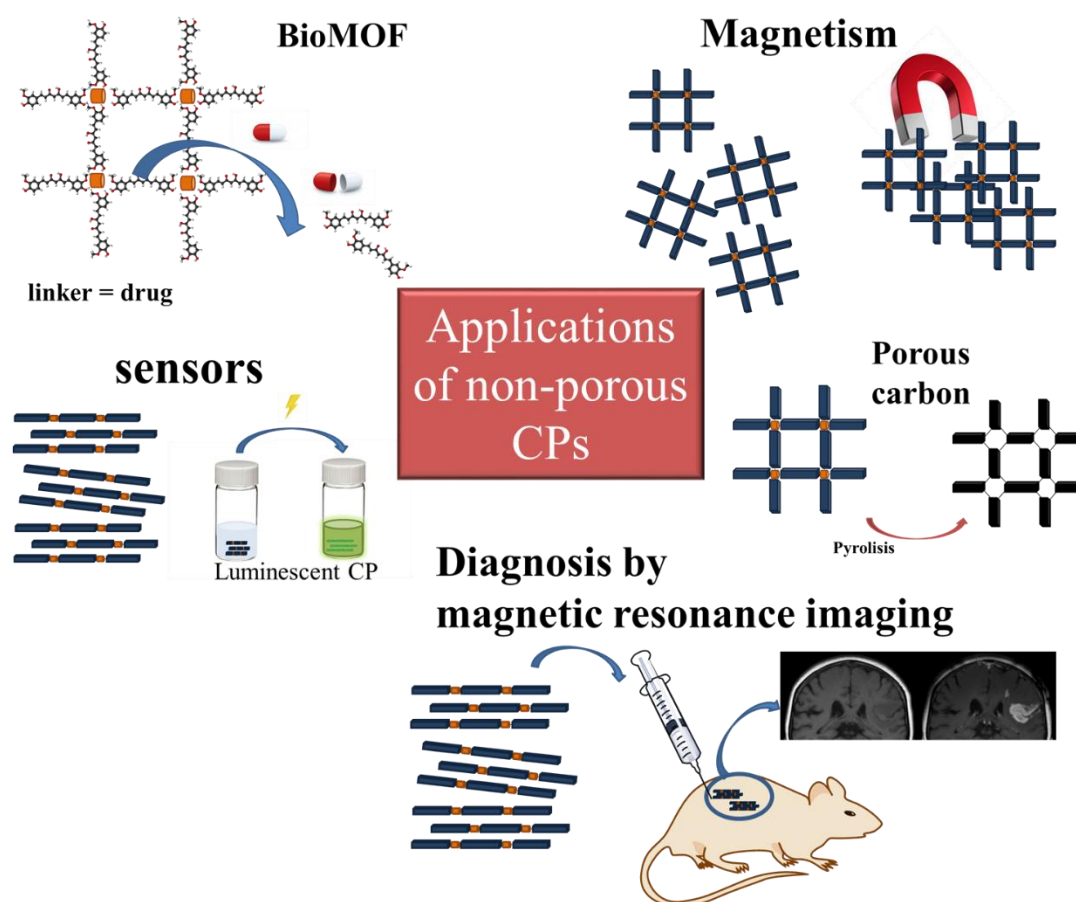
Figure 1.10. General schematic representation of applications of porous MOFs.

1.1.3. Synthesis

There are many different approaches for MOF synthesis, being the most widely used the solvothermal and controlled evaporation methods. Both are time consuming techniques that generally use toxic organic solvents. Besides, samples often require post-processing, with extensive cleaning and dry periods. Nowadays, alternative methodologies have been matured to overcome these drawbacks. The first objective has been to develop greener technologies by either reducing the amount of organic solvent used in the synthesis or by using alternative clean solvents, like ionic liquids or supercritical fluids. Moreover, complementary ways of providing energy to the reaction have been explored, such as using electrical potential (electrochemistry), electromagnetic radiation (microwaves), mechanical waves (ultrasound) or mechanical forces (mechanochemistry).[75] New synthetic methods have been developed around them, leading in some cases to new compounds that cannot be obtained by conventional routes. In Fig. 1.11, the most used techniques for MOFs synthesis are represented in chronological order of development. This thesis focuses in one of these alternatives, by developing the use of supercritical carbon dioxide for MOFs synthesis.
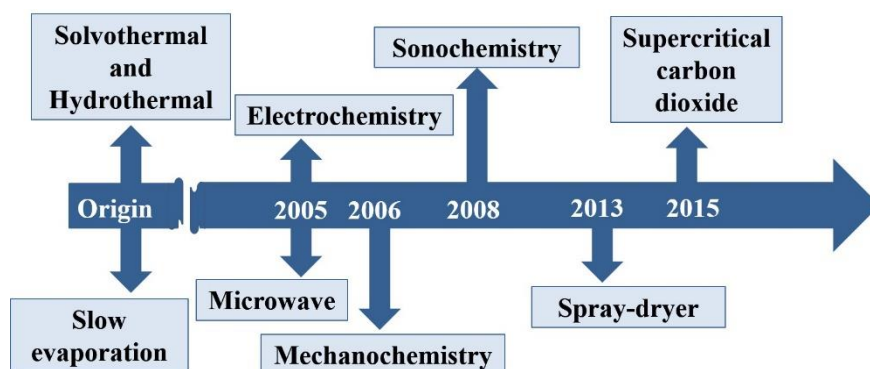
Figure 1.11. Chronological line of the main methods developed for MOFs synthesis.

In typical crystallization from solution processes, crystal growth is described through classical routes by the addition of solute (that is a monomer) from the solution to the crystal surface. However, MOFs crystallization mechanisms are being reviewed and described to proceed through the aggregation of nanoentities followed by surface recrystallization in a non-classical approach, similar to the one previously described for zeolites. This non-classical pathway can give rise to a wide variety of precursors that potentially serve as growth units for crystallization (Fig. 1.12).[76] For unknown compounds, one important experimental target objective is to obtain high quality crystals with a size large enough for crystal structure elucidation through single crystal X-ray diffraction techniques.
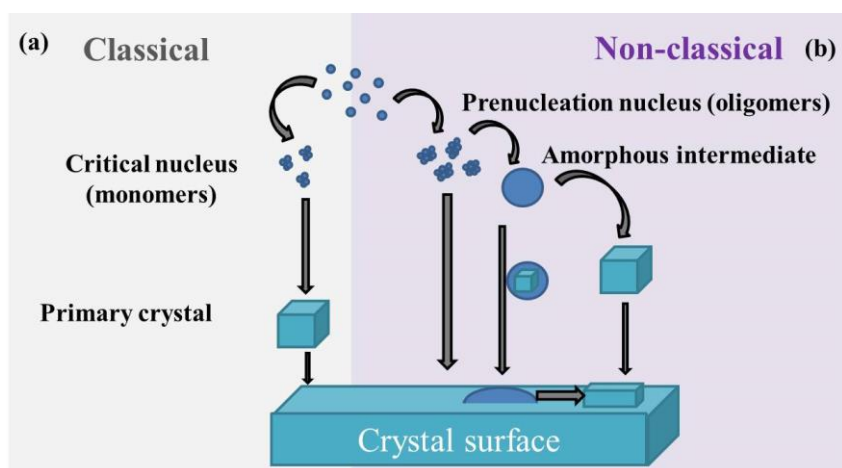
Figure 1.12. Representation of different crystallization pathways: (a) crystal growth through classical routes, which occurs by the addition of solute (monomer) from solution to the crystal; and (b) non-classical pathway, in which aggregated precursors (oligomers, amorphous particles) serve as growth units for crystallization.[76,77]

1.1.3.1. Solvothermal

The most used method for the synthesis of CPs are through reactions performed under hydrothermal (in water)[78] or solvothermal (in organic solvent) conditions.[79] These are reactions that occur above the boiling point of the solvent in tightly closed vessels under autogenous pressure.[80] Both are slow processes performed in ovens, with reaction times lasting from several hours to days.[75] The parameters used to control the product characteristics are the chosen solvent -usually high boiling point basic solvents like N,N-dimethylformamide (DMF), dimethylacetamide (DMA), but also alcohols and mixtures-, the reaction time -from hours to several days-, the temperature -from 350 to 425 K-, the autogenous pressure -straightforwardly related to the filled volume degree in the autoclave-, the pH -from neutral to basic-, the reagents concentration and the reagents molar ratio.[81] Some examples of known MOFs synthetized by this methodology are the MOF-5,[82] MOF-177[75] and HKUST-1 (Fig. 1.8).[83]

1.1.3.2. Controlled evaporation

Controlled slow evaporation is a conventional technique frequently used to crystallize large crystals. Slow evaporation leads to low supersaturation levels, and thus to the formation of a small number of nuclei, which then grow slowly.[84] The process can be carried out at low temperature, often under atmospheric conditions with no need of external energy supply.[85] Low-boiling point solvents such as methanol, chloroform or dichloromethane are generally used.

1.1.3.3. Electrochemical

An electrochemical reaction is any process caused or aided by the passage of an electric current, involving the transfer of electrons between two substances. BASF has deeply explored this methodology for MOFs synthesis, patenting in 2005 this procedure to crystallize the HKUST-1 by anodic dissolution.[86,87] Basically, the synthesis consists of immersing a metal plate that acts as the electrode in a solution with the organic linker and an electrolyte. By applying a voltage, cations are released from the metal electrode to the solution to further react with the organic linker.[88] Parameters to be controlled are the applied voltage, current density, distance between the electrodes, synthesis time, used solvent and linker, and electrolyte concentration.[89] Electrochemical synthesis offers the advantages of possibility of continuous synthesis,[87] mild conditions and reduced reaction time.[88] Moreover, MOFs are obtained without contra-ions adsorbed in the pores, which result in materials with higher surface area values than using conventional routes.[89] Further, cathodic deposition has been developed by using chemically inert electrodes and a solution that contains the organic linker and the metal ions.[88] The deposition of the MOF occurs when the pH is increased near the cathodic surface.[90,91] Electrophoretic deposition[92] and galvanic displacements are also being investigated.[93] One of the main drawbacks found for MOFs synthesis in electrochemistry is that the used solvents are polar, like water, while most linkers only present significant solubility in organic solvents.[87]

1.1.3.4. Mechanochemical

Mechanochemical reactions are induced by mechanical energy.[94,95] These reactions are performed in a mortar or mill, without the use of organic solvents, or with only a very little amount added to induce the reaction in liquid-assisted gridding.[75] In this reaction, intramolecular bonds of the reagents are broken by mechanical forces, thus inducing the chemical transformation. It is a well-known technique in metallurgy and it has penetrated into many areas of chemistry.[88] The first example of synthesis of a MOF using mechanochemistry was reported by Pichon *et al.* in 2006.[96] In the process, a Cu(II) acetate ($Cu(OAc)_2 \cdot 3H_2O$) and isonicotinic acid (INA) were milled together generating the product $[Cu(INA)_2]_n$ with acetic acid and water molecules in the pores. The technique has numerous environmental advantages, since neither external heating nor organic solvent in significant quantities is needed. In addition, activated metal oxides can also be used as substitutes of metal salts; thus, avoiding the need of eliminating the contra-ion of the metal and increasing the yield. For

example, ZnO has recently been shown to be suitable for the mechanosynthesis of several ZIF phases.[75,97,98] The main drawback of this technique is the small size and inhomogeneous morphology of the obtained crystals. Moreover, post-treatment steps with solvents, such as purification from excess reagents or secondary products, are generally needed.

1.1.3.5. Microwave

In microwave synthesis, the reaction medium is heated by the interaction of electromagnetic waves with the polarizable, conducting and/or magnetic species present in the media. This way of heating is more efficient and faster than electric methods. Important parameters to be controlled are solvent selection, running time and intensity of energy input. The technique can be used to control the morphology, particle size and phase of precipitated products.[99] Alcohols, water and ionic liquids with a high dipole moment are considered the best solvents for this synthesis.[100] In the new microwave set-ups, it is even possible to control the temperature and pressure during the reactions, i.e., solvothermal processes aided by microwave heating can be performed. The reaction time is often reduced in comparison with solvothermal processes. However, since crystallization is very fast, usually only small crystals are obtained.[75] The first synthesis of a MOF in a microwave was described by Jhung *et al*. in 2005.[101] They reported the water-based synthesis of the MIL-100(Cr) in presence of hydrofluoric acid.

1.1.3.6. Sonochemistry

In sonochemistry, the application of high-frequency ultrasound to a reaction mixture provokes enough kinetic energy to drive reactions to completion.[102,75] Ultrasounds provide unusual reaction conditions during a short period of time, related to extremely high temperatures and pressures produced by cavitation.[102] The collapse of the bubbles created by the acoustic waves produces a large energy concentration, resulting in an extremely high local temperature.[103] These processes are carried out in low vapor pressure solvents, like water, ionic liquids or glycerol.[104] The first sonochemical example reported for MOFs was the synthesis of a Zn carboxylate frameworks ($Zn_3(btc)_2 \cdot 12H_2O$) described by Qui *et al.* in 2008.[105] Further, the synthesis of several well-known MOFs has been performed by using this methodology, for example MOF-5[106] and HKUST-1 (Fig. 1.8).[107] One important disadvantage is that polar solvents are preferred for sonication, and organic linkers are often not soluble in them.

1.1.3.7. Spray-drying

The use of spray-drying technology is a new alternative for MOF synthesis developed by Maspoch's team in 2013.[108] Spray-drying methods are widely known in industry. On them, solutions of precursors are atomized through a spray into microdroplets. Precursor droplets contact a gas stream heated to a certain temperature, which causes the evaporation of the solvent leading to the formation of nanoparticles.[88] UiO-66, ZIF-8[109] and HKUST-1 (Fig. 1.8)[108] are examples of MOFs synthetized following this methodology. The main advantage is that the process can be scaled-up in a continuous mode by developing very fast reactions.[110]

1.2. Introduction to supercritical carbon dioxide technology

Currently, strong emphasis is paid on the development of more sustainable processes at industrial scale, which should be developed from the laboratory scale. Human safety and environmental concerns have become determining factors for industrial development. Many conventional chemical processes involve an excessive use of volatile organic solvents (VOCs) in the different steps. It has been estimated that currently more than 23 million tonnes of VOC are emitted to the atmosphere per year by the chemical industry.[111] Hence, the search for alternative methodologies, in which the use of VOCs is reduced or replaced, is a key objective in chemical and materials research. Among the different approaches developed to achieve this goal, the design of solvent-free processes and the use of alternative solvents with less environmental impact (green solvents) are the most used ones. By definition, a green solvent is a less toxic substitute that allows to perform the same task or process than the traditional solvent, but in an environmentally conscious manner.[112] The selected green solvent must present better EHS (environmental, health and safety) qualifications than the substituted VOC.[113] Some examples of solvents considered green are water, ethanol, propyl acetate, ethyl acetate, ionic liquids and some supercritical fluids such as carbon dioxide, water or ethanol.[114] From these alternatives, the use of supercritical carbon dioxide ($scCO_2$) as a green solvent is the main focus of this thesis. Therefore, some important concepts of supercritical fluid technology are introduced, with a particular focus on $scCO_2$. The principles, characteristics and applications in synthesis and/or processing are described. The sustainability of the process is justified by correlation with the green chemistry principles.

1.2.1. Principles and characteristics of supercritical fluids

A supercritical fluid is any substance subjected to a pressure and temperature higher than the respective critical pressure (Pc) and temperature (Tc) (Fig. 1.13).[115,116] At supercritical conditions, these fluids have characteristics of both liquids and gasses, showing an interesting combination of properties. They present high diffusivity values that enhances mass transfer properties, low viscosity and practically null surface tension similar to those of gases, while they have densities similar to liquids (Table 1.2).[116,117] Besides, the properties of SCFs can be tuned by small changes in pressure and/or temperatures, which allows tailoring fluids with the characteristics required for each application.[118] Table 1.3 provides a list of common supercritical fluids and their Tc and Pc.

Table 1.2. Comparison of typical values of physical properties of gasses, supercritical fluids and liquids.[116,119]

Properties	Gas	SCF	Liquid
Density (Kg·m⁻³)	0.6-2	200-800	600-1600
Viscosity (μPa·s)	10-30	10-50	20-300
Diffusivity (mm²·s⁻¹)	1-10	0.01-0.1	0.0001-0.001
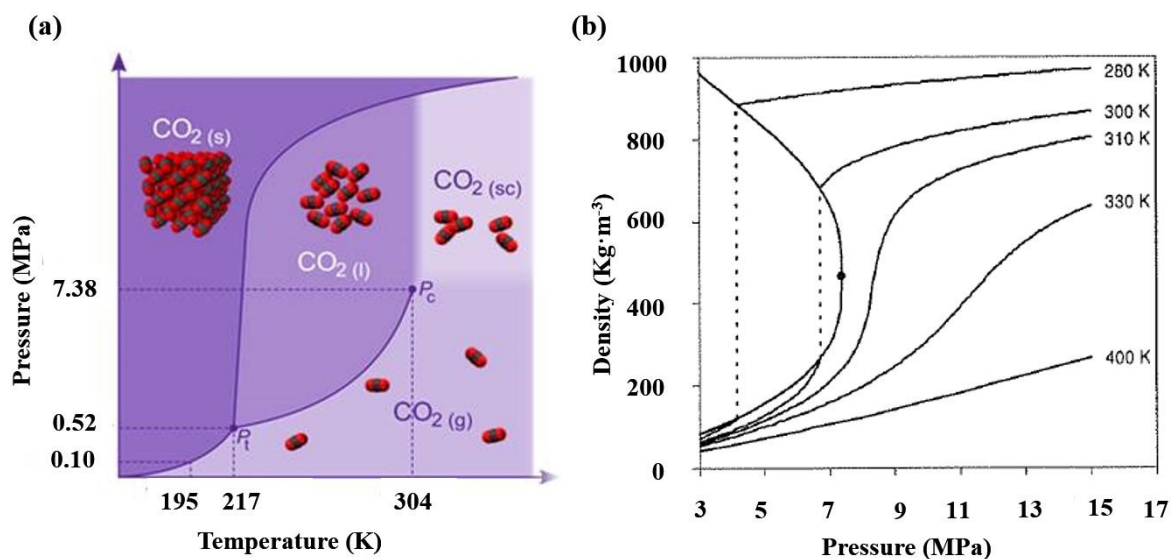
Figure 1.13. Phase diagrams of scCO₂ showing: (a) P *vs*. T, and (b) ρ *vs*. P at several temperatures.[117]

Table 1.3. Critical points of typical compounds used as SCF solvents.[120,114]

Molecule	Critical temperature T$_c$ (K)	Critical pressure P$_c$ (MPa)
CH$_4$	191	4.6
N$_2$O	309	7.2
CF$_3$H	299	4.8
CO$_2$	**304**	**7.4**
C$_2$H$_6$	305	4.9
C$_3$H$_8$	370	4.3
C$_2$H$_5$OH	514	6.1
CH$_3$OH	512	8.1
C$_3$H$_6$O	508	4.7
H$_2$O	647	22.1

Among the number of possible substances, CO$_2$ is considered the greenest option for chemical processing using SCF technology. This fluid has a low critical point (304.3 K and 7.4 MPa), is inert, inexpensive, non-inflammable and has a generally regarded as safe (GRAS) status.[115] Moreover, scCO$_2$ is considered a green solvent, as it is naturally abundant and non-toxic. Technology using scCO$_2$ is not generating greenhouse effect, since it is reusing CO$_2$ produced by other industries.[121] Chemically, CO$_2$ is a non-polar linear molecule with a strong quadrupole moment.[117] Moreover, CO$_2$ has some Lewis acid character, since in the molecule the oxygens are attracting more electrons than the carbon, thus generating a negative density charge in the oxygens. As a consequence of the quadrupole moment and the acid character, this fluid is able to dissolve volatile and low polarity compounds with relatively low molecular weight. Its capacity for solubilisation is comparable to that of dioxane or hexane.[122] If necessary, the solubility of different compounds in scCO$_2$ can be enhanced with the addition of a small amount of a co-solvent. Commonly, ethanol or acetone are used in a percentage of 5-10 v%.[123-125] The addition of a co-solvent has effect in the intermolecular forces stablished between the solvent and the solute, usually by increasing the attractive interactions.

1.2.2. Applications of scCO$_2$

Searching in the data base of the Web of Science (WOS) the concepts: *supercritical fluid** OR *SCF** OR *supercritical carbon dioxide* OR *supercritical CO$_2$* in May 2019 it arises 68,195 results. In Fig. 1.14, it can be clearly observed that the research in the field of SCFs has been increasing steadily in the last 30 years, since they were firstly proposed for industrial applications.
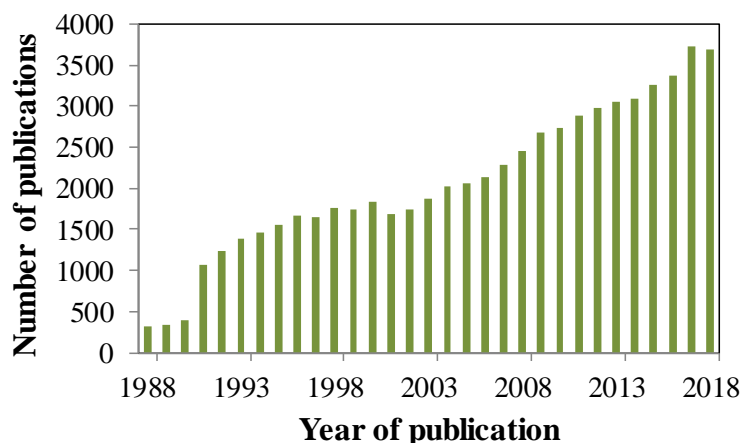
Figure 1.14. Number of publications in SCF technology (source WOS).

Particularly, scCO₂ technology has been mainly developed for applications related to food, biomedical and pharmaceutical industries.[116] Furthermore, there are many other areas, e.g., catalysis, sensors, plastics, concrete or textile, for which the technology has been used. ScCO₂ technology can be designed for many different processes, such as drying, cleaning, degreasing, impregnation, extraction, tanning and particle formation, among others.[126] The main areas of application of scCO₂ are schematized in Fig 1.15.
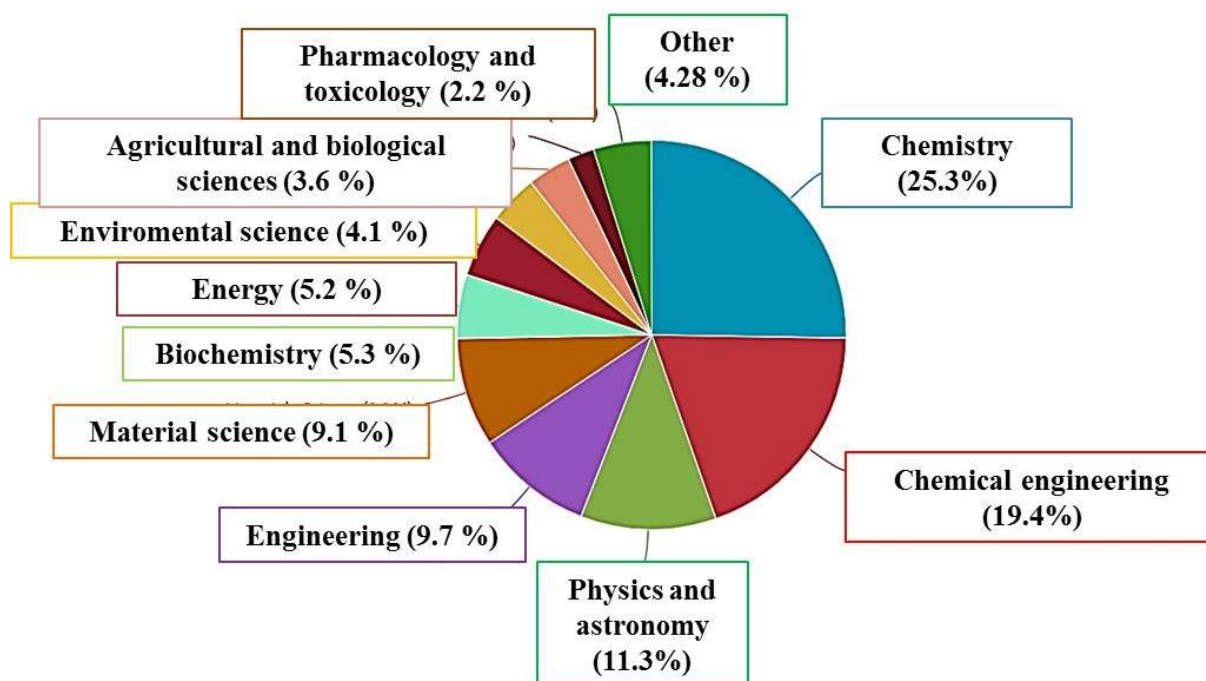
Figure 1.15. Analysis by percentage of the number of publications distributed by subject area (source Scopus data base).

1.2.2.1. Supercritical Fluid Extraction (SFE)

The earliest industrial application described for $scCO_2$ technology at industrial level was an extraction process, i.e., the decaffeination of green coffee beans, by using the $scCO_2$ as a substitute to circumvent the use of other solvents and their possible effects entirely.[127] The process was developed by Zosel at the Max Planck Institute and patented in 1963.[128] Up to now, supercritical fluid extraction (SFE) has been the most investigated and used process in the industry of $scCO_2$.[126] In SFE, one or more components (the extractants) are separated from another (the matrix) using a supercritical fluid as the extracting solvent. Extraction is usually performed from a solid matrix, although SFE from liquids has also been described.[129] The main advantage of SFE is the lack of residual solvent in the extractant at the end of the process. For that reason, it is widely used in the food, phytopharmaceutical and cosmetic industries and patented for many different applications. In Spain, one example of a well-known company that uses $scCO_2$ for SFE is DIAM Corchos SA. This company uses $scCO_2$ to eliminate trichloroanisole (TCA) from cork for further use as closing caps in wine bottles. TCA must be eliminated before cork use, since it is the product of a reaction between naturally-occurring fungi with environmental pollutants (chlorine) that causes the cork taint.[130]

1.2.2.2. Supercritical Fluid Chromatography (SFC)

Another well-known application of $scCO_2$ is in chromatography, first described in 1962 as "high-pressure gas chromatography.[126] The mobile phase in SFC is CO_2 at near or above its critical point. On one hand, the technique has many advantages with respect to liquid chromatography mainly related to short separation times achieved thanks to the high diffusivity of $scCO_2$.[131] On the other hand, the technique can be also superior to gas chromatography because it extends the molecular weight range of materials that can be separated. Moreover, thermally labile compounds can also be separated at low temperature in SFC.[132] Since $scCO_2$ is non-polar, this fluid often should be mixed with organic solvents to elute polar solutes. SFC has been applied in the pharmaceutical and food industries for the separation of unsaturated fatty acids and chiral compounds.[133-135]

1.2.2.3. Application of scCO₂ in polymer synthesis and processing

ScCO₂ has been used as an alternative to traditional organic solvents for polymer synthesis.[136] However, due to solubility drawbacks only low molecular weight compounds could be obtained. Exceptions are fluoropolymers and silicones with significant solubility in scCO₂. For instance, it has been possible the synthesis of poly(H,H-perfluorooctyl acrylate) in a homogeneous solution. This is a chemically resistant and noncorrosive material used for coatings.[137,138]

ScCO₂ is also widely used for polymers purification[139] and impregnation with soluble compounds.[140,141] These applications are based on the important plasticization effect of CO_2 when it is dissolved in amorphous or semi-crystalline polymers, thus lowering the polymer glass transition temperature. The swelling of the polymer and the further elimination of the gas lead to the formation of foams.[136] This foaming process is also widely investigated for biopolymers tissue engineering applications.[142-144]

1.2.2.4. ScCO₂ as a solvent for chemical reactions

ScCO₂ has some advantages for chemical processing, not only from an environmental point of view, but also considering its properties.[145] First, the CO_2 molecule cannot be oxidized, therefore it becomes useful as a solvent in oxidation reactions. Second, scCO₂ is an aprotic solvent, thus it can be used in reactions where labile protons could interfere in the main reaction. Third, scCO₂ is generally immune to free radical attack.[146] These advantages explain the large number of different reactions that have been studied using this medium,[145] such as hydrogenation (e.g., of cyclohexane),[147] catalytic hydroformylation,[146] Diels-Alder[148] or silanization[149,150] reaction. In addition, the preparation of inorganic nanoparticles has been studied through the decomposition of organometallic compounds in scCO₂. One example is the synthesis of gold nanoparticles from triphenylphosphine Au(I) perfluorooctanoate.[151] Moreover, reactions with catalysts have been extensively investigated in scCO₂, as in the extraction of heavy metals.[152] Nowadays, research is also focused on the use of CO_2 as a green feedstock for the sustainable synthesis of chemicals. It has been used as carbonation agent for the precipitation of inorganic carbonates.[153,154] Other examples are the hydrogenation of CO_2 to make formic acid, the synthesis of alkyl formiats[155,156] and the synthesis of organic chemicals, such as carbamates, ureas and isocyanate carbodiimides.[157]

1.2.2.5. Use of scCO₂ for precipitation and crystallization

ScCO₂ crystallization methods have already become viable alternatives to conventional organic solvent routes. The fundamental differences among the already developed supercritical crystallization techniques concern the role of scCO₂, used either as a solvent, in the rapid expansion of supercritical solutions, anti-solvent, in the group of gas anti-solvent techniques, or solute, in the particles from gas saturated solutions route.[158] A common feature in all of them is that the fluid is expanded through a restriction device or nozzle to create supersaturation in a spraying process. These methods are all recrystallization techniques applied to different materials for purification and particle size redistribution (micronization), without significantly affecting the chemical composition of the starting product. They have been developed in the pharmaceutical industry for drugs micronization and preparation of drug delivery systems.[159] Strategies for crystallization are described following, classified in three groups as a function of the CO_2 role.[116]

a) ScCO₂ as solvent

The first described scCO₂ crystallization technique was the rapid expansion of supercritical solutions (RESS) process (Fig 1.16).[160] In this case, the product was dissolved in the compressed fluid and rapidly depressurized through a nozzle, resulting in the precipitation of small and monodispersed particles.[161] The rapid expansion of the scCO₂ solution gives rise to a very steep increase in supersaturation, generated by pressure drop, in a very short period of time. Thus, homogeneous nucleation is most likely to occur, since supersaturation is homogeneously generated at the tip of the nozzle, point at which the speed of sound is reached. Scale-up of RESS process is limited by the poor solubility of many compounds in scCO₂. For products with low affinity for this solvent, polar co-solvents are used to increase the solubility.
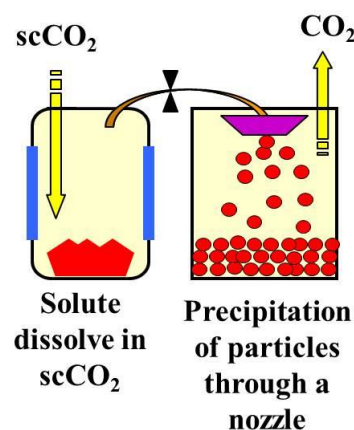
Figure 1.16. Schematic representation of RESS process.

For scCO₂, despite the current acquired knowledge in crystallization on one side and chemical reactions on the other,[162] the study of reactive crystallization processes, in which precipitation occurs by chemical reaction of two (or more) species, has not received a high level of attention. Only recently, the crystallization of cocrystals and metal-organic adducts using scCO₂ as anti-solvent and solvent, respectively, has been described.[163-165] This thesis gives new insights in this field by using scCO₂ as a solvent in the reactive crystallization process schematized in Fig. 1.17, in which reagents A (blue spheres) and B (red spheres) are mixed in scCO₂ and react after a certain induction time. In most of the cases, precipitation occurs in the presence of solid particles of one or both reagents that dissolve slowly. Heterogeneous nucleation is observed in the walls of the vial.
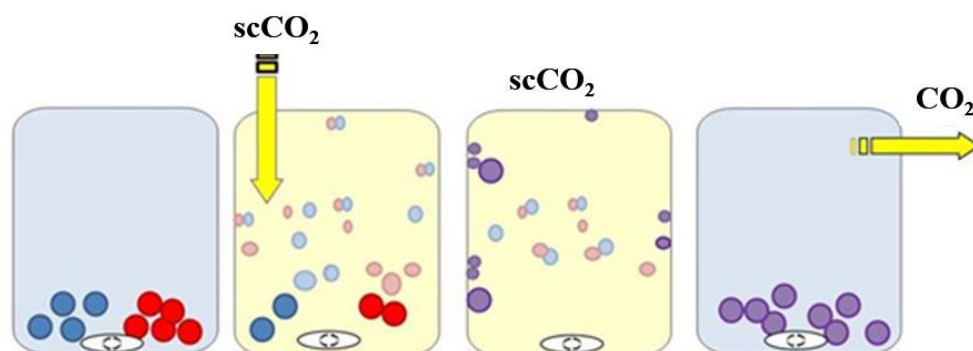
Figure 1.17. Schematic representation of heterogeneous formation of nuclei in reactive crystallization.

(b) ScCO₂ as an anti-solvent

This strategy is used for compounds with very low or null solubility in scCO₂. Several variations of the anti-solvent technique have been described, including the original batch gas anti-solvent (GAS)[166,167] or supercritical anti-solvent (SAS),[168] the semicontinuous compressed fluid anti-solvent (PCA),[169] (Fig. 1.18) and the aerosol solvent extraction system

(ASES)[170] mode operated with a coaxial nozzle. All of them rely on reducing the density and solvating power of the organic solvent, in which the solute is dissolved, by $scCO_2$ addition. Hence, $scCO_2$ must be partially or totally miscible with the liquid that contains the solute.[116] The wide variety of anti-solvent operational conditions provides high flexibility in product processing by choosing the adequate liquid solvent to dissolve the treated compound. The process has been applied to organics or organometallics, inorganic and polymeric compounds.
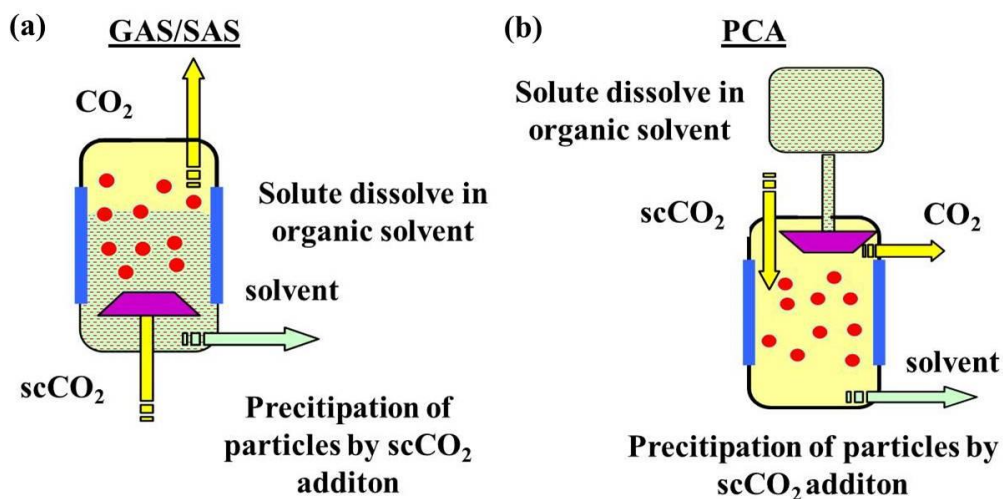
Figure 1.18. Schematic representation of two $scCO_2$ anti-solvent techniques: (a) batch GAS and SAS, and (b) semicontinuous PCA.

(c) ScCO₂ as a solute

The most known crystallization process in which $scCO_2$ can be considered as a solute is the particle formation from gas-saturated solutions (PGSS®) technique (Fig. 1.19). In this process, $scCO_2$ is dissolved (as a solute) in amorphous or semicrystalline high molecular weight materials (e.g., polymers, solid lipids or even some drugs). The pressurized gas diffuses into the product, lowering both its melting point and viscosity up to the formation of a liquid mixture. Particles are produced by spraying the mixture *via* a nozzle. During expansion, the complete evaporation of the gas occurs inducing the solidification of the liquid droplets and the formation of porous micrometric particles.[120,171] The process has been scale up in a continuous mode.[172]
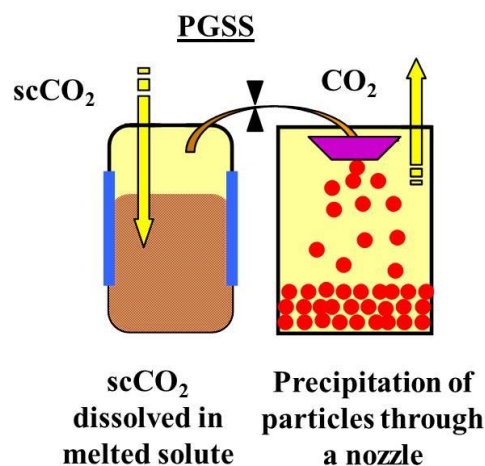
Figure 1.19. Schematic representation of PGSS process.

1.2.3. Green chemistry and scCO₂ technology

In 1998 Anastas and Warner described a list of 12 considerations in order to design processes and products that minimize or eliminate the use and generation of hazardous substance.[173] Currently, the 12 principles of green chemistry provide a road map for the design of a sustainable process. Most of these principles can be easily accomplished by using scCO₂ in the synthesis and processing of materials.[174] In short, scCO₂ avoids or minimizes the use of toxic organic solvents during synthesis and there is not residual toxic organic solvents in the final product. In addition, post-treatment or activation steps for solvent elimination are not necessary. This reduces waste generation and, moreover, scCO₂ processes are always designed to recycle the CO_2. Thus, it can be considered a zero-waste technology in regard of CO_2 production.[175] Often, the technology reuses CO_2 side-product of other industrial processes, such as in the ammonia production, which otherwise would be emitted to the atmosphere.[146] Besides, CO_2 has no inherent toxicity associated, being safe for human health.[176] Taking the correct established engineering measures, risks are limited and the exposition of workers to hazardous solvents is reduced. Within this premises, scCO₂ processes accomplish the green principles: *1) prevention of chemical waste*, 3) *design less hazardous processes,* 4) *chemical products should be as effective as possible for their designated purpose, but with minimum toxicity*, 5) *use safer solvents and auxiliaries* and, finally, 12) *minimize the potential for chemical accidents, including releases, explosions, and fires.* Additionally, scCO₂ technology is energetically efficient, since one-step process can be designed, the working volume is reduced at high-pressure and the amount of waste disposal is minimized. These aspects are related to principle 6) *energy requirements should be*

minimized. It is worth to mention that principle *8) avoid the use of chemical derivatives (blocking or protective groups)* is often also accomplished, since CO_2 is a solvent relatively inert, the protection of functional groups from solvent attack is not necessary. Moreover, CO_2 is a naturally abundant material as suggest in 7) *use renewable raw materials and feedstock.* Finally, CO_2 substitutes organic solvents, whose synthesis, use and disposal are ligated to CO_2 emissions. The use of scCO₂, in global, would decrease the total amount of CO_2 emitted to the atmosphere.[177]

All these green principles have been applied in this thesis by using mainly scCO₂ technology for the design of sustainable processes for CPs synthesis with desired characteristics.

1.3. Precedents and motivation of the thesis: CPs and scCO₂

Regarding the use of scCO₂ in CPs synthesis, the first thought has always been related to the analysis of the poor solvent capacity of this fluid for high-molecular weight or polar molecules, which, in principle, would rule out many possibilities in the synthesis of these compounds. An effective way to solve this problem is to create mixtures of solvents that own the capacity of solubilizing both polar and apolar substances. The first example of the application of this method was the successful preparation of MOFs in scCO₂ expanded organic solvents. The process mainly focused in the preparation of HKUST-1 in expanded DMF. [178-180] Mixtures comprising ionic liquids (ILs) and scCO₂, known as green "designer solvents", have also been proposed for CPs synthesis due to the possibility of tuning their specific properties for a particular need, either by changing the anion or cation in the IL or by varying the density of the scCO₂. However, literature on the use of scCO₂/IL mixtures for the synthesis of MOFs is scarce, reporting the formation of complex porous superstructures by using an unusual IL, a guanidinium salt, and fluorinated surfactants. [181-184] The addition of gas or liquid CO_2 has been described to increase the kinetics of MOFs formation in a more conventional imidazolium IL.[185] Until recently, the common use of scCO₂ in the area of MOFs has been mainly limited to the activation procedure, needed as a final step to empty the pores in porous compounds without compromising its structural integrity.[186] Activation consists in the removal of solvent molecules or other chemicals used in the synthesis and retained in the pores of the material. There are other different strategies for removing the guest molecules, like combined heating and vacuum, freeze-drying and more sophisticated methods, such as photochemical treatment. Nevertheless, the scCO₂ activation method has

given surface areas higher than the others.[186-189] This drying technology was previously designed for the preparation of aerogels. Further, the scCO$_2$ technology has been used to demonstrate single crystal-single crystal structural transformation in complex MOFs.[190] Additionally, there are some examples of the immobilization of active agents[191] and nanoparticles into porous MOFs by using scCO$_2$.[192]

The use of scCO$_2$ in the field of CPs and MOFs can go further, as it was pointed out by the research group of Domingo (Supercritical Fluids and Functional Materials (SFFM) at the ICMAB), where this thesis has been performed. In 2015 López-Periago *et al.* published an innovative example of the preparation of a 1D CP using exclusively scCO$_2$.[18] In this work, an easy, fast and eco-friendly technique for the synthesis of these compounds was outlined. Particularly, copper acetylacetonate and two bidentate linkers, namely, 4,4'-bipyridine and 4,4'-trimethylenedipyridine, were reacted under compressed CO$_2$ at 333 K and 20 MPa. During this four years, the research in CPs in scCO$_2$ has been extended in the scientific community[193,194] and industrial area.[195] Indeed, the synthesis of the imidazolate ZIF-8 phase has been deeply study in scCO$_2$. López-Domínguez *et al.* demonstrated en 2017 the formation of porous hierarchical microstructures of this phase in scCO$_2$ without any cosolvent. [196] In 2018, Marrett *et al.* proposed a scalable synthesis for ZIF-8 in scCO$_2$ directly from ZnO.[197] In 2016, the start-up ACSYNAM was created in the framework of a patented a methodology for the syntheis of MOFs with liquid and supercritical CO$_2$. Currently, the company is commercializing well-known MOFs, such as ZIF-8, HKUST-1, MOF-74 and MOF-5.[195]

In previous studies, scCO$_2$ has been used as a solvent for pore generation and modification, including in foaming, drying, impregnation and surface grafting, which have allowed the settlement of important parameters influencing the technology.[198] As a logical consequence of this evolution, it emerges the possibility of using scCO$_2$ directly to synthetize nanoporous compounds in a sustainable fashion. On the basis of the analysis of the state of the art in scCO$_2$ crystallization and conventional polymeric networks synthesis, we thought in this thesis project that the successful preparation of different CPs and MOFs was a real possibility through the right choice of building blocks. ScCO$_2$ appears as an attractive medium to synthesize these materials by reactive crystallization due to the potential solubility of numerous precursors in this fluid, including organometallic compounds and some typical organic bridging molecules, such as pyridine-based linkers. This opens new avenue in the use of scCO$_2$ for the synthesis of complex nanostructured products.

The main motivation of this thesis is the exploration of this new technology based on scCO$_2$ for the synthesis of new CPs. Indeed, there are extensive possibilities for research, with the prof-of-concept already given.[18] It becomes necessary to demonstrate if the method can be exported to other systems, stablishing a protocol. To answer some of these questions, a new methodology has been developed in this thesis to explore new single and mixed CPs with different dimensionalities, as well as the area of bioMOFs. In some cases, synthetic alternatives have been stablished when metal solubility problems have been found. A study of the effect of the solvent in the crystallization process has been performed.

1.4. References

(1) Bailar, J. C. Preparative inorganic reactions. W. L. Jolly, Interscience, New York, **1964**.

(2) Kraft, A. On the discovery and history of prussian blue. *Bull. Hist. Chem.*, **2008**, 32 (2), 61-67.

(3) Hoskins, B. F.; Robson, R. Design and construction of a new class of scaffolding-like materials comprising infinite polymeric frameworks of 3D-linked molecular rods. A reappraisal of the zinc cyanide and cadmium cyanide structures and the synthesis and structure of the diamond-related. *J. Am. Chem. Soc.,* **1990**, 112 (4), 1546-1554.

(4) Batten, S. R.; Champness, N. R.; Chen, X.-M.; Garcia-Martinez, J.; Kitagawa, S.; Öhrström, L.; O'Keeffe, M.; Suh, M. P.; Reedijk, J. Coordination polymers, metal-organic frameworks and the need for terminology guidelines. *CrystEngComm.,* **2012**, 14 (9), 3001-3004.

(5) Kondo, M.; Yoshitomi, T.; Matsuzaka, H.; Kitagawa, S.; Seki, K. Three-dimensional framework with channeling cavities for small molecules: {[M$_2$(4, 4′-Bpy)$_3$(NO$_3$)$_4$]·xH$_2$O}n (M = Co, Ni, Zn). *Angew. Chemie Int. Ed. English.,* **1997**, 36 (16), 1725-1727.

(6) Rowsell, J. L. C.; Yaghi, O. M. Metal-organic frameworks: a new class of porous materials. *Microporous Mesoporous Mater.,* **2004**, 73 (1-2), 3-14.

(7) Fromm, K. M. Coordination polymers. Design, analysis and application. By Stuart R. Batten, Suzanne M. Neville and David R. Turner. *Angew. Chemie Int.* Ed., **2009**, 48 (27), 4890-4891.

(8) Batten, S. R.; Champness, N. R.; Chen, X.-M.; Garcia-Martinez, J.; Kitagawa, S.; Öhrström, L.; O'Keeffe, M.; Paik Suh, M.; Reedijk, J. Terminology of metal-organic frameworks and coordination polymers (IUPAC Recommendations 2013). *Pure Appl. Chem.,* **2013**, 85 (8), 1715-1724.

(9) Biradha, K.; Ramanan, A.; Vittal, J. J. Coordination polymers versus metal-organic frameworks. *Cryst. Growth Des.,* **2009**, 9 (7), 2969-2970.

(10) Moghadam, P.; Li, A.; Wiggin, S. B.; Tao, A.; Maloney, A. G. P.; Wood, P. A.; Ward, S. C.; Fairen-Jimenez, D. Development of a Cambridge Structural Database Subset: A collection of metal-organic frameworks for past, present, and future. *Chem. Mater.,* **2017**, 29, 7, 2618-2625.

(11) Almeida Paz, F. A.; Klinowski, J.; Vilela, S. M. F.; Tomé, J. P. C.; Cavaleiro, J. A. S.; Rocha, J. Ligand design for functional metal-organic frameworks. *Chem. Soc. Rev.*, **2012**, 41 (3), 1088-1110.

(12) Kitagawa, S.; Kitaura, R.; Noro, S. Functional porous coordination polymers. *Angew. Chemie Int. Ed.,* **2004**, 43 (18), 2334-2375.

(13) Qiu, S.; Zhu, G. Molecular engineering for synthesizing novel structures of metal-organic frameworks with multifunctional properties. *Coord. Chem. Rev.*, **2009**, 253 (23-24), 2891-2911.

(14) Haldar, R.; Maji, T. K. Metal-organic frameworks (MOFs) based on mixed linker systems: structural diversities towards functional materials. *CrystEngComm.,* **2013**, 15 (45), 9276-9295.

(15) Eddaoudi, M. Systematic design of pore size and functionality in isoreticular MOFs and their application in methane storage. *Science.*, **2002**, 295 (5554), 469-472.

(16) Jiang, H.-L.; Makal, T. A.; Zhou, H.-C. Interpenetration control in metal-organic frameworks for functional applications. *Coord. Chem. Rev.,* **2013**, 257 (15-16), 2232-2249.

(17) James, S. L. Metal-organic frameworks. *Chem. Soc. Rev.,* **2003**, 32 (5), 276-288.

(18) López-Periago, A.; Vallcorba, O.; Frontera, C.; Domingo, C.; Ayllón, J. A. Exploring a novel preparation method of 1D metal organic frameworks based on supercritical CO_2. *Dalton Trans.,* **2015**, 44 (16), 7548-7553.

(19) Therrien, B. Coordination chemistry of 2,4,6-tri(pyridyl)-1,3,5-triazine ligands. *J. Organomet. Chem.,* **2011**, 696 (3), 637-651.

(20) Banerjee, D.; Wang, H.; Deibert, B. J.; Li, J. Alkaline earth metal-based metal-organic frameworks: synthesis, properties, and applications. Wiley-VCH Verlag GmbH & Co. KGaA: Weinheim, Germany, **2016**, 73-103.

(21) Armelao, L.; Bottaro, G.; Quici, S.; Cavazzini, M.; Scalera, C.; Accorsi, G. Synthesis and photophysical characterization of highly luminescent silica films doped with substituted 2-hydroxyphthalamide (iam) terbium complexes. *Dalton Trans.,* **2011**, 40 (43), 11530-11538.

(22) García-González, C. A.; Fraile, J.; López-Periago, A.; Saurina, J.; Domingo, C. Measurements and correlation of octyltriethoxysilane solubility in supercritical CO_2 and assembly of functional silane monolayers on the surface of nanometric particles. *Ind. Eng. Chem. Res.,* **2009**, 48 (22), 9952-9960.

(23) Dardin, A.; DeSimone, J. M.; Samulski, E. T. Fluorocarbons dissolved in supercritical carbon dioxide. NMR evidence for specific solute-solvent interactions. *J. Phys. Chem. B,* **1998**, 102 (10), 1775-1780.

(24) Mendes, R. F.; Almeida Paz, F. A. Transforming metal-organic frameworks into functional materials. *Inorg. Chem. Front.,* **2015**, 2 (6), 495-509.

(25) Pettinari, C.; Marchetti, F.; Mosca, N.; Tosi, G.; Drozdov, A. Application of metal-organic frameworks. *Polym. Int.,* **2017**, 66 (6), 731-744.

(26) Liu, J.; Chen, L.; Cui, H.; Zhang, J.; Zhang, L.; Su, C.-Y. Applications of metal-organic frameworks in heterogeneous supramolecular catalysis. *Chem. Soc. Rev.,* **2014**, 43 (16), 6011-6061.

(27) Zhang, S.-Y.; Jensen, S.; Tan, K.; Wojtas, L.; Roveto, M.; Cure, J.; Thonhauser, T.; Chabal, Y. J.; Zaworotko, M. J. Modulation of water vapor sorption by a fourth-generation metal-organic material with a rigid framework and self-switching pores. *J. Am. Chem. Soc.,* **2018**, 140 (39), 12545-12552.

(28) Furukawa, H.; Cordova, K. E.; O'Keeffe, M.; Yaghi, O. M. The chemistry and applications of metal-organic frameworks. *Science.,* **2013**, 341 (6149), 1230444 (1-12).

(29) Park, K. S.; Ni, Z.; Cote, A. P.; Choi, J. Y.; Huang, R.; Uribe-Romo, F. J.; Chae, H. K.; O'Keeffe, M.; Yaghi, O. M. Exceptional chemical and thermal stability of zeolitic imidazolate frameworks. *Proc. Natl. Acad. Sci.,* **2006**, 103 (27), 10186-10191.

(30) Kandiah, M.; Nilsen, M. H.; Usseglio, S.; Jakobsen, S.; Olsbye, U.; Tilset, M.; Larabi, C.; Quadrelli, E. A.; Bonino, F.; Lillerud, K. P. Synthesis and stability of tagged UiO-66 Zr-MOFs. *Chem. Mater.,* **2010**, 22 (24), 6632-6640.

(31) Kaye, S. S.; Dailly, A.; Yaghi, O. M.; Long, J. R. Impact of preparation and handling on the hydrogen storage properties of $Zn_4O(1,4\text{-benzenedicarboxylate})_3$ (MOF-5). *J. Am. Chem. Soc.,* **2007**, 129 (46), 14176-14177.

(32) Rowsell, J. L. C.; Yaghi, O. M. Strategies for hydrogen storage in metal-organic frameworks. *Angew. Chemie - Int. Ed.,* **2005**, 44 (30), 4670-4679.

(33) Yuan, S.; Feng, L.; Wang, K.; Pang, J.; Bosch, M.; Lollar, C.; Sun, Y.; Qin, J.; Yang, X.; Zhang, P.; Wang, Q.; Zou, L.; Zhang, Y.; Zhang, L.; Fang, Y.; Li, J.; Zhou, H-C. Stable metal-organic frameworks: design, synthesis, and applications. *Adv. Mater.,* **2018**, 30 (37), 1704303 (1-35).

(34) Lee, Y.-R.; Jang, M.-S.; Cho, H.-Y.; Kwon, H.-J.; Kim, S.; Ahn, W.-S. ZIF-8: A comparison of synthesis methods. *Chem. Eng. J.,* **2015**, 271, 276-280.

(35) Farha, O. K.; Eryazici, I.; Jeong, N. C.; Hauser, B. G.; Wilmer, C. E.; Sarjeant, A. A.; Snurr, R. Q.; Nguyen, S. T.; Yazaydın, A. Ö.; Hupp, J. T. Metal-organic framework materials with ultrahigh surface areas: is the sky the limit?. *J. Am. Chem. Soc.,* **2012**, 134 (36), 15016-15021.

(36) Bao, Z.; Chang, G.; Xing, H.; Krishna, R.; Ren, Q.; Chen, B. Potential of microporous metal-organic frameworks for separation of hydrocarbon mixtures. *Energy Environ. Sci.,* **2016**, 9 (12), 3612-3641.

(37) Wang, B.; Xie, L.-H.; Wang, X.; Liu, X.-M.; Li, J.; Li, J.-R. Applications of metal-organic frameworks for green energy and environment: new advances in adsorptive gas separation, storage and removal. *Green Energy Environ.,* **2018**, 3 (3), 191-228.

(38) Yu, J.; Xie, L.-H.; Li, J.-R.; Ma, Y.; Seminario, J. M.; Balbuena, P. B. CO_2 Capture and separations using MOFs: computational and experimental studies. *Chem. Rev.,* **2017**, 117 (14), 9674-9754.

(39) Millward, A. R.; Yaghi, O. M. Metal-organic frameworks with exceptionally high capacity for storage of carbon dioxide at room temperature. *J. Am. Chem. Soc.,* **2005**, 127 (51), 17998-17999.

(40) Trickett, C. A.; Helal, A.; Al-Maythalony, B. A.; Yamani, Z. H.; Cordova, K. E.; Yaghi, O. M. The chemistry of metal-organic frameworks for co₂ capture, regeneration and conversion. *Nat. Rev. Mater.,* **2017**, 2 (8), 1-16.

(41) Abid, H. R.; Tian, H.; Ang, H.-M.; Tade, M. O.; Buckley, C. E.; Wang, S. Nanosize Zr-metal organic framework (UiO-66) for hydrogen and carbon dioxide storage. *Chem. Eng. J.,* **2012**, 187, 415-420.

(42) He, Y.; Zhou, W.; Qian, G.; Chen, B. Methane storage in metal-organic frameworks. *Chem. Soc. Rev.,* **2014**, 43 (16), 5657-5678.

(43) Peng, Y.; Krungleviciute, V.; Eryazici, I.; Hupp, J. T.; Farha, O. K.; Yildirim, T. Methane storage in metal-organic frameworks: current records, surprise findings, and challenges. *J. Am. Chem. Soc.,* **2013**, 135 (32), 11887-11894.

(44) BASF Metal organic frameworks (MOFs): innovative fuel systems for natural gas vehicles (NGVs). *Chem. Soc. Rev.,* **2014**, 43 (16), 6173-6174.

(45) Notman N. MOFs find a use. *Chem. World,* **2017**, 2-10.

(46) Frameworks for commercial success. *Nat. Chem.,* **2016**, 8 (11), 987-987.

(47) Keskin, S.; Kizilel, S. Biomedical applications of metal organic frameworks. *Ind. Eng. Chem. Res.,* **2011**, 50 (4), 1799-1812.

(48) Horcajada, P.; Serre, C.; Vallet-Regí, M.; Sebban, M.; Taulelle, F.; Férey, G. Metal-organic frameworks as efficient materials for drug delivery. *Angew. Chemie Int. Ed.,* **2006**, 45 (36), 5974-5978.

(49) Ferey, G. A chromium terephthalate-based solid with unusually large pore volumes and surface area. *Science.,* **2005**, 309 (5743), 2040-2042.

(50) Janiak, C.; Vieth, J. K. MOFs, MILs and more: concepts, properties and applications for porous coordination networks (PCNs). *New J. Chem.,* **2010**, 34 (11), 2366-2388.

(51) Horcajada, P.; Chalati, T.; Serre, C.; Gillet, B.; Sebrie, C.; Baati, T.; Eubank, J. F.; Heurtaux, D.; Clayette, P.; Kreuz, C.; Chang, J.-S.; Hwang, Y.-K.; Marsaud, V.; Bories, P.-N.; Cynober, L.; Gil, S.; Férey, G.; Couvreur, P.; Gref, R. Porous Metal-organic-framework nanoscale carriers as a potential platform for drug delivery and imaging. *Nat. Mater.,* **2010**, 9 (2), 172-178.

(52) Bansal, D.; Pandey, S.; Hundal, G.; Gupta, R. Heterometallic coordination polymers: syntheses, structures and heterogeneous catalytic applications. *New J. Chem.,* **2015**, 39 (12), 9772-9781.

(53) Yoon, M.; Srirambalaji, R.; Kim, K. Homochiral metal-organic frameworks for asymmetric heterogeneous catalysis. *Chem. Rev.,* **2012**, 112 (2), 1196-1231.

(54) Fujita, M.; Kwon, Y. J.; Washizu, S.; Ogura, K. Preparation, clathration ability, and catalysis of a two-dimensional square network material composed of cadmium(ii) and 4,4'-bipyridine. *J. Am. Chem. Soc.,* **1994**, 116 (3), 1151-1152.

(55) Akiyama, G.; Matsuda, R.; Sato, H.; Kitagawa, S. Catalytic glucose isomerization by porous coordination polymers with open metal sites. *Chem. An Asian J.,* **2014**, 9 (10), 2772-2777.

(56) Dhakshinamoorthy, A.; Asiri, A. M.; Garcia, H. Mixed-metal or mixed-linker metal organic frameworks as heterogeneous catalysts. *Catal. Sci. Technol.,* **2016**, 6 (14), 5238-5261.

(57) Krap, C. P.; Newby, R.; Dhakshinamoorthy, A.; García, H.; Cebula, I.; Easun, T. L.; Savage, M.; Eyley, J. E.; Gao, S.; Blake, A. J.; Lewis, W.; Beton, P. H.; Warren, M. R.; Allan D. R.; Frogley, M. D.; Tang, C. C.; Cinque, G.; Yang, S.; Schröder, M. Enhancement of CO_2 adsorption and catalytic properties by Fe-doping of [Ga₂(OH)₂(L)] (H₄L = biphenyl-3,3′,5,5′-tetracarboxylic acid), MFM-300(Ga₂). *Inorg. Chem.,* **2016**, 55 (3), 1076-1088.

(58) Saha, D.; Hazra, D. K.; Maity, T.; Koner, S. Heterometallic metal-organic frameworks that catalyze two different reactions sequentially. *Inorg. Chem.,* **2016**, 55 (12), 5729-5731.

(59) Jiao, L.; Wang, Y.; Jiang, H.-L.; Xu, Q. Metal-organic frameworks as platforms for catalytic applications. *Adv. Mater.,* **2018**, 30 (37), 1703663 (1-23).

(60) Boroujeni, M. B.; Hashemzadeh, A.; Faroughi, M.-T.; Shaabani, A.; Amini, M. M. Magnetic MIL-101-SO₃ H: A Highly efficient bifunctional nanocatalyst for the synthesis of 1,3,5-triarylbenzenes and 2,4,6-triaryl pyridines. *RSC Adv.,* **2016**, 6 (102), 100195-100202.

(61) Falcaro, P.; Ricco, R.; Yazdi, A.; Imaz, I.; Furukawa, S.; Maspoch, D.; Ameloot, R.; Evans, J. D.; Doonan, C. J. Application of metal and metal oxide nanoparticles@MOFs. *Coord. Chem. Rev.,* **2016**, 307, 237-254.

(62) Zhao, M.; Deng, K.; He, L.; Liu, Y.; Li, G.; Zhao, H.; Tang, Z. Core-Shell Palladium nanoparticle@metal-organic frameworks as multifunctional catalysts for cascade reactions. *J. Am. Chem. Soc.,* **2014**, 136 (5), 1738-1741.

(63) Jeoung, S.; Sahgong, S. H.; Kim, J. H.; Hwang, S. M.; Kim, Y.; Moon, H. R. Upcycling of nonporous coordination polymers: controllable-conversion toward porosity-tuned N-doped carbons and their electrocatalytic activity in seawater batteries. *J. Mater. Chem. A,* **2016**, 4 (35), 13468-13475.

(64) Aiyappa, H. B.; Pachfule, P.; Banerjee, R.; Kurungot, S. Porous carbons from nonporous MOFs: influence of ligand characteristics on intrinsic properties of end carbon. *Cryst. Growth Des*., **2013**, 13 (10), 4195-4199.

(65) Lim, S.; Suh, K.; Kim, Y.; Yoon, M.; Park, H.; Dybtsev, D. N.; Kim, K. Porous carbon materials with a controllable surface area synthesized from metal-organic frameworks. *Chem. Commun.,* **2012**, 48 (60), 7447-7449.

(66) Angulo-Ibáñez, A.; Beobide, G.; Castillo, O.; Luque, A.; Pérez-Yáñez, S.; Vallejo-Sánchez, D. Aerogels of 1D coordination polymers: from a non-porous metal-organic crystal structure to a highly porous material. *Polymers (Basel).,* **2016**, 8 (1), 16.

(67) Miller, S. R.; Heurtaux, D.; Baati, T.; Horcajada, P.; Grenèche, J.-M.; Serre, C. Biodegradable therapeutic MOFs for the delivery of bioactive molecules. *Chem. Commun*., **2010**, 46 (25), 4526.

(68) Rojas, S.; Devic, T.; Horcajada, P. metal organic frameworks based on bioactive components. *J. Mater. Chem. B,* **2017**, 5 (14), 2560-2573.

(69) Chowdhury, M. A. Metal-organic-frameworks as contrast agents in magnetic resonance imaging. *ChemBioEng Rev*., **2017**, 4 (4), 225-239.

(70) Ricco, R.; Malfatti, L.; Takahashi, M.; Hill, A. J.; Falcaro, P. Applications of magnetic metal-organic framework composites. *J. Mater. Chem. A, 2013*, 1 (42), 13033-13045.

(71) Zhu, Y.-Y.; Zhu, M.-S.; Yin, T.-T.; Meng, Y.-S.; Wu, Z.-Q.; Zhang, Y.-Q.; Gao, S. Cobalt(II) coordination polymer exhibiting single ion magnet type field induced slow relaxation behavior. *Inorg. Chem.,* **2015**, 54 (8), 3716-3718.

(72) Liu, C.-S.; Wang, J.-J.; Yan, L.-F.; Chang, Z.; Bu, X.-H.; Sañudo, E. C.; Ribas, J. Copper(II), cobalt(II), and nickel(II) complexes with a bulky anthracene-based carboxylic ligand: syntheses, crystal structures, and magnetic properties. *Inorg. Chem.,* **2007**, 46 (16), 6299-6310.

(73) Janiak, C. Engineering coordination polymers towards applications. *Dalton. Trans*., **2003**, 3 (14), 2781-2804.

(74) Wang, H.-M.; Liu, H.-P.; Chu, T.-S.; Yang, Y.-Y.; Hu, Y.-S.; Liu, W.-T.; Ng, S. W. A luminescent terbium coordination polymer for sensing methanol. *RSC Adv*., **2014**, 4 (27), 14035-14041.

(75) Stock, N.; Biswas, S. Synthesis of metal-organic frameworks (MOFs): routes to various MOF topologies, morphologies, and composites. *Chem. Rev*., **2012**, 112 (2), 933-969.

(76) Olafson, K. N.; Li, R.; Alamani, B. G.; Rimer, J. D. Engineering crystal modifiers: bridging classical and nonclassical crystallization. *Chem. Mater*., **2016**, 28 (23), 8453-8465.

(77) Gebauer, D.; Cölfen, H. Prenucleation clusters and non-classical nucleation. *Nano Today,* **2011**, 6 (6), 564-584.

(78) Rabenau, A. The role of hydrothermal synthesis in preparative chemistry. *Angew. Chemie Int. Ed. English,* **1985**, 24 (12), 1026-1040.

(79) Lee, Y.-R.; Kim, J.; Ahn, W.-S. Synthesis of metal-organic frameworks: a mini review. *Korean J. Chem. Eng.,* **2013**, 30 (9), 1667-1680.

(80) Anumah, A.; Louis, H.; Hamzat, A. T.; Amusan, O. O. Metal-organic frameworks (MOFs): recent advances in synthetic methodologies and some applications. *Chem. Methodol.,* **2018**, 3 (11), 276-391.

(81) Rao, B. G.; Mukherjee, D.; Reddy, B. M. Novel approaches for preparation of nanoparticles. in nanostructures for novel therapy. Elsevier, **2017**,1-36.

(82) McKinstry, C.; Cathcart, R. J.; Cussen, E. J.; Fletcher, A. J.; Patwardhan, S. V.; Sefcik, J. Scalable continuous solvothermal synthesis of metal organic framework (MOF-5) crystals. *Chem. Eng. J.*, **2016**, 285, 718-725.

(83) Lestari, W. W.; Adreane, M.; Purnawan, C.; Fansuri, H.; Widiastuti, N.; Rahardjo, S. B. solvothermal and electrochemical synthetic method of HKUST-1 and its methane storage capacity. *IOP Conf. Ser. Mater. Sci. Eng.*, **2016**, 107 (1), 012030.

(84) Du, M.; Li, C.-P.; Zhao, X.-J. Metal-controlled assembly of coordination polymers with the flexible building block 4-pyridylacetic acid (Hpya). *Cryst. Growth Des.*, **2006**, 6 (1), 335-341.

(85) Dey, C.; Kundu, T.; Biswal, B. P.; Mallick, A.; Banerjee, R. Crystalline metal-organic frameworks (MOFs): synthesis, structure and function. *Acta Crystallogr. Sect. B Struct. Sci. Cryst. Eng. Mater.*, **2014**, 70 (1), 3-10.

(86) Müller, U.; Pütter, H.; Hesse, M.; Wessel, H.; Schubert, M.; Huff, J.; Guzmann, M. Method for electrochemical production of a crystalline porous metal organic skeleton material. WO/2005/049892, **2005**.

(87) Martinez Joaristi, A.; Juan-Alcañiz, J.; Serra-Crespo, P.; Kapteijn, F.; Gascon, J. Electrochemical synthesis of some archetypical Zn^{2+}, Cu^{2+}, and Al^{3+} metal organic frameworks. *Cryst. Growth Des.*, **2012**, 12 (7), 3489-3498.

(88) Rubio-Martinez, M.; Avci-Camur, C.; Thornton, A. W.; Imaz, I.; Maspoch, D.; Hill, M. R. New synthetic routes towards MOF production at scale. *Chem. Soc. Rev.*, **2017**, 46 (11), 3453-3480.

(89) Al-Kutubi, H.; Gascon, J.; Sudhölter, E. J. R.; Rassaei, L. Electrosynthesis of metal-organic frameworks: challenges and opportunities. *ChemElectroChem.*, **2015**, 2 (4), 462-474.

(90) Li, M.; Dincă, M. Selective formation of biphasic thin films of metal-organic frameworks by potential-controlled cathodic electrodeposition. *Chem. Sci.*, **2014**, 5 (1), 107-111.

(91) Li, M.; Dincă, M. Reductive electrosynthesis of crystalline metal-organic frameworks. *J. Am. Chem. Soc.*, **2011**, 133 (33), 12926-12929.

(92) Feng, J. F.; Yang, X.; Gao, S. Y.; Shi, J.; Cao, R. Facile and rapid growth of nanostructured Ln-BTC metal-organic framework films by electrophoretic deposition for explosives sensing in gas and Cr^{3+} detection in solution. *Langmuir.*, **2017**, 33 (50), 14238-14243.

(93) Ameloot, R.; Pandey, L.; Auweraer, M. Van Der; Alaerts, L.; Sels, B. F.; De Vos, D. E. Patterned Film growth of metal-organic frameworks based on galvanic displacement. *Chem. Commun.*, **2010**, 46 (21), 3735-3737.

(94) Baláž, P.; Achimovicová, M.; Baláž, M.; Billik, P.; Zara, C. Z.; Criado, J. M.; Delogu, F.; Dutková, E.; Gaffet, E.; Gotor, F. J.; Kumar, R.; Mitov, I.; Rojac, T.; Senna, M.; Streletskii, A.; Wieczorek-Ciurowa, K. Hallmarks of mechanochemistry: from nanoparticles to technology. *Chem. Soc. Rev.*, **2013**, 42 (18), 7571-7637.

(95) Nič, M., Jirát, J., Košata, B., Jenkins, A., McNaught, A. IUPAC compendium of chemical terminology Eds.; IUPAC: Research Triagle Park, NC, **2009**.

(96) Pichon, A.; Lazuen-Garay, A.; James, S. L. Solvent-free synthesis of a microporous metal–organic framework. *CrystEngComm.*, **2006**, 8 (3), 211-214.

(97) Tanaka, S.; Kida, K.; Nagaoka, T.; Ota, T.; Miyake, Y. Mechanochemical dry conversion of zinc oxide to zeolitic imidazolate framework. *Chem. Commun.*, **2013**, 49 (72), 7884-7886.

(98) Tanaka, S.; Nagaoka, T.; Yasuyoshi, A.; Hasegawa, Y.; Denayer, J. F. M. Hierarchical pore development of ZIF-8 MOF by simple salt-assisted mechanosynthesis. *Cryst. Growth Des.*, **2018**, 18 (1), 274-279.

(99) Thomas-Hillman, I.; Laybourn, A.; Dodds, C.; Kingman, S. W. Realising the environmental benefits of metal-organic frameworks: recent advances in microwave synthesis. *J. Mater. Chem. A,* **2018**, 6 (25), 11564-11581.

(100) Khan, N. A.; Jhung, S. H. Synthesis of metal-organic frameworks (MOFs) with microwave or ultrasound: rapid reaction, phase-selectivity, and size reduction. *Coord. Chem. Rev.*, **2015**, 285, 11-23.

(101) Jhung, S. H.; Yoon, J. W.; Hwang, J.-S.; Cheetham, A. K.; Chang, J.-S. Microwave synthesis of a nanoporous hybrid material, chromium trimesate. *Bull. Korean Chem. Soc.*, **2005**, 26 (6), 880-881.

(102) Safarifard, V.; Morsali, A. Applications of ultrasound to the synthesis of nanoscale metal-organic coordination polymers. *Coord. Chem. Rev.,* **2015**, 292, 1-14.

(103) Suslick, K. S. Applications of ultrasound to materials chemistry. *ChemInform,* **2010**, 26 (44).

(104) Lupacchini, M.; Mascitti, A.; Giachi, G.; Tonucci, L.; D'Alessandro, N.; Martinez, J.; Colacino, E. Sonochemistry in non-conventional, green solvents or solvent-free reactions. *Tetrahedron,* **2017**, 73 (6), 609-653.

(105) Qiu, L.-G.; Li, Z.-Q.; Wu, Y.; Wang, W.; Xu, T.; Jiang, X. Facile synthesis of nanocrystals of a microporous metal-organic framework by an ultrasonic method and selective sensing of organoamines. *Chem. Commun*., **2008**, 31, 3642-3644.

(106) Son, W.-J.; Kim, J.; Kim, J.; Ahn, W.-S. Sonochemical synthesis of MOF-5. *Chem. Commun.,* **2008**, 47, 6336-6338.

(107) Lee, J. E.; Kim, D. Y.; Lee, H.-K.; Park, H. J.; Ma, A.; Choi, S.-Y.; Lee, D.-S. Sonochemical synthesis of HKUST-1-based CuO decorated with Pt nanoparticles for formaldehyde gas-sensor applications. *Sensors Actuators B Chem*., **2019**, 292 (April), 289-296.

(108) Carné-Sánchez, A.; Imaz, I.; Cano-Sarabia, M.; Maspoch, D. A Spray-drying strategy for synthesis of nanoscale metal-organic frameworks and their assembly into hollow superstructures. *Nat. Chem*., **2013**, 5 (3), 203-211.

(109) Chaemchuen, S.; Zhou, K.; Mousavi, B.; Ghadamyari, M.; Heynderickx, P. M.; Zhuiykov, S.; Yusubov, M. S.; Verpoort, F. Spray drying of zeolitic imidazolate frameworks: investigation of crystal formation and properties. *CrystEngComm.,* **2018**, 20 (25), 3601-3608.

(110) Garzón-Tovar, L.; Rodríguez-Hermida, S.; Imaz, I.; Maspoch, D. Spray drying for making covalent chemistry: postsynthetic modification of metal-organic frameworks. *J. Am. Chem. Soc*., **2017**, 139 (2), 897-903.

(111) U.S. EPA. Volatile organic compounds emissions. **2018**.

(112) Nelson, W. M. Green solvents for chemistry: perspectives and practice. Oxford University Press, USA, **2003**.

(113) Capello, C.; Fischer, U.; Hungerbühler, K. What is a green solvent? A comprehensive framework for the environmental assessment of solvents. *Green Chem.,* **2007**, 9 (9), 927-934.

(114) Byrne, F. P.; Jin, S.; Paggiola, G.; Petchey, T. H. M.; Clark, J. H.; Farmer, T. J.; Hunt, A. J.; Robert McElroy, C.; Sherwood, J. Tools and techniques for solvent selection: green solvent selection guides. *Sustain. Chem. Process*., **2016**, 4 (1), 7.

(115) Parhi, R.; Suresh, P. Supercritical fluid technology: a review. *J. Adv. Pharm. Sci. Technol*., **2013**, 1 (1), 13-36.

(116) Domingo, C.; Subra-Paternault, P. Supercritical fluid nanotechnology advances and applications in composites and hybrid nanomaterials. Pan Stanford Publishing Pte. Ltd., **2015**.

(117) Kemmere, M. F.; Meyer, T. Supercritical carbon dioxide in polymer reaction engineering. WILEY-VCH Verlag GmbH & Co. KGaA, Weinheim, **2005**.

(118) Noyori, R. Supercritical fluids: introduction. *Chem. Rev.,* **1999**, 99 (2), 353-354.

(119) McHugh, M. A.; Krukonis, V. J. Supercritical fluid extraction: principles and practice, Boston: B.; Brenner, H., Ed. **1985**

(120) Ari, Y.; Sako, T.; Takebayashi, Y. Supercritical fluids molecular interactions, physical properties and new applications. Springer-Verlag Berlin Heidelberg, **2002**.

(121) Nalawade, S. P.; Picchioni, F.; Janssen, L. P. B. M. Supercritical carbon dioxide as a green solvent for processing polymer melts: processing aspects and applications. *Prog. Polym. Sci.,* **2006**, 31 (1), 19-43.

(122) Teoh, W. H.; Mammucari, R.; Foster, N. R. Solubility of organometallic complexes in supercritical carbon dioxide: a review. *J. Organomet. Chem.,* **2013**, 724, 102-116.

(123) Ting, S. S. T.; Tomasko, D. L.; Foster, N. R.; Macnaughton, S. J. Chemical-physical interpretation of cosolvent effects in supercritical fluids. *Ind. Eng. Chem. Res*., **1993**, 32 (7), 1482-1487.

(124) Ekart, M. P.; Bennett, K. L.; Ekart, S. M.; Gurdial, G. S.; Liotta, C. L.; Eckert, C. A. Cosolvent interactions in supercritical fluid solutions. *AIChE J.,* **1993**, 39 (2), 235-248.

(125) Casas, L.; Mantell, C.; Rodríguez, M.; Torres, A.; Macías, F. A.; Martínez de la Ossa, E. Effect of the addition of cosolvent on the supercritical fluid extraction of bioactive compounds from helianthus annuus L. *J. Supercrit. Fluids,* **2007**, 41 (1), 43-49.

(126) Brunner, G. Applications of supercritical fluids. *Annu. Rev. Chem. Biomol. Eng.* **2010**, 1 (1), 321-342.

(127) Lack, E.; Simándi, B. Supercritical fluid extraction and fractionation from solid materials. *Industrial Chemistry Library,* **2001**, 537-575.

(128) Zosel, K. Separation with supercritical gases: practical applications. *Angew. Chemie Int. Ed. English,* **1978**, 17 (10), 702-709.

(129) Sapkale, G. N.; Patil, S. M.; Surwase, U. S.; Bhatbhage, P. Supercritical fluid extraction - a review. *Int. J.* Chem. Sci., **2010**, 8 (2), 729-743.

(130) Fabricante tapón de corcho vino y champán-DIAM https://www.diam-corchos.com/ (accessed May 13, **2019**).

(131) Berger, T. A. Chromatography: Supercritical fluid, theory of supercritical fluid chromatography. in encyclopedia of separation science. Elsevier, **2007**, 1-9.

(132) Forgacs, E.; Cserha, T. Chromatography. *Food Technol*., **2003**, 88-95.

(133) Majewski, W.; Valery, E.; Ludemann-Hombourger, O. Principle and applications of supercritical fluid chromatography. *J. Liq. Chromatogr. Relat. Technol*., **2005**, 28 (7-8), 1233-1252.

(134) Alkio, M.; Gonzalez, C.; Jäntti, M.; Aaltonen, O. Purification of polyunsaturated fatty acid esters from tuna oil with supercritical fluid chromatography. *J. Am. Oil Chem. Soc.,* **2000**, 77 (3), 315-321.

(135) Geiser, F.; Schultz, M.; Betz, L.; Shaimi, M.; Lee, J.; Champion, W. Direct, Preparative enantioselective chromatography of propranolol hydrochloride and thioridazine hydrochloride using carbon dioxide-based mobile phases. *J. Chromatogr. A,* **1999**, 865 (1-2), 227-233.

(136) DeSimone, J. M.; Maury, E. E.; Menceloglu, Y. Z.; McClain, J. B.; Romack, T. J.; Combes, J. R. Dispersion polymerizations in supercritical carbon dioxide. *Science.,* **1994**, 265 (5170), 356-359.

(137) Cooper, A. I. Polymer synthesis and processing using supercritical carbon dioxide. *J. Mater. Chem*., **2000**, 10 (2), 207-234.

(138) DeSimone, J. M.; Guan, Z.; Elsbernd, C. S. Synthesis of fluoropolymers in supercritical carbon dioxide. *Science.*, **1992**, 257 (5072), 945-947.

(139) Alsoy, S.; Duda, J. L. Processing of polymers with supercritical fluids. *Chem. Eng. Technol.,* **1999**, 22 (11), 971-973.

(140) Champeau, M.; Thomassin, J.-M.; Tassaing, T.; Jérôme, C. Drug loading of polymer implants by supercritical CO₂ assisted impregnation: a review. *J. Control. Release,* **2015**, 209, 248-259.

(141) Üzer, S.; Akman, U.; Hortaçsu, Ö. Polymer swelling and impregnation using supercritical CO₂: A model-component study towards producing controlled-release drugs. *J. Supercrit. Fluids,* **2006**, 38 (1), 119-128.

(142) Xu, Z.-M.; Jiang, X.-L.; Liu, T.; Hu, G.-H.; Zhao, L.; Zhu, Z.-N.; Yuan, W.-K. Foaming of polypropylene with supercritical carbon dioxide. *J. Supercrit. Fluids,* **2007**, 41 (2), 299-310.

(143) Totaro, A.; Salerno, A.; Imparato, G.; Domingo, C.; Urciuolo, F.; Netti, P. A. PCL-HA microscaffolds for in vitro modular bone tissue engineering. *J. Tissue Eng. Regen. Med.,* **2017**, 11 (6), 1865-1875.

(144) Salerno, A.; Guarino, V.; Oliviero, O.; Ambrosio, L.; Domingo, C. Bio-safe processing of polylactic-co-caprolactone and polylactic acid blends to fabricate fibrous porous scaffolds for in vitro mesenchymal stem cells adhesion and proliferation. *Mater. Sci. Eng. C,* **2016**, 63, 512-521.

(145) Jessop, P. G.; Leitner, W. Chemical synthesis using supercritical fluids. Wiley-VCH Verlag GmbH: Weinheim, Germany, **1999**.

(146) Beckman, E. J. Supercritical and near-critical CO₂ in green chemical synthesis and processing. *J. Supercrit. Fluids***, 2004**, 28 (2-3), 121-191.

(147) Licence, P.; Ke, J.; Sokolova, M.; Ross, S. K.; Poliakoff, M. Chemical reactions in supercritical carbon dioxide: from laboratory to commercial. *Green Chem*., **2003**, 5 (2), 99-104.

(148) Ikushima, Y.; Ito, S.; Asano, T.; Yokoyama, T.; Saito, N.; Hatakeda, K.; Goto, T. A Diels-Alder Reaction in supercritical carbon dioxide medium. *J. Chem. Eng. JAPAN,* **1990**, 23 (1), 96-98.

(149) García-González, C. A.; Andanson, J. M.; Kazarian, S. G.; Domingo, C.; Saurina, J. Application of principal component analysis to the thermal characterization of silanized nanoparticles obtained at supercritical carbon dioxide conditions. *Anal. Chim. Acta,* **2009**, 635 (2), 227-234.

(150) García-González, C. A.; Saurina, J.; Ayllón, J. A.; Domingo, C. Preparation and characterization of surface silanized TiO_2 nanoparticles under compressed CO_2: reaction kinetics. *J. Phys. Chem. C,* **2009**, 113 (31), 13780-13786.

(151) Esumi, K.; Sarashina, S.; Yoshimura, T. Synthesis of gold nanoparticles from an organometallic compound in supercritical carbon dioxide. *Langmuir,* **2004**, 20 (13), 5189-5191.

(152) Sastre Cuadrillero, A. Synthesis of supported catalysts of Co, Ni and Ru using supercritical CO_2 for biomass valorization reactions, Universidad de Valladolid, **2015**.

(153) Gasc, F.; Thiebaud-Roux, S.; Mouloungui, Z. Methods for synthesizing diethyl carbonate from ethanol and supercritical carbon dioxide by one-pot or two-step reactions in the presence of potassium carbonate. *J. Supercrit. Fluids,* **2009**, 50 (1), 46-53.

(154) Domingo, C.; Loste, E.; Gómez-Morales, J.; García-Carmona, J.; Fraile, J. Calcite Precipitation by a high-pressure CO_2 carbonation route. *J. Supercrit. Fluids,* **2006**, 36 (3), 202-215.

(155) Jessop, P. G.; Hsiao, Y.; Ikariya, T.; Noyori, R. Homogeneous catalysis in supercritical fluids: hydrogenation of supercritical carbon dioxide to formic acid, alkyl formates, and formamides. *J. Am. Chem. Soc.*, **2002**, 118 (2), 344-355.

(156) Wesselbaum, S.; Hintermair, U.; Leitner, W. Continuous-flow hydrogenation of carbon dioxide to pure formic acid using an integrated scCO₂ process with immobilized catalyst and base. *Angew. Chem. Int. Ed.*, 2012,51, 8585-8588.

(157) Scondo, A.; Dumarcay-Charbonnier, F.; Marsura, A.; Barth, D. Supercritical CO_2 phosphine imide reaction on peracetylated β-cyclodextrins. *J. Supercrit. Fluids,* **2009**, 48 (1), 41-47.

(158) Teja, A. S.; Furuya, T. Supercritical fluid crystallization. in encyclopedia of separation science. Elsevier, **2000**, 4301-4307.

(159) Subramaniam, B.; Rajewski, R. A.; Snavely, K. Pharmaceutical processing with supercritical carbon dioxide. *J. Pharm. Sci.,* **1997**, 86 (8), 885-890.

(160) Matson, D. W.; Fulton, J. L.; Petersen, R. C.; Smith, R. D. Rapid expansion of supercritical fluid solutions: solute formation of powders, thin films, and fibers. *Ind. Eng. Chem. Res.*, **1987**, 26 (11), 2298-2306.

(161) Domingo, C.; Berends, E. M.; van Rosmalen, G. M. Precipitation of ultrafine benzoic acid by expansion of a supercritical carbon dioxide solution through a porous plate nozzle. *J. Cryst. Growth,* **1996**, 166 (1-4), 989-995.

(162) Darr, J. A.; Poliakoff, M. New directions in inorganic and metal-organic coordination chemistry in supercritical fluids. *Chem. Rev.*, **1999**, 99 (2), 495-542.

(163) Harscoat-Schiavo, C.; Neurohr, C.; Lecomte, S.; Marchivie, M.; Subra-Paternault, P. Influence of isomerism on recrystallization and cocrystallization induced by CO_2 as an antisolvent. *CrystEngComm.,* **2015**, 17 (29), 5410-5421.

(164) Pando, C.; Cabañas, A.; Cuadra, I. A. Preparation of pharmaceutical co-crystals through sustainable processes using supercritical carbon dioxide: a review. *RSC Adv.*, **2016**, 6 (75), 71134-71150.

(165) López-Periago, A.; Vallcorba, O.; Domingo, C.; Ayllón, J. A. Hollow microcrystals of copper hexafluoroacetylacetonate-pyridine derivative adducts via supercritical CO_2 recrystallization. *Cryst. Growth Des.,* **2016**, 16 (3), 1725-1736.

(166) Vemavarapu, C.; Mollan, M. J.; Lodaya, M.; Needham, T. E. Design and process aspects of laboratory scale SCF particle formation systems. *Int. J. Pharm.,* **2005**, 292 (1-2), 1-16.

(167) Jafari, D.; Yarnezhad, I.; Nowee, S. M.; Baghban, S. H. N. Gas-antisolvent (GAS) crystallization of aspirin using supercritical carbon dioxide: experimental study and characterization. *Ind. Eng. Chem. Res.*, **2015**, 54 (14), 3685-3696.

(168) Kalani, M.; Yunus. Application of supercritical antisolvent method in drug encapsulation: a review. *Int. J. Nanomedicine,* **2011**, 6, 1429.

(169) Yoon, T. J.; Son, W.-S.; Park, H. J.; Seo, B.; Kim, T.; Lee, Y.-W. Tetracycline nanoparticles precipitation using supercritical and liquid CO_2 as antisolvents. *J. Supercrit. Fluids,* **2016**, 107, 51-60.

(170) Bleich, J.; Müller, B. W.; Waßmus, W. Aerosol solvent extraction system a new microparticle production technique. *Int. J. Pharm.,* **1993**, 97 (1-3), 111-117.

(171) Woods, H. M.; Silva, M. M. C. G.; Nouvel, C.; Shakesheff, K. M.; Howdle, S. M. Materials processing in supercritical carbon dioxide: surfactants, polymers and biomaterials. *J. Mater. Chem.*, **2004**, 14 (11), 1663-1678.

(172) Weidner, E.; Knez, Z.; Z.A, N. Process and equipment for production and fractionation of fine particles from gas saturated solutions. WO 95/21688, **1994**.

(173) Paul T Anastas, P. T.; Warner, J. C. Green chemistry: theory and practice. Oxford University Press, **1998**.

(174) Gandhi, K.; Arora, S.; Kumar, A. Industrial applications of supercritical fluid extraction: a review., **2018**, 5 (January), 336-340.

(175) Murillo-Cremaes, N.; López-Periago, A. M.; Saurina, J.; Roig, A.; Domingo, C. A clean and effective supercritical carbon dioxide method for the host-guest synthesis and encapsulation of photoactive molecules in nanoporous matrices. *Green Chem.,* **2010**, 12 (12), 2196-2204.

(176) Wu, T.; Han, B. Supercritical carbon dioxide (CO_2) as green solvent. in innovations in green chemistry and green engineering. Springer New York: New York, NY, 2013; 297-326.

(177) García González, C. A. Use of the supercritical fluid technology for the preparation of nanostructured hybrid materials and design of the interface. Universidad Politécnica de Catalunya.

(178) Peng, L.; Zhang, J.; Xue, Z.; Han, B.; Sang, X.; Liu, C.; Yang, G. Highly mesoporous metal-organic framework assembled in a switchable solvent. *Nat. Commun.* **2014**, 5.

(179) Doan, H. V.; Fang, Y.; Yao, B.; Dong, Z.; White, T.J.; Sartbaeva, A.; Hintermair, U.; Ting, P.T. Controlled formation of hierarchical metal-organic frameworks using CO_2-expanded solvent systems. *ACS Sustainable Chem. Eng.* **2017**, 5, 7887-7893.

(180) Doan, H. V.; Hamzah, H. A.; Prabhakaran, P. K.; Petrillo, C.; Ting, V. C. Hierarchical metal-organic frameworks with macroporosity: synthesis, achievements, and challenges. *Nano-Micro Lett*., **2019**, 11:54.

(181) Zhao, Y.; Han, B.; Song, J.; Li, J.; Wang, Q. Metal-organic framework nanospheres with well-ordered mesopores synthesized in an ionic liquid/CO_2/surfactant system. *Angew. Chem. Int. Ed*., **2011**, 50, 636-639.

(183) Yu, H.; Xu, D.; Xu, Q. Dual template effect of supercritical CO_2 in ionic liquid to fabricate a highly mesoporous cobalt metal-organic framework. *Chem. Commun*., **2015**, 51, 13197-13200.

(184) Peng, L.; Zhang, J.; Li, J.; Han, B.; Xue, Z.; Zhang, B.; Shi, J.; Yang, G. Hollow metal–organic framework polyhedra synthesized by a CO_2-ionicliquid interfacial templating route. *J. Colloid Interface Sc*i., **2014**, 416, 198-204.

(185) López-Periago, A.; López-Domínguez, P.; Pérez Barrio, J.; Tobias, G.; Domingo, C. Binary supercritical CO_2 solvent mixtures for the synthesis of 3D metal-organic frameworks. *Microporous Mesoporous Mater*., **2016**, 234, 155-161.

(186) Mondloch, J. E.; Karagiaridi, O.; Farha, O. K.; Hupp, J. T. Activation of metal-organic framework materials. *CrystEngComm*., **2013**, 15 (45), 9258-9264.

(187) Nelson, A. P.; Farha, O. K.; Mulfort, K. L.; Hupp, J. T. Supercritical processing as a route to high internal surface areas and permanent microporosity in metal−organic framework materials. *J. Am. Chem. Soc.,* **2009**, 131 (2), 458-460.

(188) Meek, S. T.; Perry, J. J.; Teich-McGoldrick, S. L.; Greathouse, J. A.; Allendorf, M. D. Complete series of monohalogenated isoreticular metal-organic frameworks: synthesis and the importance of activation method. *Cryst. Growth* Des., **2011**, 11 (10), 4309-4312.

(189) Wollmann, P.; Leistner, M.; Stoeck, U.; Grünker, R.; Gedrich, K.; Klein, N.; Throl, O.; Grählert, W.; Senkovska, I.; Dreisbach, F.; Kaskel, S. High-throughput screening: speeding up porous materials discovery. *Chem. Commun*., **2011**, 47 (18), 5151-5153.

(190) Tan, F.; López-Periago, A.; Lightm M. E.; Cirera, J.; Ruiz, E.; Borrás, A.; Teixdior, F.; Viñas, C.; Domingo, C.; Planas, J. G. An unprecedented stimuli-controlled single-crystal reversible phase transition of a metal-organic framework and its application to a novel method of guest encapsulation. *Adv.Mater*., **2018**, 30, 1800726.

(191) Monteagudo-Olivan, R.; Cocero, M. J.; Coronas, J.; Rodríguez-Rojo, S. Supercritical CO_2 encapsulation of bioactive molecules in carboxylate based MOFs. *Journal CO₂ Utilitzation*, **2019**, 30, 38-47.

(192) Zhao, Y.; Zhang, J.; Song, J.; Li, J.; Liu, J.; Wu, T.; Zhang, P.; Han, B. Ru Nanoparticles immobilized on metal-organic framework nanorods by supercritical CO_2-methanol solution: highly efficient catalyst. *Green Chem.,* **2011**, 13 (8), 2078-2082.

(193) López-Periago, A. M.; Portoles-Gil, N.; López-Domínguez, P.; Fraile, J.; Saurina, J.; Aliaga-Alcalde, N.; Tobias, G.; Ayllón, J. A.; Domingo, C. metal-organic frameworks precipitated by reactive crystallization in supercritical CO_2. *Cryst. Growth Des.* **2017**, 17 (5), 2864-2872.

(194) Matsuyama, K. Supercritical fluid processing for metal-organic frameworks, porous coordination polymers, and covalent organic frameworks. *J. Supercrit. Fluids,* **2018**, 134, 197-203.

(195) Friscis, T.; Li, C.-J.; Girard, S.; Mottillo, C.; Nickels, C. W. Method for the preparation of metal-organic compounds. McGill University. US10099203B2. WO2016134459A1.

(196) López-Domínguez, P.; López-Periago, A. M.; Fernández-Porras, F. J.; Fraile, J.; Tobias, G.; Domingo, C. Supercritical CO_2 for the synthesis of nanometric ZIF-8 and loading with hyperbranched aminopolymers. applications in CO_2 capture. *J. CO₂ Util.*, **2017**, 18, 147-155.

(197) Marrett, J. M.; Mottillo, C.; Girard, S.; Nickels, C. W.; Do, J.-L. Dayaker, G.; Germann, L. S.; Dinnebier, R. E.; Howarth, A. J.; Farha, O. K. Friscic, T.; Li, C.-J. Supercritical carbon dioxide enables rapid, clean, and scalable conversion of a metal oxide into zeolitic metal-organic frameworks. *Cryst. Growth Des*. **2018**, 18, 3222-3228.

(198) López-Periago, A. M.; Domingo, C. Features of supercritical CO_2 in the delicate world of the nanopores. *J. Supercrit. Fluids,* **2018**, 134, 204-213.

CHAPTER-2

Objective

CHAPTER 2 details the objectives of this thesis based on the questions that motivated this work and the specific goals to answer them.

2.1. Objective

This thesis has been performed in the framework of a research group that has developed a methodology that uses $scCO_2$ for the synthesis of coordination polymers. As a result, an example of a 1D coordination polymer obtained in supercritical CO_2 ($scCO_2$) was published in 2015 by them.[1] This previous work opens a new window in the synthesis of coordination polymers in CO_2 by reactive crystallization. However, many scientific questions on the process remained unanswered. The possible generalization of the synthetic procedure should be performed by analyzing the influence of different experimental parameters and the feasibility of the method. The main objective of this doctoral thesis is, thus, to answer some of the scientific questions in the synthesis of coordination polymers in $scCO_2$ used as a solvent by extending the number of metal nodes and linkers to expand the typology of prepared compounds. Accordingly, precursors that favor the increase of the dimensionality of the produced coordination polymer are particularly foreseen.

The scientific objectives of this thesis are described:

1. To develop a $scCO_2$ synthetic method involving neutral N-donor terminal bi-/multi-dentate linkers as a platform to form new networks. Ditopic bipyridines, with significant solubility in $scCO_2$, and tritopic triazines are used to build the coordination polymers.

2. To implement different strategies to increase the solubility in $scCO_2$ of metal complexes used as nodes. As reactant solubility is a key parameter, a special emphasis is given to select precursors with adequate solubility. When necessary, the addition of a small amount of co-solvent or the use of an ancillary ligand are approaches tested to impart solubility to metal complexes.

3. To demonstrate that the $scCO_2$ reactive crystallization protocol can be extended to more complex networks, as those involving two different metals. These new type of materials have interesting applications in catalysis and magnetism.

4. To increase the biocompatibility of the precipitated coordination polymers by using linkers of biological origin. This objective is developed taking into account that $scCO_2$ is frequently used to extract organic compounds from natural products, which can be further used in the synthesis of bio-coordination polymers.

5. To obtain basic knowledge in crystallization mechanisms occurring in $scCO_2$ during coordination polymers synthesis. This is a transversal objective useful to analyze the non-classical crystal growth mechanisms often found in $scCO_2$.

(1) López-Periago, A.; Vallcorba, O.; Frontera, C.; Domingo, C.; Ayllón, J. A. Exploring a Novel Preparation Method of 1D Metal Organic Frameworks Based on Supercritical CO_2. *Dalton. Trans.,* **2015**, 44 (16), 7548-7553.

CHAPTER-3

Equipment, methodology and characterization

The first part of *CHAPTER 3* describes the high-pressure equipment used in this thesis, as well as the protocols for the synthesis of coordination polymers. The second part consists in a brief introduction to the used technics for the characterization of the compounds.

3.1. Equipment

The design of the equipment for carrying out the experiments of this thesis had been done, principally, taking into account two main considerations: (a) the critical conditions (Tc and Pc) of carbon dioxide that is the used solvent in supercritical conditions, and (b) the type of processing to be performed, i.e., the use of $scCO_2$ as a solvent in a chemical reaction. Since $scCO_2$ is the most used supercritical fluid, most of the high-pressure equipment in the market is designed for its use.

3.1.1. High-pressure system

In this thesis, experiments have been performed in the batch mode. Two reactors of 100 mL with different pressure rating were used (Fig. 3.1). The system is divided in two different parts: first, the compressed CO_2 source, involving a deep-tube cylinder coupled to a cooled high-pressure syringe pump, and second, the stirred and heated reactor vessel. AISI-316 stainless steel is the material employed for the majority of the components due to its chemical inertness and sturdiness.[1]

Figure 3.1. High-pressure equipment used in this thesis.

3.1.2. Building materials and elements of the scCO₂ equipment

The reactor vessel is the part of the system where the supercritical fluid is in contact with the reagents and the reaction takes place. The used reactors are cylindrical, and possess gas connectors, threads, heating resistances or a jacket, thermopars, pressure gauges, sapphire windows and closures. They were stirred with a magnetic stirrer plate by adding a magnetic bar to the vessel. The design of the closure system depends on the operations conditions, the bore diameter and the frequency of opening. Both autoclaves used in this thesis were closed by a hand-tight O-ring for quick opening:

a) A 100 mL high-pressure autoclave (TharDesign) equipped with two opposite sapphire windows was used to perform most of the experiments. The windows allow the visual inspection of the materials during the reaction. The heating system consists in four resistances located within cylindrical cavities placed in the wall of the reactor (Fig. 3.2(a)). Temperature is controlled by a thermocouple placed inside the vessel. The equipment is rated at 30 MPa at 393 K.

b) A 100 mL tubular mini-reactor (Autoclave Engineers) was used for the high temperature experiments. The system is heated with a metallic jacket in which the temperature is controlled by two thermocouples placed in the jacket and inside the vessel (Fig. 3.2 (b)). The equipment is rated at 18 MPa and 453 K.
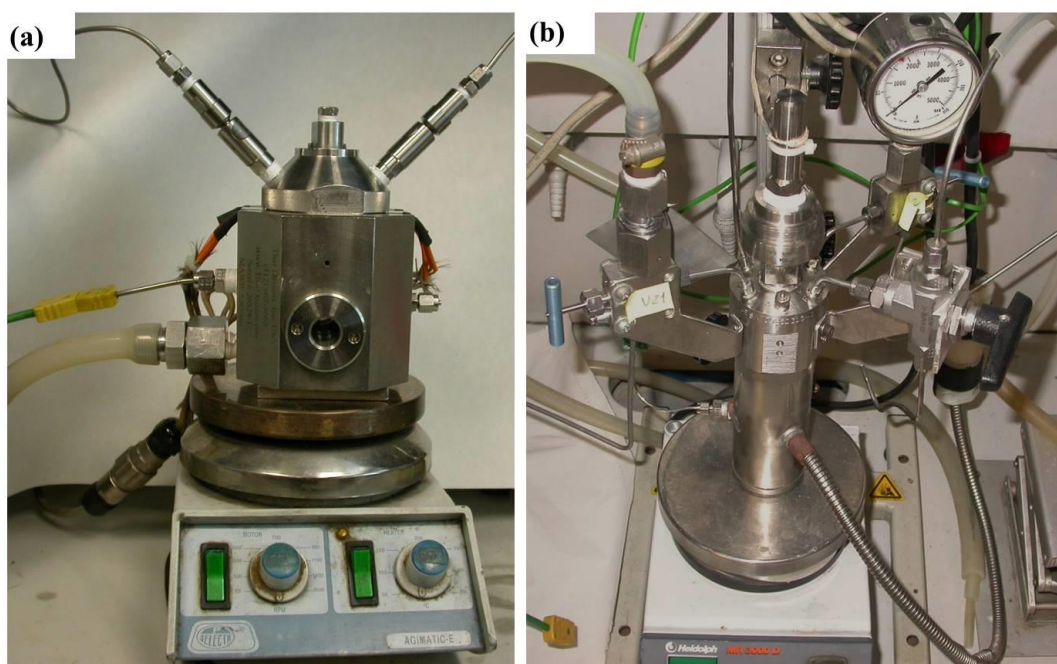

Figure 3.2. Pictures of the used high-pressure equipment: (a) TharDesign autoclave, and (b) Autoclave Engineers reactor.

Pressure pumps are essential to achieve the supercritical conditions. In this thesis, a syringe pump was used (Teleydine ISCO D260). For this pump to pressurize the system, it was necessary to first cool the liquid CO_2 to avoid cavitation. This was achieved by using a cryostat Lauda Ecoline RE 106 Chiller.

High-pressure valves are required to control the flow in the system. The used equipment has two different types of valves: ball valves that are of the on/off type (Fig. 3.3(a)) and needle valves that allow a continuous regulation of the flow (Fig. 3.3(b)).[1]
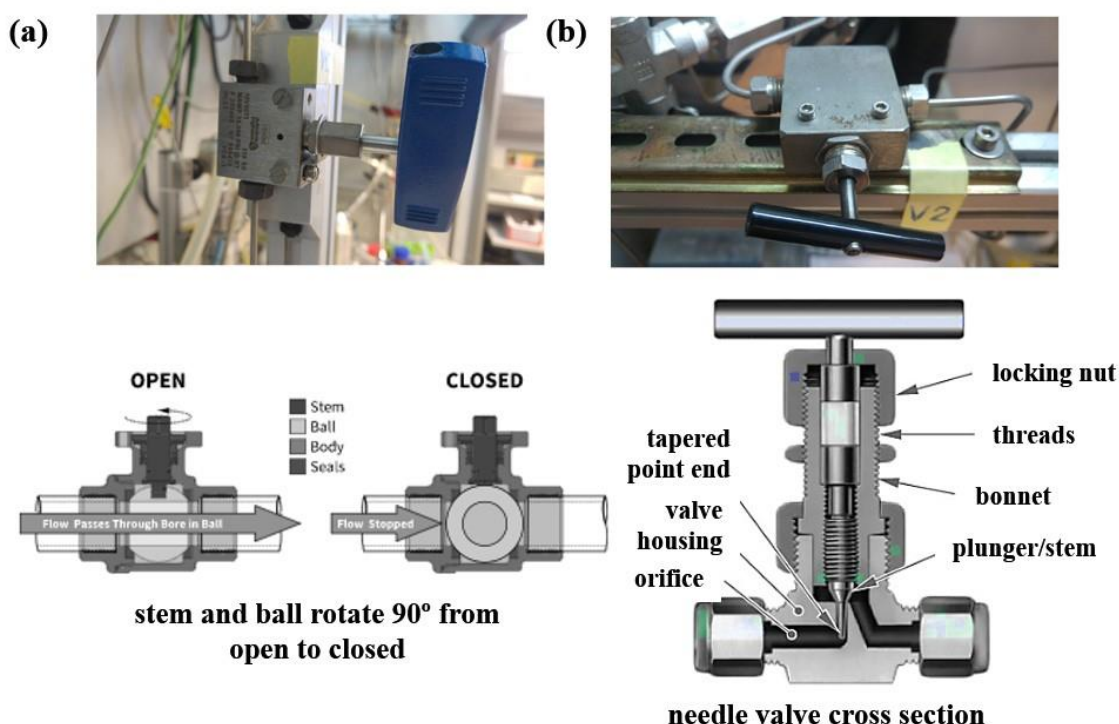

Figure 3.3. Valves in the equipment: (a) ball, and (b) needle.

High-pressure tubing is necessary for the fluid to flow to the desired point. In the used equipment, the different elements were connected by stainless steel high-pressure tube of 1/4" and 1/8".[2]

System control is necessary to monitor the process conditions, includes pressure and temperature control. The pressure was measured with both analogic manometers and digital electronic sensors; in this last one the pressure is converted into an analog electrical signal by a WIKA transducer (Fig. 3.4). The temperature was controlled by using thermopars coupled to the resistances as explained before.
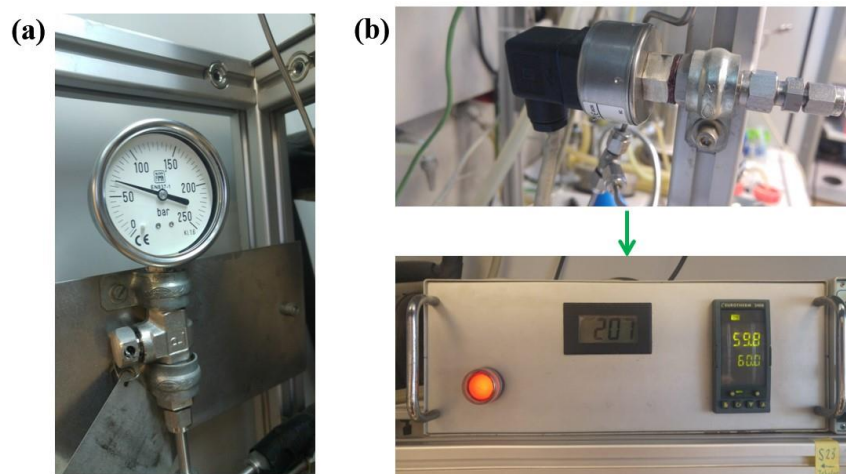
Figure 3.4. Pressure displays and controllers: (a) manometer, and (b) electronic pressure sensor and display.

Safety elements are necessary in all high-pressure system to work under harmless conditions. The used safety systems are rupture disks and release valves located at different points, particularly where a death volume of CO_2 can be accumulated. A complete or partial depressurization of the system would occur through the safety elements when an unexpected increase of pressure (higher than established for safety) occurs. The rupture disk between the $scCO_2$ bottle and the pump and the one of the tubular mini-reactor are calibrated at 19 MPa at 295 K (OSECO) (Fig. 3.5(a)). Then there is one in the TharDesign and several along the set-up calibrated at 35 MPa at 295 K (ZOOK) (Fig. 3.5(b)).
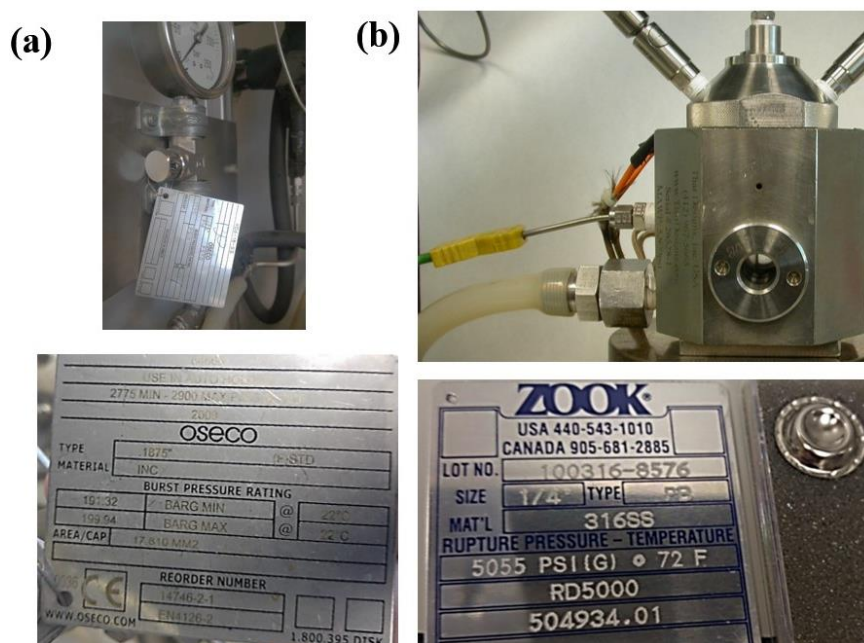
Figure 3.5. Rupture disks at: (a) the bottle and tubular mini-reactor (b) the reactor TharDesign and pump.

3.2. Description of the methodology

In a general procedure of CPs synthesis, the reagents were first placed inside a 10 mL Pyrex vial, either together in the same vial or physically separated in two different vials. The vial was capped with cellulose paper and placed inside the reactor together with a magnetic bar.

Figure 3.6. Reagents set-up in the Pyrex vial: (a) together with a magnetic bar before autoclave loading, (b) view through the autoclave windows during reaction, and (c) after synthesis.

Figure 3.7. Process flow diagram of the high-pressure equipment used in this thesis.

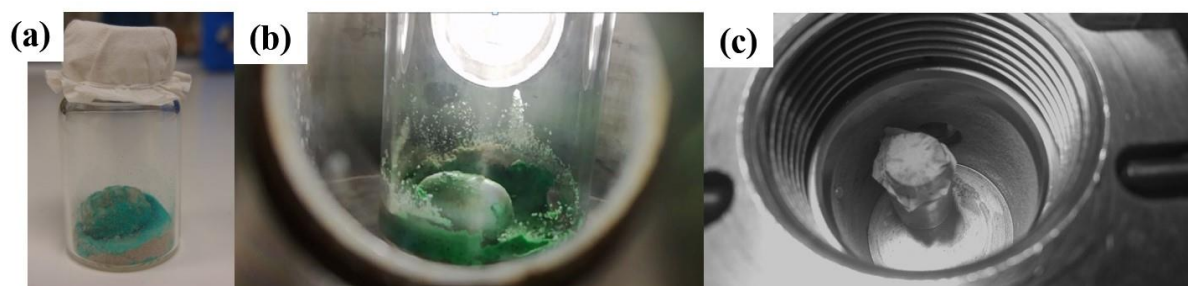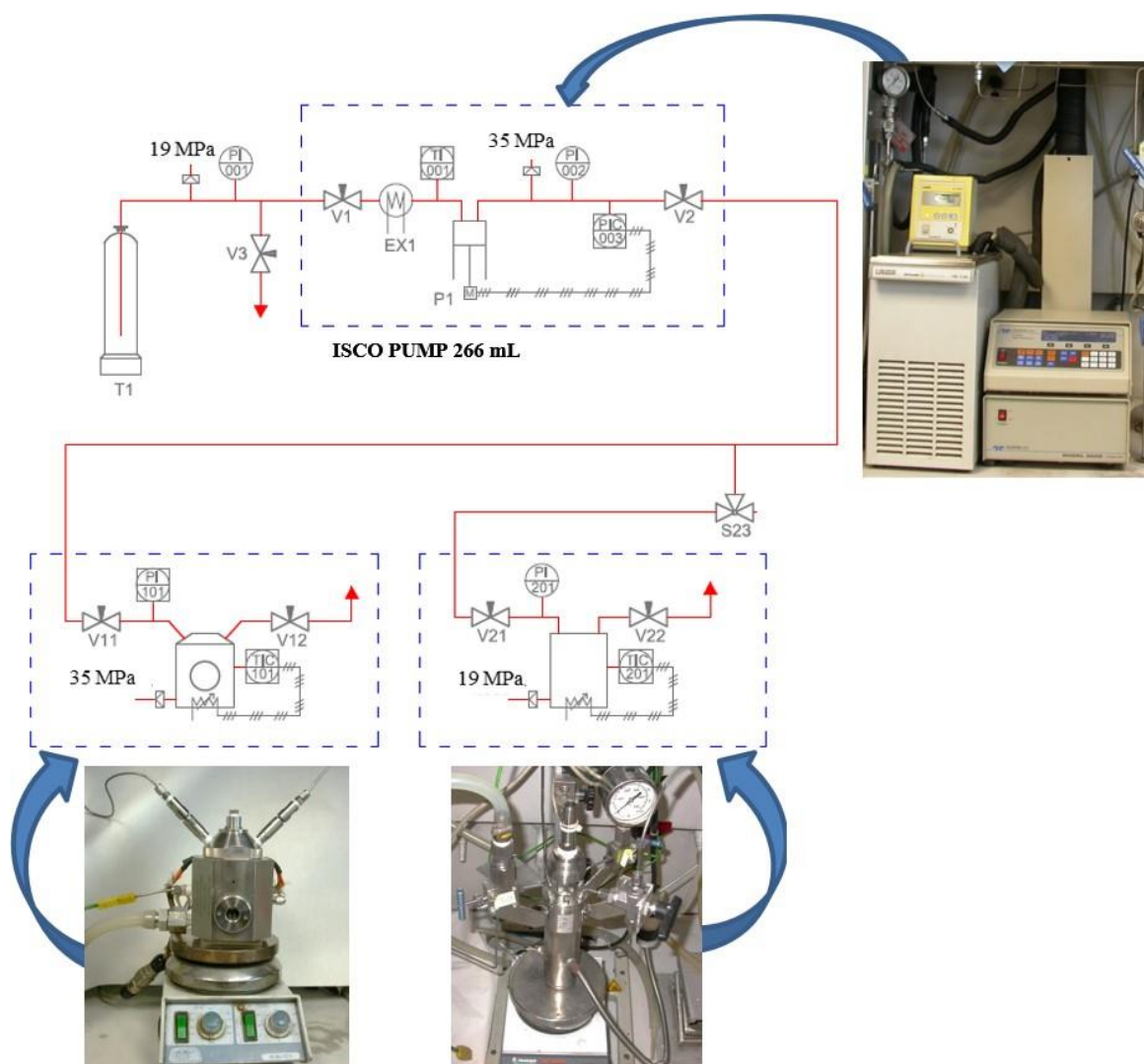The reactor is sealed at room temperature and filled with liquid CO_2 at the bottle pressure (5-6 MPa). The cooling system is set at 271 K. The used equipment is operated with one high-pressure pump and two autoclaves. Fig. 3.7 indicates the CO_2 flow during processing. V4 is the valve used to address the CO_2 flow to the corresponding reactor. The vessels are filled with CO_2 by opening valves V5 or V7. Each reactor is then heated to the working temperature of 313-333 K. After temperature stabilization, the system is pressurized to the working pressure of 15-20 MPa. Entrance valves are at that moment closed. The pressure and temperature conditions in the vessel are kept constant during the reaction time, i.e., reactions are performed under isochoric conditions until ensuring the formation of the desired product. For safety reasons, the pressure in the system part located before the reactor is decreased during synthesis.

Once the reaction is considered completed, the product is washed off of the excess of starting materials with fresh CO_2 in two depressurization/pressurization steps, from 20 to 7 MPa. This was done by opening the exit valves in the reactors (V6 or V8) to decrease the pressure to 7 MPa and by increasing again this parameter to 20 MPa by using the high-pressure pump. Finally, the system was depressurized to atmospheric pressure and cooled down to room temperature. The depressurization flow rate was controlled by using the needles valves V6 and V8. At the end of the process, the gas from the system was removed through V1 ball valve.

3.3. Characterization technics

3.3.1. Crystal structures by X-ray diffraction (XRD)

XRD is a common non-destructive characterization technique for obtaining structural information of crystalline solid materials. XRD is a primary tool for probing structure of materials due to the fact that the wavelength of X-ray is on the atomic scale and interferences can occur.[3] When a beam of X-ray interacts with the sample, the rays are scattered generating a diffraction pattern, which contains information about the atomic arrangement and content within the crystal.[4] Each time that the radiation hits a family of crystallographic planes in the appropriate angle a constructive interference appears, which is spotted by the detector. The result is a diffractogram containing the diffracted intensity at specific diffraction angles (Θ) and directions. Each of these intensities is usually called reflections and their analysis provides relevant structural information of the studied material.

In this thesis, two different X-ray diffraction techniques have been routinely used depending on the size of the crystals obtained. These techniques are powder X-ray diffraction (for polycrystalline samples) and single crystal diffraction.

Single crystal X-ray diffraction (SCXRD)

SCXRD is the most common and powerful technique to obtain detailed structural information of crystalline solid materials, including unit cell dimensions, bond-lengths, bond-angles, lattice symmetry and other details of the atomic ordering. To apply this technique, it is necessary to have a single crystal big enough and free of defects. SCXRD data are usually collected applying the rotation method, i.e., rotating the crystal in the X-ray beam while recording diffraction data, resulting on a diffraction pattern that contains the intensity and the 3D spatial arrangement of thousands of reflections. These allow reconstructing the reciprocal space and assigning Miller indices (*hkl*) to each of the reflections providing information of the crystal lattice and unit cell. Finally, the reflection intensities are used to solve and refine the full crystal structure.

In this thesis, crystals from 40 to 600 μm were selected for SCXRD using a binocular loupe with polarized light. SCXRD measurements for structure elucidation of new precipitated compounds were performed in the XALOC beamline at ALBA synchrotron.[6] Data were collected at 100 K with a 0.72931 Å wavelength using the Dectris Pilatus 6M detector placed at 120 mm from the sample. The ϕ-scans were performed from 0 to 360º in steps of 0.5º and at a collection time of 0.15 s·step^{-1}. The scan was repeated at three different κ angles (0, 45º, 90º) and merged afterwards to increase the completeness and redundancy when possible. Data were indexed, integrated and scaled by Dr. Vallcorba using XDS software, and refined with SHELXL and OLEX2 software.[7-9] Procedures for each structure elucidation are given in the respective Chapters (5,6).

Also in Chapter 4, crystal structure elucidation was performed using a single crystal (*ca.* 0.6 x 0.2 x 0.1 mm). X-ray data were collected using the Mo Kα radiation in a SMART-APEX diffractometer and treated in collaboration with Dr. Alvarez-Larena from the UAB.

Powder X-ray diffraction (PXRD)

When working with supercritical conditions it is difficult to obtain crystals big enough for single crystal structure elucidation and crystalline powders are generally obtained. PXRD is the technique of choice in these situations. As in SCXRD it provides structural information of the materials. However, in this case the diffraction pattern obtained from PXRD is the overlap of the individual SCXRD patterns of each of the random oriented crystallites in the powder sample, giving rise to diffraction rings instead of spots for each reflection. This overlap problem makes the data analysis more complicated than in SCXRD. In PXRD, the diffraction data are usually represented as a 1D pattern of the X-ray intensity as a function of the diffraction angle (2θ). Despite its limitations compared to SXRD for structure solution and refinement, PXRD has several advantages: (i) samples can be usually analyzed as obtained, without any additional manipulation; (ii) it provides bulk information and it can directly asses the crystallinity of the compound; (iii) it is straightforward to check for the presence of known crystalline phases and small variations on its cell parameters or microstructure by the analysis of the peak shapes and positions; (iv) it is very convenient for *in situ* studies (e.g., temperature variations) to detect for phase transitions.

Routine PXRD has been used for identifying and assessing the purity of the crystal phases of the obtained compounds by comparing the experimental patterns with those simulated from single-crystal data or reported in the literature. PXRD patterns were recorded in a Siemens D5000 diffractometer, using the Cu Kα (λ=1.54 Å) incident radiation. The measured 2θ range was from a 4 to 30º, where the most intense peaks for the studied compounds are and enough for phase identification. For known compounds with a reported structure, a full profile matching with the Le Bail method was used to check the crystal structure and to refine the unit cell.[10]

PXRD can also be used to elucidate the structure of unknown phases in some particular cases, e.g., for materials with small particles of only few microns but a really high crystallinity. For this purpose, PXRD with synchrotron radiation at an energy of 25 keV (λ=0.49587 Å determined with a NIST Si standard) has been used. The analysis was carried out in the high resolution endstation of Materials Science and Powder Diffraction (MSPD) beamline (BL04)[11] at the ALBA Synchrotron. Data were collected at 100 and 298 K using the Si-microstrip MYTHEN-II detector (6 modules, 1280 channels/module, 50 μm/channel and sample-to-detector distance 550 mm). Procedures for each structure elucidation are given in

the respective chapters. The measurements and the elucidation of the structures were performed in collaboration with Dr. Vallcorba from ALBA synchrotron.

Additionally, the *in situ* structural evolution of a CP with temperature has been performed from powder diffraction data obtained in the Wide angle X-ray scattering (WAXS) station of the NCDSWEET beamline at ALBA synchrotron. A Linkam TMS350 system with a beam size of 300×100 μm^2 [H × V] and an energy of 12.4 keV wavelength 0.999 Å) in transmission mode was used. Scattered radiation was recorded using a Rayonix LX255HS area detector. Measurements and data processing was performed by Dr. Solano at the ALBA Synchrotron.

3.3.2. Electron diffraction tomography (EDT)

As mentioned previously, the SCXRD structure elucidation approach can only be performed on relatively large crystals with a size of several microns. Smaller crystals can be structurally investigated by PXRD that utilizes information originated from many small crystallites simultaneously, which complicates the analysis. EDT is a specialized method applied for very small crystal structure size elucidation that works by collecting electron diffraction patterns in a transmission electron microscope (TEM).[12] Electron diffraction can deliver information about the unit cell parameters, the presence of centers of symmetry, the space group and so on. This technique allows the extraction of single crystal electron diffraction data by analysing one single small crystallite, and, thus, to analyse polyphasic systems properly.[13] An ultrafast data collection EDT strategy performed under liquid nitrogen allows to significantly reduce the data acquisition time, minimizing the damage of electron beam-sensitive materials, such as thermally labile CPs. This method, combined with the preciseness of the electron beam, provide high quality data enabling the determination of very complex structures.[14] In this thesis, EDT measurements were performed by the team of Dr. Mugnaioli at the CNI@NEST in Italy. The EDT data was collected by a Zeiss Libra 120 TEM equipped with a LaB$_6$ electron source, in-column omega energy filter and Nanomegas Digistar P1000 for beam precession. A parallel beam of about 150 nm in diameter was obtained in Köhler illumination by the insertion of a 5 μm condenser aperture, and the crystal position was tracked in scanning-transmission electron microscopy (STEM) mode. 3D diffraction data were acquired in steps of 1° in precession-assisted nano-diffraction mode (precession angle 1°) and recorded by an ASI MEDIPIX single electron detector camera (14 bit, 512×512 pixels), after filtering out the inelastic scattering.

3.3.3. Infrared spectroscopy (IR)

IR is mainly used for the qualitative identification of molecules by detection of their functional groups. Each molecule displays a characteristic IR spectrum. Infrared radiation is absorbed by the bonds stablished between atoms and the transmitted signal is transformed into a spectrum by Fourier transform (FT) giving FTIR data. Measurements in FTIR are performed after mixing a sample of the studied material with potassium bromide (KBr). Contrarily, attenuated total reflection (ATR) is a technique that enables samples to be examined directly without further preparation. While FTIR is a technique that analyses the bulk of the sample, ATR-FTIR is a surface technique with a penetration depth of around 1 or 2 μm. ATR-FTIR is fast and simple, however with FTIR high resolution can sometimes be obtained. Both modes of FTIR were used in this thesis for analysis by using a JASCO FT/IR-4700 instrument.

In FTIR transmission technique the angle of incidence is equal to zero, while in ATR-FTIR the IR beam enters the ATR crystal at an angle of typically 45° (relative to the crystal surface) and is totally reflected at the crystal to sample interface. Changes in the angle of incidence of the infrared radiation have two main outcomes on the ATR spectrum. First, the angle of incidence has an effect on the number of reflections in the ATR crystal which affects the infrared absorbance intensity of the spectrum. As the angle of incidence increases, the number of reflections decreases and the absorbance intensity decreases. Second, modifying the angle of incidence also changes the depth of penetration. If the angle of incidence is increased, the depth of penetration is decreased as well as the absorbance intensity. Some optical properties of materials can be precisely determined by combining ATR-FTIR measurements made at different angles of incidence. Some commercial ATR cells have the possibility to change the incident angle. In this thesis, for surface analysis of deposited layers, a Vertex 70 fully digital ATR-FTIR spectrometer with reflection measurement at an incident angle of 68º was used.

3.3.4. Ultraviolet and visible absorption spectroscopy (UV-Vis)

UV-Vis absorption liquid spectroscopy consists in the he measurement of the attenuation of a beam of light after it passes through the liquid sample. The UV extends from 100-400 nm and the visible spectrum from 400-800 nm. When the sample is irradiated, the valence electrons of some molecules absorb the light and the electrons are promoted to higher energetic orbitals. This generates empty orbitals. UV-Vis spectroscopy is based on the measurement of the ratio

of the passed light with respect to the incident light in the wavelength range from the UV to the visible. The degree of absorption is recorded and plotted *vs.* the wavelength. This is one of the most simplified and economical method for examining analyte concentration, since a change in concentration produces a change in absorbance. The technique is versatile and gives rapid response regarding quantitative information. The quantification is performed by making a calibration curve by collecting the UV-Vis spectrum of a variety of different concentration samples in the linear range. This technique was used in this thesis for the estimation of solutes dissolved in water in drug release experiments. Measurements were performed in a Varian Cary 5000.

3.3.5. Elemental analysis (E.A.)

The purpose of E.A. is to determine the relative quantity of a particular element within a material. Usually, the mass fractions of carbon, nitrogen and hydrogen (C, H, N) are determined. The technique is based in the instantaneous and complete oxidation of the sample by combustion with oxygen at approximately 1200 K. In this thesis, C, H, N values were measured and compared with the theoretical expected values of stoichiometric known CPs. This allows estimating the purity of the compounds. For unknown compounds, elemental analysis data can be used to guess the stoichiometric composition. Measurements were performed in a Thermo Carlo Erba Flash 2000.

3.3.6. N$_2$ adsorption isotherms

Textural properties are assessed by measuring in the sample the adsorption/desorption isotherm of N$_2$ at low temperature (77 K) as a function of pressure. Usually, measurements are performed from vacuum to the relative pressure of 1. Textural properties, i.e., pore size distribution, surface area and pore volume, are extracted from data in the isotherm by using several mathematical models, each one adequate for the different pore-size regions.[15-17] Often, the method developed by Brunauer, Emmett, and Teller (BET) is used for the determination of the surface area of mesoporous materials (2-50 nm).[18] The method proposed by Barrett, Joyner and Halenda (BJH)[19] remains the most popular way of deriving the pore size distribution from the isotherm.[20] For micropores (< 2 nm), the t-plot method proposed by Lippens and the Boer is commonly used.[19]
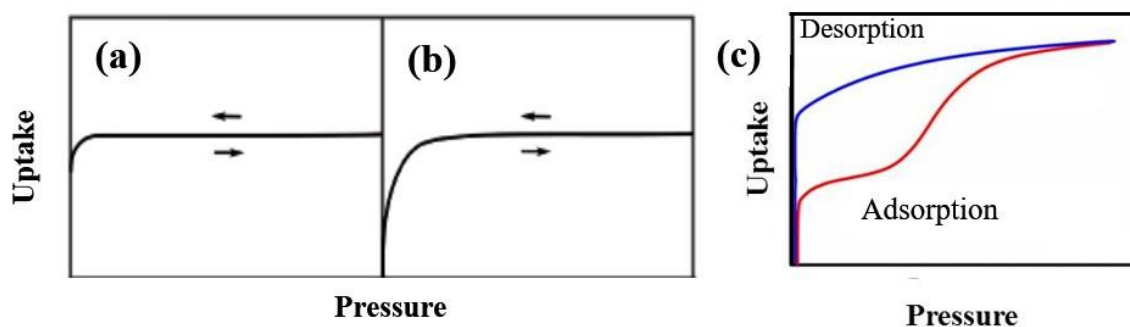
Figure 3.8. N_2 adsorption isotherms for: (a) mainly narrow micropores in rigid MOFs, (b) wider micropores and possible small mesopores in rigid MOFs, and (c) flexible microporous MOFs.

Most of the developed MOFs are microporous materials with the reversible Type I isotherm (Fig. 3.8(a)), in which significant adsorption is limited to very low adsorption pressures governed by the internal pore volume rather than by the surface area. Type I is one of the six isotherms classified by the IUPAC.[18,17] Recently, new types of isotherms have been described for MOFs due to their unique properties, like structural flexibility.[22] Flexible porous crystals are defined as porous solids that possess both a highly ordered network and structural transformability. They are bistable or multistable crystalline materials with long range structural ordering, a reversible transformability between structures, and permanent porosity.[23] A typical adsorption behavior often found for flexible microporous MOFs is shown in Fig. 3.8(b). During adsorption, a gradual or sudden opening from narrow to large pore occurs at certain pressure giving a stepped isotherm. Usually, the desorption lacks of any step, resulting in a large hysteresis loop.

The textural properties in this thesis were determined by N_2 adsorption at 77 K using an ASAP 2000 Micromeritics Inc. Samples were first degassed at 333 or 393 K for 24 h. The specific surface area was determined by the BET method. The pore volume was calculated using the BJH method from the adsorption branch of the isotherm. Micropore values were estimated by the t-plot method. In addition, in Chapter 4, CO_2 adsorption experiments were carried out to evaluate the potential use of these materials as CO_2 capture adsorbents. Samples were first degassed at 333 K for 24 h and then measured at 273 K using an ASAP 2000 from Micromeritics Inc.

3.3.7. Scanning electron microscopy (SEM)

Scanning electron microscopy allows the observation in three dimensions of the morphology of the samples at the micro and nanoscale. Samples need to be electrically conductive at least at the surface to prevent electrostatic charge and blurry images.[24] Metallization with a thin layer of Au, Pt or Pd is needed for samples that are not conductive. In this thesis, SEM images were taken with a Quanta Fei 200 microscope, used to observe the morphology of the precipitated compounds and for studying and following the crystal growth of some compounds. Samples were first coated with Au/Pd using a K550 Sputter Coater (Coating Attatchment Emitech).

3.3.8. Energy-dispersive X-ray spectroscopy (EDS)

Backscattered electron images in the SEM display compositional contrast that results from different atomic number elements and their distribution. EDS is a chemical surface technique used in conjunction with SEM for samples microanalysis. The EDS technique detects X-rays emitted during the bombardment of the sample with an electron beam to identify what the particular elements are and their relative proportions. Characteristics X-rays of different elements are separately detected to create an energy spectrum. The technique is limited to elements with atomic number higher than 11 (Na). Features or phases smaller than 1 µm can be analyzed. Both chemical compositional maps of the bulk sample and composition lines of a single crystal can be created. In this thesis, EDS was used to assess the presence of metals in powdered samples of different compounds and for the semi-quantitative analysis of the metal percentage. The used equipment was a FEI Magellan 400L HXR SEM coupled to an Ultim Extreme (Oxford Instruments) EDS detector. Measurements were performed by depositing the samples in a silicon wafer. This support was used instead of the common carbon type in order to be able to evaluate the C percentage without interference from the support. Samples were coated with a Pt layer with a thickness of 5 nm. These measurements were performed to estimate the chemical composition of new materials and for the assessment of metals percentage in heterometallic compounds.

3.3.9. Thermogravimetric analysis (TGA)

Thermogravimetric analysis is used to study the thermal stability of compounds by monitoring the weight loss of mass with the increase of temperature in a controlled flow of gas. The instrument consists of a sample pan supported by a precision balance.[25] In this thesis, two different instruments were used for TGA studies. A Netzsch-STA 449 F1 Jupiter was used to process the samples in N_2 flow, while a TA Instruments SDT Q600a was employed with synthetic air (20 % oxygen and 80 % nitrogen).

3.3.10. Nuclear magnetic resonance spectroscopy (NMR)

NMR spectroscopy is a technique used for the analysis of molecular structures and for the identification of unknown chemicals. The most commonly used NMR isotopes are ^{1}H and ^{13}C, used to analyses the carbon-hydrogen framework of different compounds by measuring the interaction and resonance frequency of nuclear spins when placed in a powerful magnetic field. Many other isotope with an odd number of protons and non-zero nuclear spin can be studied by high-field NMR spectroscopy.[26] NMR techniques can involve liquid (solution) and solid states. In this thesis, ^{1}H and ^{13}C-NMR characterization was performed after dissolving the sample in deuterated chloroform, the solvent most commonly used because of its low price. ^{1}H-NMR spectra were recorded on an NMR-FT Bruker AC-250 MHz spectrometer, while ^{13}C-NMR data was obtained in an NMR-FT Bruker Avance II 300 spectrometer. The technique was also applied to ascertain the purity of some starting materials used for synthesis.

3.3.11. Fluorescence microscope (FM)

The fluorescence microscope is used to generate an image in compounds with fluorophores.[27] In this thesis, the FM was used to detect the presence of intrinsically fluorescent substances. Images were recorded in an optical OLYMPUS Bx51 microscope (DP20 camera) with a fluorescent U-RFL-T mercury lamp accessory.

3.3.12. Superconducting quantum interference magnetometer (SQUID)

The SQUID is used to measure subtle magnetic fields.[28] The magnetic susceptibility (χ) indicates the magnetization of a material in an applied magnetic field. There are two main types of SQUID: direct current (DC) and alternating current (AC). DC systems are used to determine the equilibrium value of the magnetization in a sample.[29] Because of the need of

superconductivity, DC devices work only at very low temperatures. AC becomes indispensable for investigations of phase transitions and magnetic relaxations in, for example, paramagnetic salts, spin glass, low dimensional magnets and superconductivity materials. AC measurements are performed in a static magnetic field generated by alternating current and are very sensitive to small changes in the magnetization field.[30] In this thesis, DC and AC magnetic measurements were performed in a Quantum Design MPMS-5S magnetometer.

3.3.13. Inductively coupled plasma mass spectrometry (ICP-MS)

ICP-MS is used for atoms quantification in samples by coupling a method that generates ions (ICP) with a system able to separate and detect those (MS). It can be employed to analyse all the elements that possess an ionization potential lower than the one of argon.[31] In this thesis, an ICP-MS 7700x Agilent instrument with a collision cell of He was used for analysis. The samples were previously digested in a microwave with hydrochloric acid and nitric acid during 30 min at 453 K and 20 min at 473 K. The technique was used for metals quantification in heterometallic compounds.

3.3.14. X-ray photoelectron spectroscopy (XPS)

XPS is used to determine the chemical composition of the surface of a sample (less than 10 nm of thickness). All the elements with the exception of the lighter ones, H and He, can be detected. This technique also provides information about the bonding of the elements and the oxidation state. XPS spectra are obtained by irradiating the material with a beam of X-rays and measuring the kinetic energy and number of electrons that escape from the surface. Each element produces a characteristic set of XPS peaks at a specific binding energy.[32] In this thesis, a XPS Kratos AXIS Supra instrument was used for the surface characterization of homo and heterometallic compounds. Al-Kα monochromatic radiation (20 eV) emitted at 225 W (15 mA / 15 kV) was used for analysis. The penetration deep was 7 nm. Data treatment was performed by Dr. Marbán (INCAR-CSIC, Spain).

Summary of the used techniques and their application in this thesis

Table 3.2. Summary of the used techniques and their application in this thesis.

Technique	Localization	Chapter
PXRD	(Cu) ICMAB (CSIC)	4, 5 and 6, 7
PXRD	synchrotron ALBA	4, and 5, 6
SCXRD	synchrotron ALBA	5 and 6
SCXRD	(Mo) UAB	4
WAXS	synchrotron ALBA	6
EDT	CNI@NEST (Italy)	7
FTIR	ICMAB (CSIC)	7
ATR-FTIR	ICMAB (CSIC)	4 and 7
UV-Vis	ICMAB (CSIC)	7
E.A.	London Metropolitan Univ. (UK)	4, 5 and 6, 7
N_2 adsorption isotherm	ICMAB (CSIC)	4,6 and 7
SEM	ICMAB (CSIC)/UAB	4, 5 and 6, 7
EDS	ICN2 (CSIC)	5 and 6
TGA	INCAR (CSIC)	6 and 7
NMR	ICMAB (CSIC)/UAB	4
FM	ICMAB (CSIC)	4
SQUID	UB	5
ICP-MS	INCAR (CSIC)	5
XPS	INCAR (CSIC)	5

3.4. References

(1) Jessop, P. G., Leitner, W. Chemical synthesis using supercritical fluids. Eds. Wiley-VCH Verlag GmbH. Weinheim, Germany, **1999**.

(2) Success, E. Y. Connector and tubing solutions technical guide. (accessed May 26, **2019**).

(3) Dann, S. E. Characterization of solids. in reactions and characterization of solids. Ed. Royal Society of Chemistry: Cambridge, **2007**, 48-80.

(4) Sharma, R.; Bisen, D.; Shukla, U.; Sharma, B. X-ray diffraction: a powerful method of characterizing nanomaterials. *Recent Res. Sci. Technol.*, **2012**, 4 (8), 77-79.

(5) Arndt, U. W.; Wonacott, A. J. The rotation method in crystallography. Amsterdam: Elsevier/North Holland Biomedical Press. **1977**.

(6) Juanhuix, J.; Gil-Ortiz, F.; Cuní, G.; Colldelram, C.; Nicolás, J.; Lidón, J.; Boter, E.; Ruget, C.; Ferrer, S.; Benach, J. Developments in optics and performance at BL13-XALOC, the macromolecular crystallography beamline at the ALBA synchrotron. *J. Synchrotron Radiat.*, **2014**, 21 (4), 679-689.

(7) Kabsch W. XDS. *Acta Crystallogr Sect D Biol Crystallogr*., **2010**, 66(2), 125-132.

(8) Sheldrick, G. M. A short history of SHELX. *Acta Cryst. A,* **2008**, 64, 112-122.

(9) Dolomanov, O. V.; Bourhis, L. J.; Gildea, R. J.; Howard, J. A. K.; Puschmann, H. OLEX2: A complete structure solution, refinement and analysis program. *J. Appl. Crystallogr.,* **2009**, 42 (2), 339-341.

(10) Le Bail, A. Whole powder pattern decomposition methods and applications: a retrospection. *Powder Diffr.,* **2005**, 20 (4), 316-326.

(11) Fauth, F.; Peral, I.; Popescu, C.; Knapp, M. The new material science powder diffraction beamline at ALBA synchrotron. *Powder Diffr*., **2013**, 28, S360-S370.

(12) Simancas, J.; Simancas, R.; Bereciartua, P. J.; Jorda, J. L.; Rey, F.; Corma, A.; Nicolopoulos, S.; Pratim Das, P.; Gemmi, M.; Mugnaioli, E. Ultrafast electron diffraction tomography for structure determination of the new zeolite ITQ-58. *J. Am. Chem. Soc.,* **2016**, 138 (32), 10116-10119.

(13) Corrêa, C. A.; Klementov, M. Structural analysis of nanocrystals by 3D electron diffraction tomography. *WDS'14 Proceedings of Contributed Papers-Physics*, **2014**, 67-72.

(14) Gemmi, M.; La Placa, M. G. I.; Galanis, A. S.; Rauch, E. F.; Nicolopoulos, S. Fast Electron diffraction tomography. *J. Appl. Crystallogr.,* **2015**, 48 (3), 718-727.

(15) Thommes, M.; Kaneko, K.; Neimark, A. V.; Olivier, J. P.; Rodriguez-Reinoso, F.; Rouquerol, J.; Sing, K. S. W. Physisorption of gases, with special reference to the evaluation of surface area and pore size distribution (IUPAC technical report). *Pure Appl. Chem.,* **2015**, 87 (9-10), 1051-1069.

(16) Kitagawa, S.; Kitaura, R.; Noro, S. Functional porous coordination polymers. *Angew. Chemie Int. Ed*., **2004**, 43 (18), 2334-2375.

(17) Donohue, M.; Aranovich, G. Classification of Gibbs adsorption isotherms. *Adv. Colloid Interface Sci.,* **1998**, 76-77, 137-152.

(18) Lowell, S.; Shields, J. E.; Thomas, M. A.; Thommes, M. Characterization of porous solids and powders: surface area, pore size, and density. *Choice Rev. Online*, **2005**, 42 (09), 42-5288.

(19) Yohn, S.; Long, D.; Fett, J.; Patino, L. Regional versus local influences on lead and cadmium loading to the great lakes region. *Appl. Geochemistry*, **2004**, 19 (7), 1157-1175.

(20) Barrett, E. P.; Joyner, L. G.; Halenda, P. P. The determination of pore volume and area distributions in porous substances. I. computations from nitrogen isotherms. *J. Am. Chem. Soc.,* **1951**, 73 (1), 373-380.

(21) Sing, K. The use of nitrogen adsorption for the characterisation of porous materials. Colloids surfaces a physicochem. *Eng. Asp.*, **2001**, 187-188, 3-9.

(22) Yang, Q.-Y.; Lama, P.; Sen, S.; Lusi, M.; Chen, K.-J.; Gao, W.-Y.; Shivanna, M.; Pham, T.; Hosono, N.; Kusaka, S.; Perry, J. J.; Ma, S.; Space, B.; Barbour, L. J.; Kitagawa, S.; Zaworotko, M. J. Reversible switching between highly porous and nonporous phases of an interpenetrated diamondoid coordination network that exhibits gate-opening at methane storage pressures. *Angew. Chemie Int. Ed.,* **2018**, 57 (20), 5684-5689.

(23) Horike, S.; Shimomura, S.; Kitagawa, S. Soft porous crystals. *Nat. Chem*., **2009**, 1 (9), 695-704.

(24) Han, W.; Jiao, H.; Fox, D. Scanning electron microscopy. In springer tracts in modern physics; *Tsinghua University Press Limited*, **2018**, 272, 35-68.

(25) Malič, B.; Kupec, A.; Kosec, M. Thermal analysis in chemical solution deposition of functional oxide thin films. Springer Vienna: Vienna, **2013**, Vol. 9783211993, 163-179.

(26) Dais, P.; Spyros, A. Nuclear magnetic resonance in chemical analysis of food: techniques and applications. *Elsevier*, **2012**, 91-115.

(27) Sanderson, M. J.; Smith, I.; Parker, I.; Bootman, M. D. Fluorescence microscopy. *Cold Spring Harb. Protoc*., **2014**, 10 (10), 1-36.

(28) Hatscher, S.; Schilder, H.; Lueken, H.; Urland, W. Practical guide to measurement and interpretation of magnetic properties (IUPAC technical report). *Pure Appl. Chem*., **2005**, 77 (2), 497-511.

(29) Martien, D. Introduction to: Cc Susceptibility. *Quantum Des*. **1994**, 4.

(30) Marcon, P.; Ostanina, K. Overview of methods for magnetic susceptibility measurement. *Prog. Electromagn. Res. Symp*., **2012**, 5, 420-424.

(31) Thomas, R. I. Practical Guide to ICP-MS. Marcel Dekker, Inc. **2004**.

(32) Aziz, M.; Ismail, A. F. X-ray photoelectron spectroscopy (XPS). Tsinghua University Press Limited, **2017**.

New approach to crystallize CPs built of metal complexes with low solubility in scCO₂

CHAPTER 4 describes different approaches for the synthesis of coordination polymers with starting materials that possess low solubility in supercritical carbon dioxide. This Chapter is based on two published articles:

4.1. Introduction

As it was previously mentioned in the general introduction (Chapter 1), the interest of the research community in coordination polymers (CPs) has recently grown enormously, owed to the outstanding properties and numerous applications that such materials possess. The number of developed methods of synthesis for these compounds has also risen accordingly, ranging from solvothermal, microwave-assisted, mechanochemical, electrochemical and sonochemical methods, among others. New developed methods for CPs preparation are focused on the use of unconventional solvents, including supercritical fluids, ionic liquids and fluorinated solvents.

Recently, the study of the synthesis of coordination polymers in the presence of supercritical CO_2 ($scCO_2$) has become a burgeoning direction in chemistry and materials science. Indeed, the low surface tension and viscosity of supercritical solvents, particularly the green $scCO_2$, make them suitable fluids to process porous systems.[1] However, $scCO_2$ has a poor solvent power for high-molecular weight and polar molecules, which, in principle, would rule out many possibilities in CPs synthesis. An effective way to solve this problem is to create mixtures of $scCO_2$ with other solvents that own the capacity of solubilizing both polar and apolar building units needed for CPs synthesis. One example is the use of combinations of $scCO_2$ and organic solvents (e.g., dimethylformamide), known as expanded switchable solvents.[2] Another explored option has been the ionothermal synthesis carried out in mixtures of $scCO_2$ and an ionic liquid.[3,4] Further, a generic method for the crystallization of CPs in $scCO_2$ is being developed in the research group of Domingo *et al.* at ICMAB, with focus on the synthesis of one- (1D),[5] two- (2D)[6] and three-dimensional (3D)[7] MOFs. In $scCO_2$, fluorinated compounds have shown to have a significant solubility.[8] For that reason, neutral metal complexes with fluorinated ligands are chosen in this project as the main precursor candidates for MOFs synthesis. However, not all interesting metal centers, fluorinated or not, are found soluble in this fluid. Hence, a comprehensive analysis of different approaches to be used for crystallization in $scCO_2$ of CPs build of metal complexes that present a negligible solubility in this medium is firstly performed in this Chapter. The research focuses on tuning and controlling building unit's solubility in $scCO_2$ by the modification of the experimental parameters and/or the use of additives. Aside of studying the influence of the running time in the different reactions, the addition of additives is the main experimental parameter

scrutinized in this work. To increase the solubility of the metal precursor, the use of either ethanol as a co-solvent or *tert*-butylpyridine (*t*-bpy) as ancillary ligand for the metal complex is assayed. Herein, main factors influencing CPs crystallization in scCO$_2$ are rationalized taking as a model the reaction of either a metal diethyl oxaloacetate (M(deox)$_2$) or a metal trifluoroacetate (M(tfa)$_2$) complex, both having low solubility in this fluid, with a highly soluble bidentate pyridine linker. For comparison, crystallization was also carried out in conventional solvents.

First, coordination polymers with formula [M(deox)$_2$(bpy)]$_n$ (M=Co(II), Cu(II), Mn(II), Ni(II) or Zn(II); deox=diethyl oxaloacetate and bpy=4,4'-bipyridine) were precipitated with a laminar morphology and nanometric thickness. The first synthetic approach was based on the use of conventional liquid solvents (ethanol and methanol), in which [M(deox)$_2$(H$_2$O)$_x$] and bpy precursors are very soluble. In the same way, the preparation of these coordination polymers in scCO$_2$ should be favored by achieving a significant solubility of the reagents in this medium. However, when dealing with metal complexes, this can be a limiting step, since most of them are insoluble in scCO$_2$. To increase the solubility either ethanol was added as a co-solvent or [M(deox)$_2$(H$_2$O)$_x$] was modified to [M(deox)$_2$(*t*-bpy)$_2$]·nH$_2$O (*t*-bpy=*tert*-butylpyridine). Next, the acquired knowledge on the use of proper additives to enhance the solubility of precursors in scCO$_2$ was applied to the preparation of other family of coordination polymers, based on (M(tfa)$_2$) (tfa=trifluoroacetate) with a low or null solubility in scCO$_2$.[9] Two previously described and four new 2D MOFs were precipitated of this compound using this procedure. In short, to increase the solubility of the metal precursor, four methods were used: (i) increase of the running time, (ii) use of ethanol as a co-solvent, (iii) addition of *t*-bpy as modified metal complex, and (iv) addition of *t*-bpy *in situ* in the reaction media.

Morphology control is, at present, a subject of great interest, since it is intimately related to potential applications of the synthetized CPs, besides its structure.[10] These materials are often obtained as large micrometre-sized polycrystalline powders using the settled synthetic methods. Since the development of graphene science, the interest in the preparation of two-dimensional (2D) nanostructured materials has grown steadily due to their potential technological applications.[11–13] In many cases, 2D structures exhibit superior properties to their 3D counterparts.[14,15] Preparation of material with a 2D morphology is a challenge in the case of materials whose structure is not layered, and thus has not a natural tendency to form

flakes or nanosheets.[16] Among the non-carbon-based, non-layered 2D porous materials, zeolites[17] or hybrid materials,[1] have received notable interest due to their interesting properties making them suitable for applications in electronics, photovoltaic uses, membranes, energy storage, catalysis, sensing, or biotechnology.[18] 2D nanosheet materials possess planar morphology with thicknesses generally ranging from atomic/molecular level to ~ 100 nm, however much larger lateral dimensions are generally found. The synthesis approaches for obtaining such materials involve in many occasions top-down methodologies, where bulk layered materials are prepared, followed by exfoliation or delamination.[19–21] Growth on crystalline surfaces is another strategy used to obtain MOF nanosheets.[22] Likewise, coordination polymers with a 2D nanosheet morphology have been prepared by top-down approaches, in which the layers are obtained from the cleavage of the interlayer interactions throughout mechanical forces expressed over the bulk material. 2-D nanosheets can also be prepared by bottom-up strategies applied in solution synthesis.[23] To control the 2D morphology in the precipitated crystals, a general approach has been the use of surfactants or inorganic ions, which are adsorbed on specific crystallographic faces retarding their growth.[24,25] An alternative method to obtain platelet-like microcrystals has been recently developed in our laboratories based on the use of scCO$_2$ as a solvent. The technique has previously been used for the precipitation of organometallic molecular adducts[26] and 1D coordination polymers.[5] An important objective of the work performed in this Chapter was to develop additional ways to obtain 2D nanostructures of the precipitated CPs involving M(deox)$_2$ and M(tfa)$_2$ transition metal complexes and bipyridine linkers. The described method to achieve significant solubility enhancement in scCO$_2$ of the metal precursor allowed the use of the supercritical fluid reactive deposition technique for the preparation of thin films of the synthetized CPs by exposing the supercritical solution to a modified substrate. Preliminary results on the surface deposition of one of the M(tfa)$_2$ studied products are also presented and discussed, showing the potential of the developed solubility enhancement protocols for the preparation of thin films of a wide variety of organometallic and hybrid compounds.

4.2. Materials and methods

4.2.1. Materials

Copper(II) chloride dihydrate (CuCl$_2$·2H$_2$O, ≥99%), cobalt(II) acetate tetrahydrate (Co(CH$_3$COO)$_2$·4H$_2$O, reagent grade), manganese(II) acetate tetrahydrate (Mn(CH$_3$COO)$_2$·4H$_2$O, ≥99%), nickel(II) acetate tetrahydrate (Ni(CH$_3$COO)$_2$·4H$_2$O, ≥98%) and zinc sulphate heptahydrate (ZnSO$_4$·7H$_2$O, ≥98%) were used as the metal sources. The diethyl oxalacetate sodium salt (Na(deox), C$_8$H$_{11}$O$_5$Na) was used as the reactant to form the starting coordination complex. Copper(II) trifluoroacetate hydrate (Cu(tfa)$_2$) and zinc(II) trifluoroacetate hydrate (Zn(tfa)$_2$) were also used as metal centers.

Tert-butylpyridine (*t*-bpy) was used as the ancillary ligand aid to form adducts. 4,4′-bipyridine (bpy), 2-bis(4- pyridyl)ethylene (bpe) and 1,3-bis(4-pyridyl)propane (bpp) were used as linkers for the construction of coordination polymers.

N-(3-triethoxysilylethyl)pyridine was the used silane for surface modification. Silicon wafers of 5x5 mm from TED PELLA, INC were the used substrates for surface deposition.

Reagents and most liquid solvents (methanol, heptane and dichloromethane (DCM)) were purchased from Sigma Aldrich. Ethanol (EtOH) was purchased from Panreac. CO$_2$ (99.995%) was supplied by Carburos Metálicos S.A. (Spain).

4.2.2. Experimental protocols

Synthesis of precursor [M(deox)$_2$(H$_2$O)$_x$] (M=Cu(II) x=1; M=Co(II), Mn(II), Ni(II), Zn(II) x=2)

The used synthetic method is a modification of the previously described procedure by Hay,[27] in which a commercial sodium salt of diethyloxaloacetate (Na(deox)) was used instead of the acid (Hdeox). The commercial Na(deox) (≥ 95%) contained a traces of water insoluble impurity that was eliminated by filtration.

[Co(deox)$_2$(H$_2$O)$_2$]. A solution of 0.890 g (3.57 mmol) of Co(CH$_3$COO)$_2$·4H$_2$O in 30 mL of water was mixed with a filtered solution of 1.52 g (7.23 mmol) of Na(deox) in 70 mL of water. The pink precipitate formed was filtered off and rinsed with 3 x 20 mL of water. The recovered powder was dried at room temperature. Yield 92 % (1.55 g, 1.56 mmol). E.A. % calc. for CoC$_{16}$H$_{26}$O$_{12}$ C: 40.94 %, H: 5.58 %; found C: 40.70%, H: 5.47 %.

[Cu(deox)₂(H₂O)]. 1.02 g (4.85 mmol) of Na(deox) was added to a solution of 0.32 g (1.88 mmol) of CuCl₂·2H₂O in 30 mL of MeOH and stirred for 5 minutes. Then, 10 mL of water was added producing an immediate green crystalline precipitate. The solid was recovered, redissolved in ethanol, and the solution was left to stand in a crystallizer. The crystals obtained were washed with 2 x 20 mL of water, and then recrystallized from ethanol. Yield 70 % (0.60 g, 1.32 mmol). E.A. % calc. for $CuC_{16}H_{24}O_{11}$ C: 42.15 %, H: 5.31%; found C: 42.08 %, H: 5.20 %.

[Mn(deox)₂(H₂O)₂]. A solution of 0.880 g (3.59 mmol) de Mn(CH₃COO)₂·4H₂O in 30 mL of water was added to a filtered solution of 0.52 g (7.23 mmol) of Na(deox) in 70 mL of water. The yellow precipitate was filtered off and rinsed with 2 x 20 mL of water. The resulting solid was dried at room temperature and then recrystallized from ethanol. Yield 56 % (0.930 g, 2.00 mmol). E.A. % calc. for $MnC_{16}H_{26}O_{12}$ C: 41.30 %, H: 5.63 %; found C: 41.12 %, H: 5.45 %.

[Ni(deox)₂(H₂O)₂]. 2.03 g (9.66 mmol) of Na(deox) was added to a solution of 1.18 g (4.74 mmol) of Ni(CH₃COO)₂·4H₂O in 50 mL of MeOH. The mixture was filtered to eliminate a small amount of insoluble solid. Then, 20 mL of water were added to the solution producing a light green precipitate. The solid was recovered, redissolved in 25 mL of ethanol, and the solution was left to stand in a crystallizer. The crystals obtained were washed with 3 x 10 mL of water, and then recrystallized from ethanol. Yield 59 % (1.32 g, 2.81 mmol). E.A. % calc. for $NiC_{16}H_{26}O_{12}$ C: 40.97 %, H: 5.58 %; found C: 40.94 %, H: 5.47 %.

[Zn(deox)₂(H₂O)₂]. A filtered solution of 0.684 g (2.38 mmol) of ZnSO₄·7H₂O in 30 mL of water was added to a solution of 1.00 g (4.76 mmol) of Na(deox) in 90 mL of water. The white precipitate formed was filtered off and rinsed with 3 x 10 mL of water. The recovered powder was dried at room temperature. ^{1}H-NMR (CDCl₃, 250 MHz) δ: 5.65 (s, 1H, EtOOC-COC*H*-COOEt), 4.21 and 4.16 (m, *J* 7.1 Hz, 4H, CH₃C*H₂*-), 2.48 (s, broad, H₂O), 1.30 and 1.26 (m, *J* 7.1 Hz, 6H, C*H₃*CH₂-). ^{13}C-NMR (CDCl₃, 250 MHz) δ: 174.5, 167.1, 166.1 (EtOO*C*-*C*OC*H*-*C*OOEt), 88.8 (EtOOC-CO*C*H-COOEt), 62.0 and 60.5 (-O-*C*H₂CH₃), 14.2 and 13.9 (-O-CH₂*C*H₃). Yield 65 % (0.740 g, 1.56 mmol). E.A. % calc. for $ZnC_{16}H_{26}O_{12}$ C: 40.39 %, H: 5.50 %; found C: 40.33 %, H: 5.57 %.

Synthesis of [M(deox)₂(*t*-bpy)₂]·nH₂O molecular adducts

[M(deox)₂(H₂O)ₓ] prepared precursors were mixed with a small excess of *t*-bpy to form M:*t*-bpy complexes with stoichiometry 1:2. The mixture was grinded by hand in an agate mortar, pestle for 10 min, and allow to stand in a laboratory cabinet for a day. With this procedure, the excess of *t*-bpy was evaporated and the initial pasty mixture quickly evolucionate into a powder.

[Co(deox)₂(t-bpy)₂]·H₂O. Orange color. E.A. % calc. for $CoC_{34}H_{50}O_{11}N_2$ C: 56.58 %, H: 6.98 %, N: 3.88 %; found C: 55.92 %, H: 6.93 %, N: 3.69 %.

[Cu(deox)₂(t-bpy)₂]·2H₂O. Green color. E.A. % calc. for $CuC_{34}H_{52}O_{12}N_2$ C: 54.86 %, H: 7.04 %, N: 3.76 %; found C: 54.79 %, H: 7.26 %, N: 3.66 %.

[Mn(deox)₂(t-bpy)₂]·1.5H₂O. Yellow color. E.A. % calc. for $MnC_{34}H_{51}O_{11.5}N_2$ C: 56.19 %, H: 7.07 %, N: 3.85 %; found C: 56.47 %, H: 7.81 %, N: 3.83 %.

[Ni(deox)₂(t-bpy)₂]. Greyish-green color. E.A. % calc. for $NiC_{34}H_{48}O_{10}N_2$ C: 58.05 %, H: 6.88 %, N: 3.98 %; found C: 57.93 %, H: 7.07 %, N: 4.18 %.

[Zn(deox)₂(t-bpy)₂·2H₂O. White powder. E.A. % calc. for $ZnC_{34}H_{52}O_{12}N_2$ C: 54.73 %, H: 7.02 %, N: 3.75 %; found C: 54.81 %, H: 6.85 %, N: 3.77 %. ^{1}H-NMR (CDCl₃, 250 MHz) δ: 8.5 and 7.39 (s, 2H+2H, $(CH_3)_3C-C_5H_4N$), 5.73 (s, 1H, EtOOC-COC*H*-COOEt), 4.27 and 4.22 (mq+q, *J* 7.1 Hz, 2H + 2H, CH₃C*H₂*-), 2.15 (s, broad, H₂O), 1.35,1.28 (m, 15 H, *J* 7.1 Hz, C*H₃*) and 1.33 (s, 9H, (C*H₃*)₃-).^{13}C-NMR (CDCl₃, 250 MHz) δ: 174.8, 170.4, 165.8 (EtOO*C*-*C*OC*H*-*C*OOEt), 87.9 (EtOOC-CO*C*H-COOEt), 61.4 and 60.3 (-O-*C*H₂CH₃), 14.3 and 14.1 (-O-CH₂*C*H₃), 162.0, 149.2 121.5 ((CH₃)₃C-N*C*₅H₄), 34.9 (*C*-(CH₃)₃, *t*-bpy) 30.25 (-CH₃, *t*-bpy).

Conventional preparation of [M(deox)₂(bpy)]ₙ 1D-coordination polymers.

[Co(deox)₂(bpy)]ₙ. A solution of 250 mg (0.53 mmol) of [Co(deox)₂(H₂O)₂] in 30 mL of MeOH was added to a solution of 83 mg (0.53 mmol) of bpy in 120 mL of MeOH. The orange precipitate formed was filtered off, washed with methanol, and left to dry at room temperature. Yield 94 % (300 mg. 0.50 mmol). E.A. % calc. for $CoC_{26}H_{30}O_{10}N_2$ C: 52.98 %, H: 5.13 %, N: 4.75 %; found: C: 51.86 %, H: 4.88 %, N: 5.01 %.

[Cu(deox)₂(bpy)]ₙ. A solution of 140 mg (0.31 mmol) of [Cu(deox)₂(H₂O)] in 20 mL of MeOH was added to a solution of 50 mg (0.32 mmol) of bpy in 10 mL of MeOH. The crystalline precipitate formed was filtered off, washed with MeOH, and left to dry at room temperature. Yield 93 % (170 mg; 0.29 mmol). E.A. % calc. for $CuC_{26}H_{30}O_{10}N_2$ C: 52.57 %, H: 5.09 %. N: 4.72 %; found C: 52.34 %, H: 5.02 %, N: 4.49 %.

[Mn(deox)₂(bpy)]ₙ. A solution of 100 mg (0.21 mmol) of [Mn(deox)₂(H₂O)₂] in 20 mL of DCM was added to a solution of 33 mg (0.23 mmol) of bpy in 20 mL of DCM. Then, 10 mL of heptane were added. This final mixture was left to evaporate to dryness. The obtained solid was washed with 5 mL of DCM, and the solid was further recrystallized in 20 mL of ethanol. Yield 77 % (97 mg, 0.16 mmol). E.A. % calc. for $MnC_{26}H_{30}O_{10}N_2$ C: 53.34 %, H: 5.16%. N: 4.78 %; found C: 53.18 %, H: 5.36 %, N: 4.85 %.

[Ni(deox)₂(bpy)]ₙ. A solution of 103 mg (0.22 mmol) of [Ni(deox)₂(H₂O)₂] in 20 mL of EtOH was added to a solution of 36 mg (0.22 mmol) of bpy in 50 mL of EtOH. The precipitate formed was filtered off, and recrystallized from methanol. Yield 75 % (98 mg, 0.16 mmol). E.A. % calc. for $NiC_{26}H_{30}O_{10}N_2$ C: 52.99 %, H: 5.13 %, N: 4.75 %; found C: 52.87 %, H: 5.15 %, N: 4.84 %.

[Zn(deox)₂(bpy)]ₙ (H₂O)₁/₄. A solution of 255 mg (0.54 mmol) of [Zn(deox)₂(H₂O)₂] in 30 mL of MeOH was added to a solution of bpy in 120 mL of MeOH. The white precipitate formed was filtered off, washed with methanol, and left to dry at room temperature. Yield 93 % (304 mg, 0.50 mmol). E.A. % calc. for $ZnC_{26}H_{30}O_{10}N_2+1/4 H_2O$ C: 52.01 %, H: 5.12 %, N: 4.67 %; found C: 51.72 %, H: 5.20 %, N: 4.97 %.

ScCO₂ preparation of CPs

Sample preparation under scCO₂ was carried out in the high-pressure equipment described in Chapter 3.

[M(deox)₂(bpy)]ₙ 1D CPs

Method A. Preparation using ethanol as a co-solvent. A Pyrex vial was charged with *ca.* 150 mg of [M(deox)$_2$(H$_2$O)$_x$] and 2 mL of ethanol. In a separated vial, a 5-10 % excess of bpy, respect to the required amount for the formation of the 1:1 polymer, was added. The glass pots were covered with cellulose paper and placed inside the reactor. The vial containing the metal reagent was stirred with a magnetic bar to facilitate dissolution. The reactor was sealed and filled with liquid CO_2, then heated at 333 K. Next, the system was pressurized with a syringe pump up to 20 MPa. The conditions remained the same during 2.5 h to ensure the total formation of the desired products. The precipitated product was washed off the excess of reagents and by-products with a continuous flow of fresh scCO$_2$, by following four cycles of pressurization/depressurization from 20 to 7 MPa at the working temperature. Finaly the product was recovered after despresuritzation to atmospheric presure and cooled down to room temperature.

Method B. Preparation from [M(deox)$_2$(t-bpy)$_2$]·nH$_2$O adducts. Similarly to the previous procedure, the autoclave was charged with *ca.* 150–200 mg of the metal complex [M(deox)$_2$(t-bpy)$_2$]·nH$_2$O adduct and 1.05 equivalents of the organic linker bpy. The procedure and experimental conditions were the same than those already explained for the previous case.

[M(tfa)₂(dpy)]ₙ 2D CPs

In each experiment, the autoclave was charged with *ca.* 200 mg of M(tfa)$_2$ and a weighted amount of each studied dipyridin (dpy), calculated slightly in excess of the quantity needed to achieve the molar ratio 1:2 for M(II):dpy. The reagents were added into a 10 mL Pyrex vial together with a small magnetic stir bar. The vial was capped with filter paper. The reactor was sealed at ambient temperature and filled with liquid CO_2 at 6 MPa, while stirring at 500 rpm. In a typical experiment, the system was then heated at 333 K and the pressure was increased up to 20 MPa. These working conditions were maintained for a period of 3 h. Finally, the reactor was depressurized to atmospheric pressure and cooled to room temperature. Four different methods were used to obtain the desired end-product, which are described following:

Method A. The reaction time was increased from 3 h in the standard protocol to 60 h.

Method B. 2 mL of EtOH were added as a co-solvent to the Pyrex vial together with the CP reagents.

Method C. A metal complex intermediate containing the *t*-bpy unit, with formulae [M(tfa)$_2$(*t*-bpy)$_x$], was prepared by reacting M(tfa)$_2$ with an excess of liquid *t*-bpy. After partial evaporation of the *t*-bpy excess, the composition of the recovered intermediate complexes was determined by E.A. as x=2.3 and 2.5 for Zn(II) and Cu(II), respectively. In the CP synthesis experiments, the intermediate was added to the Pyrex vial instead of the corresponding M(tfa)$_2$ hydrate.

Method D. The *t*-bpy was added to the Pyrex vial as free ancillary ligand, thus avoiding the necessity of synthetizing the intermediate. Different ratios of M(II):*t*-bpy were experimentally tested.

Surface deposition of [Cu(tfa)$_2$(bpy)$_2$]$_n$

Crystals of [Cu(tfa)$_2$(bpy)$_2$]$_n$ complex were immobilized onto different silicon wafer surfaces using scCO$_2$. The substrate was first activated by cleaning with freshly prepared "piranha" solution (H$_2$SO$_4$:H$_2$O$_2$ 3:1 v/v) for 30 min. The activated surface was then functionalized with N-(3-triethoxysilylethyl)pyridine following a scCO$_2$ published procedure.[28] Both modified surfaces were separately introduced in the reactor with weighted amounts of Cu(tfa)$_2$, bpy and *t*-bpy in a 1:2:0.14 molar ratio. The surface was treated in scCO$_2$ at 20 MPa and 333 K for 3 h. The collected surface was thoroughly blown with a stream of nitrogen to eliminate the excess of powder not grafted onto the wafer.

4.2.3. Characterization

Structural elucidation

The obtained precipitates were first characterized by powder X-ray diffraction (PXRD) at room temperature using a Siemens D-5000 diffractometer with Cu Kα radiation in the 2θ range of 5–30°. For compounds with a reported structure, the Le Bail method was used to extract intensities (I$_{hkl}$) from powder diffraction data, making them suitable to refine the unit cell.[29] Single crystal structure of different M(deox)$_2$ derivatives was determined using Mo Kα radiation in a SMART-APEX diffractometer. An empirical absorption correction was applied (SADABS).[30] The structure was solved by direct methods (SHELXS-86) and refined by full-

matrix least-squares methods on F^2 for all reflections (SHELXL-2016).[31] Non-hydrogen atoms were refined using anisotropic displacement parameters. Hydrogen atoms bonded to carbon atoms were placed in calculated positions with isotropic displacement parameters fixed at 1.5 (CH_3) or 1.2 (CH_2 and CH) times the Ueq (equivalent isotropic displacement parameter) of the corresponding carbon atoms. In $[Cu(deox)_2(H_2O)]$, one hydrogen atom of water was located in a difference Fourier map and its position parameters were refined; the other water hydrogen was generated and a rotating group refinement was used. For both hydrogens, isotropic displacement parameters fixed at 1.5 times the Ueq of the corresponding oxygen atom were used. In $[Co(deox)_2(t\text{-}bpy)_2]\cdot H_2O$ the only water hydrogen of the asymmetric unit was located in a difference Fourier map and refined with an isotropic displacement parameter fixed at 1.2 times the Ueq of the corresponding oxygen atom. The analysis of principal mean square atomic displacements during the last cycles of refinement pointed to the presence of conformational disorder in some ethyl groups. In the case of $[Cu(deox)_2(H_2O)]$, this kind of disorder has been modelled in two ethyl groups refining two methyl groups for each one of them with the sum of the occupation factors fixed at 1 and using geometrical restraints. Similarly, in the case of $[Co(deox)_2(t\text{-}bpy)_2]\cdot H_2O$, one disordered ethyl group has been modelled using also two disorder components for both carbon atoms.

Crystal data and further refinement details for $[Cu(deox)_2(H_2O)]$ are presented in Table 4.1. Selected distances and angles are provided in Table 4.2. Hydrogen bond distances and angles are included in Table 4.3. Crystal data and details of structure refinement for $[Co(deox)_2(t\text{-}bpy)_2]\cdot H_2O$ are included in Table 4.4. Selected distances and angles are provided in Table 4.5. Hydrogen bond distances and angles are included in Table 4.6.

Crystal structures have been deposited at the CCDC and allocated the deposition numbers CCDC 1549267 and 1549268.

Table 4.1. Crystal data and structure refinement for [Cu(deox)$_2$(H$_2$O)].

Empirical formula	C$_{16}$ H$_{24}$ Cu O$_{11}$	Crystal size	0.58 x 0.17 x 0.08 mm^3
Formula weight	455.89	Theta range for data collection	1.67 to 28.81°.
Temperature	296(2) K	Index ranges	$-11 \leqq h \leqq 11$, $-31 \leqq k \leqq 32$, $-13 \leqq l \leqq 14$
Wavelength	0.71073 Å	Reflections collected	16544
Crystal system	Monoclinic	Independent reflections	5068 [R(int) = 0.0333]
Space group	P2$_1$/c	Completeness to theta = 25.00°	100.0 %
Unit cell dimensions	a = 8.6672(5) Å	Absorption correction	Semi-empirical from equivalents
	b = 24.3174(15) Å	Max. and min. transmission	1 and 0.859
	c = 10.4133(6) Å	Refinement method	Full-matrix least-squares on F^2
	β 108.696(1)°.	Data / restraints / parameters	5068 / 0 / 279
Volume	2078.9(2) Å^3	Goodness-of-fit on F^2	1.024
Z	4	Final R indices [I >2sigma(I)]	R1 = 0.0492, wR2 = 0.1242
Density (calculated)	1.457 Mg/m^3	R indices (all data)	R1 = 0.0848, wR2 = 0.1414
Absorption coefficient	1.104 mm^{-1}	Largest diff. peak and hole	0.405 and -0.392 e.Å^{-3}
F(000)	948		

Table 4.2. Selected bond lengths [Å] and angles [°] for [Cu(deox)$_2$(H$_2$O)].

Selected bond lengths [Å] for [Cu(deox)$_2$(H$_2$O)]	
Cu(1)-O(19)	1.919(2)
Cu(1)-O(12)	1.930(2)
Cu(1)-O(14A)	1.9425(19)
Cu(1)-O(24A)	1.954(2)
Cu(1)-O(1)	2.298(2)

Selected angles [°] for [Cu(deox)$_2$(H$_2$O)]			
O(19)-Cu(1)-O(12)	88.12(8)	O(14A)-Cu(1)-O(24A)	85.16(8)
O(19)-Cu(1)-O(14A)	168.65(9)	O(19)-Cu(1)-O(1)	91.90(9)
O(12)-Cu(1)-O(14A)	92.87(8)	O(12)-Cu(1)-O(1)	97.40(9)
O(19)-Cu(1)-O(24A)	92.45(8)	O(14A)-Cu(1)-O(1)	99.17(9)
O(12)-Cu(1)-O(24A)	172.72(9)	O(24A)-Cu(1)-O(1)	89.83(9)

Table 4.3. Selected hydrogen bond parameters [Cu(deox)$_2$(H$_2$O)] (D=hydrogen donator and A= hydrogen acceptor).

D-H⋯A	D-H [Å]	H⋯A [Å]	D⋯A [Å]	D-H⋯A [°]	D⋯H⋯A [°]
O(1)-H(1A)⋯O(11B)^i	0.82	2.52	3.173(3)	137	
O(1)-H(1A)⋯O(12)^i	0.82	2.25	3.014(3)	155	65
O(1)-H(1B)⋯O(19)^i	0.76(4)	2.47(4)	2.938(3)	121(4)	
O(1)-H(1B)⋯O(21A)^i	0.76(4)	2.15(4)	2.901(3)	168(5)	69.9(11)

i: 2-x, 2-y, 2-z

Table 4.4. Crystal data and structure refinement for [Co(deox)$_2$(*t*-bpy)$_2$]·H$_2$O.

Empirical formula	C$_{34}$ H$_{50}$ Co N$_2$ O$_{11}$	Crystal size	0.26 x 0.22 x 0.11 mm^3
Formula weight	721.69	Theta range for data collection	1.46 to 28.82°.
Temperature	296(2) K	Index ranges	-15≦ h≦ 15, -15≦ k≦15, -37≦ l≦ 36
Wavelength	0.71073 Å	Reflections collected	29341
Crystal system	Tetragonal	Independent reflections	4726 [R(int) = 0.0597]
Space group	P -4 2$_1$ c	Completeness to theta = 25.00°	100.0 %
Unit cell dimensions	a = 11.6167(6) Å	Absorption correction	Semi-empirical from equivalents
	b = 11.6167(6) Å	Max. and min. transmission	1 and 0.856
	c = 27.9840(14) Å	Refinement method	Full-matrix least-squares on F^2
Volume	3776.4(3) Å^3	Data / restraints / parameters	4726 / 0 / 245
Z	4	Goodness-of-fit on F^2	1.033
Density (calculated)	1.269 Mg/m^3	Final R indices [I>2sigma(I)]	R1 = 0.0439, wR2 = 0.0892
Absorption coefficient	0.511 mm^{-1}	R indices (all data)	R1 = 0.0828, wR2 = 0.1014
F(000)	1532	Largest diff. peak and hole	0.190 and -0.246 e.Å^{-3}

Table 4.5. Selected bond lengths [Å] and angles [°] for [Co(deox)$_2$(t-bpy)$_2$]·H$_2$O

Selected bond lengths [Å] and angles [°] for [Co(deox)$_2$(t-bpy)$_2$]·H$_2$O	
Co(1)-O(1)	2.026(2)
Co(1)-O(1)#1	2.026(2)
Co(1)-O(4)	2.086(2)
Co(1)-O(4)#1	2.086(2)
Co(1)-N(1)	2.183(3)
Co(1)-N(1)#1	2.183(3)

Selected angles [°] for [Co(deox)$_2$(t-bpy)$_2$]·H$_2$O			
O(1)-Co(1)-O(1)#1	94.61(13)	O(4)-Co(1)-N(1)	88.47(10)
O(1)-Co(1)-O(4)	89.74(9)	O(4)#1-Co(1)-N(1)	91.87(10)
O(1)#1-Co(1)-O(4)	175.23(9)	O(1)-Co(1)-N(1)#1	89.58(10)
O(1)-Co(1)-O(4)#1	175.23(9)	O(1)#1-Co(1)-N(1)#1	90.11(10)
O(1)#1-Co(1)-O(4)#1	89.74(9)	O(4)-Co(1)-N(1)#1	91.87(10)
O(4)-Co(1)-O(4)#1	85.97(12)	O(4)#1-Co(1)-N(1)#1	88.47(10)
O(1)-Co(1)-N(1)	90.11(10)	N(1)-Co(1)-N(1)#1	179.53(15
O(1)#1-Co(1)-N(1)	89.58(10)		

Symmetry transformations used to generate equivalent atoms: #1 -x,-y+1,z

Table 4.6. Selected hydrogen bond parameters for [Co(deox)$_2$(t-bpy)$_2$]·H$_2$O] (D=hydrogen donator and A= hydrogen acceptor).

D-H···A	D-H [Å]	H···A [Å]	D···A [Å]	D-H···A [°]	D···H···A [°]
O(10)-H(10)···O(1)	0.84(6)	2.32(6)	3.011(5)	139(5)	
O(10)-H(10)···O(2)	0.84(6)	2.50(7)	3.214(4)	143(6)	67.6(18)

Structure elucidation of unknown phases involving M(tfa)$_2$ metal complex was attempted by synchrotron PXRD analysis carried out on a high resolution powder diffraction end station of the MSPD beamline (BL04) at the ALBA synchrotron (see Chapter 3).[32] Samples were first ground on an agate mortar and introduced on a glass capillary tube of 0.7 mm diameter. They were then measured in the transmission mode at room temperature and 100 K by using Si-microstrip MYTHEN-II detector (6 modules, 1280 channels/module, 50 μm/channel, sample-to-detector distance 550 mm) at an energy of 25 keV (wavelength=0.49587 Å determined with the NIST Si standard). This specific characterization method was useful for the structural resolution of the compound [Cu(tfa)$_2$(bpp)$_2$]$_n$, in which the indexing of the powder pattern was done in the transmission mode at room temperature and 100 K with DICVOL06,[33] obtaining an orthorhombic unit cell with preliminary parameters 19.384(17), 17.753(12), 8.840(8) and figures of merit M_{20}=10.4 and F_{20}=68.3 (0.0035,83). The crystal structure was

determined using the direct-space strategy implemented in DAjust[34] and TALP software[35] followed by a final restrained Rietveld refinement with RIBOLS (H-atoms have been placed to calculated positions at the end). Although the crystal structure was initially solved and refined in the *I ba*2 space group, the reduction of the symmetry to *I* 2/*a* lead to a small improvement of the overall fit (intensities and atomic distances). However, slight distortions on the bpp chain and Cu position, leading to probable disorder, suggest that the symmetry may be even lower. Unfortunately, it has not been yet possible to refine the structure in a lower symmetry space group with the current diffraction data due to the large number of parameters. Crystallographic data and refinement details are summarized in Table 4.7. Unfortunately, this structure is provisional and it is not submitted to the CCDC.

Table 4.7. Crystallographic details for [Cu(tfa)$_2$(bpp)$_2$]$_n$ crystal structure at 100 and 300 K.

	100 K		300 K
Molecular Formula		Cu1 C30 O4 N4 F6 H28	
Formula weight		686.11	
Crystal System		Monoclinic	
Space group		*I* 2/*a*	
a (Å)	19.2236(9)		19.4019(7)
b (Å)	8.7930(5)		8.8495(4)
c (Å)	17.7258(10)		17.8044(8)
Beta (º)	90.006(5)		90.006(4)
Volume (Å^3)	2996(1)		3057.0(4)
Z		4	
Calc. density (g/cm^3)	1.521		1.360
Wavelength (Å)		0.49587	
Profile function		Pseudo Voigt	
2θ range used (º)		2.500 – 27.000	
No. of reflections		1333	
Data points		4084	
Parameters		80	
Restraints		76	
R_{wp} (%)	8.4		8.1
R_{Bragg} (%)	2.8		2.9
Goodness of fit (χ)	6.3		8.6

Composition analysis

Elemental analysis (E.A.) was carried out using a Flash EA2000 Thermo Fisher Scientific analyser. Attenuated total reflection Fourier transform infrared (ATR-FTIR) spectra were recorded using a PerkinElmer Spectrum One spectrometer equipped with a Universal ATR sampling accessory. The spectra were collected with a 2 cm^{-1} spectral resolution in the 4000–650 cm^{-1} range. 1H-NMR spectra were recorded on an NMR-FT Bruker AC-250 MHz spectrometer in deuterated chloroform ($CDCl_3$); chemical shifts are referenced to the residual proton signal of the deuterated solvent and are given in ppm. ^{13}C-NMR spectra were recorded on an NMR-FT Bruker Avance II 300 in $CDCl_3$; chemical shifts are referenced to the signals of the deuterated solvent and are given in ppm.

Textural properties and morphological characteristics

The textural properties were determined by N_2 adsorption measurements at 77 K applying the BET method, using an ASAP 2000 from Micromeritics Inc. Samples were first degassed at 333 K for 24 h. The morphological features were examined first by optical microscopy and next by scanning electron microscopy (SEM) with a Zeiss Merlin FE-SEM apparatus and a QUANTA FEI 200 FEGESEM microscope.

Surface analysis

Surfaces were characterized by attenuated total reflection Fourier transform infrared spectroscopy (ATR-FTIR) in a Vertex 70 fully digital FTIR spectrometer with reflexion measurement at an incident angle of 68°. Optical fluorescence microscope images of the silanized surface grafted samples were performed using an OLYMPUS Bx51 microscope (DP20 camera) with a U-RFL-T mercury lamp accessory.

4.3. Results and discussion

4.3.1. Structural and morphological caracterization of CPs

4.3.1.1. Metal-deox complexes linked by 4-4'bipyridine

[M(deox)₂(H₂O)ₓ] metal precursor

In this work, the use of metal complexes of the diethyl oxaloacetate ligand was first proposed, since the presence of two ester groups in the deox ligand was expected to impart solubility to these compounds in scCO₂.[36] The synthesis of $[M(deox)_2(H_2O)_x]$ (M=Cu, x=1; M=Co, Mn, Ni or Zn, x=2) complexes was previously described in the literature.[27] However, these compounds had not been further revisited for applications in synthetic chemistry as intermediate reagents. Both E.A. data and ATR-FTIR recorded spectra of precursor $[M(deox)_2(H_2O)_x]$ complexes (Fig. 4.1) matched the previously reported results.[27] Most significant bands in the ATR-FTIR spectra are those characteristic of the oxaloacetate group, i.e., C=O ($\sim$1710 cm^{-1}), C=C ($\sim$1640 cm^{-1}), C-O ($\sim$1550 cm^{-1}) and C=C-H ($\sim$1240 cm^{-1}), and the O-H stretching band at 3300-3500 cm^{-1} corresponding to water molecules. In the initial report describing these complexes, the mode of coordination of the ligand to the cation metal center was not fully resolved.
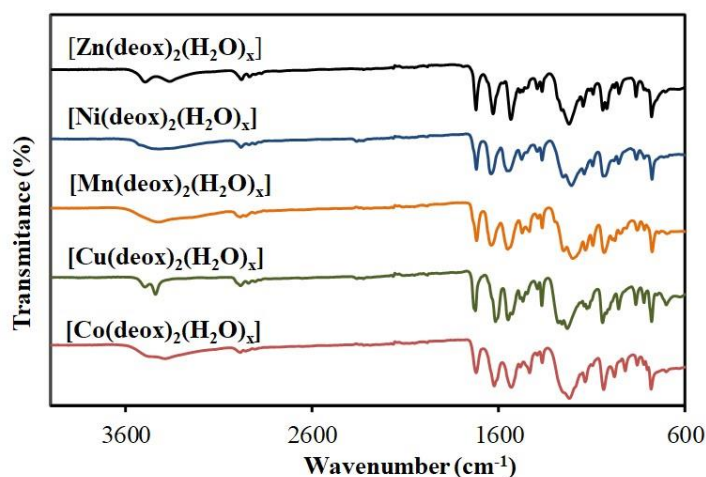
Figure 4.1. ATR-FTIR recorded spectra of $[M(deox)_2(H_2O)_x]$.

Difficulties arisen form the fact that Hdeox exists as two tautomeric enol forms in equilibrium. A priori, deprotonation and chelating of resultant anion to a metal cation would define the formation of a ring of either 5 or 6 members respectively (Fig. 4.2). In this work,

further characterization of these complexes was carried out to ascertain the ligand coordination mode.
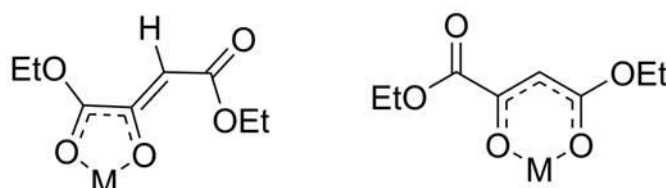
Figure 4.2. Hypothetical coordination modes of deox ligand.

In the recorded ^{1}H-NMR spectrum of diamagnetic $[Zn(deox)_2(H_2O)_2]$ complex (Fig. 4.3), the two ethyl groups have very similar shifts, causing signals overlapping (two triplets for the two -CH_3 groups at δ 1.30; 1.26 ppm, and two quartets for the -CH_2- groups at δ 4.21; 4.16 ppm). These similarities and the peak corresponding to the CH group situated between carbonyls, at 5.66 ppm, is compatible with the formation of the six members ring. The signal corresponding to water hydrogens was found shifted to a lower field (δ 2.45 ppm) respect to the position of free water (δ 1.56 ppm), indicating that water molecules were directly linked to the metal. Thus, zinc completes a distorted octahedral coordination. A similar coordination is anticipated for the three other paramagnetic $[M(deox)_2(H_2O)_2]$ compounds with the same stoichiometry, i.e., for Co, Mn and Ni). The ^{13}C-NMR spectrum of $[Zn(deox)_2(H_2O)_2]$ (Fig. 4.3(b)) shows eight signals, confirming the equivalence of the two deox ligands, and is also compatible with the enolate anion forming a 6 membered ring after metal coordination.
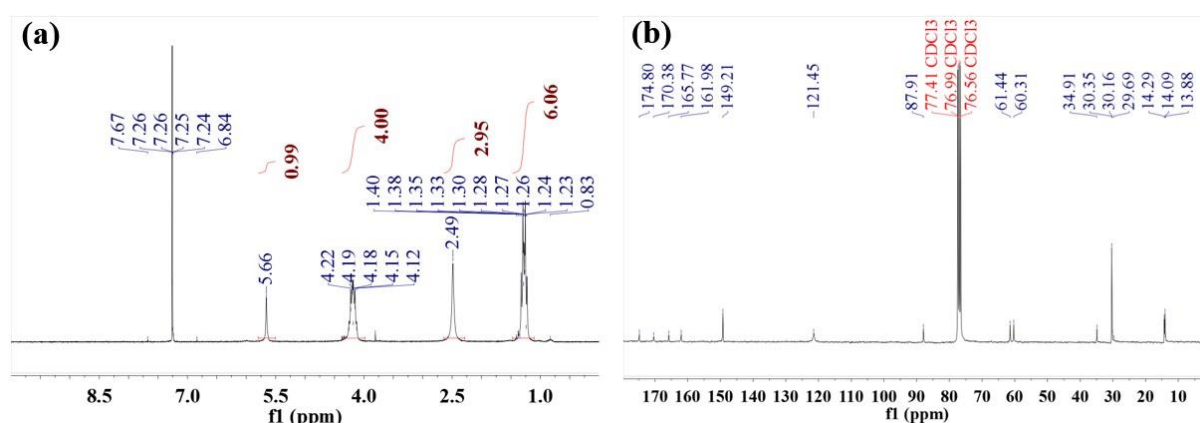
Figure 4.3. NMR spectra measured in $CDCl_3$: (a) ^{1}H- NMR of $[Zn(deox)_2(H_2O)_2]$, and (b) ^{13}C- NMR of $[Zn(deox)_2(H_2O)_2]$.

Powder XRD analysis showed that all metal complexes were crystalline as it can be observed in Fig. 4.4(a). Unfortunately, only the recrystallization of $[Cu(deox)_2(H_2O)]$ in ethanol gave a

single-crystal of enough quality for crystal structure elucidation by XRD. Phase purity of the bulk samples was confirmed by powder X-ray diffraction (Fig. 4.4(b)).
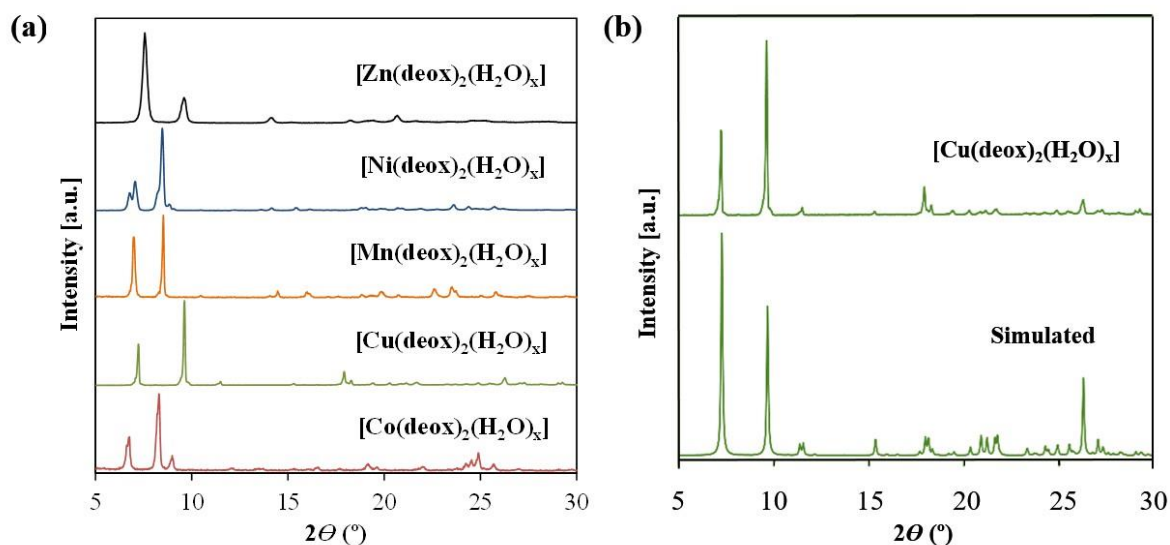

Figure 4.4. PXRD patterns of: (a) [M(deox)$_2$(H$_2$O)$_x$] and (b) [Cu(deox)$_2$(H$_2$O)] (up) and calculated from resolved crystal structure (down).

Fig. 4.5(a) shows the structure of the [Cu(deox)$_2$(H$_2$O)] molecular complex. Crystal data and details of structure refinement were included in Table 4.1-4.3. The structure shows that the ligand acts in a similar way to the β-diketonate, forming a ring of six members. Cu-O distances (from 1.92 to 1.95 Å) are similar to those reported for copper acetylacetonate.[37,30] The two ligands are non-equivalent. The β-ketoester and the ethoxy groups are oriented in *cis*. The Cu(II) presented a square-based pyramid coordination geometry, whose base is defined by four oxygen atoms attached to two ligands of the metal diethyloxalacetate, meanwhile the other oxygen belongs to a water molecule occupying the axial position (distance Cu-O= 2.299(2) Å). The copper atom is slightly shifted from the basal plane away to the water molecule (0.15 Å). Water molecules formed strong intermolecular hydrogen bonds (Fig. 4.5(b)) between adjacent molecules. These supramolecular interactions define centrosymmetric dimers. A similar arrangement has been recently reported for a copper complex containing a 2-hydroxy-4-aryl-4-oxo-2-butenoate ligand.[38]
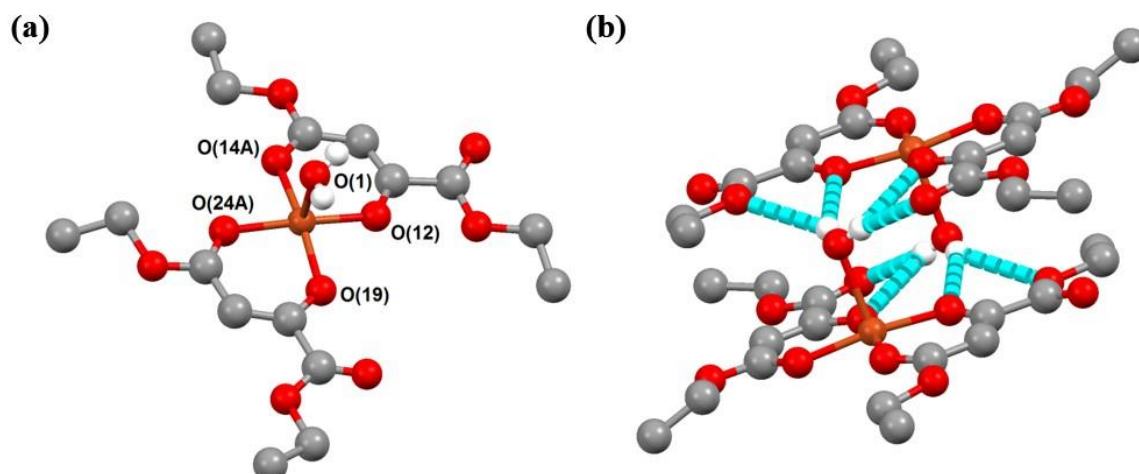
Figure 4.5. Molecular structure of [Cu(deox)$_2$(H$_2$O)]: (a) asymmetric unit, and (b) hydrogen bonding between an adjacent pair of molecules. Hydrogen atoms, except those involved in the intermolecular interaction, have been removed for clarity. Intramolecular hydrogen bonds are drawn as dashed blue lines. O red, C grey, Cu orange and H withe.

[M(deox)$_2$(t-bpy)$_2$]·nH$_2$O molecular adducts

Initial experiments showed that the different [M(deox)$_2$(H$_2$O)$_x$] studied complexes have from moderate to null solubility in scCO$_2$. Co(II) and Zn(II) complexes showed moderate solubility (mole fraction $<10^{-5}$), while the copper Cu(II) complex was only slightly soluble. These observations correlate with the solubility behavior of these complexes in diethyl ether. The complexes formed by Mn(II) and Ni(II) were both completely insoluble in both scCO$_2$ and diethyl ether. Among the factors influencing the solubility of organometallic complexes in scCO$_2$, the effect of the ligands has been described to be very important. For instance, the introduction of ligands possessing fluorinated groups or alkyl chains, have been shown to improve the solubility of such complexes.[39] On the contrary, the occurrence of intermolecular hydrogen-bonding between the complex solvates acts negatively in the solubility in scCO$_2$.[27] As a way to overcome the deficient solubility of most [M(deox)$_2$(H$_2$O)$_x$] complexes in scCO$_2$, the use of an additional ligand was proposed. A useful and somehow straightforward method to increase the solubility of [M(deox)$_2$(H$_2$O)$_x$] complexes in apolar solvents in general, and scCO$_2$ in particular, was to prepare a derivative containing a group or ligand prone to interact with apolar solvents.[37,40] The ligand t-bpy, with the bulky apolar *tert*-butyl group, was chosen for this purpose. The introduction of an apolar ligand such as t-bpy in the [M(deox)$_2$(H$_2$O)$_x$] complexes would displace water molecules bonded to metal cation, thus decreasing the strength of the intermolecular forces. Besides, the included *tert*-butyl group would interact favorably with CO$_2$. [M(deox)$_2$(t-bpy)$_2$]·nH$_2$O adducts were prepared by a mechanochemical

approach, taking advantage of the liquid nature of the free *t*-bpy. E.A. data revealed that water molecules were not completely removed from the initial precursors, except for the nickel complex. ATR-FTIR confirmed the presence of water in the Co, Cu, Mn and Zn complexes (OH stretching band at ~3500-3300 cm^{-1}, Fig. 4.6). The maximum usual coordination number for all of the metal cations studied was six. The four oxygen atoms from two deox and the two nitrogen atoms from pyridine ligands must saturate the coordination sphere of the cation. Hence, it is reasoned that water molecules are not directly bonded to the metal cations, but undergoing intramolecular hydrogen bonding with the ligands that contain several hydrogen-bonding acceptors.
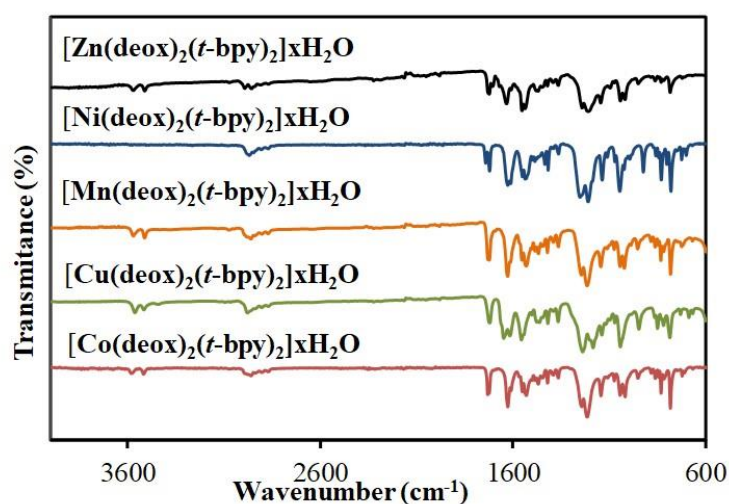
Figure 4.6. ATR-FTIR spectra of [M(deox)$_2$(*t*-bpy)$_2$]·xH$_2$O.

Characterization of [Zn(deox)$_2$(*t*-bpy)$_2$]·2H$_2$O by ^{1}H-NMR spectroscopy supports this hypothesis (Fig. 4.7(a)). Water signal was shifted to lower field (~ δ 2.10 ppm) respect to free water, but lesser than that observed for the [Zn(deox)$_2$(H$_2$O)$_2$] complex, in which presumably water molecules were directly linked to Zn(II). The most intense signal in the spectrum corresponded to the overlapping of the methyl signals assigned to the two *t*-bpy ligands and the methyl groups of the deox ligand. The methylene groups generated two very close quartets centered at δ 4.27 and δ 4.22 ppm. The broadened aromatic hydrogen signals could be attributed to the *t*-bpy free rotation.[41] The equivalence of the two deox ligands and the two *t*-bpy pyridines was confirmed by the ^{13}C-NMR spectrum (Fig. 4.7(b)).
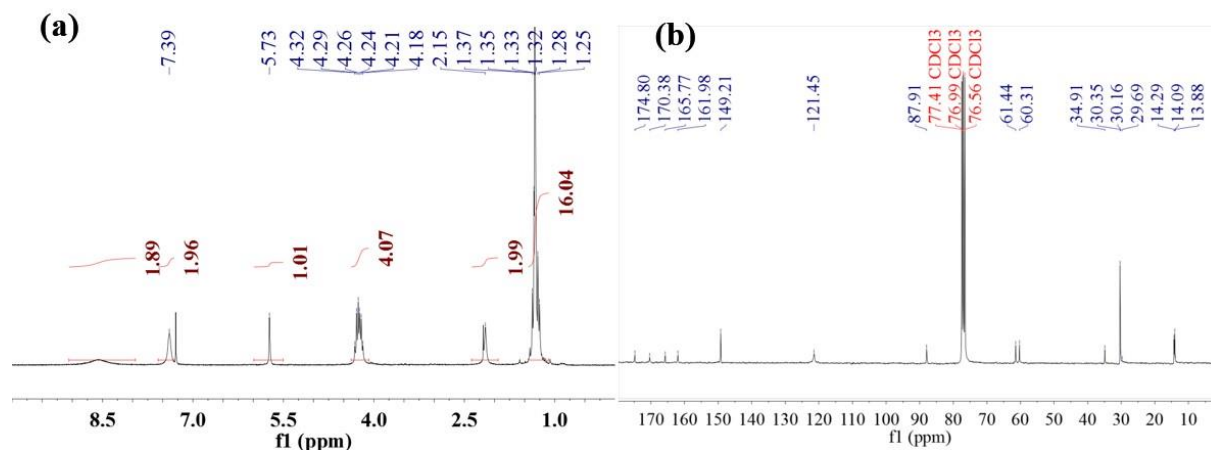
Figure 4.7. NMR spectra measured measured in $CDCl_3$: (a) ^{1}H-NMR of $[Zn(deox)_2(t\text{-bpy})_2]\cdot 2H_2O$, and (b) ^{13}C-NMR of $[Zn(deox)_2(t\text{-bpy})_2]\cdot 2H_2O$.

Powder XRD analysis showed that all metal complexes were crystalline (Fig. 4.8(a)). The great similarity of the pattern of samples $[M(deox)_2(t\text{-bpy})_2]\cdot xH_2O$ (M=Co, n=1; M=Mn, n=1.5 and M= Zn, n=2) strongly suggest that they have closely related structures. $[Co(deox)_2(t\text{-bpy})_2(H_2O)]$ recrystallization in DCM gave a single-crystal of enough quality for XRD crystal structure elucidation. Phase purity of the bulk samples was confirmed by powder X-ray diffraction (Fig. 4.8(b)).
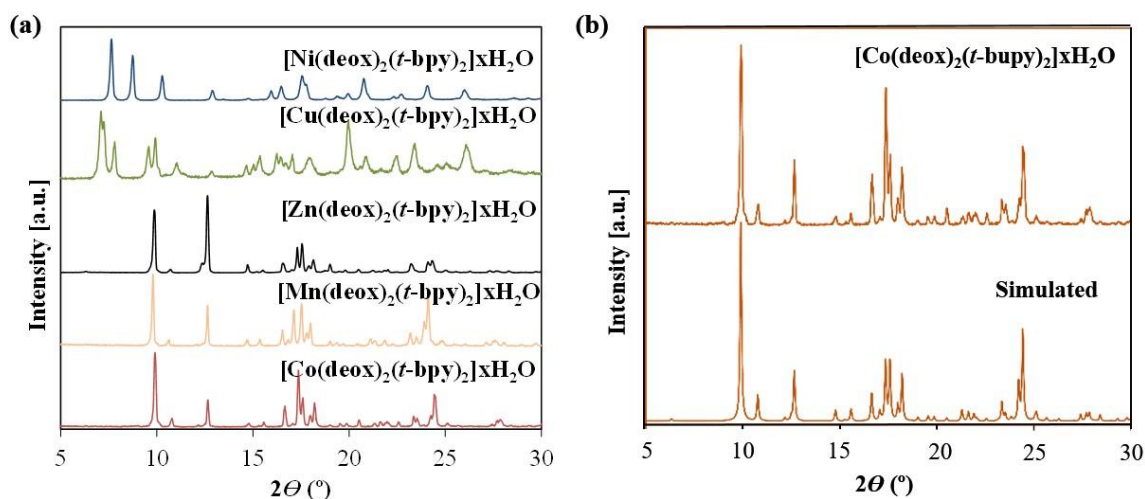
Figure 4.8 PXRD patterns of: (a) $[M(deox)_2(t\text{-bpy})_2]\cdot xH_2O$ and (b) $[Co(deox)_2(t\text{-bpy})_2]\cdot H_2O$ (up) and calculated from resolved crystal structure (down).

Fig. 4.9 shows the structure of the $[Co(deox)_2(t\text{-bpy})_2]\cdot H_2O$ molecular complex. Crystal data and details of structure refinement are included in table 4.4-4.6. observed previously for the $[Cu(deox)_2(H_2O)]$ complex, the structure shows that the deox ligand acts in a similar way to the β-diketonate, together forming a ring of six members. The asymmetric unit contains only

half-molecule. A C_2 axis, parallel to the [001] direction through Co(II) and O (water) atoms, generates the other half. Co(II) presented a distorted octahedral coordination geometry, linked by four oxygen atoms from the two deox ligands in *a* plane and two nitrogens from the *t*-bpy ligand in a perpendicular axis (distances Co(II)–N, 2.18 Å). Co(II)–O distances (from 2.02; 2.09 Å) were similar to those reported by cobalt bisacetylacetonate dehydrate.[42] The β-ketoester and the ethoxy groups were oriented in *cis.* This arrangement allowed a water molecule been clamped by hydrogen bonds, but there were no water molecules directly bonded to the metal cation, as previously reasoned. There were no other strong intermolecular bonds, which explain the observed high solubility of this complex in apolar solvents.
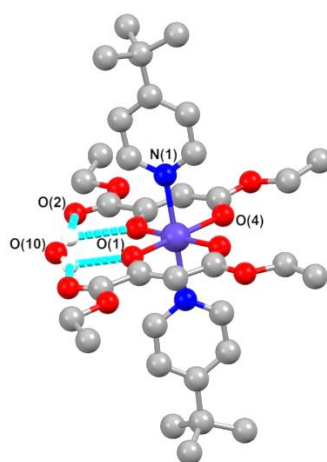

Figure 4.9. Crystal structure of [Co(deox)₂(*t*-bpy)₂]·H₂O. All H atoms except those of water molecules were omitted for clarity. Intramolecular hydrogen bonds are drawn as dashed blue lines. O red, C grey, N dark blue, Co purple and H withe.

The solubility of all [M(deox)₂(*t*-bpy)₂]·nH₂O molecular adducts was tested towards scCO₂ using the same high-pressure equipment described previously. It was found that all of the complexes obtained had a solubility greater than $3 \cdot 10^{-4}$ mol fraction. Hence, the introduced *t*-bpy ligand produced an enormous increase in the solubility of the different deox complexes in scCO₂, easing the way in which they can further react with other species. This finding opens a very important new window into the research of metal complexes in scCO₂.

[M(deox)₂(bpy)]ₙ 1D CPs.

Metal(II)-diethyloxaloacetate coordination polymers were first prepared using a conventional liquid solvent approach. The synthesis of coordination polymers involving bpy as the organic linker has been extensively studied.[43] The developed conventional synthesis approach is very straightforward, and consists of mixing a metal complex solution in alcohol with another

solution of the bpy linker in an equimolar ratio. The obtained product must be purified by solvent rinsing, although for Ni and Mn a recrystallization step was needed. The end products were obtained as colored powders being, green, white, pink dark yellow and turquoise blue for the metals Cu, Zn, Co, Mn and Ni complexes, respectively, with formulae $[M(deox)_2(bpy)]_n$, except for $[Zn(deox)_2(bpy)]_n(H_2O)_{2/3}$ that seems to adsorb a small amount of water according the data obtained by E.A.

The ATR-FTIR of all of the $[M(deox)_2(bpy)]_n$ compounds (Fig. 4.10(a)) showed the most characteristic bands of these complexes, i.e., C=O (~ 1710 cm^{-1}), C=C (~ 1640 cm^{-1}), C-N (~ 1500 cm^{-1}), C-O (~ 1550 cm^{-1}) and C=C-H (~ 1240 cm^{-1}). For all of the studied metals, the recorded spectra were alike. Likewise, the X-ray powder diffraction patterns obtained were similar, with only slight deviations in the relative intensity of the main peaks (Fig. 4.10(b)). These results indicate that the studied coordination polymers, with independence of the metal used, have very similar crystal structure.
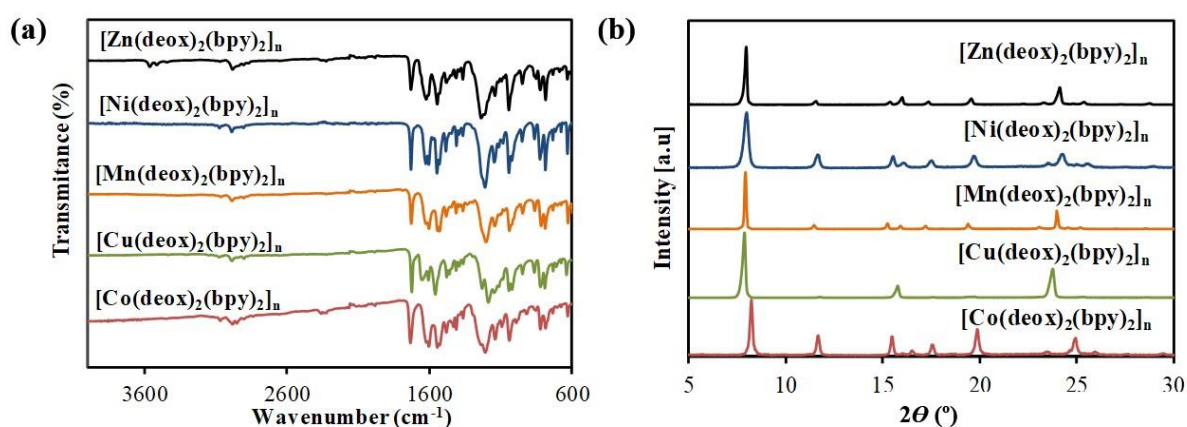

Figure 4.10. Characterization of $[M(deox)_2(bpy)]_n$: (a) ATR-FTIR spectra, and (b)PXRD of samples precipitated in alcohol solvent.

Following previous findings related to the synthesis of 1D coordination polymers in scCO₂,[5] this route was used to prepare $[M(deox)_2(bpy)]_n.$ The synthesis of such compounds in scCO₂ relies on the fact that reagents used (metal complex and organic linker) must have enough solubility in scCO₂ to react and to form an insoluble coordination polymer. $[M(deox)_2(H_2O)_x]$ complexes, showing a moderate solubility in scCO₂ (Co and Zn), were allowed to react with bpy in the high-pressure autoclave for a long time (up to 24 h). Targeted products were obtained, but with a large percentage of impurities, which made this approach unsuitable for the preparation of such complexes. To overcome this problem, a 2 % v/v of ethanol was

employed as a co-solvent. The addition of a small amount of ethanol has shown to increase substantially the solubility of hydrated coordination compounds by possibly breaking the hydrogen bonds between the molecules.[36,44] The reaction mixture was left under supercritical conditions for 2.5 h to ensure the full development of the final product at the highest yield. Alternatively, [M(deox)$_2$(bpy)]$_n$ was also prepared from different mixtures of [M(deox)$_2$(*t*-bpy)$_2$]·nH$_2$O and bpy in pure scCO$_2$. Since *t*-bpy complexes have high solubility in scCO$_2$, the addition of co-solvents was not necessary. The final products were recovered after 2 h of reaction, as fluffy powders with the same colors of their equivalents obtained by traditional liquid solvents. Powder X-ray spectrum and ATR-FTIR characterization confirmed that for each metal the same compound is produced independently on which of the synthetic methods were used (Figs. 4.11-4.13).
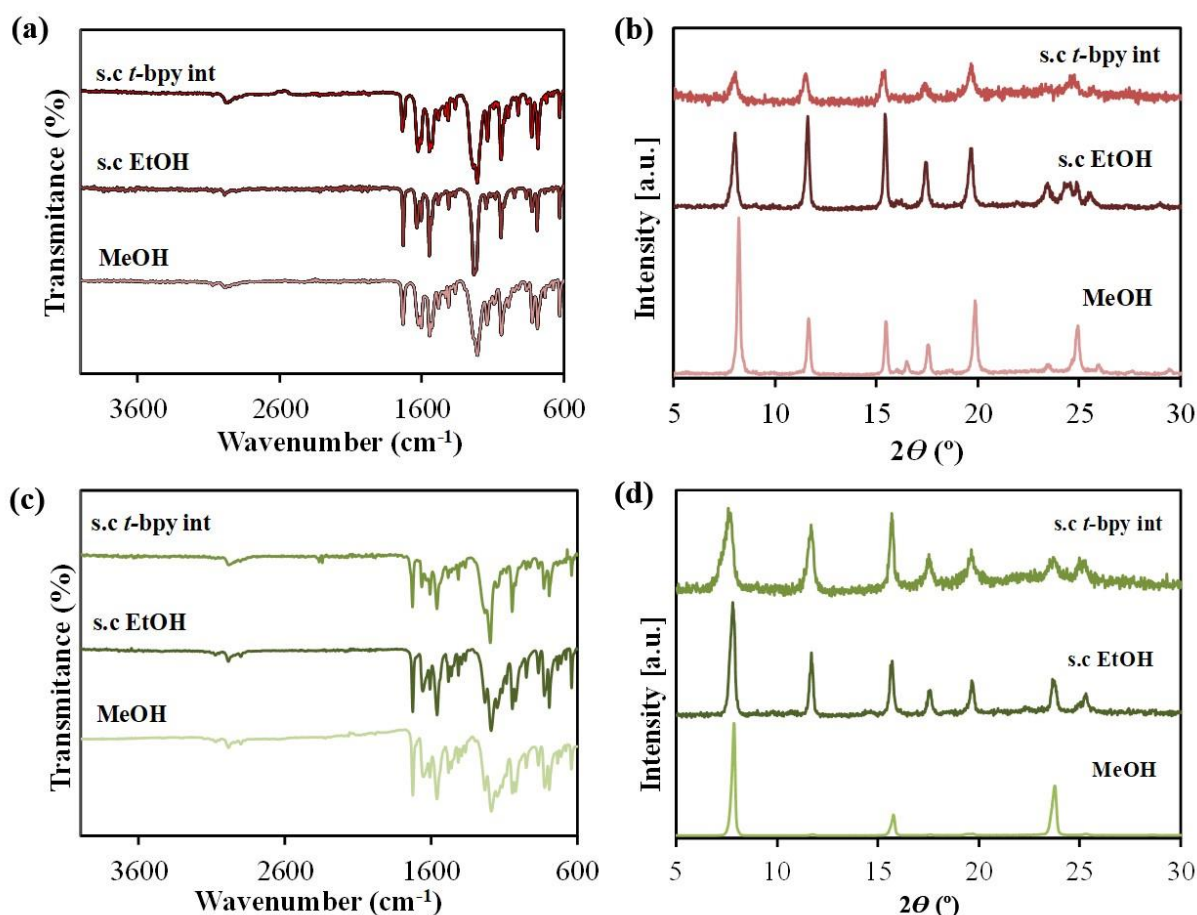

Figure 4.11. Characterization of 1D Co and Cu-deox CPs precipitated in different solvents: **(a)** ATR-FTIR spectra and (b) and PXRD patterns of [Co(deox)$_2$(bpy)]$_n$ samples precipitated in methanol (bottom), scCO$_2$ with 2% ethanol (middle) and neat scCO$_2$ from [Co(deox)$_2$(*t*-bpy)$_2$]·H$_2$O; and (c) ATR-FTIR spectra and (d) PXRD patterns of [Cu(deox)$_2$(bpy)]$_n$ samples precipitated in methanol (bottom), scCO$_2$ with 2% ethanol (middle) and neat scCO$_2$ from [Cu(deox)$_2$(*t*-bpy)$_2$]·2H$_2$O.
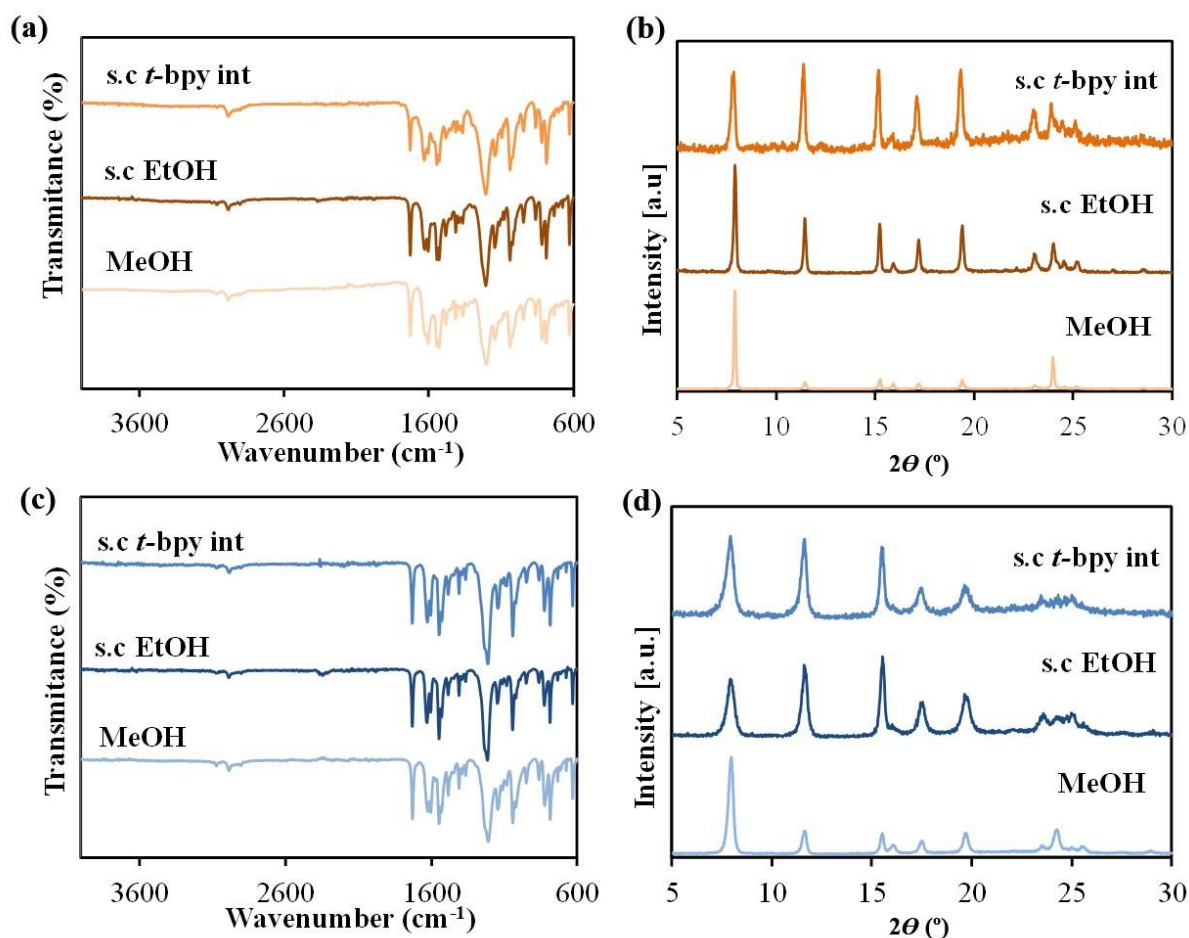
Figure 4.12. Characterization of 1D Mn and Ni-deox CPs precipitated in different solvents: (a)ATR-FTIR spectra and (b) PXRD patterns of $[Mn(deox)_2(bpy)]_n$ samples precipitated in ethanol (bottom), scCO₂ with 2% ethanol (middle) and neat scCO₂ from $[Mn(deox)_2(t\text{-}bpy)]\cdot1.5H_2O$; and **(c)** ATR-FTIR spectra and (d)PXRD patterns of $[Ni(deox)_2(bpy)]_n$ samples precipitated in methanol (bottom), scCO₂ with 2% ethanol (middle) and neat scCO₂ from $[Ni(deox)_2(t\text{-}bpy)_2]$.
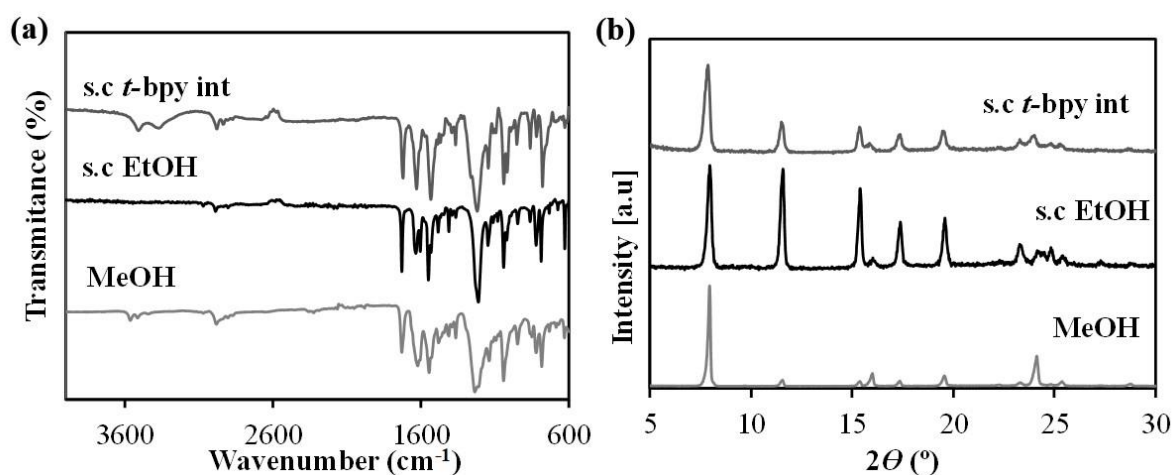

Figure 4.13. Characterization of 1D $[Zn(deox)_2(t\text{-}bpy)_2]\cdot2H_2O$ in different solvents: (a) ATR-FTIR spectra and (b) PXRD patterns of samples precipitated in methanol (bottom), scCO₂ with 2% ethanol (middle) and neat scCO₂ from $[Zn(deox)_2(t\text{-}bpy)_2]$.

Crystal Morphology of [M(deox)₂(bpy)]ₙ coordination polymers

The morphology of the [M(deox)₂(bpy)]ₙ coordination polymer precipitated samples was examined by SEM. The different synthetic methods gave place to products with different morphologies. All of the [M(deox)₂(bpy)]ₙ samples grew forming bidimensional micrometric sheets of nanometric thickness. However, the size, the aggregation or agglomeration of the platelets and the evolution of these sheets followed different pathways.

The morphology of [M(deox)₂(bpy)]ₙ samples obtained by direct precipitation in methanol can be described as precipitated 2D sheets. Zn(II), Cu(II), Co(II) and Mn(II) CPs produced 2D sheets of nanometric thickness and micrometric lengths (Fig. 4.14(a,d,e,f), respectively). The precipitated 2D sheets are stacked in a layer by layer parallel manner, which is clearly observed for Zn(II) and Mn(II) compounds (Fig. 4.14(b,f), respectively). In contrast, the [Ni(deox)₂(bpy)]ₙ compound (Fig. 14(c)) showed platelets of considerably smaller size than the other studied coordination polymers, with a less oriented aggregation mode.
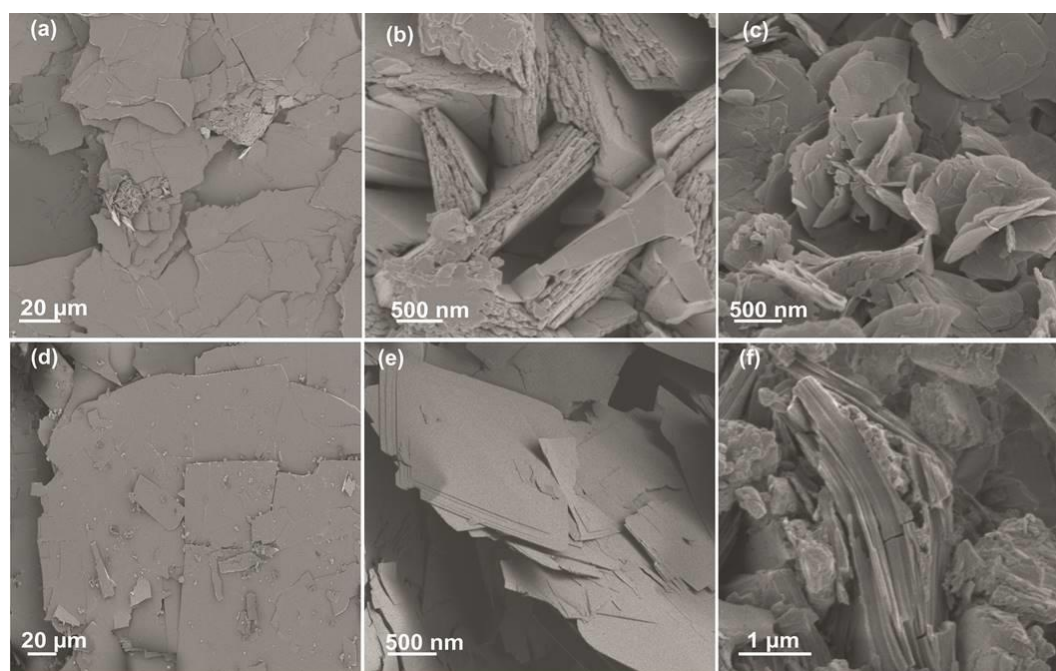

Figure 4.14. SEM micrographs of [M(deox)₂(bpy)]ₙ samples obtained by conventional methods: (a) and (b) [Zn(deox)₂(bpy)]ₙ, in which (b) is a lateral view of the particles showing the aggregated platelets, (c) [Ni(deox)₂(bpy)]ₙ, (d) [Cu(deox)₂(bpy)]ₙ, (e) [Co(deox)₂(bpy)]ₙ, and (f) [Mn(deox)₂(bpy)]ₙ

A complete different scenario was found in samples obtained by the supercritical method, either by using ethanol as a co-solvent or the *t*-bpy derivative. In both approaches, it can be observed that all products consist of neat flower-like spherical microstructures resembling a

desert-rose type structure, with diameters of different sizes depending on the metal used, but composed by multiple assembled nanoflakes with a thickness of about 20–30 nm (Fig. 4.15). The measured diameter for the flower-like particles varied from nano to micrometre scales. The largest sizes were found for those samples precipitated in $scCO_2$ using ethanol as a co-solvent, forming microparticles of several microns (Fig. 4.15(a,c,e,g,i)). In contrast, small dimensions of only few microns were observed for samples obtained through the *t*-bpy derivative (Fig. 4.15(b,d,f,h,j)). Using this approach, the smallest size was found for the $[Ni(deox)_2(bpy)]_n$ complex, with flowers of ~ 200 nm (Fig. 4.15(d)).
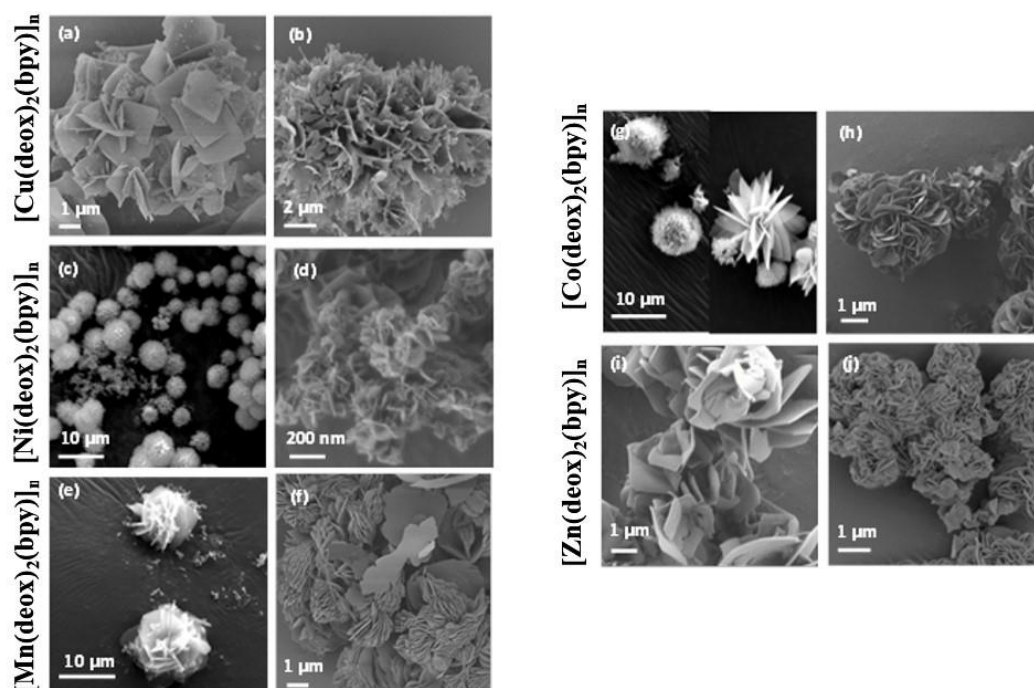

Figure 4.15. SEM micrograph of flower like for $[M(deox)_2(bpy)]_n$ phases either using $scCO_2$ and EtOH as co-solvents (left) or *t*-bpy as ligand aid (right).

The formation mechanism of these structures is difficult to ascertain. However, taking into account mechanisms described in the literature for similar end morphologies,[45-47] and a careful analysis of the SEM micrographs obtained from the as-synthesised samples, a mechanism can be proposed based on the combination of oriented self-assembly of primary particles, crystal growth and Ostwald ripening. The proposed detailed mechanism is depicted in Fig. 4.16. SEM micrographs were taken from experiments performed at different reaction times. The precipitation mechanism was constructed mainly by observation of the SEM micrographs taken from the $[Cu(deox)_2(bpy)]_n$ coordination polymer. However, pictures of other metals are also shown, since they are the most representative photos of specific growth steps.
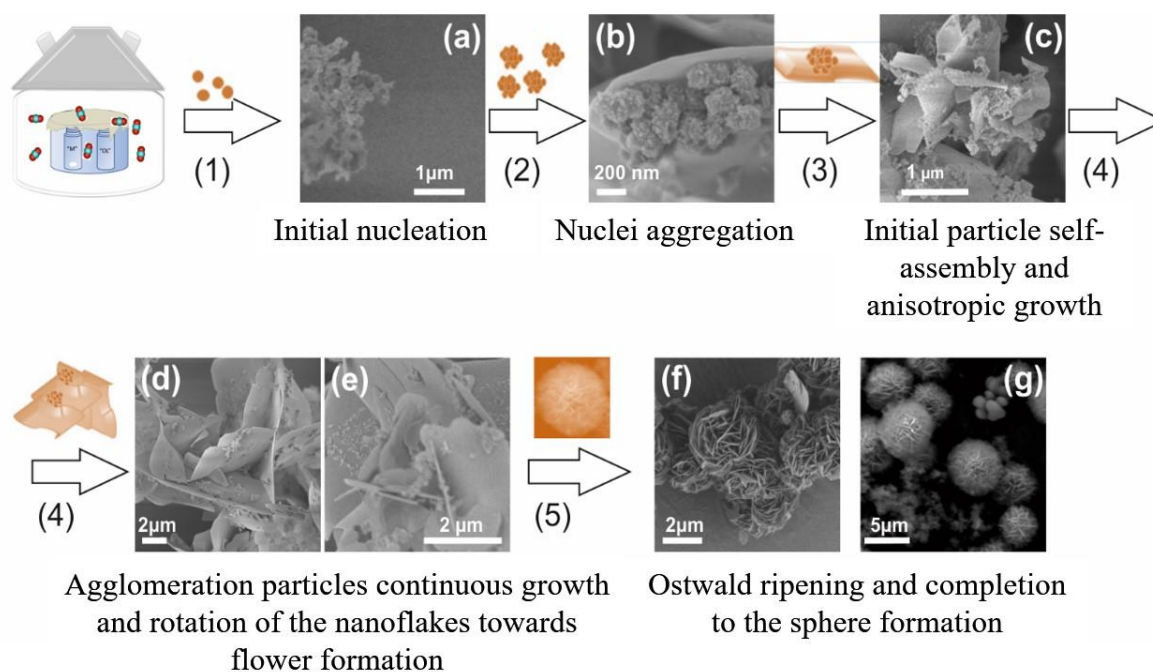
Figure 4.16. A proposed crystal growth mechanism for the formation of the flower like nanostructures. SEM pictures (a,b,c,d) corresponded to the phase $[Cu(deox)_2(bpy)]_n$, (e) was taken from sample $[Mn(deox)_2(bpy)]_n$, while f and g were obtained from the phase $[Ni(deox)_2(bpy)]_n$.

In the reactor, it was observed that nucleation starts right after the mixture of the reagents, when the bpy binds the metal complex (step 1). The thermodynamic instability of the newly formed nuclei is overcome by their aggregation, thus minimizing the interfacial area (Fig. 4.16(a); step 2). This process is reflected in the SEM pictures taken from the Cu(II) complex, in which large aggregates of 50-80 nm, constituted by clusters of only few nanometers, can be observed (Fig. 4.16(b)). The aggregates undergo oriented attachment giving place to nanoflakes (Fig. 4.16(c); step 3). Hereafter, it follows the continuous growth and the rotation of the nanoflakes to form the flower-like structure (step 4). This initial oriented petal spreads from the center of the flower towards the outside, and *simultaneously* attached to the adjacent flakes (Fig. 4.16(d,e)). This hierarchical architecture is clearly seen in the SEM pictures of $[Mn(deox)_2(bpy)]_n$ precipitated in scCO₂ and EtOH (Figs. 4.16(e) and 4.16(f)). Finally, Ostwald ripening results on the formation of spherical microflowers. For the studied systems, the most finished flowers were found for the $[Ni(deox)_2(bpy)]_n$ coordination polymer (Fig. 4.16(c,d)).

Textural properties of $[M(deox)_2(bpy)]_n$ materials and CO₂ adsorption studies

The textural properties of the $[M(deox)_2(bpy)]_n$ products synthesized in scCO₂ were studied by low temperature N₂ adsorption. BET analysis revealed surface area values in the order of

20 m^{2}g^{-1} for most of the studied samples, with the exception of the [Ni(deox)$_2$(bpy)]$_n$ product precipitated in scCO$_2$ using 2 % ethanol as a co-solvent, which displayed values in the order of 70 m^{2}g^{-1}. Additionally, CO$_2$ adsorption experiments were carried out to evaluate the potential use of these materials as CO$_2$ capture adsorbents. Measured values at 273 K were in the order of 0.3-0.5 mmol·g^{-1}. These records, even not being negligible, are relatively small in comparison to the quantities reported for other phases proposed for CO$_2$ capture in the literature, such as 3D metal organic frameworks like ZIF-8, with a CO$_2$ adsorption in the order of *ca.* 1.8 mmol g^{-1}.[48]

4.3.1.2. Metal-tfa complexes linked by a bipyridine derivative

Different reactions between dpy linkers and M(II) trifluoroacetate were surveyed under scCO$_2$ with and without the addition of additives. The structures of the used bipyridines reagents are schematized in Fig. 4.17. Results of tested combinations are presented in Table 4.8.
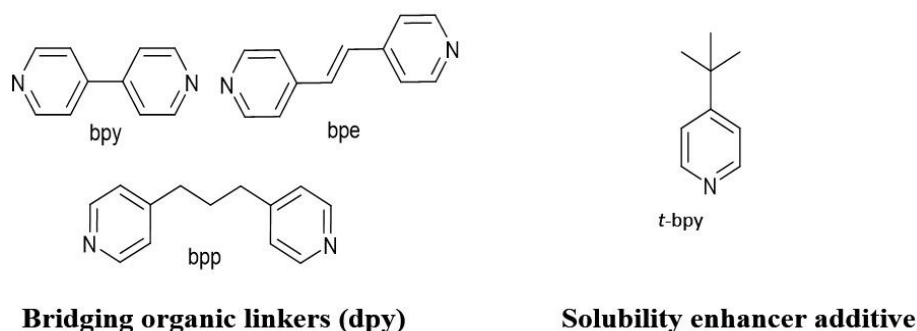

Bridging organic linkers (dpy)   **Solubility enhancer additive**

Figure 4.17. Structures of the used bpy derivatives (dpy) and additive.

Taking into account the known general solvating properties of scCO$_2$, M(II) trifluoroacetates were chosen as building units, instead of the most commonly used M(II) acetates, expecting that the presence of the fluorinated group infers certain solubility to the metal complexes in this fluid.[39] However, under working conditions, the two studied trifluoroacetates presented a negligible solubility in scCO$_2$. The three studied bidentate pyridines are all highly soluble in scCO$_2$,[9] but showed a different dissolution behavior. Although with long stirring times the added amount of each organic linker (100-200 mg) could be totally solubilized in scCO$_2$ under working experimental conditions, the kinetics of dissolution were not the same. The high melting point bpy and bpe linkers (*ca.* 383 and 423 K, respectively) were slowly solubilized in this fluid. On the contrary, the low melting point bpp (*ca.* 333 K) was melted after CO$_2$ addition and rapidly dissolved in the supercritical phase.

Table 4.8. Experimental conditions and reagents concentration used in the different experiments.

Metal	Linker	Additive	t [h]	$M^{(II)}$:*t*-bpy added molar ratio				
Zn(II)	bpy	---	60	1:0				
		EtOH	3	1:0				
		t-bpy(int)[a]	3	1:2.5				
		t-bpy[b]	3	1:2		1:0.5	1:0.14	
	bpe	---	60	1:0				
		EtOH	3	1:0				
		t-bpy(int)	3	1:2.5				
		t-bpy	3			1:0.5		1:0.05
	bpp	---	3	1:0				
		EtOH	3	1:0				
Cu(II)	bpy	*t*-bpy(int)	3	1:2.5				
		t-bpy	3		1:1		1:0.14	1:0.05
	bpe	*t*-bpy(int)	3	1:2.5				
		t-bpy	3			1:0.5	1:0.14	1:0.05
	bpp	*t*-bpy(int)	3	1:2.5				
		t-bpy	3	1:2	1:1	1:0.5	1:0.14	

[a] added as intermediate M(tfa)$_2$(*t*-bpy)$_{2.5}$
[b] added as a liquid.

The crystal structures of two of the precipitated MOFs were previously described in the literature: [Zn(tfa)$_2$(bpp)$_2$]$_n$[49] and [Zn(tfa)$_2$(bpe)$_2$]$_n$.[50] The other synthetized products corresponded to new phases. For them, crystal structure resolution was attempted from synchrotron PXRD. Preliminary results for [Cu(tfa)$_2$(bpp)$_2$]$_n$ were obtained directly from the powder precipitated in scCO$_2$ but the structure of the other three new phases, involving either Zn(tfa)$_2$ or Cu(tfa)$_2$ and bpy and Cu(tfa)$_2$ and bpe, could not be elucidated. These samples were characterized in regard of the composition by using E.A. Samples giving clear stoichiometric values were chosen to characterize the rest of compounds: [Zn(tfa)$_2$(bpy)$_2$]$_n$ prepared using Method D, i.e., with free added *t*-bpy (M:bpy molar ratio 1:2) (EA % calculated for ZnC$_{24}$H$_{16}$F$_6$N$_4$O$_4$: C 47.74, H 2.67, N 9.28; found C 47.85, H 2.57, N 9.12); and [Cu(tfa)$_2$(bpy)$_2$]$_n$ (EA % calculated for CuC$_{24}$H$_{16}$F$_6$N$_4$O$_4$: C 47.89, H 2.68, N 9.31: found C 47.74, H 2.83, N 8.84) and [Cu(tfa)$_2$(bpe)$_3$]$_n$ (EA % calculated for CuC$_{40}$H$_{30}$F$_6$N$_6$O$_4$: C 57.45, H 3.62, N 10.05; found C 57.16, H 3.39, N 10.22) both prepared using Method C, i.e., from the intermediate Cu(tfa)$_2$(*t*-bpy)$_{2.5}$. The XRD patterns obtained from these specific samples, considered as the purest ones, are herein used to ascertain the precipitation of the targeted end products by comparison.

It is worth mentioning that a reaction based on mechanochemistry cannot be technically discarded a priori in processes carried out mixing two solids under stirring. To confirm the absence of the mechanochemical effect on the supercritical synthesis of the described 2D MOFs, each organic linker was stirred at 500 rpm with a metal-containing precursor in control tests performed at 333 K in the absence of scCO$_2$. For bpe and bpy linkers, it was confirmed that the soft agitation used in the high-pressure reactor *per se* did not lead to the transformation of the precursors. On the contrary, the low melting point bpp linker gave the targeted coordination polymer by mechanochemistry. However, under used supercritical conditions, the bpp was melted after CO$_2$ addition and immediately dissolved in the supercritical phase; therefore, any mechanochemical effect can also be discarded in this case.

Reactions performed under neat scCO$_2$ (Method A)

The first system chosen to analyze the different crystallization methods developed in this study was constituted by Zn(tfa)$_2$ hydrate combined with any of the three different linear dipyridines shown in Fig. 4.17. Following the standard protocol, the Zn(tfa)$_2$ was first allowed to react at 20 MPa and 333 K during 3 h with bpy, bpe or bpp in the absence of any additive. A pure crystalline precipitate was only obtained for the pair Zn(tfa)$_2$ and bpp, in which the simulated XRD pattern from the single crystal structure found in the literature[49] was in accordance with the one recorded for the synthetized [Zn(tfa)$_2$(bpp)$_2$]$_n$ (Fig. 4.18(a)(A,B)). The Le Bail refinement of the XRD data (Fig. 4.18(b)) also gave a clear match between reported and found values, indicating the formation of a solid with the reported crystal structure. This compound is described with a structure consisting in a square-grid network of [Zn(bpp)$_2$]$_n^{2n+}$ with a (4,4) topology. A double layer is formed due to the interpenetration of two 2D networks. For bpe and bpy linkers, mixtures of solids containing the end product, some unidentified phases and reagents were recovered. As previously mentioned, the low melting point bpp linker was totally dissolved in the supercritical fluid in the first stage of the reaction, thus increasing the driving force for crystallization. Moreover, the total dissolution of this linker could even change the polarity of the scCO$_2$, probably acting as a co-solvent. This behavior would help Zn(tfa)$_2$ dissolution and fastened the reaction between both building units giving the expected end product after only 3 h of reaction.
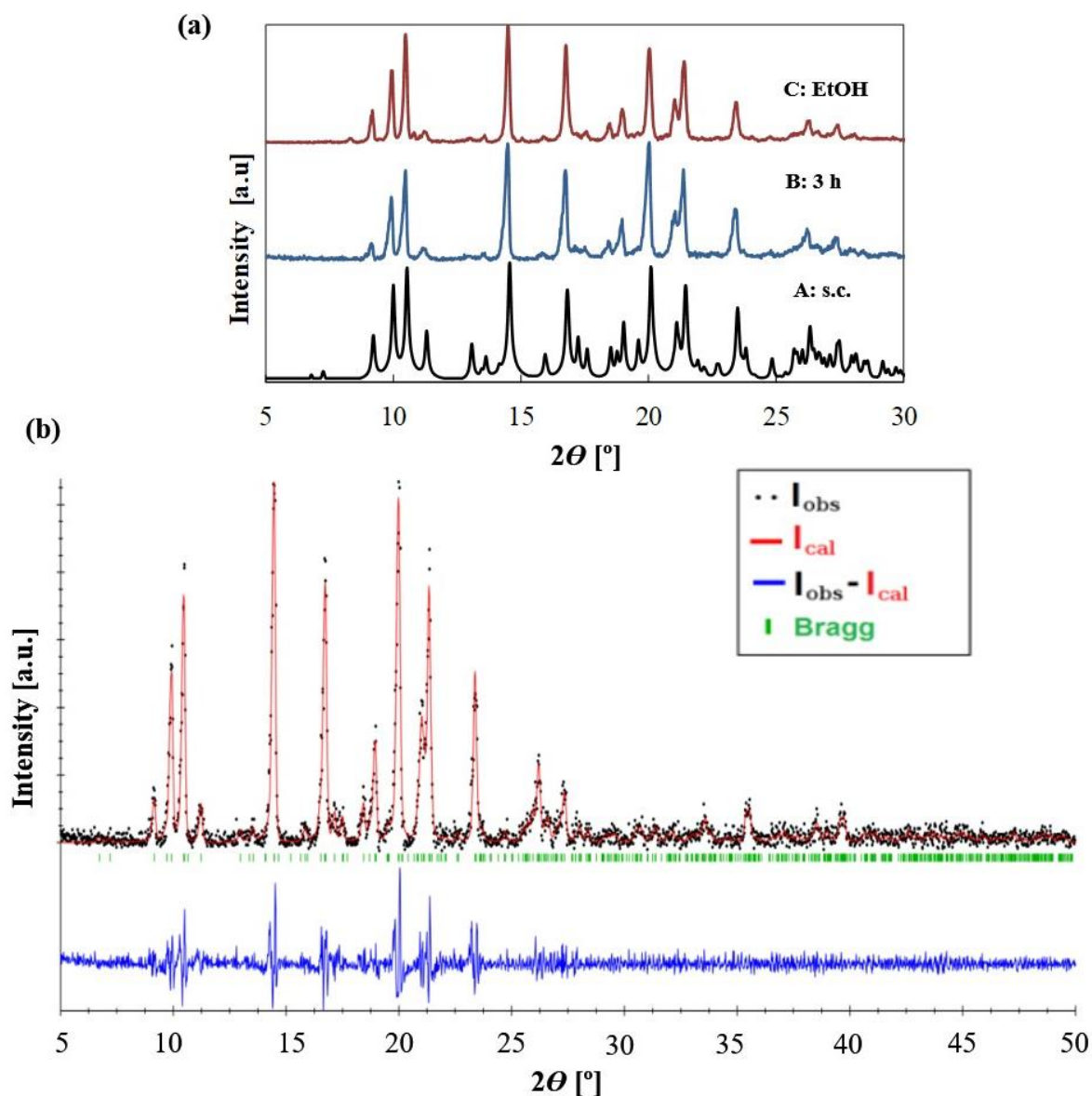
Figure 4.18. (a) PXRD patterns of [Zn(tfa)₂(bpp)₂]ₙ precipitated in different solvents: (A) simulated from single crystal reported data,[50] and synthetized in scCO₂ (B) pristine and (C) with EtHO; and (b) Le Bail whole pattern decomposition plot. The crystallographic data is described in ref.,[50] being fairly coincident with refined lattice parameters for the precipitated sample: Δa/a=0.004, Δb/b=0.003, Δc/c=0.001, and Δβ/(β-90)=0.008.

The formation of pure coordination polymers involving Zn(tfa)₂ and bpe or bpy was further attempted by increasing the running time to 60 h (Method A). In each case, a crystalline solid was obtained. The powder XRD pattern recorded for the precipitate involving bpe was coincident with the one reported for [Zn(tfa)₂(bpe)₂]ₙ after simulation from the single crystal structure[50] (Fig. 4.19(a)(A,B)), although the precipitated solid contained small amounts of unreacted precursors (e.g., peaks at 2θ 6.6 and 7.4° in pattern B). For [Zn(tfa)₂(bpy)₂]ₙ, XRD

data indicates the precipitation of a crystalline solid, but unfortunately without a resolved structure (Fig. 4.19(b)(A)). In neat scCO$_2$, SEM analysis indicated that polyhydric crystals were obtained for compounds involving Zn(II) and the three studied linkers. [Zn(tfa)$_2$(bpp)$_2$]$_n$ (Fig. 4.20(a)) and [Zn(tfa)$_2$(bpy)$_2$]$_n$ (Fig. 4.20(g)) precipitated as 1-10 μm micrometric particles, while [Zn(tfa)$_2$(bpe)$_2$]$_n$ (Fig. 4.20(c)) crystals displayed sizes significantly smaller, of only few hundred nanometers.
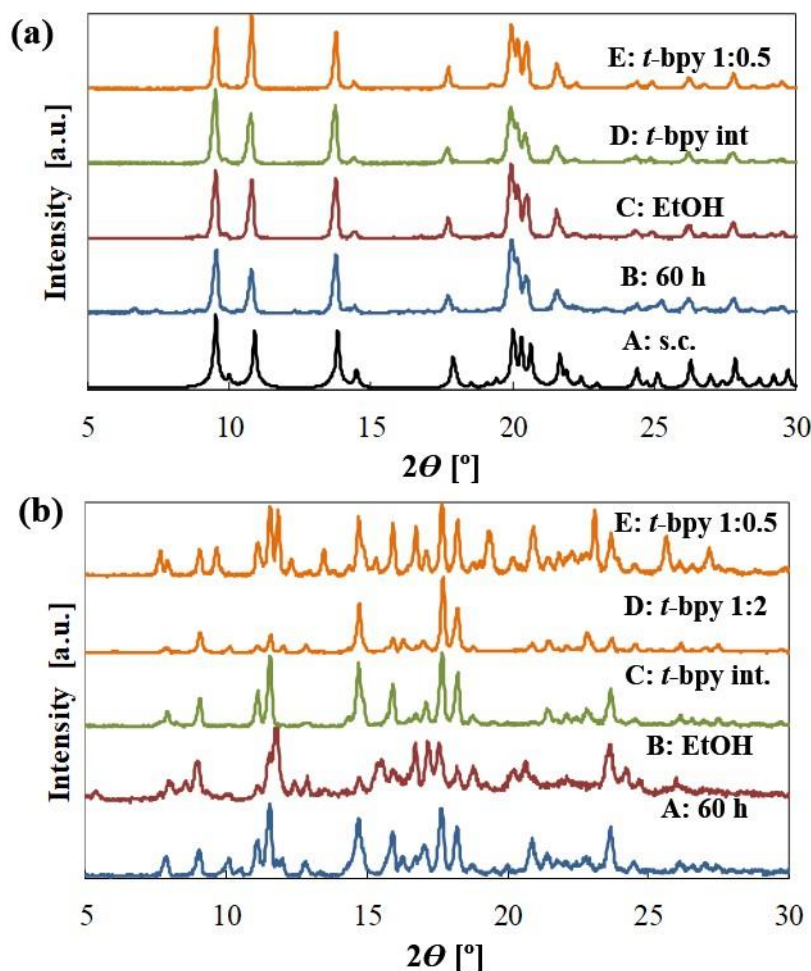

Figure 4.19. PXRD patterns obtained for the precipitated [Zn(tfa)$_2$(dpy)$_2$]$_n$ CPs: (a) [Zn(tfa)$_2$(bpe)$_2$]$_n$ with (A) simulated from single crystal reported data,[51] and synthetized in scCO$_2$ (B) pristine in 60 h and (C) with EtHO, D using the Zn(tfa)$_2$(t-bpy)$_{2\,3}$ intermediate, E adding free t-bpy in a Zn(II): t-bpy 1:0.5 molar ratio; and (b) [Zn(tfa)$_2$(bpy)$_2$]$_n$, synthetized in scCO$_2$ (A) pristine in 60 h, (B) with EtOH, (C) using the Zn(tfa)$_2$(t-bpy)$_{2\,3}$ intermediate, and adding free t-bpy in M(II): t-bpy molar ratios of (D) 1:2, and (E) 1:0.5.
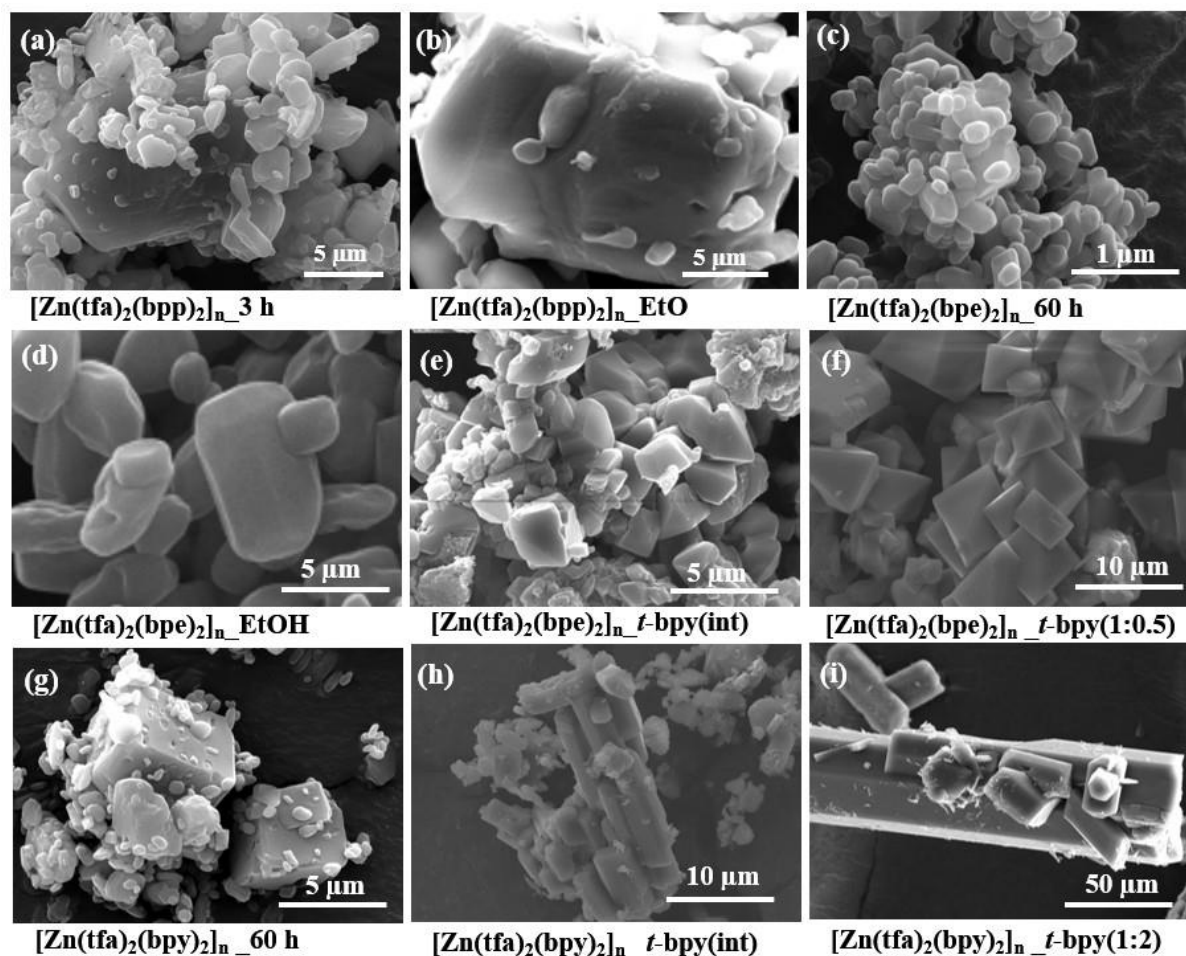
Figure 4.20. SEM micrographs of the $[Zn(tfa)_2(dpy)_2]_n$ precipitated samples described in Table 4.7: (a,c,g) in neat scCO₂, (b,d) with EtOH, (e,h) with *t*-bpy solid intermediate, and (f,i) with added free *t*-bpy.

Reactions performed by adding a co-solvent (method B)

To overcome the solubility problems in scCO₂ associated with the metal complexes, 2 v% of ethanol was added as a co-solvent to the reactor. The addition of EtOH not only rises de polarity of the solvent mixture, but also increases substantially the solubility of hydrated coordination compounds, like $M(tfa)_2 \cdot xH_2O$ reagents used in this work, by breaking the hydrogen bonds stablished between metal complex molecules.[44] Following the standard protocol of 20 MPa, 333 K and 3 h running time, the formation of the targeted $[Zn(tfa)_2(bpp)_2]_n$, $[Zn(tfa)_2(bpe)_2]_n$ and $[Zn(tfa)_2(bpy)_2]_n$ coordination polymers was achieved by following Method B (Fig. 4.18(a)). However, $[Zn(tfa)_2(bpy)_2]_n$ was still precipitated as a contaminated phase (Fig. 4.19(b)). For $[Zn(tfa)_2(bpe)_2]_n$, with a known structure, the Le Bail refinement, performed using the crystallographic data presented in ref.[50], giving an excellent match between reported and obtained XRD data (Fig. 4.21). This compound is described with

a structure consisting in square-grid networks of $[Zn(bpe)_2]_n^{2n+}$ with a (4,4) topology. The sheets are further interpenetrated in a 2D→2D inclined fashion. Trifluoroacetate anions placed in *trans* positions to the Zn(II) center restrict further interpenetration. In general, larger crystals were precipitated in systems involving EtOH as a co-solvent in comparison to those obtained in pure scCO₂ (compare images in Fig. 4.20(a,b) for $[Zn(tfa)_2(bpp)_2]_n$ and Fig. 4.20(c,d) for $[Zn(tfa)_2(bpe)_2]_n$). The increase in size can be linked to the higher solubility of the reagents in media with ethanol co-solvent with respect to neat scCO₂, thus favoring crystal growth *vs.* nucleation.
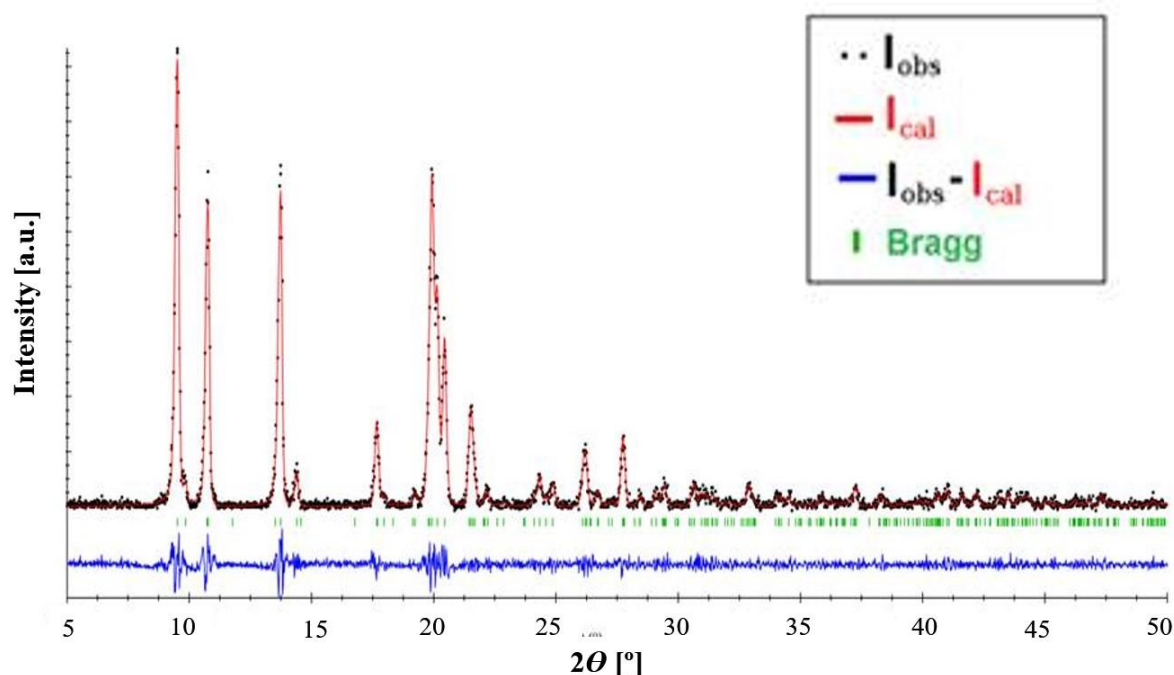

Figure 4.21. Le Bail whole pattern decomposition plot for $[Zn(tfa)_2(bpe)_2]_n$ sample. The crystallographic data is described in ref.[51] The refined lattice parameters for the precipitated sample were fairly coincident with reported data: Δa/a=0.007, Δb/b=−0.010, Δc/c=0.005.

Reactions performed by adding an ancillary ligand (methods C and D)

In a previous work, it was shown that a very useful, and somehow straightforward, method to increase the solubility of metal complexes in scCO₂ was to prepare an intermediate enclosing a ligand prone to interact with apolar solvents, like bulky apolar pyridines.[36] From them, the *t*-bpy, having the bulky apolar *tert*-butyl group (Fig. 4.17), interacts favorably with CO₂ molecules. This ligand can be added to the reaction media either as a part of a solid precursor or as a pristine liquid. In the first approach, a precursor of the type $M(tfa)_2(t\text{-bpy})_x$ is first synthetized. The addition of this ligand to the metal hydrate displaces the water molecules

bonded to the metal cation by decreasing the strength of intermolecular hydrogen bonding among metal complexes and enabling its molecular dissolution. This method was the one previously tested for CPs involving $M(deox)_2$ and bpy.[51] Here, an intermediate of the type $Zn(tfa)_2(t\text{-}bpy)_{2.3}$ was synthetized and further reacted in $scCO_2$ with either bpe or bpy (Method C). XRD characterization showed that using this method, pure phases of the difficult to crystallize $[Zn(tfa)_2(bpe)_2]_n$ and $[Zn(tfa)_2(bpy)_2]_n$ compounds could be straightforward crystallized in neat $scCO_2$ in runs of only 3 h (Fig. 4.19(a,c)). The effectiveness of Method C was also examined for similar reactions involving Cu(II) instead of Zn(II), for which the intermediate $Cu(tfa)_2(t\text{-}bpy)_{2.5}$ was synthetized. For the bpp linker reacted with $Cu(tfa)_2(t\text{-}bpy)_{2.5}$ during 3 h, E.A. indicated that a coordination polymer of stoichiometry $[Cu(tfa)_2(bpp)_2]_n$ was precipitated. This stoichiometry is similar to the one previously deduced for the complex involving Zn(II) and bpp. The found crystal structure can be described as a stacking of 2D nets (on the *bc* plane) along the *a* direction (Fig. 4.22). This crystal packing is practically equivalent to the Zn(II) analog; and both can be described by the same space group *C* 2/*c*, although for the Cu(II) compound the setting *I* 2/*a* has been used for convenience. The unit cells, however, are substantially different, with values of $a=21.2605(14)$, $b=17.6423(10)$, $c=18.6323(10)$ Å, $\beta=115.85°$ for Zn(II) and $a=26.3317$ $b=8.8495$ $c=19.4019$, Å, $\beta=137.46°$ for Cu(II).
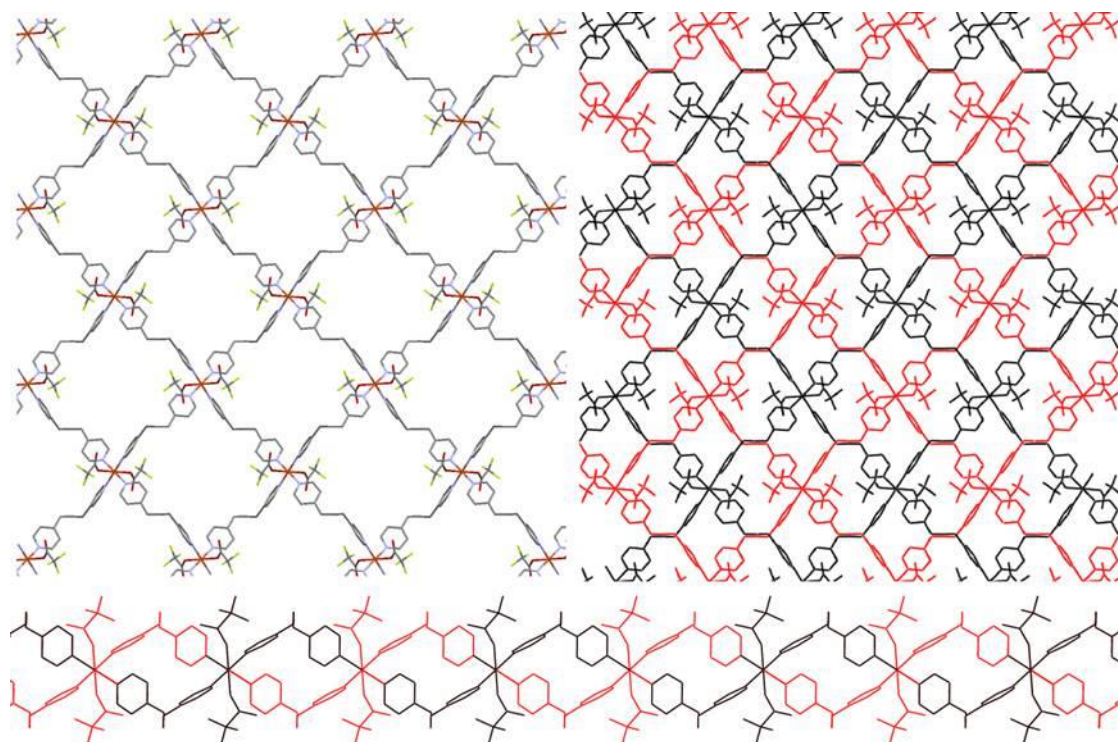
Figure 4.22. Crystal structure of $[Cu(tfa)_2(bpp)_2]_n$: (top, left) representation of the 2D→2D coplanar interpenetration network, each individual network has been colored in red and black; (top, right) single 2D network, view along *a* axis; and (bottom) transversal view of the interpenetrated networks along *b* axis.

The simulated powder pattern from the refined data and the recorded powder XRD profile were coincident (Fig. 4.23(a)(A,B)). EA data indicated that the combination of $Cu(tfa)_2$ and bpe or bpy produced $[Cu(tfa)_2(bpe)_3]_n$ and $[Cu(tfa)_2(bpy)_2]_n$ CPs, respectively (Fig. 4.23(b,c(A)). The $[Cu(tfa)_2(bpe)_3]_n$ was the only 2D MOF of the studied series with a different stoichiometry. In its crystalline structure (not resolved), likely not all bpe molecules are directly coordinated to Cu(II) centers,[52] or perhaps some of them act as a monodentate anion, as previously reported for other compounds.[53]
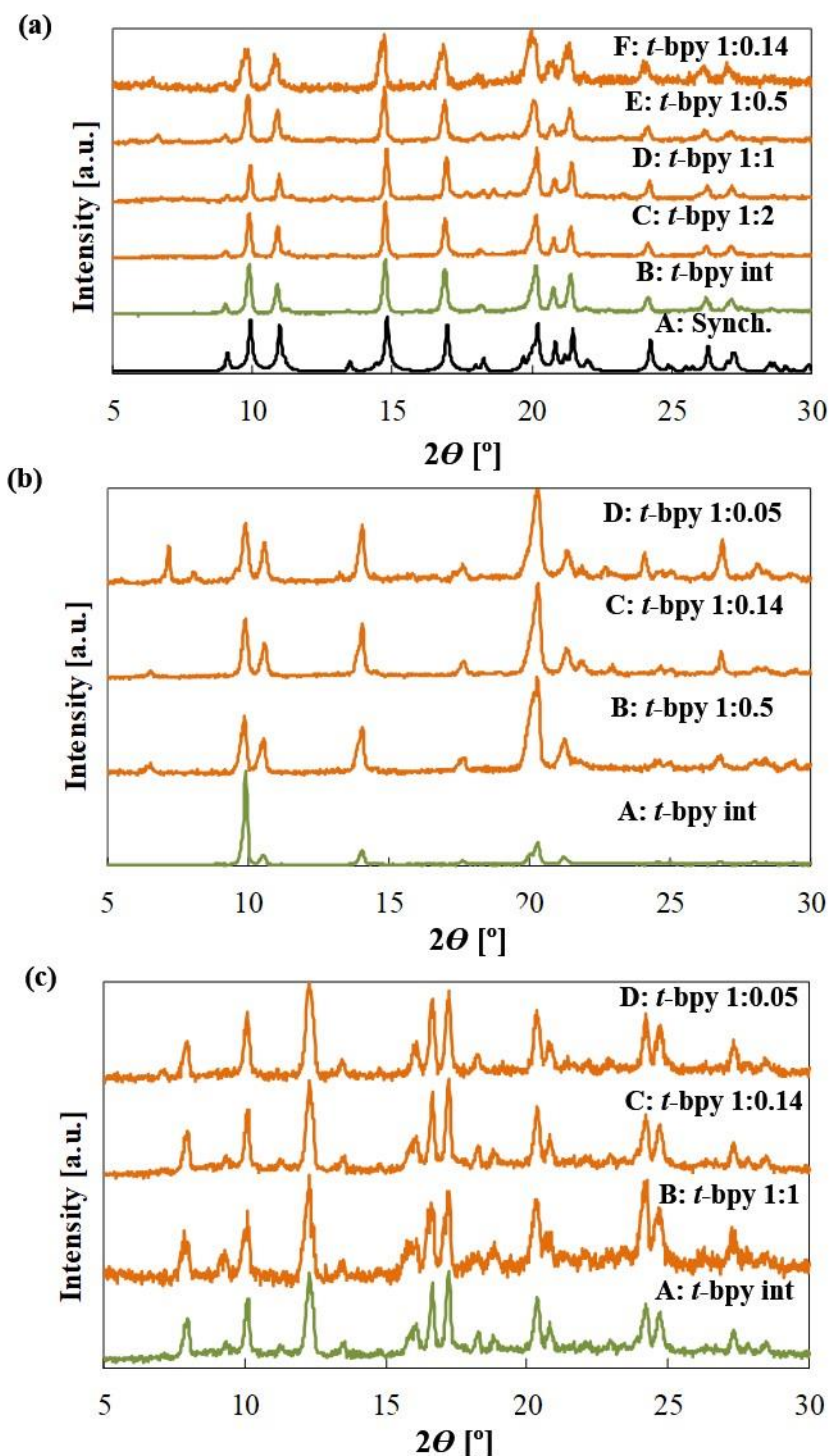
Figure 4.23. PXRD patterns obtained for precipitated: (a) [Cu(tfa)$_2$(bpp)$_2$]$_n$ (A) simulated from single crystal data, and synthetized in scCO$_2$ (B) using the Cu(tfa)$_2$(*t*-bpy)$_{2\,5}$ intermediate and adding free *t*-bpy in M(II):*t*-bpy molar ratios of (C) 1:2, (D) 1:1, (E) 1:0.5 and (F) 1:0.14; (b) [Cu(tfa)$_2$(bpe)$_3$]$_n$ synthetized in scCO$_2$ (A) using the Cu(tfa)$_2$(*t*-bpy)$_{2\,5}$ intermediate and adding free *t*-bpy in M(II):*t*-bpy molar ratios of (B) 1:0.5, (C) 1:0,14, and (D) 1:0.05; and (c) [Cu(tfa)$_2$(bpy)$_2$]$_n$ synthetized in scCO$_2$ (A) using the Cu(tfa)$_2$(*t*-bpy)$_{2\,5}$ intermediate, and adding free *t*-bpy in M(II): *t*-bpy molar ratios of (B) 1:1, (C) 1:0,14 and (D) 1:0.05.

A common observation in all those experiments is that the ancillary ligand *t*-bpy was never incorporated to the final coordination polymer. On the contrary, it was released to the supcritical phase once its substitution by the dpy linker was effective. Based on this finding, a new approach was designed in which the *t*-bpy was directly added to the reactor to allow this secondary ligand to thermodynamically compete *in situ* with the dpy for the metal positions (Method D). Moreover, it was observed experimentally that the amount of added secondary ligand can be reduced considerably, in some cases even 50 times, and still get the crystalline expected end product. In this protocol, the process of MOF crystallization is envisioned as starting with the formation of an intermediate of the type $M(tfa)_2(t\text{-bpy})_x$ by the favored reaction of $M(tfa)_2$ with solubilized *t*-bpy. Then, the soluble intermediate can react with solubilized dpy linker forming the thermodynamically stable coordination polymer, which precipitates. The released *t*-bpy ligand turns out to the solution and can react over with remaining $M(tfa)_2$ molecules, thus having a catalyst-like behavior. The mechanism is schematized in Fig. 4.24. Table 4.8 displays the M(II):*t*-bpy molar ratios studied in the different experiments, ranging from 1:2 to 1:0.05. For systems involving either Zn(II) or Cu(II) and free *t*-bpy in molar ratios from 1:2 to 1:0.5, the recorded XRD patterns, in general, revealed the precipitation of the expected phase after only 3 h of reaction time (Fig. 4.19(a(E),c(D)) for Zn(II) and Fig. 4.23(a(C,D,E), b(B),c(B)) for Cu(II)). An exception to this rule was the CP $[Zn(tfa)_2(bpy)_2]_n$, which could not be obtained pure at molar ratios lower that 1:2. For Cu(II) compounds, the linker concentration was further lowered to 1:0.14 and 1:0.05 M ratios. All over again, pure compounds were obtained for bpp, bpe and bpy linkers (Fig. 4.23(a(F),b(C),c(C,D)), with the exception of $[Cu(tfa)_2(bpy)_2]_n$ precipitated at the lowest molar ratio of 1:0.05 (Fig. 4.23(b)(D)), which showed some extra peaks at 2θ of 7.1 and 8.1° assigned to reagents or intermediate. As a general rule, $[Zn(tfa)_2(dpy)_2]$ could be crystallized as pure compounds at molar ratios of 1:0.5 or higher, while $[Cu(tfa)_2(dpy)_{2/3}]$ were obtained with a high degree of purity at molar ratios as low as 1:0.05. For both metals, an exception to this rule was the MOFs involving the bpy linker, which were more difficult to crystallize. This behavior is related to the lack of flexibility of this short dipyridine linker. The influence on the morphology of the addition of *t*-bpy and its concentration was studied in the precipitated pure compounds. For $[Zn(tfa)_2(bpe)_2]_n$, polyhydric micrometric crystals were obtained either by using the intermediate or by adding free *t*-bpy in the relatively high molar ratio of 1:0.5 (Fig. 4.20(e,f)). In both cases, crystals were better shaped than those obtained in both neat scCO₂ and with EtOH co-solvent (Fig. 4.20(c,d)). Crystals obtained using Method

D (Fig. 4.20(f)) were better crystallized than those obtained following Method C (Fig. 4.20(e)), likely due to slow crystal growth kinetics occurring in the former. For $[Zn(tfa)_2(bpy)_2]_n$, the presence of *t*-bpy in the medium clearly influences the morphology of the precipitated crystals by changing the general shape from isometric polyhedral particles obtained in neat $scCO_2$ (Fig. 4.20(g)) to elongated crystals (Fig. 4.20(h,i)). Aside of increasing the solubility of the metal complex, the *t*-bpy can also act as a modulator by preferential absorption in some crystal faces during crystal growth, so inhibiting or slowing down the growth in these directions and giving different morphologies.
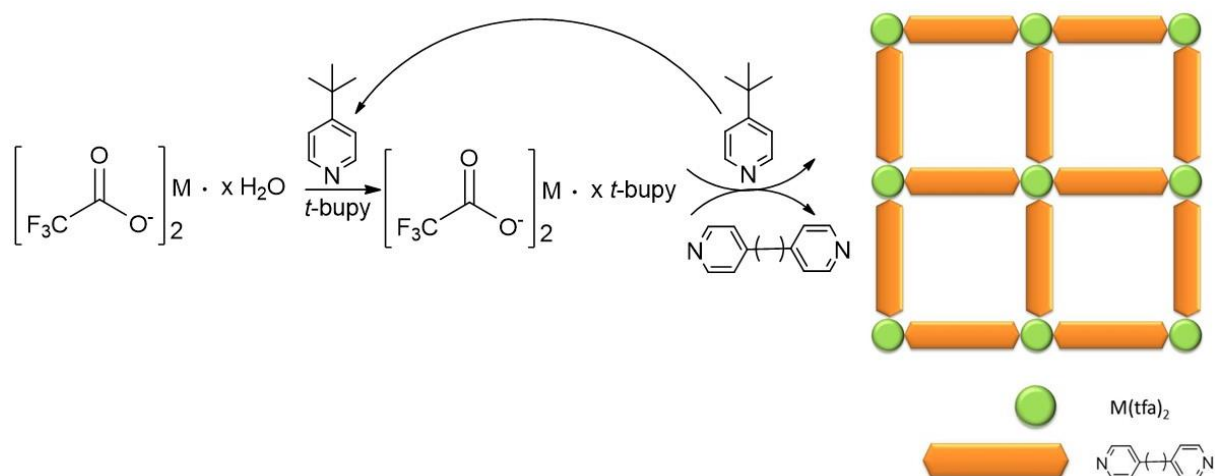

Figure 4.24. Schematic representation of the pathway used for $[M(tfa)_2(dpy)_2]_n$ synthesis following Method D, showing the recirculation of the *t*-bpy towards $M(tfa)_2$.

The SEM analysis was extended to the precipitated $[Cu(tfa)_2(bpp)_2]_n$. In a reaction media involving a relatively high concentration of *t*-bpy, i.e., the one with the intermediate $[Cu(tfa)_2(t\text{-bpy})_{2.5}]$ and those with Cu(II):*t*-bpy molar ratios of 1:1, small particles of 1–3 µm were precipitated (Fig. 4.25(a,b)). On the contrary, significantly larger crystals, higher than 5 µm, were obtained in reactions involving low concentrations of the ancillary ligand, e.g., M(II):*t*-bpy molar ratios of 1:0.5 and 1:0.14 (Fig. 4.25(c,d)).
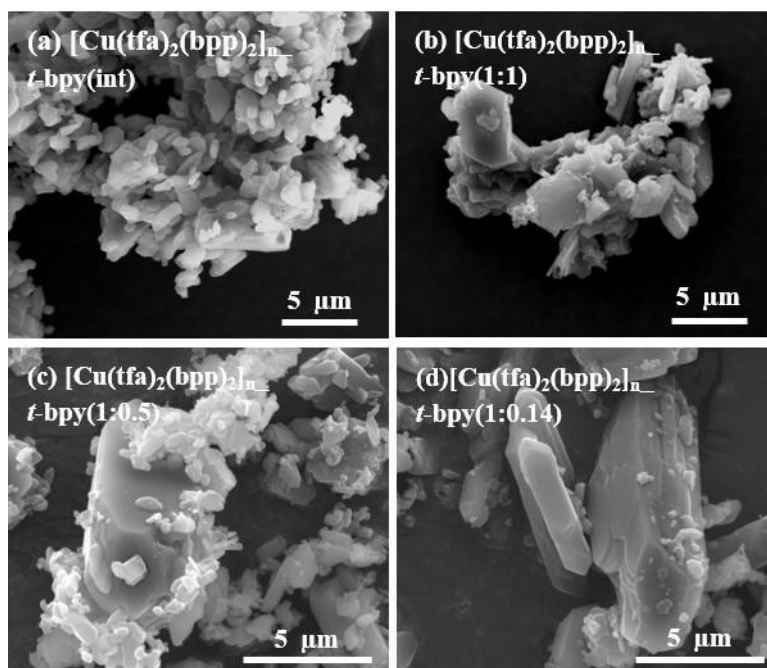
Figure 4.25. SEM micrographs of the different precipitated samples of $[Cu(tfa)_2(bpp)_2]_n$ CP in the presence of *t*-bpy added as: (a) intermediate, or free in Cu(II):bpp molar ratios of (b) 1:1, (c) 1:0.5, and (d) 1:0.14.

4.3.1.3. Surface deposition of $[Cu(tfa)_2(bpy)_2]_n$

Supercritical CO_2 is increasingly considered as an appropriate medium to manipulate surfaces of both flat substrates and geometrically intricate nanostructures, thanks to its unique properties of low viscosity, near-zero surface tension, chemical inertness, high diffusivity and tunable solvation properties.[54] The different steps of supercritical surface deposition of films can be examined under three main categories: (i) the dissolution of the precursors in scCO₂, (ii) sorption of at least one of the precursors on the surface, and (iii) growth of the film by reactive crystallization. These three important facets of the method have been examined in this work for the formation of the $[Cu(tfa)_2(bpy)_2]_n$ CP on the flat surface of silicon wafer. During the first section of this article, we have demonstrated that the solubility of the metallic precursor can be increased by adding small amounts of free *t*-bpy to the reaction medium, thus fulfilling the first requirement for crystals deposition. The affinity of the surface of the silicon wafer for the CP reagents was increased by creating specific absorption sites. The modification was performed either by developing surface hydroxyl groups or by grafting molecules of a trialkoxysilane with ethylpyridine functionality (Fig. 4.26).
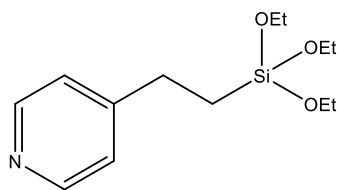
N-(3-(triethoxysilylethyl)pyridine

Figure 4.26. Structures of the used N-(3-triethoxysilylethyl)pyridine.

Hence, CP crystal growth on the surface was studied for the $[Cu(tfa)_2(bpy)_2]_n$ product, which was deposited on silicon wafer previously hydroxylated and further decorated with triethoxy ethylpirydine (Fig. 4.27(a,b)). The anhydrous $scCO_2$ silanization method has demonstrated to be a versatile and efficient process to form well-ordered self-assembled monolayers in different substrates.[55] In this case, the pyridine silane acts as a coupling agent, since, at the same time, it is an anchoring moiety to the substrate (by the triethoxy side) and an initiator for the MOF nucleation (by the pyridine side). The deposition process was performed following the $scCO_2$ standard procedure (20 MPa, 333 K and 3 h), with a small amount of added free *t*-bpy (molar ratio to the metal of 1:0.14), in a non-stirred reactor.
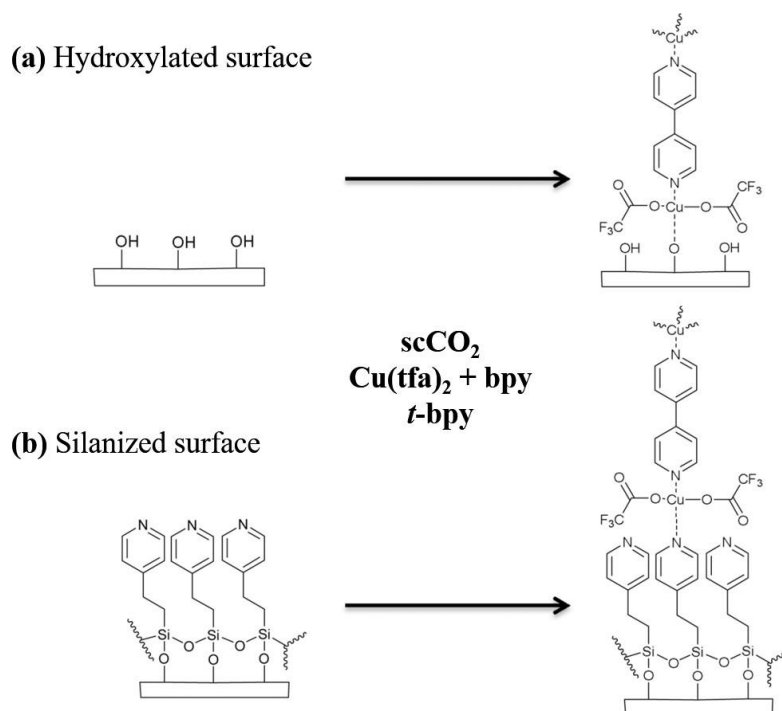

Figure 4.27. Schematic representation of the pathway used for $[Cu(tfa)_2(bpy)_2]_n$ deposition, following method D, on surfaces previously treated with N-(3-triethoxysilylethyl)pyridine.

The silanized surface of the silicon wafer was analyzed in regard of the composition by using ATR-FTIR spectroscopy (Fig. 4.28). The most representative spectral bands of the 2-(4-pyridylethyl)triethoxysilane appear at 2887 and 2932 cm^{-1}, corresponding to the symmetric and antisymmetric stretching modes of the CH_2 moiety, and at 1618 cm^{-1} assigned to C-N stretching (Fig. 4.28(A)). All those bands were also observed after CP precipitation on the functionalized surface (Fig. 4.28(B)). In addition, the sample involving deposited $[Cu(tfa)_2(bpy)_2]_n$ displayed the trifluoracetate signals at 1693 and 1640 cm^{-1} for C-O and C-C, respectively. The silanized silicon wafer surface becomes fluorescent after silanization due to the ethylpyridine functionality. The observed continuous fluorescence indicates that, following the supercritical procedure, the surface was completely covered with the silane (Fig. 4.28 top); although, some excess of the molecule was noticed in some spots, forming small drops. After $[Cu(tfa)_2(bpy)_2]_n$ deposition, the fluorescence disappeared or diminished in the area covered by the MOF (Fig. 4.28 bottom). Fluorescence images indicate that at the short running time of 3 h, the treated surface was not completely covered by MOF crystals.
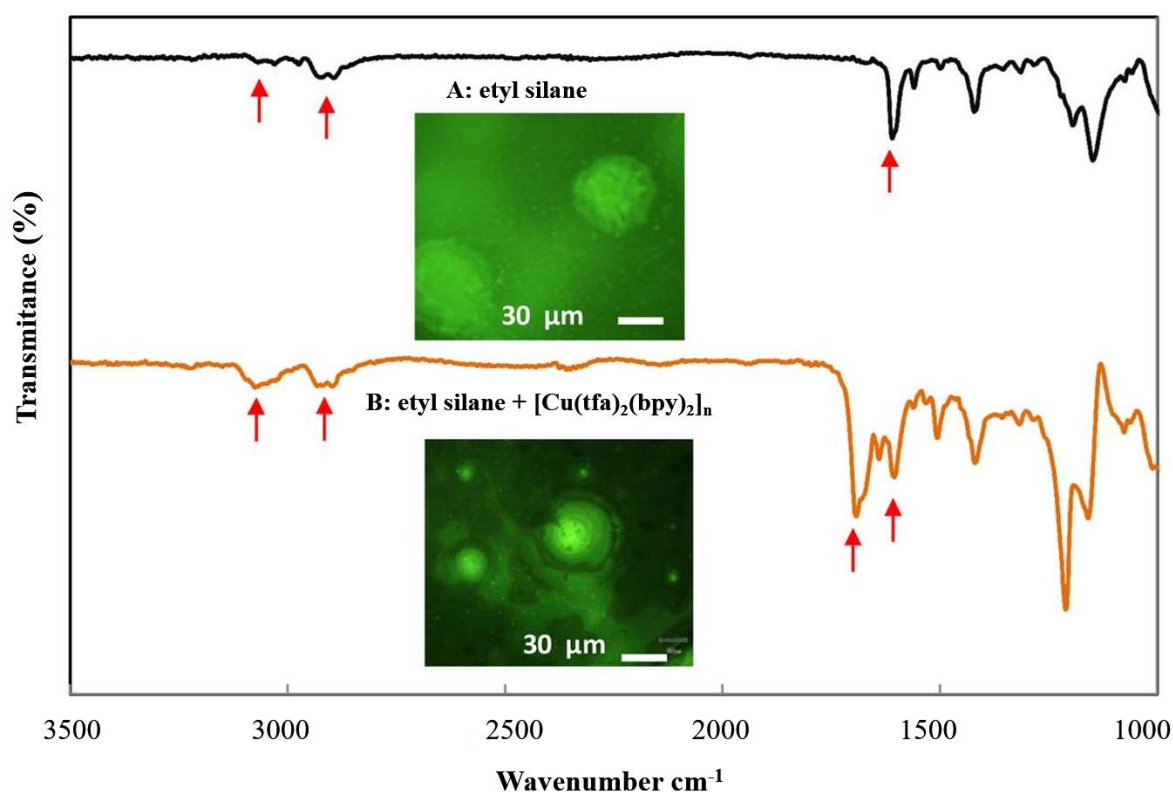

Figure 4.28. ATR-FTIR spectra recorded for (A) the silanized wafer substrate, and (B) after $[Cu(tfa)_2(bpy)_2]_n$ deposition. Arrows are signaling the most representative bands (see text). Pictures obtained for the treated silicon wafer using a fluorescence microscope are also included.

SEM analysis was performed for precipitated particles in both hydroxylated and silanized surfaces. For comparison, Fig. 4.29(a,b) shows the polyhedral crystals, with prismatic and bipyramid habit, of [Cu(tfa)$_2$(bpy)$_2$]$_n$ precipitated in the bulk. For hydroxylated surfaces, small well-crystallized polyhedral crystals were deposited partially covering the surface (Fig. 4.29(c)). Mainly small crystals (*ca.* 3×1×0.5 μm) with prismatic habit were deposited (Fig. 4.29(d)). For surfaces modified with a pyridine silane, the covering degree was significantly reduced in comparison with hydroxylated supports (Fig. 4.29(e and c, respectively)). In this case, the predominant observed morphology was constituted by few micrometers crystals with truncated pyramidal habit. Individual crystals deposited on the surface of the wafer displayed a top smooth crystal face free of screw dislocations (Fig. 4.29(f)). Oriented attachment crystal growth is often proposed for the formation of structures of zeolites and MOFs,[56] and can also be an optional mechanism in this case.
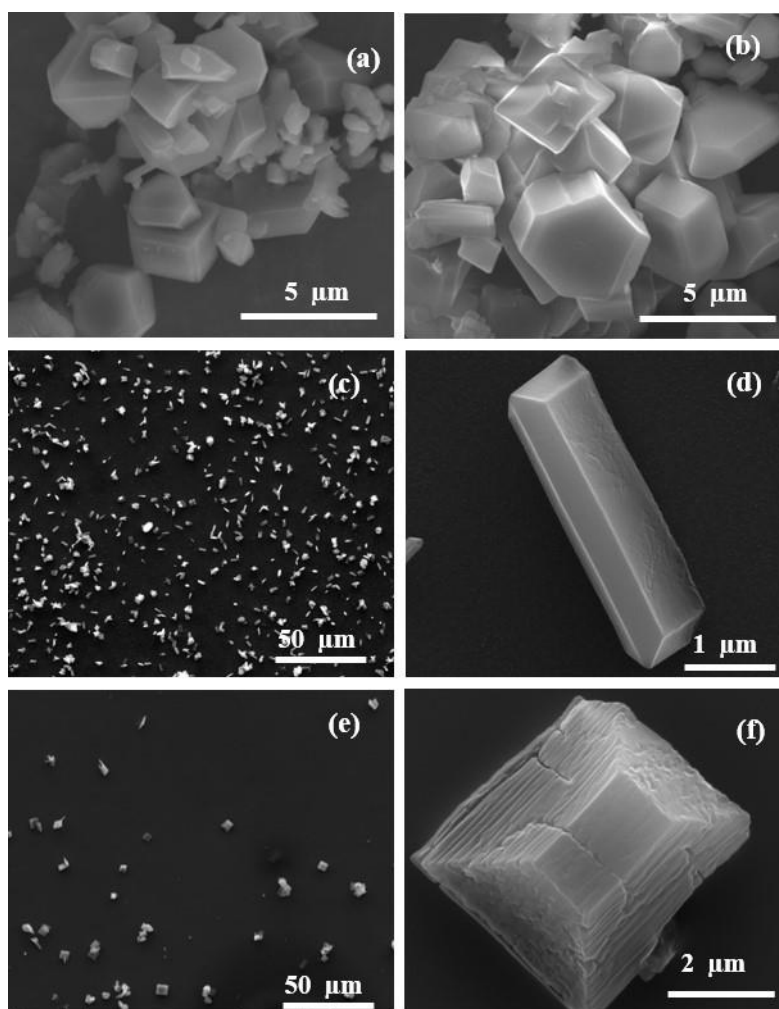

Figure 4.29. SEM images obtained for [Cu(tfa)$_2$(bpy)$_2$]$_n$: (a,b) bulk crystals, and deposited on silicon wafer (c,d) hydroxylated , and (e,f) treated with silane.

4.4. Conclusions

One of the biggest obstacles of scCO$_2$ technology for CPs preparation is the lack of solubility of many metal complexes. The solubility of polar compounds in scCO$_2$ has historically been increased by adding small quantities of co-solvent to the fluid, such as ethanol or acetone. On one hand, this approach decreases the processing time, increases yield and makes possible to use milder processing conditions. On the other hand, it complicates system thermodynamics and increases capital cost. In the specific case of porous CPs, the presence of co-solvents in the system could complicate the precipitation of highly porous systems due to solvent adsorption, filling the pores. This work demonstrates the efficiency of alternative procedures to increase metallic reagents solubility by using the *t*-bpy as ancillary ligand. This finding opens new fascinating windows towards the reactivity of metal complexes in scCO$_2$.
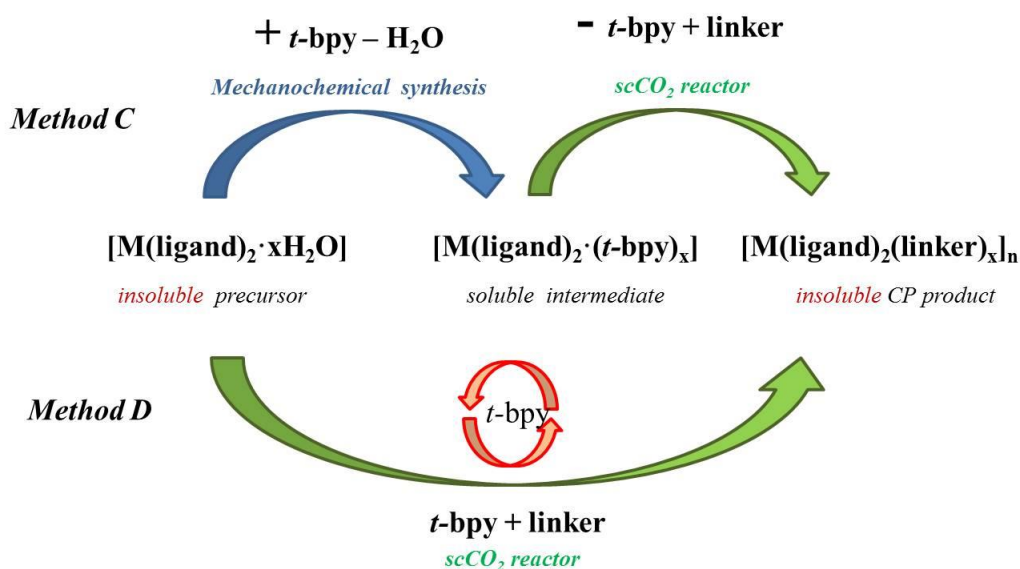
Figure 4.30. Scheme of the alternative procedures used to increase metallic reagents solubility by using the *t*-bpy as ancillary ligand.

The *t*-bpy forms and adduct with the metal complex, highly increasing its solubility. In the first approach, the adduct was pre-synthetized before supercritical processing. This was demonstrated by the preparation of [M(deox)$_2$(*t*-bpy)$_2$] and [M(tfa)$_2$(*t*-bpy)$_{2\,5}$] derivatives, which was carried out to successfully increase the solubility of the metal complexes in scCO$_2$. The synthesis of these solid intermediates can be avoided just by adding small amounts of free *t*-bpy ligand to the reaction media, thus upgrading the synthetic protocol by reducing the number of reaction steps needed to achieve the objective. The process has been tested for the

highly insoluble [M(tfa)₂] system. Using these procedures, a collection of 1D CPs [M(deox)₂(bpy)]ₙ M= Co(II), Cu(II), Mn(II), Ni(II) and Zn(II) and 2D CPs involving Zn(II) or Cu(II) trifluoroacetate and several linear dipyridines could be synthetized in scCO₂.

Modulation of the solubility and thus, of the coordination equilibrium, arises from the introduced ancillary ligand, competing with CP's bridging linkers for coordination to the metal ions. The ancillary ligand lacks of further binding sites, thus hindering additional assembly of the crystal network in this direction and inducing some control over the CP crystal size and shape. Shape control allowed to present preliminary results of the potentials of the scCO₂ technique for the *in situ* growth of CPs on surfaces. The polymer can be grafted to the surface through either hydroxyl groups or silane coupling agents, thus enhancing film stability. Further studies are needed to increase thin film quality.

4.5. References

(1) Cooper, A. I. Porous materials and supercritical fluids. *Adv. Mater.,* **2003**, 15 (13), 1049-1059.

(2) Peng, L.; Zhang, J.; Xue, Z.; Han, B.; Sang, X.; Liu, C.; Yang, G. Highly mesoporous metal-organic framework assembled in a switchable solvent. *Nat. Commun.*, **2014**, 5 (1), 4465, 1-7.

(3) Zhao, Y.; Zhang, J.; Han, B.; Song, J.; Li, J.; Wang, Q. Metal-organic framework nanospheres with well-ordered mesopores synthesized in an ionic liquid/CO₂/surfactant system. *Angew. Chemie Int. Ed.*, **2011**, 50 (3), 636-639.

(4) López-Periago, A.; López-Domínguez, P.; Pérez Barrio, J.; Tobias, G.; Domingo, C. Binary Supercritical CO₂ solvent mixtures for the synthesis of 3D metal-organic frameworks. *Microporous Mesoporous Mater.,* **2016**, 234, 155-161.

(5) López-Periago, A.; Vallcorba, O.; Frontera, C.; Domingo, C.; Ayllón, J. A. Exploring a novel preparation method of 1D metal organic frameworks based on supercritical CO₂. *Dalton. Trans.*, **2015**, 44 (16), 7548-7553.

(6) López-Periago, A. M.; Portoles-Gil, N.; López-Domínguez, P.; Fraile, J.; Saurina, J.; Aliaga-Alcalde, N.; Tobias, G.; Ayllón, J. A.; Domingo, C. metal-organic frameworks precipitated by reactive crystallization in supercritical CO₂. *Cryst. Growth Des.* **2017**, 17 (5), 2864-2872.

(7) López-Domínguez, P.; López-Periago, A. M.; Fernández-Porras, F. J.; Fraile, J.; Tobias, G.; Domingo, C. Supercritical CO₂ for the synthesis of nanometric ZIF-8 and loading with hyperbranched aminopolymers. applications in CO₂ capture. *J. CO₂ Util.*, **2017**, 18, 147-155.

(8) Dardin, A.; DeSimone, J. M.; Samulski, E. T. Fluorocarbons dissolved in supercritical carbon dioxide. NMR evidence for specific solute-solvent interactions. *J. Phys. Chem. B*, **1998**, 102 (10), 1775-1780.

(9) Gupta, R. B.; Shim, J.-J. Solubility in supercritical carbon dioxide; CRC Press, **2006**.

(10) Tan, J.-C.; Saines, P. J.; Bithell, E. G.; Cheetham, A. K. Hybrid nanosheets of an inorganic-organic framework material: facile synthesis, structure, and elastic properties. *ACS Nano*, **2012**, 6 (1), 615-621.

(11) Song, X.; Hu, J.; Zeng, H. Two-dimensional semiconductors: recent progress and future perspectives. *J. Mater. Chem. C*, **2013**, 1 (17), 2952-2969.

(12) Rodenas, T.; Luz, I.; Prieto, G.; Seoane, B.; Miro, H.; Corma, A.; Kapteijn, F.; Llabrés i Xamena, F. X.; Gascon, J. Metal-organic framework nanosheets in polymer composite materials for gas separation. *Nat. Mater.,* **2015**, 14 (1), 48-55.

(13) Zhao, M.; Wang, Y.; Ma, Q.; Huang, Y.; Zhang, X.; Ping, J.; Zhang, Z.; Lu, Q.; Yu, Y.; Xu, H.; Zhao, Y.; Zhang, H. Ultrathin 2D metal-organic framework nanosheets. *Adv. Mater.,* **2015**, 27 (45), 7372-7378.

(14) Rao, C. N. R.; Ramakrishna Matte, H. S. S.; Maitra, U. Graphene analogues of inorganic layered materials. *Angew. Chemie Int. Ed.,* **2013**, 52 (50), 13162-13185.

(15) Flügel, E. A.; Ranft, A.; Haase, F.; Lotsch, B. V. Synthetic routes toward MOF nanomorphologies. *J. Mater. Chem.,* **2012**, 22 (20), 10119-10133.

(16) Wang, F.; Wang, Z.; Shifa, T. A.; Wen, Y.; Wang, F.; Zhan, X.; Wang, Q.; Xu, K.; Huang, Y.; Yin, L.; Jiang, C.; He, J. Two-dimensional non-layered materials: synthesis, properties and applications. *Adv. Funct. Mater.*, **2017**, 27 (19), 1603254, 1-21.

(17) Čejka, J.; Morris, R. E.; Nachtigall, P.; Roth, W. J. Layered inorganic solids. *Dalton Trans.,* **2014**, 43 (27), 10274-10275.

(18) Nasilowski, M.; Mahler, B.; Lhuillier, E.; Ithurria, S.; Dubertret, B. Two-dimensional colloidal nanocrystals. *Chem. Rev.*, **2016**, 116 (18), 10934-10982.

(19) Sasaki, T.; Ebina, Y.; Kitami, Y.; Watanabe, M.; Oikawa, T. Two-dimensional diffraction of molecular nanosheet crystallites of titanium oxide. *J. Phys. Chem. B*, **2001**, 105 (26), 6116-6121.

(20) Kondo, A.; Tiew, C. C.; Moriguchi, F.; Maeda, K. Fabrication of metal-organic framework nanosheets and nanorolls with N-donor type bridging ligands. *Dalton Trans.,* **2013**, 42 (43), 15267-15270.

(21) Quah, H. S.; Ng, L. T.; Donnadieu, B.; Tan, G. K.; Vittal, J. J. Molecular scissoring: facile 3D to 2D conversion of lanthanide metal organic frameworks via solvent exfoliation. *Inorg. Chem.*, **2016**, 55 (21), 10851-10854.

(22) Sakata, K.; Kashiyama, S.; Matsuo, G.; Uemura, S.; Kimizuka, N.; Kunitake, M. Growth of two-dimensional metal-organic framework nanosheet crystals on graphite substrates by thermal equilibrium treatment in acetic acid vapor. *ChemNanoMat.,* **2015**, 1 (4), 259-263.

(23) Lahiri, N.; Lotfizadeh, N.; Tsuchikawa, R.; Deshpande, V. V.; Louie, J. Addition to "hexaaminobenzene as a building block for a family of 2D coordination polymers." *J. Am. Chem. Soc.,* **2017**, 139 (5), 2119-2119.

(24) Ezrahi, S.; Tuval, E.; Aserin, A. Properties, main applications and perspectives of worm micelles. *Adv. Colloid Interface Sci.,* **2006**, 128-130, 77-102.

(25) Yin, Y.; Alivisatos, A. P. Colloidal nanocrystal synthesis and the organic-inorganic interface. *Nature*, **2005**, 437 (7059), 664-670.

(26) López-Periago, A.; Vallcorba, O.; Domingo, C.; Ayllón, J. A. Hollow microcrystals of copper hexafluoroacetylacetonate-pyridine derivative adducts via supercritical CO_2 recrystallization. *Cryst. Growth Des.*, **2016**, 16 (3), 1725-1736.

(27) Hay, R. Carboxylic esters as ligands. I. Metal chelates of diethyl oxaloacetate. *Aust. J. Chem.*, **1964**, 17 (7), 759-764.

(28) López-Periago, A. M.; Sandoval, W.; Domingo, C. Chemical modification of nanometric TiO_2 particles by anchoring functional silane molecules in supercritical CO_2. *Appl. Surf. Sci.,* **2014**, 296, 114-123.

(29) Le Bail, A. Whole powder pattern decomposition methods and applications: a retrospection. *Powder Diffr.* **2005**, 20 (4), 316-326.

(30) Bruker (**2003**) SADABS, Version 2.05, Bruker AXS Inc., Madison, Wisconsin, USA.

(31) Sheldrick, G. M. A short history of SHELX. *Acta Crystallogr. Sect. A Found. Crystallogr.*, **2008**, 64 (1), 112-122.

(32) Fauth, F.; Peral, I.; Popescu, C.; Knapp, M. The new material science powder diffraction beamline at ALBA synchrotron. *Powder Diffr.*, **2013**, 28 (S2), S360-S370.

(33) Boultif, A.; Louër, D. Powder pattern indexing with the dichotomy method. *J. Appl. Crystallogr.*, **2004**, 37 (5), 724-731.

(34) Vallcorba, O.; Rius, J.; Frontera, C.; Peral, I.; Miravitlles, C. DAJUST: A suite of computer programs for pattern matching, space-group determination and intensity extraction from powder diffraction data. *J. Appl. Crystallogr.***, 2012**, 45 (4), 844-848.

(35) Vallcorba, O.; Rius, J.; Frontera, C.; Miravitlles, C. TALP: A Multisolution direct-space strategy for solving molecular crystals from powder diffraction data based on restrained least squares. *J. Appl. Crystallogr.*, **2012**, 45 (6), 1270-1277.

(36) Teoh, W. H.; Mammucari, R.; Foster, N. R. Solubility of organometallic complexes in supercritical carbon dioxide: a review. *J. Organomet. Chem.*, **2013**, 724, 102-116.

(37) Starikova, Z. A.; Shugam, E. A. *Zh. Strukt. Khim.*, **1969**, 10, 290-293.

(38) Joksimović, N.; Baskić, D.; Popović, S.; Zarić, M.; Kosanić, M.; Ranković, B.; Stanojković, T.; Novaković, S. B.; Davidović, G.; Bugarčić, Z.; Janković, N. Synthesis, characterization, biological activity, DNA and BSA binding study: novel copper (II) complexes with 2-hydroxy-4-aryl-4-oxo-2-butenoate. *Dalton Trans.*, **2016**, 45 (38), 15067-15077.

(39) Lagalante, A. F.; Hansen, B. N.; Bruno, T. J.; Sievers, R. E. Solubilities of copper(II) and chromium(III) beta-diketonates in supercritical carbon dioxide. *Inorg. Chem.*, **1995**, 34 (23), 5781-5785.

(40) Starikova, Z. A.; Shugam, E. A. Crystal chemical data for inner complexes of β-diketones. *J. Struct. Chem.*, **1969**, 10 (2), 267-269.

(41) Saxena, P.; Thirupathi, N. Reactions of Cd(OAc)₂·2H₂O with variously substituted pyridines. efforts to unravel the factors that determine structure/nuclearity of the products. *Polyhedron*, **2015**, 98, 238-250.

(42) Bullen, G. J. The crystal structure of cobalt(II) bisacetylacetone dihydrate. *Acta Crystallogr.*, **1959**, 12 (10), 703-708.

(43) Biradha, K.; Sarkar, M.; Rajput, L. Crystal engineering of coordination polymers using 4,4′-bipyridine as a bond between transition metal atoms. *Chem. Commun.*, **2006**, 40, 4169-4179.

(44) Tenorio, M. J.; Cabañas, A.; Pando, C.; Renuncio, J. A. R. Solubility of Pd(Hfac)₂ and Ni(Hfac)₂·2H₂O in supercritical carbon dioxide pure and modified with ethanol. *J. Supercrit. Fluids*, **2012**, 70, 106-111.

(45) Karizi, F. Z.; Safarifard, V.; Khani, S. K.; Morsali, A. Ultrasound-assisted synthesis of nano-structured 3D zinc(II) metal-organic polymer: precursor for the fabrication of ZnO nano-structure. *Ultrason. Sonochem.*, **2015**, 23, 238-245.

(46) Naseri, M.; Fotouhi, L.; Ehsani, A.; Dehghanpour, S. Facile electrosynthesis of nano flower like metal-organic framework and its nanocomposite with conjugated polymer as a novel and hybrid electrode material for highly capacitive pseudocapacitors. *J. Colloid Interface Sci.*, **2016**, 484, 314-319.

(47) Yang, H. M.; Song, X. L.; Yang, T. L.; Liang, Z. H.; Fan, C. M.; Hao, X. G. Electrochemical synthesis of flower shaped morphology mofs in an ionic liquid system and their electrocatalytic application to the hydrogen evolution reaction. *RSC Adv.*, **2014**, 4 (30), 15720-15726.

(48) McEwen, J.; Hayman, J.-D.; Ozgur Yazaydin, A. A comparative study of CO₂, CH₄ and N₂ adsorption in ZIF-8, zeolite-13X and BPL activated carbon. *Chem. Phys.*, **2013**, 412, 72-76.

(49) Kokunov, Y. V.; Gorbunova, Y. E.; Kovalev, V. V.; Kozyukhin, A. S. 2D-layered structure of coordination polymer, zinc trifluoroacetate-1,3-bis(4-pyridyl)propane. *Russ. J. Inorg. Chem.*, **2014**, 59 (3), 187-191.

(50) Nagarathinam, M.; Vittal, J. J. Solid-state synthesis of coordination polymers for [2+2] photoreactions by grinding. *Aust. J. Chem.*, **2010**, 63 (4), 589.

(51) Portoles-Gil, N.; Parra-Aliana, R.; Álvarez-Larena, Á.; Domingo, C.; Ayllón, J. A.; López-Periago, A. Bottom-up approach for the preparation of hybrid nanosheets based on coordination polymers made of metal-diethyloxaloacetate complexes linked by 4,4′-bipyridine. *CrystEngComm.*, **2017**, 19 (34), 4972-4982.

(52) Marin, G.; Tudor, V.; Kravtsov, V. C.; Schmidtmann, M.; Simonov, Y. A.; Muller, A.; Andruh, M. Extended structures constructed from alkoxo-bridged binuclear complexes as nodes and bis(4-pyridyl)ethylene as a spacer. *Cryst. Growth Des.*, **2005**, 5 (1).

(53) Zhang, C.; Cao, Y.; Zhang, J.; Meng, S.; Matsumoto, T.; Song, Y.; Ma, J.; Chen, Z.; Tatsumi, K.; Humphrey, M. G. Modulation of third-order nonlinear optical properties by backbone modification of polymeric pillared-layer heterometallic clusters. *Adv. Mater.*, **2008**, 20 (10), 1870-1875.

(54) Subra-Paternault, P.; Domingo, C. ScCO$_2$ techniques for surface modification of micro- and nanoparticles. in surface modification of nanoparticle and natural fiber fillers. Wiley-VCH Verlag GmbH & Co. KGaA: Weinheim, Germany, **2015**, 109-150.

(55) Domingo, C.; Loste, E.; Fraile, J. Grafting of trialkoxysilane on the surface of nanoparticles by conventional wet alcoholic and supercritical carbon dioxide deposition methods. *J. Supercrit. Fluids,* **2006**, 37 (1), 72-86.

(56) Olafson, K. N.; Li, R.; Alamani, B. G.; Rimer, J. D. Engineering crystal modifiers: bridging classical and nonclassical crystallization. *Chem. Mater.*, **2016**, 28 (23), 8453-8465.

CHAPTER-5

Synthesis of Heterometallic CPs

CHAPTER 5 describes the one-step synthesis of new homometalic and heterometalic coordination polymers build of cobalt and/or zinc. A large bipyridine molecule was used as the organic linker. All new CPs were structurally resolved and the magnetic properties of cobalt containing compounds were studied.

5.1. Introduction

Coordination polymers (CPs) or metal-organic frameworks (MOFs) comprise metal nodes, usually transition metals or metallic clusters, connected in a crystalline network by multipodal organic linkers through coordination bonds. One of the unique features of these extended structures is the tunability in the design, based on the concept of the modification of the composition and geometry of the repeating unit. This includes not only the use of different organic linkers or metal clusters, but also the preparation of multivariate CPs with more than one linker and/or inorganic building unit in the design.[1] New functionalities and applications are described for these hybrid polymers, particularly in heterogeneous catalysis by designing systems with more than one active center.[2] One of the earliest synthetic routes described to introduce heterogeneity in CPs was through the organic part, by pre-mixing in the solvothermal synthesis more than one bridging unit. This design is used for compounds involving highly flexible organic linkers, which are difficult to crystallize in networks with high symmetry factors. The addition of an auxiliary linker, typically a bipyridine or dicarboxylic acid, increases the dimensionality and rigidity of the framework, often providing permanent porosity to the end product.

Another option to introduce heterogeneity is to use a mixture of metals. Most representative heterometallic frameworks are schematized in Fig. 5.1. Pioneering studies in bimetallic networks concern compounds with several inorganic clusters of different geometry.[3–5] Next, infinite networks have also been shaped with single heteronuclear nodes involving two metals with different oxidation state.[6–8] Finally, multilayer core-shell or multidomain single crystals of heterometallic CPs exists for compounds with lattice match.[9–12] Indeed, the latter has been extended to systems with 10 different divalent metals, possessing a wide range of ionic radii sizes, and a single linker.[13] Core-shell structures can also be obtained by post-synthetic transmetalation,[14] a process in which *quasi* complete exchange of metals ions would be possible by increasing sufficiently the processing time. Transmetalation is proposed for the preparation of isostructural networks difficult to obtain by a direct synthetic strategy, like those involving Ti(III), V(II), Cr(II) and Fe(II) cations.[15,16] It is worth mentioning that this is a single crystal-to-single crystal process kinetically viable only for porous compounds with enhanced internal diffusion.[17,18]
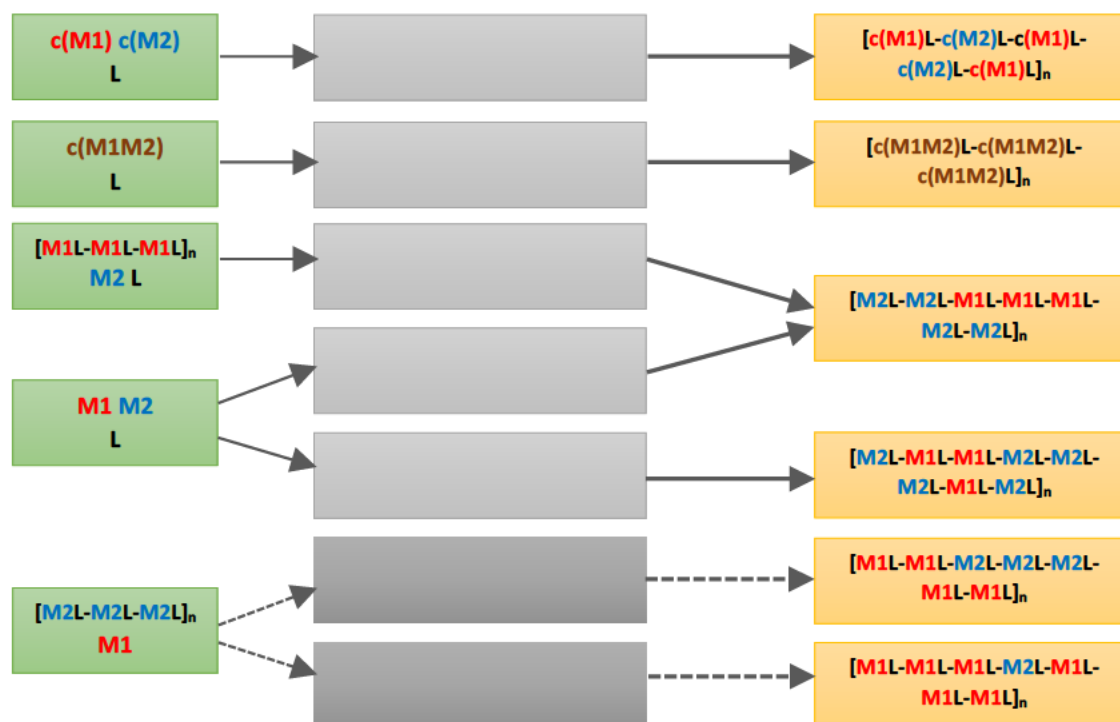
Figure 5.1. Typical heterometallic frameworks combined with the linker **L**. In A and B, pre-formed homometallic clusters (c(M1) and c(M2)) and heteronuclear clusters (c(M1M2)) are, respectively shown. Compounds in C and D are core-shell structures in which the two homometallic components have lattice match. In C, crystals are precipitated by soaking seed particles of the most stable CP $[M1L-M1L-M1L]_n$ in a solution of the second metal M2 and the ligand L. In D, sophisticated core-shell MOFs are prepared by co-precipitation of M1/L and M2/L pairs with different nucleation rate, in which the faster precipitating compound (M1L) forms the core and the second precipitates latter as the shell (M2L). Contrarily, in E the statistic co-precipitation of both phases in small domains occurs by using M1/L and M2/L pairs with similar nucleation rate. F and G describe post-synthetic transmetalation, in which crystals of the MOF with the lowest stability $[M2L-M2L-M2L]_n$ are soaked in a solution of the second metal M1 in the absence of ligand. Core-shell structures are obtained at short processing periods (F), while quasi total replacements can be obtained at high running times (G).

Multivariate CPs are usually solvothermally prepared, either in routes of one-pot synthesis or by post-synthetic exchange or cationic substitution. In general, the later can only be used for metals that occupy chemically identical lattice positions, while the former can also be used for systems in which the position of the different cations is not interchangeable. The interest of the study performed in this Thesis focuses on developing heterometallic solid-solution systems by the one-pot co-precipitation method performed in either supercritical CO_2 ($scCO_2$) or ethanol (EtOH) solvent. The system chosen for study involves a ditopic bipyridyl derivative, the 1,4-bis(4-pyridylmethyl)benzene (bpymb) linker, and Zn(II) and/or Co(II) metal center (Fig 5.1).
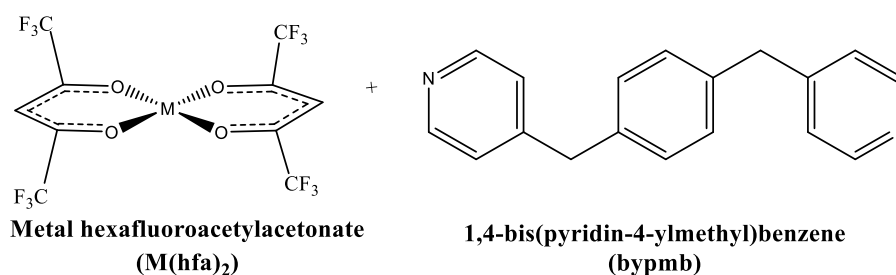
Figure 5.1. Chemical structures of metal complex M(hfa)$_2$ and organic ligand bypmb.

Zn(II) and Co(II) are cations with similar radius, valence and coordination geometry.[19-23] As a consequence, this two metals have been deeply study to form heterometallic MOFs, in particular those with a zeolitic imidazolate framework, such as ZIF-8 and ZIF-67.[24-27] In this work, four new compounds were crystallized: one involving Zn(II), two involving Co(II) and one involving the mixture of Zn(II) and Co(II). The structure of all of them was elucidated by single crystal synchrotron X-ray diffraction.

As it was mentioned in Chapter 1, due to particular arrangement of the metal nodes in CPs some interesting magnetic properties can arise.[28] These materials are sometimes named as magnetic framework composites (MFCs).[29] The magnetic properties can be controlled with external stimuli, offering applications in catalysis, sensing, recording and targeted drug release. The focus is in the design of single molecule magnets (SMMs) and single-molecular chains (SMCs). These materials are molecular objects that display slow magnetic relaxation upon removal of a magnetizing field at low temperatures. This is often induced from the effect of high-spin ground state and uniaxial magnetic anisotropy in the metals.[30] In the last decade, a large number of publications appears treating this kind of materials.[31] SMMs found a potential interest in data storage and molecular electronics. There are numerous examples of mixed-metal CPs made with 3d-4f combinations that possess magnetic properties.[32-35] However, there are only few examples of CPs with magnetic properties involving transition metals, specifically cobalt.[36-39] In order to improve the magnetic properties some approaches were commonly used to minimize intermolecular interactions. For example, the incorporation of diamagnetic rigid ligands[40] or the use of magnetic dilution introducing diamagnetic ions in the framework.[41] Hence, for compounds involving Co(II), the alternating current magnetic susceptibility was evaluated in order to investigate the magnetic properties. Compounds involving Co(II) and Zn(II)/Co(II) behave as SMMs with potential applications in high-density information storage, quantum computing and molecular spintronic.[42]

5.2. Experimental

5.2.1. Materials

Zinc hexafluoroacetylacetonate dihydrate ($Zn(hfa)_2 \cdot 2H_2O$) and cobalt hexafluoroacetylacetonate hydrate ($Co(hfa)_2 \cdot xH_2O$) were chosen as the metal complexes node precursors. These reagents, ethanol (EtOH) and chloroform ($CHCl_3$) were all purchased from Sigma Aldrich. 1,4-bis(4-pyridylmethyl)benzene (bpymb) was selected as the organic linker and obtained from Cymit. Compressed CO_2 (99.95%) was supplied by Carburos Metálicos S.A.

5.2.2. Equipment and methods

Crystallization runs were carried out in two different solvents, $scCO_2$ and EtOH. Reactions in $scCO_2$ were performed in a 5 mL Pyrex vial placed into a 100 mL high-pressure autoclave (TharDesign). The vial was charged with *ca.* 100 mg of either Zn(II) or Co(II) metal complex and 1 equivalent of bpymb, together with a small magnetic bar. After capping the vial with cellulose paper, $scCO_2$ was added up to a pressure of 15 MPa at 333 K, and the system was stirred at 500 rpm. For the precipitation of mixed Zn(II)/Co(II) CPs, similar conditions as for the single metal compound were used, but with a 0.5:0.5 molar ratio of the mixed metal source. After a running period of 3 h, the product was washed with fresh $scCO_2$. The autoclave was then depressurized and cooled down to room temperature before recovering a dry powdered sample. For the crystallization tests completed in EtOH, each reagent (*ca.* 100 mg of metal complex and 1 equivalent of bpymb) was separately dissolved in 20 mL of solvent, then mixed in a 100 mL flask and stirred at 500 rpm for 3 h at room temperature. In all cases, the recovered samples were filtered, rinsed with fresh EtOH and air dried.

The layering technique was used to obtain crystals with enough quality for single-crystal synchrotron XRD study. The used solutions were obtained by dissolving 4.5 mg of bpymb in 12 mL of EtOH:$CHCl_3$ (25:75) and 9 mg of metal complex in 2 mL of EtOH. The layering was settled by placing the bpymb solution at the bottom of a vial and slowly adding the metal solution on the top. The vial was then capped and left at room temperature for 1 week to allow the slow liquid-liquid diffusion of one solution into another.

5.2.3. Characterization

Routine powder X-ray diffraction (PXRD) patterns of the precipitated compounds were recorded in a Siemens D5000 diffractometer, using the Cu Kα incident radiation in the 2θ range of 5 to 30º. Single-crystal X-ray diffraction (SCXRD) experiments for three of the new compounds namely Zn(1), Zn/Co(4) and Co(2) were performed in the XALOC beamline at ALBA synchrotron (Spain).[43-46] Data were collected at 100 K with a 0.72931 Å wavelength using the Dectris Pilatus 6M detector placed at 120 mm from the sample. The ϕ-scans were performed from 0 to 360º in steps of 0.5º and at a collection time of 0.15 s·step-1. The scan was repeated at three different κ angles (0, 45º, 90º) and merged afterwards to increase the completeness and redundancy when possible. Data were indexed, integrated and scaled using the XDS software. The crystal structures were solved by intrinsic phasing (SHELXT) and refined with SHELXL (version 2014/7)[47] using Olex2 as graphical interface. Co(3) crystal structure was refined from synchrotron powder XRD data collected in the high resolution powder diffraction endstation of the MSPD beamline (BL04) at the ALBA synchrotron.[48] Data were collected at 100K and 298 K using the Si-microstrip MYTHEN-II detector (6 modules, 1280 channels/module, 50 μm/channel, sample-to-detector distance 550 mm) at an energy of 20 keV (wavelength=0.61978 Å determined with the NIST Si standard).

Crystallographic data for all compounds are summarized in Tables 5.1 and 5.2, and the corresponding CIF files have been deposited in the Cambridge Crystallographic Data Centre (CCDC) 1950459-1950462.

Table 5.1. Crystallographic synchrotron SXRD data for Zn(1), Zn/Co(4) and Co(2).

	Zn(1)	Zn/Co(4)	Co(2)
Molecular formula (MF)	$C_{28}H_{18}F_{12}N_2O_4Zn$	$C_{28}H_{18}F_{12}N_2O_4Co_{0.47}Zn_{0.53}$	$C_{28}H_{18}F_{12}N_2O_4Co$
Formula weight	739.82	736.82	733.38
Crystal system, space group	Triclinic, P $\bar{1}$	Triclinic, P $\bar{1}$	Triclinic, P $\bar{1}$
a (Å)	8.900(2)	8.930(7)	8.77040(7)
b (Å)	9.8940(13)	9.880(5)	9.15990(6)
c (Å)	17.5110(17)	17.570(9)	10.04300(11)
α (°)	104.699(10)	104.57(6)	62.9720(6)
β (°)	96.02(2)	96.38(3)	71.4100(7)
γ (°)	97.45(3)	97.45(8)	80.8890(6)
V (Å^3)	1463.6(5)	1470.9(17)	681.113(11)
Z (according to MF)	2	2	1
D_{calc} (g·cm^3)	1.679	1.664	1.788
T (K)	100	100	100
Wavelength (Å)	0.72932	0.72929	0.72931
μ (mm^{-1})	1.016	0.869	0.799
F(000)	740	737	367
Crystal size (mm^3)	0.13x0.06x0.04	0.13x0.08x0.06	0.10x0.06x0.03
hkl ranges	-12≤h≤12 -14≤k≤14 -24≤l≤24	-12≤h≤12 -13≤k≤13 -24≤l≤24	-13≤h≤13 -14≤k≤14 -14≤l≤14
θ range (°)	2.213 to 31.393	1.243 to 30.427	2.515 to 34.125
Reflections collected/ unique [R_{int}]	39373/8283 [0.056]	104899/8256 [0.053]	40318/4595 [0.036]
Completeness to θ (%)	95.4	99.8	99.6
Data/restrains/parameters	8283/31/438	8256/0/434	4595/0/215
Goodness of fit on F^2	1.063	1.065	1.096
R_1 / wR_2 [$I>2\sigma(I)$]	0.0331/0.0838	0.0348/0.0964	0.0288/0.0790
R_1 / wR_2 (*all data*)	0.0348/0.0850	0.0357/0.0971	0.0289/0.0794
Largest. Diff. peak and hole (e Å^{-3})	0.657 and -0.496	0.796 and -0.600	0.549 and -0.607

Table 5.2. Crystallographic syncrotron PXRD data Co(3).

	Co(3)
Molecular formula (MF)	$C_{28}H_{18}F_{12}N_2O_4Co$
Formula weight	733.38
Crystal system, space group	Triclinic, P $\bar{1}$
a (Å)	8.9127(4)
b (Å)	9.8610(5)
c (Å)	17.5409(9)
α (°)	104.4(2)
β (°)	96.3(2)
γ (°)	97.5(2)
V (Å^3)	1464.1(19)
Z (according to MF)	2
D_{calc} (g·cm^3)	1.664
T (K)	100
Wavelength (Å)	0.61978
μ (mm^{-1})	0.482
$F(000)$	734.0
Meas. 2θ range, stepsize (°)	1.026 to 45.246, 0.006
Profile function	Pseudo-Voigt
2θ range used (°)	1.800 to 34.998
Num. of reflections	2803
Data points	5533
Restrains/parameters	172/156
R_{wp}	0.077
R_{exp}	0.010
$\chi_{Rietveld}$ / $\chi_{Pattern\_matching}$	1.90

Samples chemical composition was estimated by elemental analysis (E.A., Thermo Carlo Erba Flash 2000). The percentage of each metal in mixed metal structures was determined by inductively coupled plasma mass spectrometry (ICP-MS, Agilent 7700x) after digesting the solid in hydrochloric and nitric acids. Metal distribution was assessed by energy dispersive spectroscopy (EDS, FEI Magellan 400L) in a high resolution SEM (Ultim Extreme Oxford Inst.), placing the sample on a holder of silicon wafer and metalizing with Pt. *Ex-situ* X ray photoelectron spectroscopy (XPS) was carried out in a XPS Spectrometer Kratos AXIS Supra using Al-Kα monochromatic (20 eV) radiation emitted at 225 W (15 mA / 15 kV). DC and AC magnetic measurements were performed in a Quantum Design MPMS-5S magnetometer.

5.3. Results and discussion

5.3.1. Structural description

Table 5.3 describes the different scenarios that can be considered for bimetallic CPs synthesis as a function of processing conditions. Trials were performed in $scCO_2$ and EtOH solvents. $M(hfa)_2$ complexes were chosen because of their high solubility in $scCO_2$, which is determined by the high fluoride content in the molecule.[49] Moreover, these complexes were found to also be highly soluble in EtOH. Under working experimental conditions, the used amount of bpymb organic linker was totally solubilized in both tested solvents. Crystallization using $scCO_2$ is here considered more favorable than the solvothermal method to achieve random metal distribution, thanks to the fast precipitation kinetics usually achieved in this fluid with low solvent power. Hence, inhomogeneity due to the different nucleation rate of each M_x/L pair can be minimized. Indeed, after the addition of $scCO_2$ to the vial holding the reagents, an immediate episode of massive nucleation in the solution bulk was observed with a very short induction time. As a consequence, the recovered sample was a powder made of few micron crystalline particles. Moreover, the use of $scCO_2$ enhances the yield by reducing post-processing filtering and drying steps. Crystallization in EtOH also yielded too small crystals but by using layering method larger crystals were successfully produced that allowed SCXRD structure elucidation.

Table 5.3. Solvents of synthesis and composition of the different precipitated phases.

Sample	Solvent	Phase	Crystal structure	E.A. (C,H,N) [%wt]
Zn(sc)	$scCO_2$	Zn(1)	A	f. 45.52, 2.43, 3.88 c. 45.46, 2.45, 3.79
Zn(Et)	EtOH			f. 45.60, 2.68, 3.87 c. 45.46, 2.45, 3.79
Co(sc)	$scCO_2$	Co(2)	B (with impurities of A)	f. 45.71, 2.36, 3.94 c. 45.86, 2.47, 3.82
Co(Et)	EtOH	Co(3)	A	f. 45.69, 2.36, 3.91 c. 45.86, 2.47, 3.82
Zn/Co(sc)	$scCO_2$	Zn/Co(4)	A	f. 45.7, 2.36, 3.94 c. 45.66, 2.46, 3.80
Zn/Co(Et)	EtOH			

Crystal structures of samples precipitated in $scCO_2$ and EtOH were first assessed by PXRD (Fig. 5.2). The patterns of compounds incrystallized in $scCO_2$ (Zn(1) and Zn/Co(4)) and compounds crystallized in EtOH (Zn(1), Co(3) and Zn/Co(4)) were all similar, indicating isostructurality. On the contrary, the different XRD pattern displayed by the compound crystallyxed in $scCO_2$ Co(2) pointed to a dissimilar structure. The differences were also reflected in the observed color of the precipitated samples. Any compound involving only Zn(II) exhibits a white color, while the products with pure Co(II) reflect either an orange color for Co(2) or orange-brown for Co(3). This last color was also observed for the Zn(II)/Co(II) samples. Three of the newly synthetized phases, i.e., Zn(1), Co(2), and Zn/Co(4) (Table 5.1) could be individually elucidated by SCXRD with a synchrotron radiation source, using the best crystals properly grown in the layering set-up. It is worth mentioning that the bulk power of phase Co(3) is contaminated with crystals of Co(2). Its crystal structure was refined from synchrotron powder diffraction data taking as the initial model the isostructural Zn/Co(4) structure solved from single-crystal diffraction data. In the following, the structures of these compounds are described grouped in two types with similar characteristics (structures A and B in Fig. 5.3).
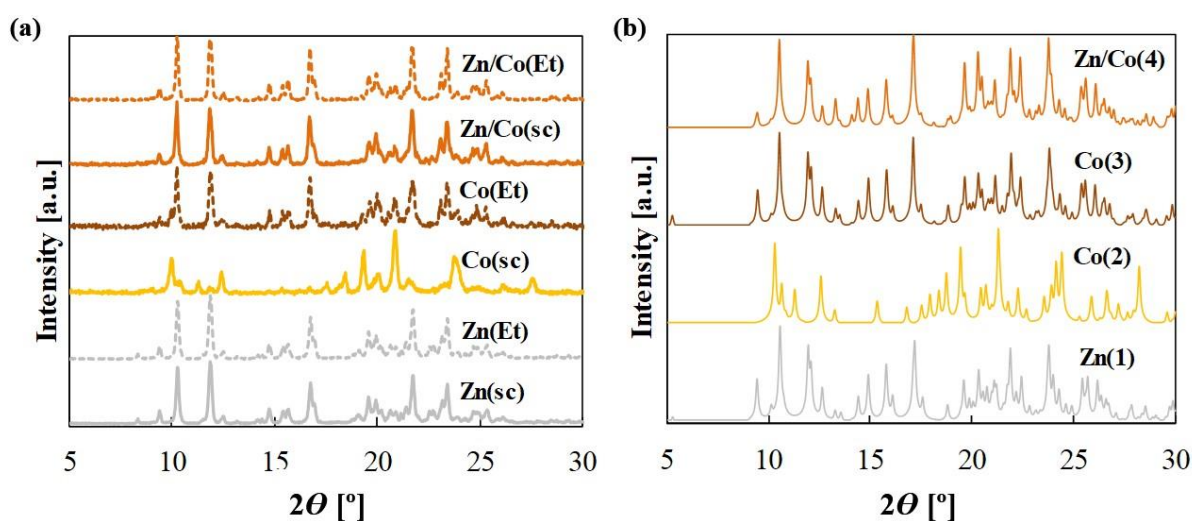

Figure 5.2. PXRD patterns of: (a) precipitated samples, and (b) simulated from single-crystal data.
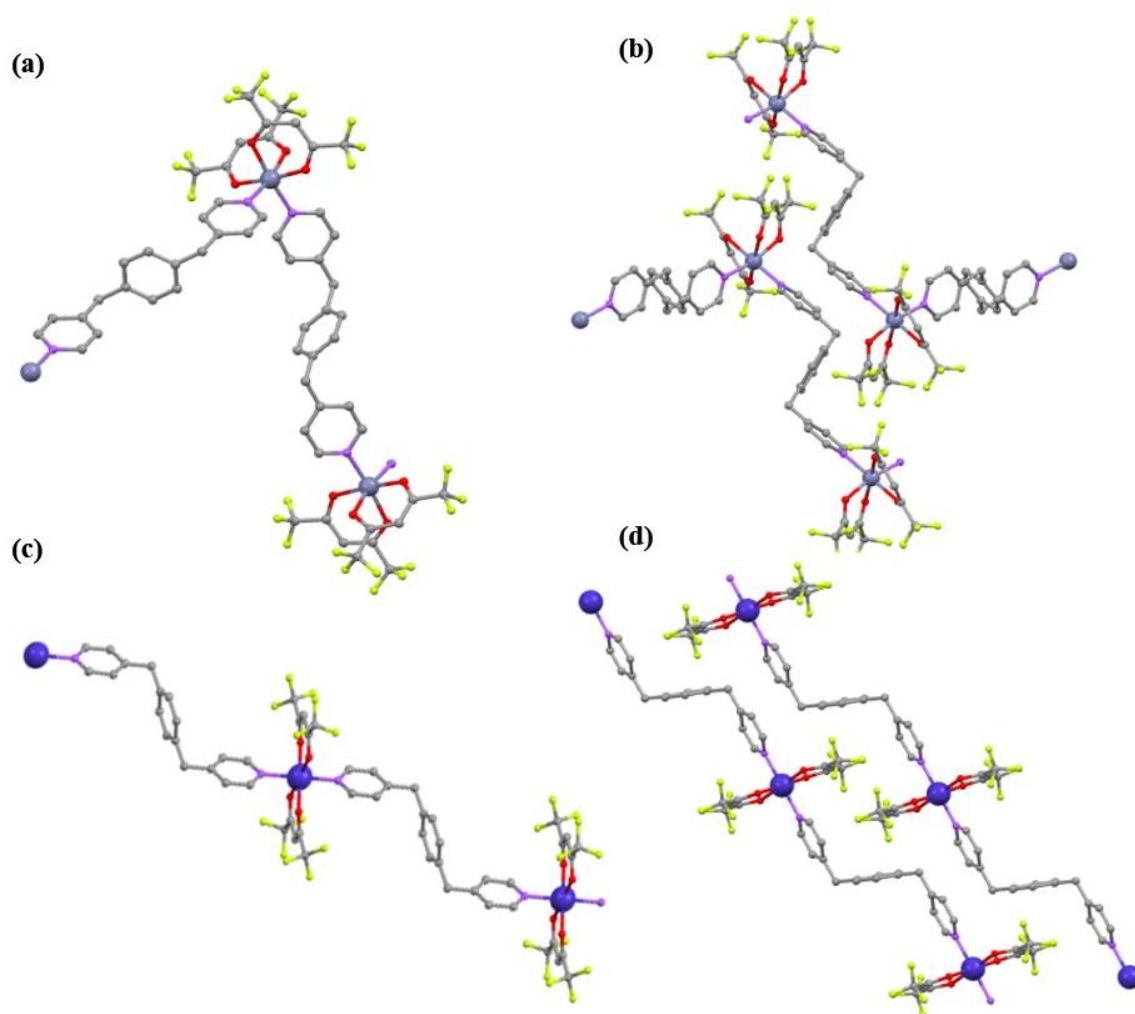
Figure 5.3. Schematic representation of structures: (a,b) A (Zn(1), Co(3), Zn/Co(4)), and (c,d) B Co(2). Color code: C grey, N violet, F yellow, Zn silver and Co blue, H atoms are omitted for clarity.

Structure A: **Zn(1), Co(3) and Zn/Co(4)** crystallize in the triclinic P -1 space group, with unit cell parameters of a=8.900(2), 8.9127(4) and 8.930(7) Å, b=9.8940(13), 9.8610(5) and 9.880(5) Å and c=17.5110(17), 17.5409(9) and 17.570(9) Å, respectively. The crystallographic angles were very similar for the three of them, with values between α=104.4-104.7º, β=96.0-96.4º and γ=97.4-97.5º. For this structure, the asymmetric unit involves an hexacoordinated metal linked to two bpymb (half) molecules and two hfa groups (Fig. 5.3(a)), thus giving a stoichiometry of $[M(hfa)_2(bpymb)]_n$. The two bpymb linkers are located in relative *cis* positions, forming N-M-N angles of 95.0, 89.1 and 91.5º for Zn(1), Co(3) and Zn/Co(4), respectively. As a consequence, the structure extends in zig-zag chains often found in 1D CPs.[50] For all compounds, F···H-C$_{ar}$ and F···F weak interactions are stablished among chains resulting in stable 3D crystals (Fig. 5.3(b)).

Despite the larger covalent radii of Co (1.26 Å) vs. Zn (1.22 Å),[51] the unit cell volumes of the Co(3) and Zn(1) compounds are the practically the same (1464 Å^3). On the other side, the mixed metal compound shows a significantly larger value (1471 Å^3) likely originated by the slim distortion introduced in the network by the presence of two metals with distinct radii.

Structure B: Co(2)) crystallizes in the triclinic P -1 space group, with unit cell parameters of a=8.77040(7) Å, b=9.15990(6) Å and c=10.04300(11) Å, and α=62.9720(6)º, β=71.4100(7)º and γ=80.8890(6)º. As occurs in the isostructural A compounds, the asymmetric unit involves hexacoordinated Co(II) linked to two bpymb molecules and two hfa groups (Fig. 5.3(c)), with a stoichiometry of [M(hfa)$_2$(bpymb)]$_n$. However, in this case the two bpymb linkers are located at *trans* positions, with an N-Co-N angle of 180.0º. The polymer extends in 1D chains, that interacts between them through F···F intermolecular weak bond, and are compactly packed. (Fig. 5.3(d)).

Comparing Co(2) and Co(3) topologies, it becomes evident that the structural differences are mainly originated from the *cis/trans* isomerism of bpymb ligand in the metallic node. The rest of the structure is similar, since in both cases the bpymb linker adopts a Z configuration and the coordination of the Co(II) is completed with two hfa units. This change in the N-Co-N also induces a noticeable variation in the density of the crystal, 1.788 g/cm^3 in Co(2) and 1.664 g/cm^3 in Co(3). In both structures the shorter metal-metal distances are intermolecular ones (~9 Å) while the intra-chain metal-metal distances are larger (~16 Å).

5.3.2. Composition and spatial arrangement of Zn(II) and Co(II) in mixed metal CPs

The phase purities of the different precipitated compounds were confirmed by comparison of routine PXRD patterns and simulated profiles calculated from single crystal structures (Fig. 5.3(a,b)). E.A. data also confirms a stoichiometry of [M(hfa)$_2$bpymb]$_n$ found for all the different compounds (Table 5.2). Quantification of the two metals in the heterometallic compound was performed by ICP-MS in a sample of the Zn/Co(4) phase prepared in scCO$_2$ with a starting molar ratio of Zn(II):Co(II) metals of 0.5:0.5. The measured molar ratio value was of 0.54:0.46 for Zn(II):Co(II). Furthermore, the molar ratio detected by EDS analysis was of 0.51:0.49, coincident with the ICP-MS determined data. Both values were very close to the synthesis added amount of each metal.

The preparation of the heterogeneous CP produces the Zn/Co(4) phase with structure A suggesting that this framework is the thermodynamically most stable, even the phases

involving pure Co(II) might crystallize in different polymorphic crystal lattices depending on the solvent. This behavior was confirmed in an extra experiment performed in scCO$_2$ with an initial molar ratio Zn(II):Co(II) of 20:80. The product was an heterometallic compound with stoichiometry [Zn$_{0.15}$Co$_{0.85}$(hfa)$_2$bpymb]$_n$ and A-type framework. Hence, even a small amount of Zn(II) present in the Co(II) scCO$_2$ solution directs the crystallization to the A structure, instead to B that is the framework found for homometallic Co(2) in this solvent. i.e., the mixture of Zn(II)/Co(II) produces a precipitate with a lattice match phase. One additional advantage of the co-precipitation method is that the metal content of the resulting heterometallic compound can be controlled through varying the molar ratio of the starting mixture.
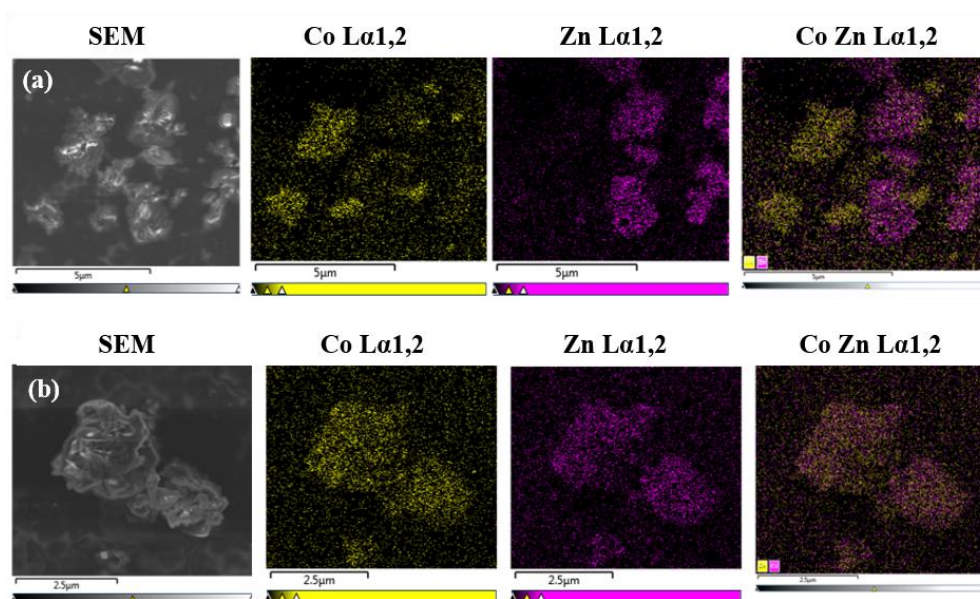

Figure 5.4. EDS mapping of: (a) physical mixture of Zn(1) and Co(3), and (b) Zn/Co(4) sample.

EDS general spectra with nanometric resolution were acquired at different spots of the CPs SEM images to investigate metal distribution. Results of Zn/Co(4) are described in comparison with a physical mixture of the two parent Zn(1) and Co(3) compounds (Fig. 5.4(a)). As an illustrative example, the elemental mapping data obtained for Zn/Co(4) with Zn(II):Co(II) molar ratio 0.5:0.5 is shown in Fig. 5.4(b). The physical mixture displayed Zn(II) and Co(II) segregated in the different homometallic crystal specimens. On the contrary, the mapping of Zn/Co(4) shows an identical distribution of Zn(II) and Co(II) in the analyzed sections, which suggests that both ions are evenly spread throughout the particles. Additionally, the EDS spectrum obtained for one whole particle indicated the production of a phase with equal distribution of both metals, showing intermixing of Zn(II) and Co(II) atoms,

thus confirming the incorporation of both cations within the Zn/Co(4) individual crystals (Fig. 5.5). From an energetic point of view, mixing of metals for heterometallic Zn/Co(4) with framework A seems to be favored energetically when compared to segregating into domains of homometallic MOFs. This behavior has been theoretically demonstrated for other heterometallic MOFs involving Mg/Ni and Mg/Cd.[52]
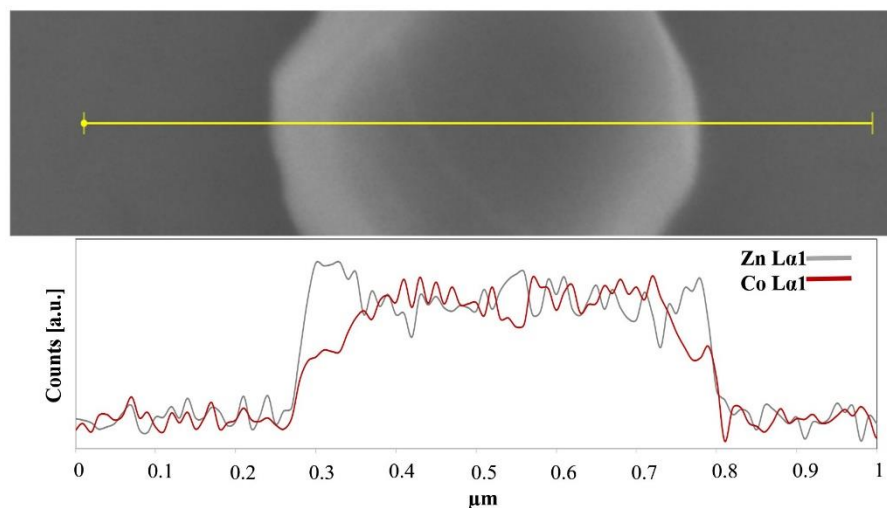

Figure 5.5. Line scan performed by EDS in a single crystal of the Zn/Co(4) sample.

5.3.3. Surface analysis

XPS is a powerful tool to collate information on the chemical compositions of materials surface, their coordination chemistry and degradation behavior. Moreover, the technique has also been proposed to help on the detection of the spatial position of the different metals in heterometallic CPs. For compounds with an even distribution of metals, the coordination environment of each cation would be influenced by the presence of adjacent metals of different characteristics. Hence, significant shifts in the binding energies would be observed in the mixed metal compound compared to the corresponding isostructural homometalic products. However, most of the described scenarios did not display any shift in the binding energy of the metals, indicating that the heterometallic compound is constituted by multidomain single-crystals. For them, the interaction between the two kinds of metals is negligible and thus not shown by XPS. This is the case for the samples studied in this work (Fig. 5.6).
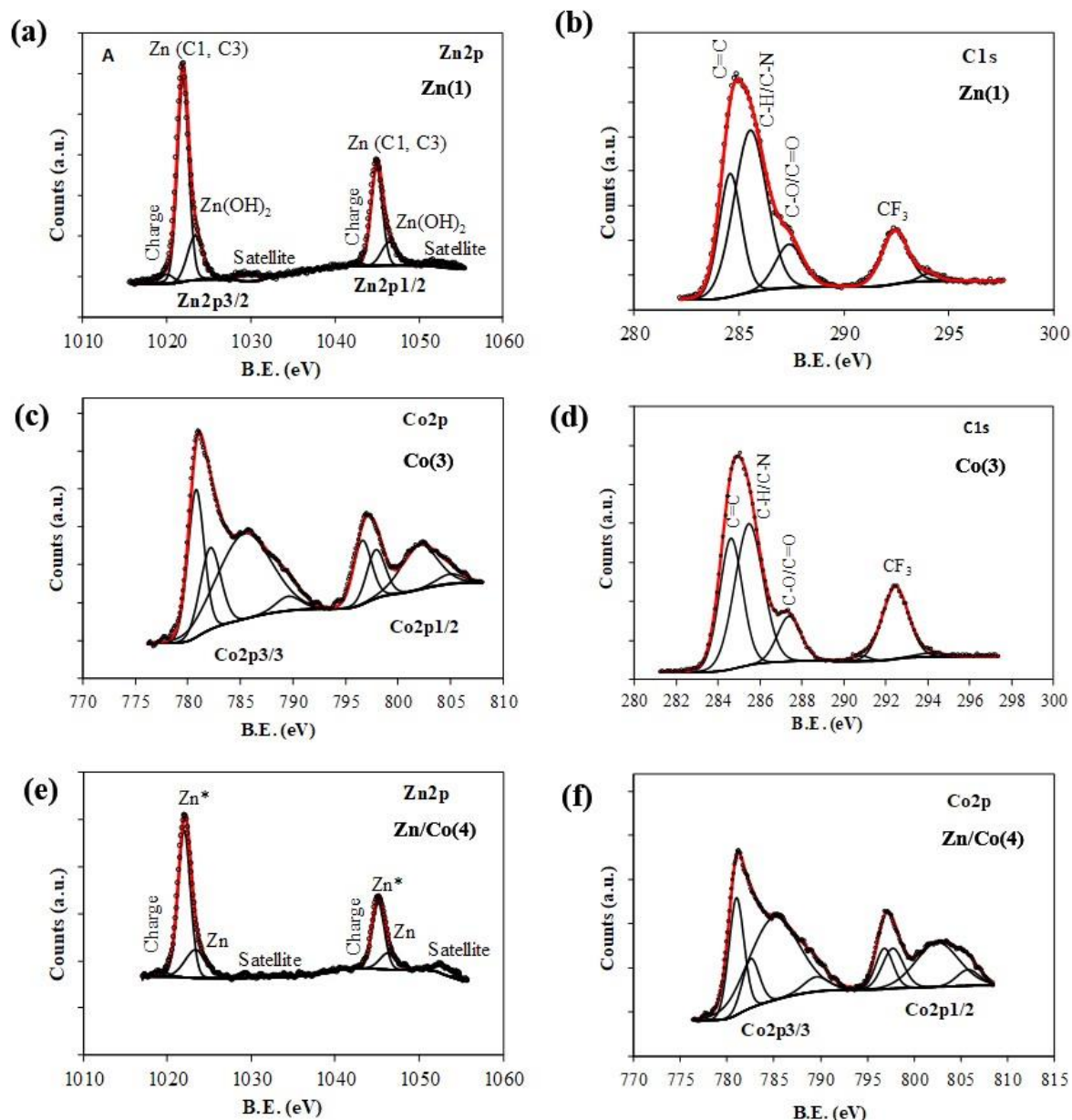
Figure 5.6. XPS regions for: (a) Zn2p and (b) C1s in Zn(1) sample, (c) Co2p and (d) C1s in Co(3) sample, and (e) Zn2p and (f) Co2p in Zn/Co(4) sample.

The clarest spectra was the one obtained for Zn(1) sample, obtained in $scCO_2$, in which the low binding energy peak in the Zn2p3/2 region was placed at 1021.9 eV. The same peak for the Zn/Co(4) sample, crystallized in $scCO_2$, appeared at 1022.1 eV, i.e., with a negligible binding energy shift. The deconvolutions peaks for the Co2p3/2 sub-region were also similar in the Co(3) and Zn/Co(4) sample. The analysis of the total amount of Zn(II) and Co(II) in an equimolar Zn/Co(4) sample indicated a surface rich in Co(II), with a Zn(II):Co(II) molar ratio of 0.38:0.62. In $scCO_2$, this fact likely reflects the faster nucleation of the Zn(II) phase with

respect to the isostructural Co(II) phase, since in this fluid the most stable product for homometallic Co(II) solutions was always the Co(2) phase with framework B.

Moreover, it is worth to mention that surface changes during XPS measurements are often observed due to partial degradation of the surface.[53] For the compounds synthetized in this work, an evident change of color was observed as a function of the measurement time, which was as clear indication of the degradation process provoked by the X-ray radiation. A quantitative analysis performed on the basis of the percentage of the different atoms in each sample (Table 5.4) allows to estimate that the percentage of surface degradation was higher than 50 mol% for the three studied samples Zn(1), Co(3) and Zn/Co(4).

Table 5.4. XPS atomic surface composition of the different studied samples.

	Zn(1)	**Co(3)**	**Zn/Co(4)**
Metal	Zn 3.4	Co 2.5	Zn 1.3 Co 2.1
C	59.1	53.5	56.2
O	8.3	8.4	10.4
N	4.2	3.7	3.0
F	25.0	31.9	26.9
C/N	14.1	14.3	18.6
O/N	2.0	2.2	3.5
C/Metal	17.5	21.6	16.4
F/N	5.9	8.5	8.9

5.3.4. Magnetic properties

The objective of using co-precipitation for the shaping of heterometallic products is to obtain structures that ensure homogeneous properties throughout the whole material. This can be achieved either by complete mixing of metals occupying statistically the node positions or by forming small monometallic domains within the framework. Experimental proofs of random incorporation are not straightforward. On one hand, SCXRD technique offers limited information in deciphering the spatial arrangement of Zn(II) and Co(II) components in the heterometallic structure, since the two metals are close enough in the periodic table to have too low X-ray diffusion contrast to be distinguished. On the other hand, EDS mapping has nanometric, but not atomic, resolution. Studying a specific property can be an indirect method to assess the type of metals distribution (ordered or randomly). Indeed, Co(II) is a common metal used in CPs for the magnetic properties. Hence, the comparison of the magnetic

properties of homometallic and the heterometallic CPs involving Co(II) can give some information of products structure. In this work, the alternating current magnetic susceptibility of the three new CPs containing Co(II) were analyze by a SQUID at low temperatures. The preliminary results suggest that the isoestrucural Co(3) and Zn/Co(4) CPs have very similar magnetic properties. The results for Co(2) are less consistent, since the analyzed samples by XRD undicated a mixing of phases, i.e., Co(2) and Co(3) in different proportions.

The magnetic susceptibility curves (χT) *vs.* temperature (T) and magnetization vs. HT^{-1} (H= external magnetic field) for Co(3) and Zn/Co(4) were similar (Figs 5.7 and 5.8). A Co(II) ion in octahedral symmetry and weak crystal field usually has an important first order spin orbit coupling (SOC) and can be described with the first order SOC Hamiltonian. However, at low temperatures only the two lowest Kramers doublets (KD) will be populated and, phenomenologically, the zero field splitting (ZFS) Hamiltonian can be used to study the magnetic properties of these compounds, facilitating their study and comparison with other published compounds. The ZFS Hamiltonian, as implemented in the PHI package,[54] was employed for the simultaneous fit of the experimental susceptibility and magnetization curves (eq. 5.1).

$$\hat{H} = \frac{D}{3}\,\hat{O}_k^q \,+\, E\hat{O}+ \mu_B(g_x\hat{S}_xB_x+g_y\hat{S}_xB_y+g_z\hat{S}_zB_z) \qquad \text{(eq. 5.1)}$$

where S is the spin (and their spin operators), D is the axial anisotropy, E the rhombic anisotropy, μ_B is the Bohr magneton, B is the magnetic field vector and $\hat{O}_k^q$ is the equivalent Stevens operator. The first two terms are related to the crystal-field Hamiltonian (following the operator equivalent technique),[55] and the last term is connected to the Zeeman Hamiltonian.[56] The parameters D, E, and g were selected to correlate the data and for comparison with published results. Both phases Co(3) and Zn/Co(4) showed preliminary similar positive ZFS anisotropy (D > 0), which has been already observed in other SMMs of Co(II).[57] Co(3) has a D of 46 cm^{-1}, an E of 10 cm^{-1} and a g of 2.5. For the heterometallic Zn/CO(4) compound, these values were estimated as D=55 cm^{-1}, E=13 cm^{-1} and g=2.4. The obtained D values are similar to other published values for Co(II) CPs.[58]
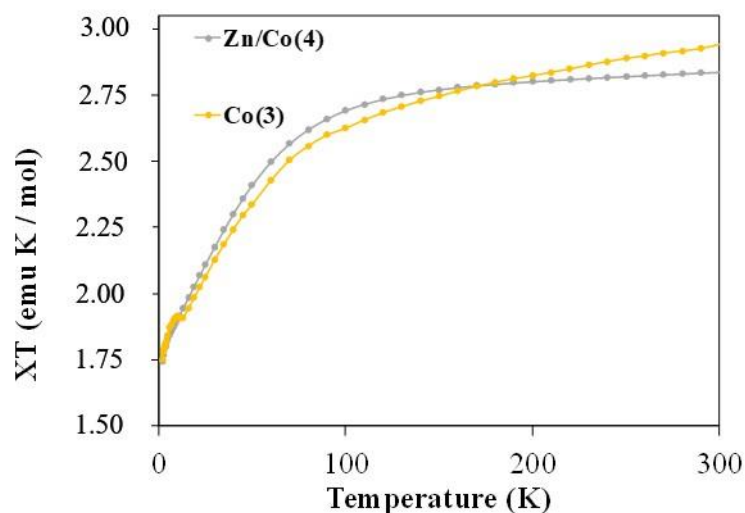
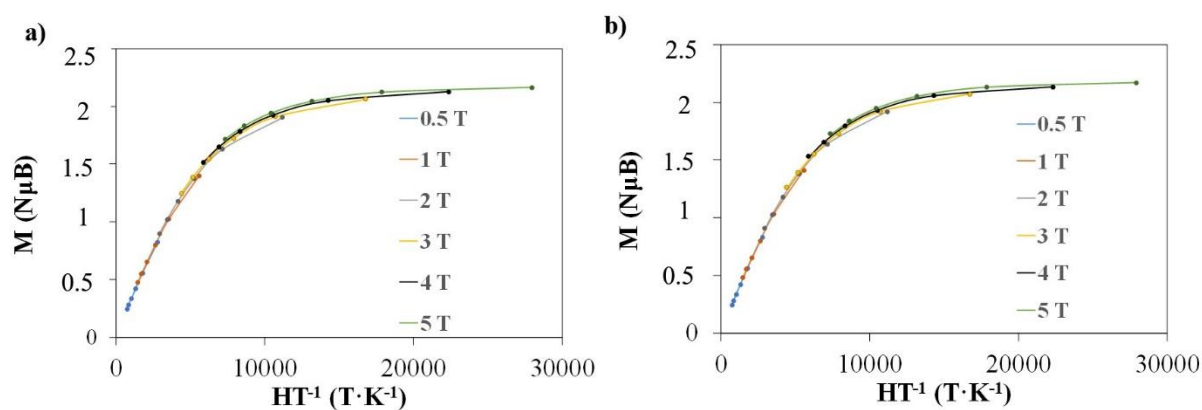**Figure 5.7**. Magnetic susceptibility curve for Co(3) and Zn/Co(4).

Figure 5.8. Magnetization *vs.* HT^{-1} curve for: (a) Zn/Co(4), and (b) Co(3). Lines indicate fitting values and dots experimental values.
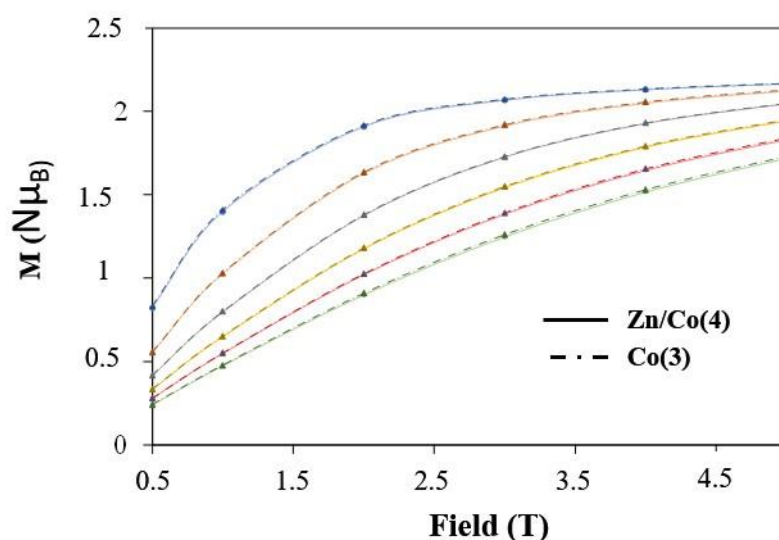

Figure 5.9. Comparison of magnetization for Co(3) and Zn/Co(4).

Dynamic magnetic measurements showed also a similar behavior for Co(3) and Zn/Co(4), depending on the temperature and the field (Figs 5.10 and 5.11) in regard of the imaginary part of the magnetic susceptibility. These results show that in both cases the new CPs possess a SMM behavior. For both isoestructural CPs the relaxation times presented the same tendency (Fig 5.12).
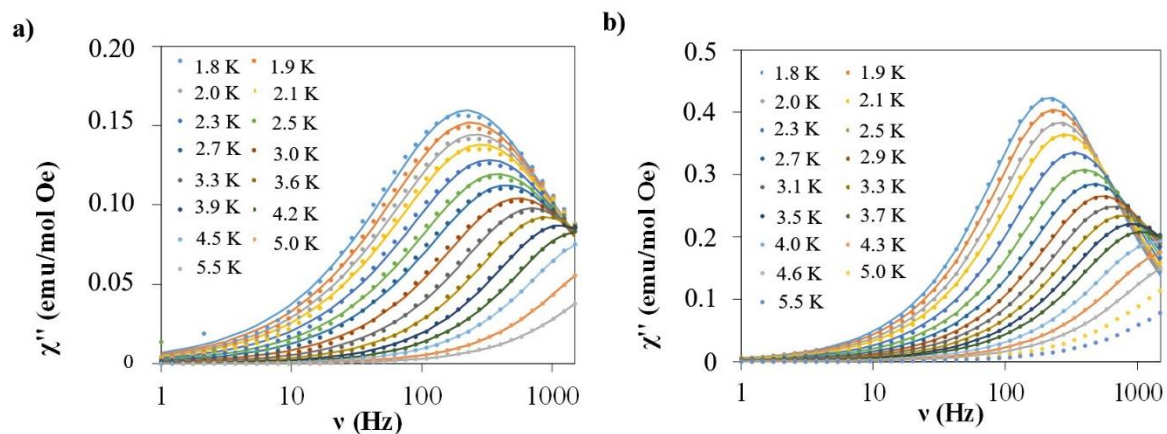

Figure 5.10. Representation of the dependency of the imaginary magnetic susceptibility *vs.* temperature at different temperatures and 1500 Oe: (a) Zn/Co(4), and (b) Co(3).
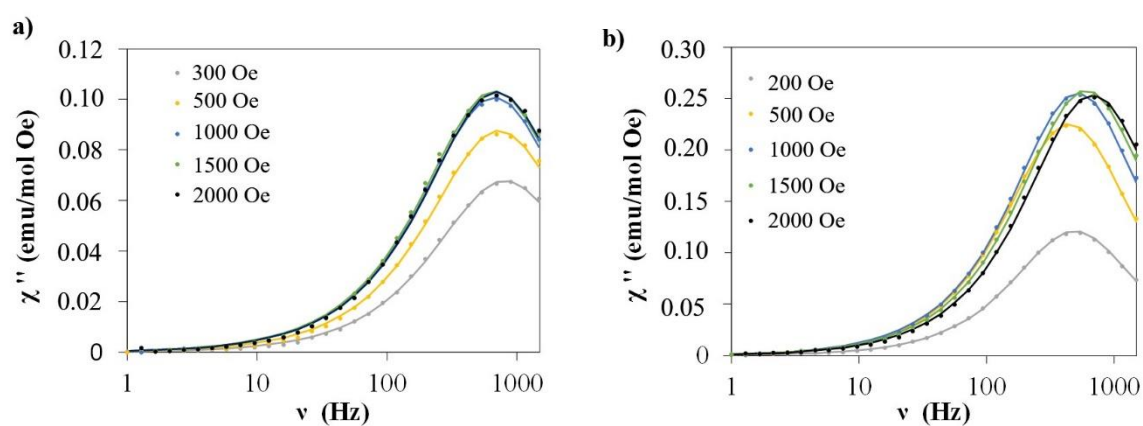

Figure 5.11. Representation of the dependency of the imaginary magnetic susceptibility *vs.* frequency at different temperatures and 3.5 K: (a) Zn/Co(4) and (b) Co(3).
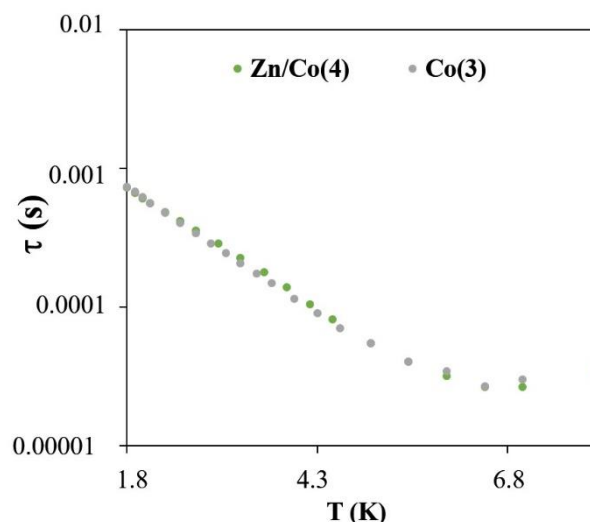
Figure 5.12. Comparison of relaxation time vs. temperature for Zn/Co(4) and Co(3).

The addition of a diamagnetic metal in the framework, sometimes called magnetic dilution, has been demonstrated to be a good method to increase the relaxation time in SMM due principally to the decrease of dipolar interactions.[59,60] In this case, the addition of zinc in a framework of cobalt did not produce significant differences. The intermolecular and intramolecular distance between the cobalt centers of the same chain and between cobalt units of different chains were already large enough and, therefore, the addition of the diamagnetic ion did not provide significant differences in the magnetic behavior.[60,61] Unfortunately, with these magnetic results, it is not possible to ascertain the distribution of the metals inside the framework, e.g., random or ordered.

5.4. Conclusions

This work involves the synthesis and characterization of novel homometallic and heterometallic coordination polymers. Specifically, CPs with a large bipyridine molecule and cobalt and/or zinc metal complex were synthetized in $scCO_2$ and ethanol. Two different group of phases were structurally elucidated. The first group involves isostructural Zn(1), Co(3) and Zn/Co(4), structures that situtate the linkers in *cis* position in the metal. The second involves Co(2), with the linkers in *trans*. Crystallographicalle, it has not been possible to localize the exact possition in the netwrek of each metal in heterometallic compounds. However, isostructural compounds involving Co(II), i.e., Co(3) and Zn/Co(4) present interesting magnetic properties, since they have a SMM behavior. Both CPs have similar magnetic properties, with good anisotropic D values. This study suggests that the distances between

cobalts are long enough in the structure, so an increase of the magnetic properties in the heterometallic CP was not observed after Zn(II) addition. These results open a window to design more complex frameworks, 2D or 3D with more than one metal following the same procedure.
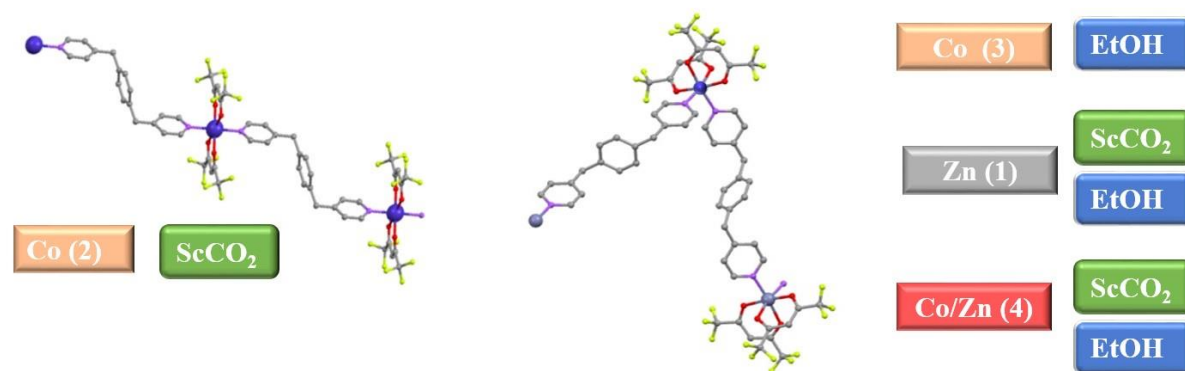

Figure 5.13. Schematic representation of *trans* and *cis* molecular arrangement for $[Co/Zn(hfa)_2(bpymb)]_n$ CPs synthetized in scCO$_2$ and EtOH.

5.5. References

(1) Furukawa, H.; Müller, U.; Yaghi, O. M. "Heterogeneity within order" in metal-organic frameworks. *Angew. Chemie Int. Ed.,* **2015**, *54* (11), 3417-3430.

(2) Dhakshinamoorthy, A.; Asiri, A. M.; Garcia, H. Mixed-metal or mixed-linker metal organic frameworks as heterogeneous catalysts. *Catal. Sci. Technol.,* **2016**, *6* (14), 5238-5261.

(3) Tu, B.; Pang, Q.; Ning, E.; Yan, W.; Qi, Y.; Wu, D.; Li, Q. Heterogeneity within a mesoporous metal–organic framework with three distinct metal-containing building units. *J. Am. Chem. Soc.,* **2015**, 137 (42), 13456-13459.

(4) Ghoshal, D.; Ghosh, A. K.; Maji, T. K.; Ribas, J.; Mostafa, G.; Zangrando, E.; Ray Chaudhuri, N. Different topologies in heterometallic frameworks of copper(II) with bridging ligand: syntheses, crystal structures, thermal and magnetic properties. *Inorganica Chim. Acta,* **2006**, *359* (2), 593-602.

(5) Yuan, S.; Qin, J.-S.; Li, J.; Huang, L.; Feng, L.; Fang, Y.; Lollar, C.; Pang, J.; Zhang, L.; Sun, D.; Alsalme, A.; Cagin, T.; Zhou, H.-C. Retrosynthesis of multi-component metal-organic frameworks. *Nat. Commun.,* **2018**, *9* (1), 808.

(6) Wang, Y.; Bredenkötter, B.; Rieger, B.; Volkmer, D. Two-dimensional metal-organic frameworks (MOFs) constructed from heterotrinuclear coordination units and 4,4′-biphenyldicarboxylate ligands. *Dalton Trans.,* **2007**, No. 6, 689-696.

(7) He, X.; Lu, C.-Z.; Yuan, D.-Q. Two 3D porous cadmium tetrazolate frameworks with hexagonal tunnels. *Inorg. Chem.,* **2006**, *45* (15), 5760-5766.

(8) Zhang, Y.; Chen, B.; Fronczek, F. R.; Maverick, A. W. A Nanoporous Ag-Fe mixed-metal-organic framework exhibiting single-crystal-to-single-crystal transformations upon guest exchange. *Inorg. Chem.,* **2008**, *47* (11), 4433-4435.

(9) Furukawa, S.; Hirai, K.; Nakagawa, K.; Takashima, Y.; Matsuda, R.; Tsuruoka, T.; Kondo, M.; Haruki, R.; Tanaka, D.; Sakamoto, H.; Shimomura, S.; Sakata, O.; Kitagawa, S. Heterogeneously hybridized porous coordination polymer crystals: fabrication of heterometallic core-shell single crystals with an in-plane rotational epitaxial relationship. *Angew. Chemie Int. Ed.,* **2009**, *48* (10), 1766-1770.

(10) Lee, H. J.; Cho, Y. J.; Cho, W.; Oh, M. Controlled isotropic or anisotropic nanoscale growth of

coordination polymers: formation of hybrid coordination polymer particles. *ACS Nano,* **2013**, *7* (1), 491-499.

(11) Sibille, R.; Mazet, T.; Malaman, B.; Wang, Q.; Didelot, E.; François, M. Site-dependent substitutions in mixed-metal metal-organic frameworks: a case study and guidelines for analogous systems. *Chem. Mater.,* **2015**, *27* (1), 133-140.

(12) Tanasaro, T.; Adpakpang, K.; Ittisanronnachai, S.; Faungnawakij, K.; Butburee, T.; Wannapaiboon, S.; Ogawa, M.; Bureekaew, S. Control of polymorphism of metal-organic frameworks using mixed-metal approach. *Cryst. Growth Des.,* **2018**, *18* (1), 16-21.

(13) Wang, L. J.; Deng, H.; Furukawa, H.; Gándara, F.; Cordova, K. E.; Peri, D.; Yaghi, O. M. Synthesis and characterization of metal-organic framework-74 containing 2, 4, 6, 8, and 10 different metals. *Inorg. Chem.,* **2014**, *53* (12), 5881-5883.

(14) Carson, C. G.; Ward, J.; Liu, X. T.; Schwartz, J.; Gerhardt, R. A.; Tannenbaum, R. Dopant-controlled crystallization in metal-organic frameworks: the role of copper(II) in zinc 1,4-benzenedicarboxylate. *J. Phys. Chem. C,* **2012**, *116* (29), 15322-15328.

(15) Kim, M.; Cahill, J. F.; Fei, H.; Prather, K. A.; Cohen, S. M. Postsynthetic ligand and cation exchange in robust metal–organic frameworks. *J. Am. Chem. Soc.,* **2012**, *134* (43), 18082-18088.

(16) Brozek, C. K.; Dincă, M. Ti^{3+}, $V^{2+/3+}$, $Cr^{2+/3+}$, Mn^{2+}, and Fe^{2+} substituted MOF-5 and redox reactivity in Cr- and Fe-MOF-5. *J. Am. Chem. Soc.,* **2013**, *135* (34), 12886-12891.

(17) Das, S.; Kim, H.; Kim, K. Metathesis in single crystal: complete and reversible exchange of metal ions constituting the frameworks of metal-organic frameworks. *J. Am. Chem. Soc.,* **2009**, *131* (11), 3814-3815.

(18) Hon Lau, C.; Babarao, R.; Hill, M. R. A route to drastic increase of CO_2 uptake in Zr metal organic framework UiO-66. *Chem. Commun.,* **2013**, *49* (35), 3634.

(19) Song, X.; Kim, T. K.; Kim, H.; Kim, D.; Jeong, S.; Moon, H. R.; Lah, M. S. Post-synthetic modifications of framework metal ions in isostructural metal-organic frameworks: core-shell heterostructures via selective transmetalations. *Chem. Mater.,* **2012**, *24* (15), 3065-3073.

(20) Song, X.; Jeong, S.; Kim, D.; Lah, M. S. Transmetalations in two metal-organic frameworks with different framework flexibilities: kinetics and core-shell heterostructure. *CrystEngComm.,* **2012**, *14* (18), 5753.

(21) Lee, W. R.; Ryu, D. W.; Phang, W. J.; Park, J. H.; Hong, C. S. Charge effect of foreign metal ions and the crystal growth process in hybridized metal-organic frameworks. *Chem. Commun.,* **2012**, *48* (88), 10847.

(22) Fei, H.; Cahill, J. F.; Prather, K. A.; Cohen, S. M. Tandem postsynthetic metal ion and ligand exchange in zeolitic imidazolate frameworks. *Inorg. Chem.,* **2013**, *52* (7), 4011-4016.

(23) Sun, D.; Sun, F.; Deng, X.; Li, Z. Mixed-metal strategy on metal-organic frameworks (MOFs) for functionalities expansion: Co substitution induces aerobic oxidation of cyclohexene over inactive Ni-MOF-74. *Inorg. Chem.*, **2015**, *54* (17), 8639-8643..

(24) Tang, J.; Salunkhe, R. R.; Liu, J.; Torad, N. L.; Imura, M.; Furukawa, S.; Yamauchi, Y. Thermal Conversion of core-shell metal-organic frameworks: a new method for selectively functionalized nanoporous hybrid carbon. *J. Am. Chem. Soc.,* **2015**, *137* (4), 1572-1580.

(25) Chen, Y.-Z.; Wang, C.; Wu, Z.-Y.; Xiong, Y.; Xu, Q.; Yu, S.-H.; Jiang, H.-L. From bimetallic metal-organic framework to porous carbon: high surface area and multicomponent active dopants for excellent electrocatalysis. *Adv. Mater.,* **2015**, *27* (34), 5010-5016.

(26) Saliba, D.; Ammar, M.; Rammal, M.; Al-Ghoul, M.; Hmadeh, M. Crystal growth of ZIF-8, ZIF-67, and their mixed-metal derivatives. *J. Am. Chem. Soc.,* **2018**, *140* (5), 1812-1823.

(27) Hillman, F.; Zimmerman, J. M.; Paek, S.-M.; Hamid, M. R. A.; Lim, W. T.; Jeong, H.-K. Rapid microwave-assisted synthesis of hybrid zeolitic-imidazolate frameworks with mixed metals and mixed linkers. *J. Mater. Chem. A,* **2017**, *5* (13), 6090-6099.

(28) Ricco, R.; Malfatti, L.; Takahashi, M.; Hill, A. J.; Falcaro, P. Applications of magnetic metal-organic framework composites. *J. Mater. Chem. A,* **2013**, 1 (42), 13033.

(29)Jeon, I.-R.; Clérac, R. Controlled association of single-molecule magnets (SMMs) into coordination networks: towards a new generation of magnetic materials. *Dalton Trans.*, **2012**, 41 (32), 9569.

(30) Dey, A.; Das, S.; Kundu, S.; Mondal, A.; Rouzières, M.; Mathonière, C.; Clérac, R.; Suriya Narayanan, R.; Chandrasekhar, V. Heterometallic heptanuclear [Cu$_5$Ln$_2$] (Ln = Tb, Dy, and Ho) Single-Molecule Magnets Organized in One-Dimensional Coordination Polymeric Network. *Inorg. Chem.*, **2017**, 56 (23), 14612-14623.

(31) Alexandru, M.-G.; Visinescu, D.; Shova, S.; Lloret, F.; Julve, M.; Andruh, M. Two-dimensional coordination polymers constructed by [Ni^{II}Ln^{III}] Nodes and [W^{IV}(Bpy)(CN)$_6$]$^{2-}$ spacers: a network of [Ni^{II}Dy^{III}] single molecule magnets. *Inorg. Chem.*, **2013**, 52 (23), 11627-11637.

(32) Habib, F.; Korobkov, I.; Murugesu, M. Exposing the intermolecular nature of the second relaxation pathway in a mononuclear cobalt(II) single-molecule magnet with positive anisotropy. *Dalton Trans.*, **2015**, 44, 6368-6373.

(33) Andruh, M.; Costes, J.-P.; Diaz, C.; Gao, S. 3D-4F combined chemistry: synthetic strategies and magnetic properties. *Inorg. Chem.*, **2009**, 48 (8), 3342-3359.

(34) Dey, A.; Das, S.; Palacios, M. A.; Colacio, E.; Chandrasekhar, V. Single-molecule magnet and magnetothermal properties of two-dimensional polymers containing heterometallic [Cu^{5}Ln^2] (Ln= Gd^{III}and Dy^{III}) Motifs. *Eur. J. Inorg. Chem.*, **2018**, (15), 1645-1654.

(35) Campo, J.; Falvello, L. R.; Forcén-Vázquez, E.; Sáenz De Pipaón, C.; Palacio, F.; Tomás, M. A Symmetric, Triply Interlaced 3-D Anionic MOF that exhibits both magnetic order and SMM behaviour. *Dalton Trans.*, **2016**, 45 (42), 16764-16768.

(36) Zhu, Y. Y.; Zhu, M. S.; Yin, T. T.; Meng, Y. S.; Wu, Z. Q.; Zhang, Y. Q.; Gao, S. Cobalt(II) coordination polymer exhibiting single-ion-magnet-type field-induced slow relaxation behavior. *Inorg. Chem.*, **2015**, 54 (8), 3716–3718.

(37) Ion, A. E.; Nica, S.; Madalan, A. M.; Shova, S.; Vallejo, J.; Julve, M.; Lloret, F.; Andruh, M. Two-dimensional coordination polymers constructed using, simultaneously, linear and angular spacers and cobalt(II) nodes. new examples of networks of single-ion magnets. *Inorg. Chem.*, **2015**, 54 (1), 16-18.

(38) Zhu, Y. Y.; Yin, T. T.; Liu, C. W.; Gao, C.; Wu, Z. Q.; Zhang, Y. Q.; Wang, B. W.; Gao, S. field-induced slow magnetic relaxation in a hydrogen-bonding linked Co(II) 1D supramolecular coordination polymer. *Supramol. Chem.*, **2014**, 27 (II), 401-406..

(39) Brunet, G.; Safin, D. A.; Jover, J.; Ruiz, E.; Murugesu, M. Single-molecule magnetism arising from cobalt(II) nodes of a crystalline sponge. *J. Mater. Chem. C*, **2017**, 5 (4), 835-841.

(40) Ganivet, C. R.; Ballesteros, B.; De La Torre, G.; Clemente-Juan, J. M.; Coronado, E.; Torres, T. Influence of peripheral substitution on the magnetic behavior of single-ion magnets based on homo- and heteroleptic Tb^{III}bis(phthalocyaninate). *Chem. - A Eur. J.*, **2013**, 19 (4), 1457-1465.

(41) Jiang, S. Da; Wang, B. W.; Su, G.; Wang, Z. M.; Gao, S. A Mononuclear dysprosium complex featuring single-molecule-magnet behavior. *Angew. Chemie - Int. Ed.*, **2010**, 49 (41), 7448-7451.

(42) Gatteschi, D.; Sessoli, R.; Villain, J. Molecular nanomagnets. Oxford University Press, **2006**.

(43) Juanhuix, J.; Gil-Ortiz, F.; Cuní, G.; Colldelram, C.; Nicolás, J.; Lidón, J.; Boter, E.; Ruget, C.; Ferrer, S.; Benach, J. Developments in optics and performance at BL13-XALOC, the macromolecular crystallography beamline at the ALBA synchrotron. *J. Synchrotron Radiat.*, **2014**, 21 (4), 679-689.

(44) Kabsch, W. XDS. *Acta Crystallogr. Sect. D Biol. Crystallogr.*, **2010**, 66 (2), 125-132.

(45) Sheldrick, G. M. Crystal Structure Refinement with SHELXL. *Acta Crystallogr. Sect. C Struct. Chem.*, **2015**, 71 (1), 3-8.

(46) Dolomanov, O. V.; Bourhis, L. J.; Gildea, R. J.; Howard, J. A. K.; Puschmann, H. OLEX2 : a complete structure solution, refinement and analysis program. *J. Appl. Crystallogr.*, **2009**, 42 (2), 339-341.

(47) Sheldrick, G. M. A short history of SHELX. *Acta Cryst. A,* **2008**, 64, 112-122.

(48) Fauth F., Peral I., Popescu C. and Knapp M., "The new material science powder diffraction beamline at ALBA synchrotron," *Powder Diffraction,* **2013***,* 28,2, 360-370.

(49) Teoh, W. H.; Mammucari, R.; Foster, N. R. Solubility of organometallic complexes in supercritical carbon dioxide: a review. *J. Organomet. Chem.,* **2013***, 724*, 102-116.

(50) Leong, W. L.; Vittal, J. J. One-dimensional coordination polymers: complexity and diversity in structures, properties, and applications. *Chem. Rev.,* **2011***, 111* (2), 688-764.

(51) Cordero, B.; Gómez, V.; Platero-Prats, A. E.; Revés, M.; Echeverría, J.; Cremades, E.; Barragán, F.; Alvarez, S. Covalent radii revisited. *Dalton Trans.,* **2008**, No. 21, 2832-2838.

(52) Howe, J. D.; Morelock, C. R.; Jiao, Y.; Chapman, K. W.; Walton, K. S.; Sholl, D. S. Understanding structure, metal distribution, and water adsorption in mixed-metal MOF-74. *J. Phys. Chem. C,* **2017**, *121* (1), 627-635.

(53) Cano, A.; Lartundo-Rojas, L.; Shchukarev, A.; Reguera, E. Contribution to the coordination chemistry of transition metal nitroprussides: a cryo-XPS study. *New J. Chem.,* **2019**, *43* (12), 4835-4848.

(54) Chilton, Nicholas F.; Anderson, R.P.; Turner, L.D.; Soncini, A.; Murray, K.S. PHI: A powerful new program for the analysis of anisotropic monomeric and exchange-coupled polynuclear d- and f-block complexes. *Journal of Computational Chemistry*, **2013**, 34, 1164-1175.

(55) Gomez-Coca, S.; Cremades, E.; Aliaga-Alcalde, N.;´ Ruiz, E. Huge magnetic anisotropy in a trigonal-pyramidal nickel(II) complex. *Inorg. Chem.,* **2014**, 53, 676-678.

(56) Abragam, A.; Bleaney, B. Electron paramagnetic resonance of transition ions. Oxford University Press: Oxford, U.K., **1970**.

(57) Gómez-Coca, S.; Urtizberea, A.; Cremades, E.; Alonso, P. J.; Camón, A.; Ruiz, E.; Luis, F. Origin of slow magnetic relaxation in Kramers ions with non-uniaxial anisotropy. *Nature Communications,* **2014**, 5, 4300.

(58) Wu, Y.; Tian, D.; Ferrando-Soria, J.; Cano, J.; Yin, L.; Ouyang, Z.; Wang, Z.; Luo, S.; Liu X.; Pardo, E. Modulation of the magnetic anisotropy of octahedral cobalt(II) single-ion magnets by finetuning the axial coordination microenvironment. *Inorg. Chem.Front*., **2019**, 6, 848-856.

(59) Upadhyay, A.; Singh, S. K.; Das, C.; Mondol, R.; Langley, S. K.; Murray, K. S.; Rajaraman, G.; Shanmugam, M. Enhancing the effective energy barrier of a Dy(III) SMM using a bridged diamagnetic Zn(II) ion. *Chem. Commun*., **2014**, 50, 8838-8841.

(60) Oyarzabal,I.; Ruiz, J.; Seco, J. M.; Evangelisti, M.; Camón, A.; Ruiz, E.; Aravena, D.; Colacio, E. Rational electrostatic design of easy-axis magnetic anisotropy in a Zn^{II}–Dy^{III}–Zn^{II} single-molecule magnet with a high energy barrier. *Chem. - A Eur. J*., **2014**, 20, 14262-14269.

(61) Zhu, Y. Y.; Zhu, M. S.; Yin, T. T.; Meng, Y. S. Wu, Z. Q.; Zhang Y. Q.; Gao, S. Cobalt(II) coordination polymer exhibiting single-ion-magnet-type field-induced slow relaxation behavior. *Inorg. Chem.,* **2015**, 54,8, 3716-3718.

(62) Rinehart, J. D.; Long, J. R. Slow magnetic relaxation in homoleptic trispyrazolylborate complexes of neodymium(III) and uranium(III). *Dalton Trans.,* **2012**, 41, 13572-13574.

CHAPTER-6

Tunable synthesis of 3-tpt CPs

CHAPTER 6 describe an original, sustainable and scalable process for the preparation of diverse coordination polymers involving Cu(II) as the metal center and 2,4,6-tris(3-pyridyl)-1,3,5-triazine (3-tpt) as the organic linker. This work shows that the structural richness of coordination polymers is not only attained through the selection of the metal node and linker, but also by the synthetic conditions while keeping the reagents untouched. Hence, the use of three different polarity solvents (scCO$_2$, EtOH and CHCl$_3$) allowed the crystallization of five new Cu(II) compounds (**1-5**), with different Cu(II)/3-tpt ratios, e.g., 1, 1.5 and 2, from which the crystal structures were elucidated. Moreover, a reversible phase transition has been observed among two phases, with unprecedented control of the 3-tpt conformation.

6.1. Introduction

The richness of metal-organic linker combinations allows for the design of a large variety of metal-organic frameworks (MOFs), also known as coordination polymers (CPs), with different structures and properties. These materials are proposed for numerous applications, such as those related to adsorption, catalysis and biomedicine.[1,2] With the ability of modifying the organic linker, either by extending the molecular size or by varying the isomer conformation, the topology, pore size and channel structure of the MOFs can be tuned. For the last years, our research group has been working on the green and scalable synthesis of a series of 1D and 2D bipyridine-based MOFs.[3-5] As a logical extension of this work, trigonal polypyridyl connectors of the type 2,4,6-tris(n-pyridyl)-1,3,5-triazine (n-tpt with n=2, 3 or 4) are used in this study as linkers in the construction of new MOFs. The n-tpt molecule is considered a remarkable building block in supramolecular chemistry, since it can support different types of interactions, namely coordination, hydrogen bond and electrostatic attraction, while also favoring aromatic stacking and $\pi-\pi$ contacts.[6] The growing interest in the synthesis of MOFs containing n-tpt units is related to its core's planar geometry ideally suited to generate highly symmetrical structures. A clear example is the 4-tpt linker, with exclusively 3-fold symmetry, widely used in MOFs chemistry.[7] The 2-tpt isomer can be organized in a symmetric or asymmetric conformation,[8] even though the asymmetric conformation is the only one observed in crystal structures involving metals.[9] The 3-tpt linker has been barely used in coordination chemistry, since it can afford arbitrary isomerism by virtue of 180º rotation on inter-ring C-C bonds (A and B isomers; left of Fig. 6.1). The asymmetric conformation has emerged in macrocycles, cages and capsules constructed by reaction with transition metals;[10-13] in metal salts involving triply protonated units[14] and in some polymeric structures.[15,16] Few 1D and 3D MOFs have been described involving either 3-tpt conformation.[17-19]

The isomerism makes the synthesis and characterization of well-defined complexes or coordination networks involving 3-tpt linker quite difficult. The main objective of this work is to extend and organize the knowledge in the use of 3-tpt as a linker for MOFs synthesis, modulated through selecting proper experimental parameters, i.e., solvent polarity. Moreover, considerable attention is paid to develop sustainable synthetic methods using green solvents, such as ethanol (EtOH) or supercritical carbon dioxide (scCO$_2$),[20-22] and low toxicity metal acetylacetonate (hexafluoroacetylacetonate (Cu(hfa)$_2$)) nodes.[23] Five new structures involving

infinite arrays of self-assembled 3-tpt and Cu(hfa)$_2$ units were straightforwardly crystallized. All of them were crystallographycally solved, resulting in three 1D and two 2D products. One of these 1D structures has a significant porosity with a flexible behavior induced by N$_2$ adsorption. Solvent phase transition between compounds was finally revised, giving the key parameters to control the isomeric conformation of 3-tpt in the different structures.

6.2. Experimental

6.2.1. Materials

Cu(hfa)$_2$·H$_2$O (Aldrich), with molecular formula Cu(C$_5$HF$_6$O$_2$)$_2$·H$_2$O, was chosen as the metal complex. The organic linker 3-tpt was obtained from Cymit. EtOH and CHCl$_3$ were purchased from Sigma Aldrich. Compressed CO$_2$ (99.95%) was supplied by Carburos Metálicos S.A.

6.2.2. Equipment and methods

Crystallization runs were performed in either scCO$_2$, EtOH or CHCl$_3$. Reactions in scCO$_2$ were performed in a 5 mL Pyrex vial placed into a 100 mL high-pressure autoclave with two opposite sapphire windows (TharDesign, descrived in Chapter 3). Reagents solubility was qualitatively estimated by visual inspection of the vial through the sapphire windows. The vial was charged with 200 mg of the metal complex (4·10-3 M) and 0.5 equivalents (60 mg) of the organic linker, together with a small magnetic bar, and capped with cellulose paper. Experiments were performed at 20 MPa and 333 K. The vial was stirred at 500 rpm. After a running period of 24 h, the product was washed with fresh scCO$_2$ to eliminate residual copper complex. The autoclave was then depressurized and cooled down to room temperature to recover a green powder that was rinsed with chloroform and air dried.

In a typical crystallization test performed in either CHCl$_3$ or EtOH, each reagent was added separately in 15 mL of organic solvent and then mixed in a 50 mL screw-top Pyrex vial. For CHCl$_3$, crystallization assays were performed at room temperature in closed vials filled with a solution of 150 mg of Cu(hfa)$_2$·H$_2$O (1·10^{-2} M) and 2 equivalents (45 mg) of 3-tpt, in experiments of 24 h. For EtOH, reagents concentration was varied from diluted (150 mg of Cu(hfa)$_2$·H$_2$O, 1·10^{-2} M) to concentrated (400 mg of Cu(hfa)$_2$·H$_2$O, 2.8·10^{-2} M), in open vessels holding dispersed 3-tpt in a ratio of 0.5 equivalents (50 to 125 mg). Crystallization runs were completed at 298 K in runs of 24 h, which implied a solvent volume reduction of

ca. two thirds. In all cases, the recovered sample was rinsed with chloroform to remove residual organic linker and air dried.

6.2.3. Characterization

Crystal structures and phase transformation

Routine powder X-ray diffraction (PXRD) patterns of the precipitated **1**-**4** compounds were recorded in a Siemens D5000 diffractometer, using the Cu Kα incident radiation. The focus was from a 2θ of 4 to 20º, range of the most intensity peaks for the studied phases. Single-crystal X-ray diffraction (SCXRD) experiments for pristine 3-tpt and **1-5** compounds were performed in the XALOC beamline[24] at ALBA synchrotron (Spain). Data were collected at 100 K with a 0.72931 Å wavelength (0.82654 Å for compound 5) using the Dectris Pilatus 6M detector placed at 120 mm from the sample. The ϕ-scans were performed from 0 to 360º in steps of 0.5º and at a collection time of 0.15 s·step^{-1}. The scan was repeated at three different κ angles (0, 45º, 90º) and merged afterwards to increase the completeness and redundancy when possible. Data were indexed, integrated and scaled using the XDS software.[25] The crystal structures were solved by intrinsic phasing and refined with SHELXL (version 2014/7)[26] using Olex2 as graphical interface.[27] The CHCl$_3$ solvent molecules inside the structure of compound **2** could not be modelled and the disordered density was masked using the PLATON/SQUEEZE method[28] in the final refinement (1.2 Å probe radius, 0.2 Å grid space). Crystallographic data for all compounds are summarized in Tables 6.1-6.6 and the corresponding CIF files have been deposited in the Cambridge Crystallographic Data Centre (CCDC 1894846-1894851).

Table 6.1. Crystallographic data for 3-tpt.

Molecular formula (MF)	$C_9H_6N_3$
Formula weight	156.17
Crystal system, space group	Orthorhombic, P *n m a*
a (Å)	19.718(3)
b (Å)	19.188(3)
c (Å)	3.7150(5)
α (º)	90
β (º)	90
γ (º)	90
V (Å^3)	1405.6(3)
Z (according to MF)	8
ρ (g·cm^{-3})	1.476
Temperature (K)	100
Wavelength (Å)	0.72931
μ (mm-1)	0.099
F (000)	648
hkl ranges	$-26 \leq h \leq 26$, $-25 \leq k \leq 25$, $-4 \leq l \leq 4$
θ range (deg)	2.120 to 29.091
Reflections collected/unique [R_{int}]	103070/1734 [0.074]
Completeness to θ (%)	97.4
Data/parameters/restraints	1734/116/0
Goodness-of-fit on F^2	1.159
Final *R* indices [I > 2σ(I)]	$R_1 = 0.0712$, $wR_2 = 0.2108$
R indices (all data)	$R_1 = 0.0720$, $wR_2 = 0.2119$
Largest diff peak and hole (eÅ^{-3})	0.41, -0.40

Table 6.2. Crystallographic data for **1**.

Molecular formula (MF)	$C_{33}H_{15}Cu_{1.5}F_{18}N_6O_6$
Formula weight	1028.82
Crystal system, space group	Monoclinic, P $2_1/n$
a (Å)	9.113(9)
b (Å)	16.503(8)
c (Å)	27.080(12)
α (º)	90
β (º)	96.915(15)
γ (º)	90
V (Å^3)	4043(5)
Z (according to MF)	4
ρ (g·cm^{-3})	1.690
Temperature (K)	100
Wavelength (Å)	0.72931
μ (mm-1)	0.987
F (000)	2034
hkl ranges	$-11 \leq h \leq 11$, $-20 \leq k \leq 20$, $-33 \leq l \leq 33$
θ range (deg)	1.486 to 27.115
Reflections collected/unique [R_{int}]	47894/7882 [0.080]
Completeness to θ (%)	95.1
Data/parameters/restraints	7882/583/0
Goodness-of-fit on F^2	1.084
Final R indices [I > 2σ(I)]	$R_1 = 0.1068$, $wR_2 = 0.2935$
R indices (all data)	$R_1 = 0.1347$, $wR_2 = 0.3218$
Largest diff peak and hole (eÅ^{-3})	2.22, -0.92

Table 6.3. Crystallographic data for **2**.

Molecular formula (MF)	$C_{33}H_{15}Cu_{1.5}F_{18}N_6O_6$
Formula weight	1028.82
Solvent Accessible Volume, SAV (%)	736
Electrons found in SAV	258
$CHCl_3$ units per MF (from e- in SAV)	1
Crystal system, space group	Triclinic, P $\bar{1}$
a (Å)	8.968(4)
b (Å)	15.894(3)
c (Å)	30.924(5)
α (º)	89.807(7)
β (º)	87.597(14)
γ (º)	82.659(12)
V (Å^3)	4368(2)
Z (according to MF)	4
ρ (g·cm^{-3})	1.565
Temperature (K)	100
Wavelength (Å)	0.72931
μ (mm-1)	0.869
F (000)	2034
hkl ranges	$-10 \leq h \leq 10$, $-19 \leq k \leq 19$, $-38 \leq l \leq 38$
θ range (deg)	1.326 to 27.115
Reflections collected/unique [R_{int}]	54421/15488 [0.092]
Completeness to θ (%)	86.8
Data/parameters/restraints	15488/1165/0
Goodness-of-fit on F^2	1.034
Final R indices [I > 2σ(I)]	$R_1 = 0.1049$, $wR_2 = 0.2916$
R indices (all data)	$R_1 = 0.1073$, $wR_2 = 0.2931$
Largest diff peak and hole (eÅ^{-3})	1.27, -0.85

Table 6.5. Crystallographic data for **3**.

Molecular formula (MF)	$C_{33}H_{21}Cu_{1\,5}F_{18}N_6O_6 \cdot 3(H_2O)$
Formula weight	1082.33
Crystal system, space group	Triclinic, P $\bar{1}$
a (Å)	9.927(2)
b (Å)	13.2590(13)
c (Å)	19.104(3)
α (º)	70.643(4)
β (º)	79.230(11)
γ (º)	68.350(8)
V (Å^3)	2199.0(6)
Z (according to MF)	2
ρ (g·cm^{-3})	1.690
Temperature (K)	100
Wavelength (Å)	0.72931
μ (mm-1)	0.918
F (000)	1065
hkl ranges	$-14 \le h \le 14$, $-18 \le k \le 18$, $-27 \le l \le 27$
θ range (deg)	1.162 to 31.394
Reflections collected/unique [R_{int}]	80301/12761 [0.031]
Completeness to θ (%)	95.1
Data/parameters/restraints	12761/610/0
Goodness-of-fit on F^2	1.056
Final R indices [I > 2σ(I)]	$R_1 = 0.0543$, $wR_2 = 0.1672$
R indices (all data)	$R_1 = 0.0552$, $wR_2 = 0.1682$
Largest diff peak and hole (eÅ^{-3})	1.97, -1.22

Table 6.6. Crystallographic data for **4**.

Molecular formula (MF)	$C_{28}H_{14}CuF_{12}N_6O_4$
Formula weight	789.99
Crystal system, space group	Monoclinic, C 2/*c*
a (Å)	34.511(9)
b (Å)	6.679(8)
c (Å)	26.110(12)
α (º)	90
β (º)	98.431(15)
γ (º)	90
V (Å³)	5953(8)
Z (according to MF)	8
ρ (g·cm⁻³)	1.763
Temperature (K)	100
Wavelength (Å)	0.72931
µ (mm-1)	0.911
F (000)	3144
hkl ranges	$-47 \le h \le 47$, $-9 \le k \le 9$, $-36 \le l \le 36$
θ range (deg)	1.224 to 30.428
Reflections collected/unique [R_{int}]	50826/8037 [0.033]
Completeness to θ (%)	96.0
Data/parameters/restraints	8037/462/0
Goodness-of-fit on F^2	1.049
Final *R* indices [I > 2σ(I)]	$R_1 = 0.0310$, $wR_2 = 0.0845$
R indices (all data)	$R_1 = 0.0339$, $wR_2 = 0.0860$
Largest diff peak and hole (eÅ⁻³)	0.65, -0.74

Table 6.4. Crystallographic data for **5**.

Molecular formula (MF)	$C_{38}H_{16}Cu_2F_{24}N_6O_8$
Formula weight	1267.65
Crystal system, space group	Triclinic, P $\bar{1}$
a (Å)	8.935(3)
b (Å)	11.3950(7)
c (Å)	22.2660(14)
α (º)	89.559(9)
β (º)	86.667(3)
γ (º)	79.764(9)
V (Å^3)	2227.1(8)
Z (according to MF)	2
ρ (g·cm^{-3})	1.890
Temperature (K)	100
Wavelength (Å)	0.82654
μ (mm-1)	1.679
F (000)	1248
hkl ranges	$-11 \leq h \leq 11$, $-15 \leq k \leq 15$, $-30 \leq l \leq 30$
θ range (deg)	1.065 to 34.179
Reflections collected/unique [R_{int}]	86416/10135 [0.070]
Completeness to θ (%)	86.5
Data/parameters/restraints	10135/706/0
Goodness-of-fit on F^2	1.029
Final *R* indices [I > 2σ(I)]	$R_1 = 0.0631$, $wR_2 = 0.1790$
R indices (all data)	$R_1 = 0.0671$, $wR_2 = 0.1834$
Largest diff peak and hole (eÅ^{-3})	1.96, -1.29

In situ 2D wide angle X-ray scattering WAXS measurements were performed at NCD-SWEET beamline at ALBA synchrotron light source (Spain) to investigate the evolution of phase **3** with temperature. Small crystals were introduced in a borosilicate capillary ($\varnothing$=1.5 mm), which was placed in a Linkam TMS350 system and heated from 313 to 393 K under dynamic vacuum while recording *in situ* WAXS 2D patterns. The step-wise temperature profile consisted of a temperature ramp of 1 K·min^{-1} with a dwell time of 20 min each 20 K and a frame rate of 1 frame·min^{-1}. The *in situ* WAXS 2D patterns were measured with an incident X-ray beam size of 300 × 100 μm^2 [H × V] and an energy of 12.4 keV (wavelength: 0.999 Å) in transmission mode. Scattered radiation was recorded using a Rayonix LX255HS area detector (active area 85 x 255 mm^2 [H × V], a pixel size of 44 x 44 μm^2 [H × V]) placed at 94.62 mm from the sample position. Raw data consisted of a collection of 2D images that

were reduced to 1D data using a designed pipeline in DAWN software,[29] which consisted on data masking (e.g., beamstop) and background subtraction (e.g., air, capillary) followed by a reciprocal space calibration using Cr_2O_3 and finally an azimuthal data integration. The resulting 2θ angle at 12.4 keV was converted to Cu Kα radiation (1.54 Å) for better comparison with data collected using the laboratory source.

Solid state characterization

Crystal morphology was observed by scanning electron microscopy (SEM) in a QUANTA FEI 200 FEG-ESEM microscope. Samples chemical composition was assessed by elemental analysis (E.A., Thermo Carlo Erba Flash 2000). As a complementary characterization for stoichiometry validation, Cu(II) weight percentages were measured by energy dispersive spectroscopy (EDS, FEI Magellan 400L) in a high resolution SEM (Ultim Extreme Oxford Inst.), placing the sample on a holder of silicon wafer and metalizing with Pt. Thermogravimetric (TG) analysis, performed up to 800 K in air, was used to determine the thermal stability of the products (TA Instruments SDT Q600). The textural properties were determined by N_2 adsorption/desorption at 77 K using an ASAP 2000 Micromeritics Inc. equipment. When noticeable, the micropore surface area was calculated by the t-method. For composition elucidation and thermal or textural characterization, samples were first degassed at 333 K for 24 h to eliminate adsorbed solvent molecules.

6.3. Results and Discussion
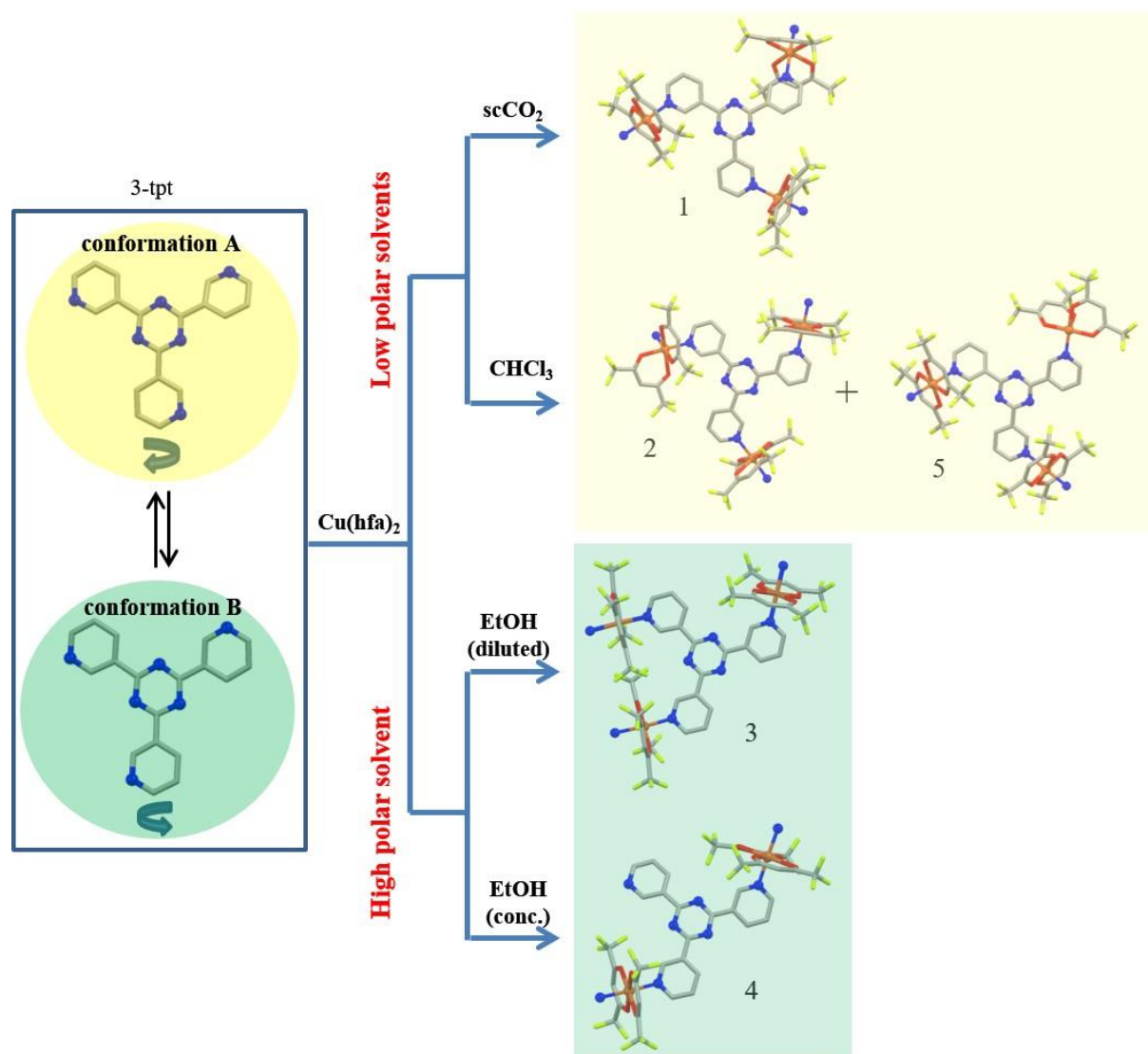
Figure 6.1. Preparation of Cu(II) organic frameworks **1** to **5**. Cu(II) coordination environment and isomer of 3-tpt is obtained from the solved X-ray crystal structures. H atoms are omitted for clarity. Color code: C grey; O red; N blue, Cu orange and F yellow.

6.3.1. Crystal structure of 3-tpt

As mentioned in the introduction, the 3-tpt molecule has a conformational degree of freedom, since it can either retain a 3-fold symmetry (conformation A) or reduce the symmetry through rotation of 180º of one of the three triazine-pyridyl bonds (conformation B) (Fig. 6.1, left). The structure of this compound has not been found described in the literature and, thus, it was elucidated in this work by synchrotron SCXRD, after recrystallization of commercial 3-tpt in $CHCl_3$. 3-tpt crystallizes in the orthorhombic space group Pnma (Fig. 6.2 and Table 6.1). In this structure, two sets of N positions were found related by a 180º rotation, with an occupancy molar ratio of 0.5:0.5, which confirms that the 3-tpt structure is constituted by a 1:1 mixture of conformations A and B.
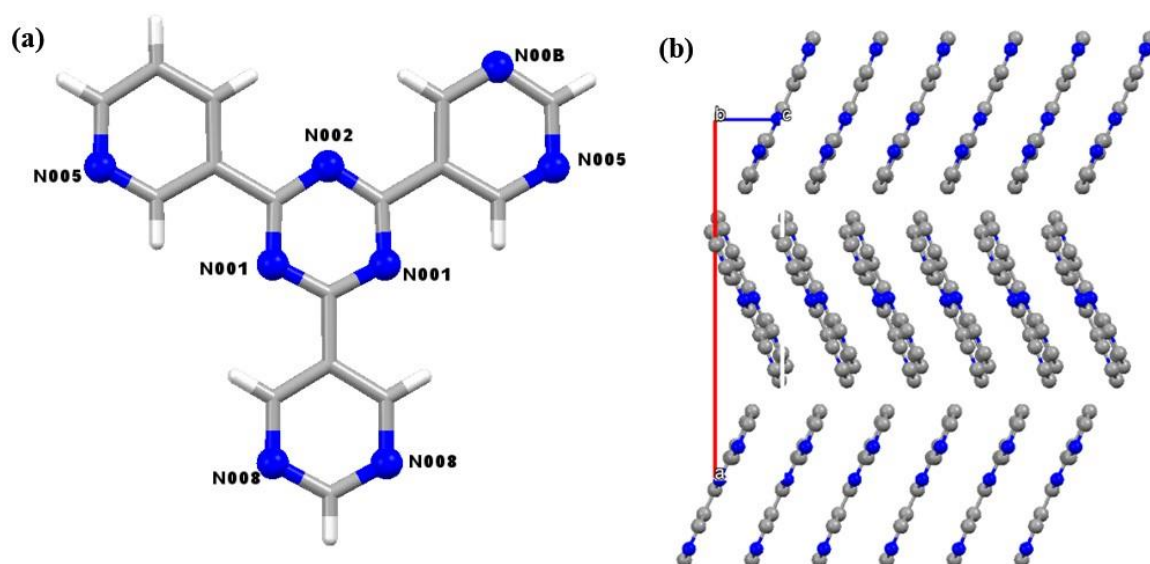
Figure 6.2. Plot of the crystal structure of 3-tpt: (a) view of the 3-tpt unit, and (b) packing of the molecules in the crystal. Color code: C grey; N blue and H white.

6.3.2. Solvent crystallization and crystal structures of compounds 1 to 5

The difficulty of forming discrete metal-assemblies involving the 3-tpt linker resides in controlling the orientation of the pyridyl groups prior to coordination to the metal centers.[6] Methods for orientation control have not been get described, but rather a collection of diverse structures with various 3-tpt conformations has been published.[30] In this work, five different MOFs (compounds **1** to **5**) were prepared using 3-tpt and $Cu(hfa)_2 \cdot H_2O$ in various conditions with the objective of rationalizing the influence of the experimental parameters on 3-tpt conformation. In brief, the compounds were obtained by using three different solvents, with increasing polarity: $scCO_2$ (**1**), $CHCl_3$ (**2** and **5**) and EtOH.

Although $scCO_2$ is considered as the most non-polar solvent, $CHCl_3$ is also defined as non-polar, whereas EtOH is clearly a polar solvent.[31,32] The PXRD patterns of compounds **1** to **4** were consistent with those simulated from their respective crystal structures (Fig. 6.3), thus confirming their phase purity. Compound **5** is an elusive intermediate product, and its precipitation as a bulk powder has not been possible. Table 6.7 gives structural and compositional characterization data for these compounds. Fig. 6.1 and Figs. 6.4-6.6, 6.8-6.9 show several perspectives of the 3-tpt isomers and Cu(II) coordination for the different compounds in their respective crystal structures. Crystallographic data for **1**-**5** are summarized in Tables 6.2-6.6 in the experimental section. In the following, the structure of each of these compounds is described, grouped by the characteristics found for the 3-tpt isomer.
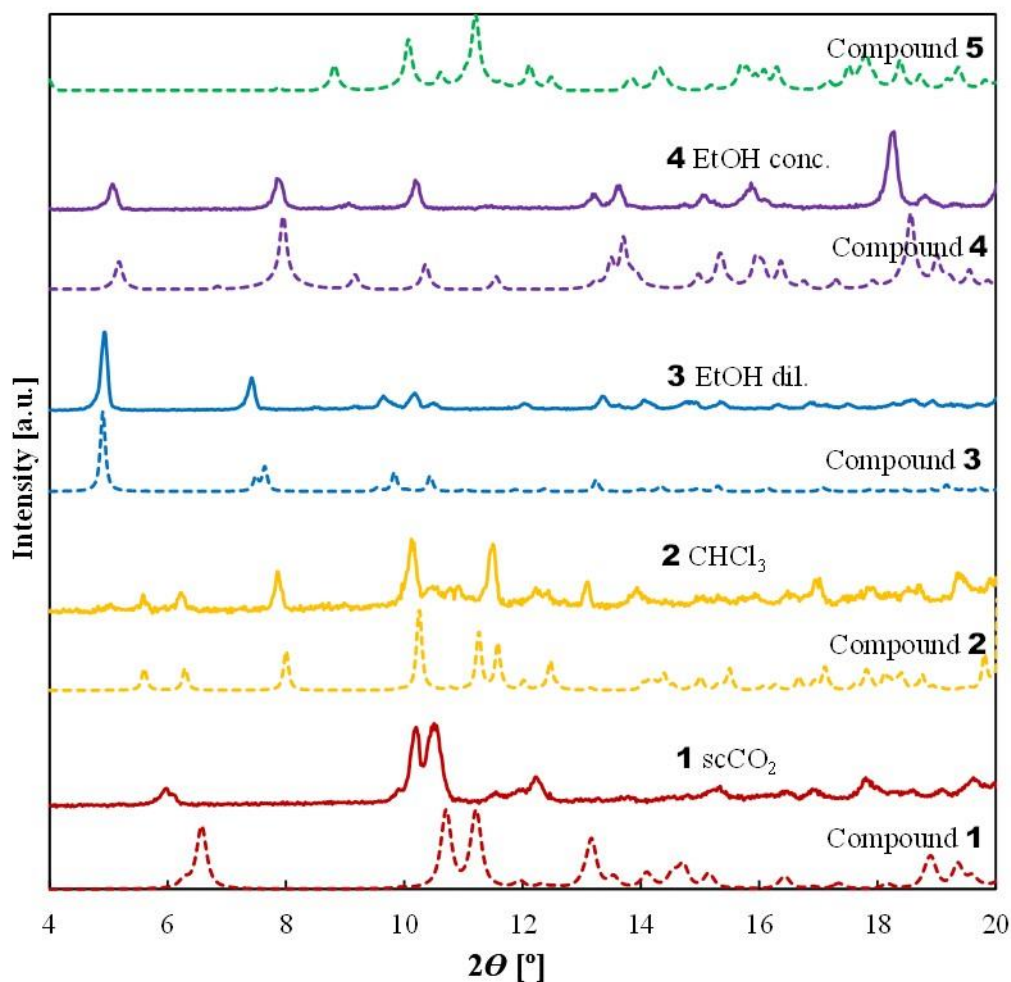
Figure 6.3. PXRD patterns of samples crystallized in the different studied solvents: straight lines correspond to measurements performed for the bulk powder, while dotted lines represent the calculated profiles from single-crystal structures (CuK*α* wavelength). Shifts in 2*Θ* are associated to the used low measurement temperature of 100 K in single-crystal *vs.* routine PXRD data acquired at room temperature.

Table 6.7. Structural and compositional characterization of the crystallized compounds.

C.	Space group	Stoichiometry	3-tpt conform.	Elemental analysis C, H, N [wt%]	EDS[1] Cu [wt%]
1	Monoclinic $P2_1/n$	$[(Cu(hfa)_2)_{1.5}(3\text{-tpt})]_n$	A, tridentate	c.[2] 38.53, 1.47, 8.17 f.[3] 38.32, 1.27, 8.33	c.9.3 f.10.8
2	triclinic $P\text{-}1$	$[(Cu(hfa)_2)_{1.5}(3\text{-tpt})]_n$ $\cdot nCHCl_3$	A, tridentate	c. 38.51, 1.46, 8.17 f. 38.49, 1.31, 8.31	c.9.3 f.11.0
3	triclinic $P\text{-}1$	$[(Cu(hfa)_2)_{1.5}(3\text{-tpt})]_n$ $\cdot 3nH_2O$	B, tridentate	c. 36.60, 1.95, 7.76 f. 36.47, 1.35, 8.09	c.9.3 f.11.0
4	monoclinic $C/2c$	$[(Cu(hfa)_2)(3\text{-tpt})]_n$	B, bidentate	c. 42.57, 1.79, 10.64 f. 42.63, 1.73, 10.66	c.8.0 f.9.5
5	Triclinic $P\text{-}1$	$[(Cu(hfa)_2)_2(3\text{-tpt})]_n$	A, tridentate	---	---

[1] Calculated for the dehydrated samples and recalculated to include H contribution.
[2] c.=calculated; [3] f.=found.

Compounds with 3-tpt linkers in A conformation

Compound **1** *[(Cu(hfa)₂)₁.₅(3-tpt)]ₙ* crystallizes in the monoclinic *P*2₁/*n* space group. As shown in Figs. 6.1 and 6.4, the 3-tpt acts as a tridentate linker displaying the symmetric conformation A. Each N atom of the pyridyl moieties in the 3-tpt is coordinated to a one Cu(II) atom. Each Cu(II) atom is coordinated by four O atoms equatorially and two N atoms axially to form hexacoordinated octahedral complexes. Therefore, two hfa groups coordinate each Cu(II) atom with a *trans* configuration. Cu–OOC and Cu–N bond lengths range from 1.983 to 2.258 Å and 2.017 to 2.062 Å, respectively. The tridentate coordination of the 3-tpt moieties in **1** adopts a 6⁶-grid topology (Fig. 6.7(a)) to produce a nearly planar 2D layer. Supramolecular self-assembly of the 2D layers provides a non-porous 3D structure.
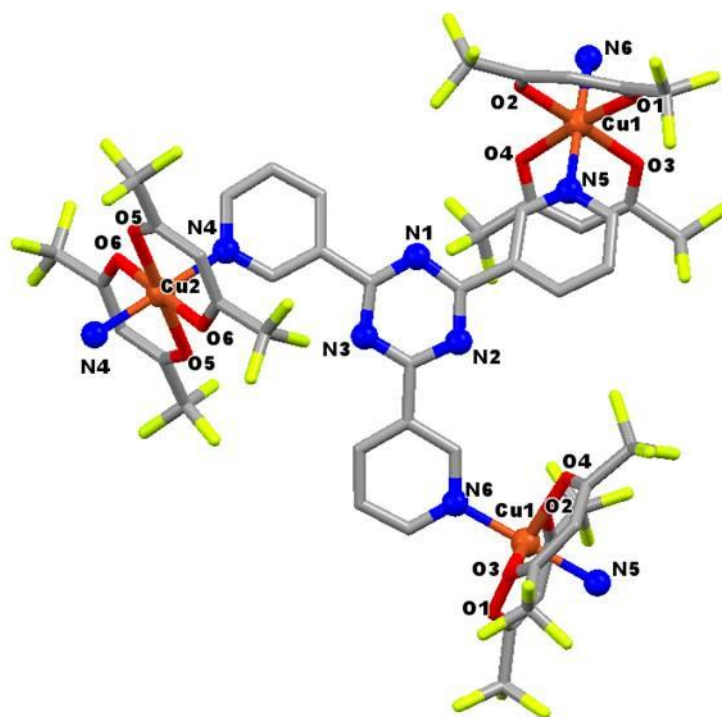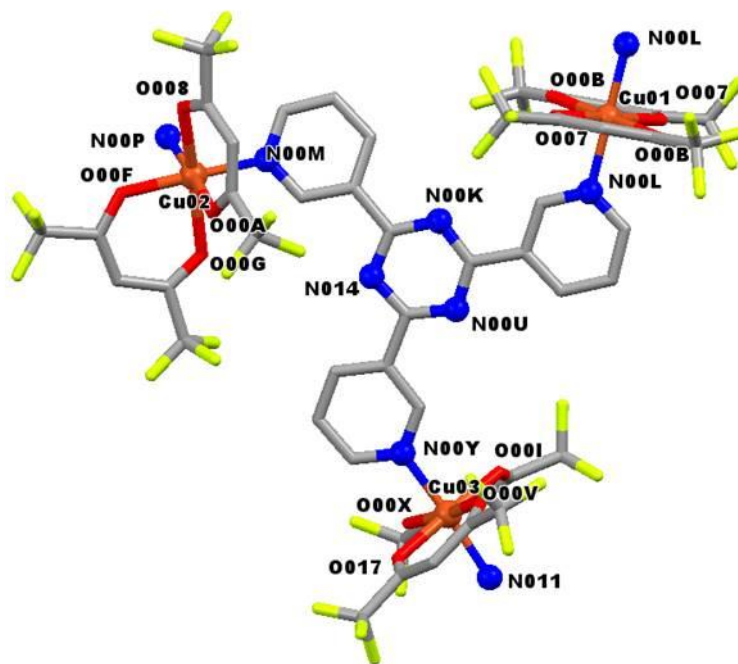
Figure 6.4. Plot of the crystal structure of **1** with a view of the 3-tpt units coordinated to Cu(II). H atoms are omitted for clarity. Color code: C grey; O red; N blue, Cu orange and F yellow.

Compound **2** *[(Cu(hfa)$_2$)$_{1.5}$(3-tpt)]$_n$·nCHCl$_3$* crystallizes in the triclinic P-1 space group. As in the case of **1**, the crystal structure for this compound shows the 3-tpt acting as a tridentate linker with A conformation (Figs. 6.1 and 6.5). Each Cu(II) atom is also hexacoordinated, however, the arrangement of the linker around the metal is slightly different in this case. Cu01 and Cu03 are coordinated by four O atoms equatorially and two N atoms axially, that is, two hfa groups coordinate each of these Cu(II) atoms with a *trans* configuration. However, the third Cu02 atom is coordinated by three O atoms equatorially and one O atom and one N atom axially, that is, two hfa groups coordinate to this Cu(II) atom with a *cis* configuration. Cu–OOC and Cu–N bond lengths range from 1.963 to 2.306 Å and 2.006 to 2.042 Å, respectively. The tridentate coordination of the 3-tpt moieties in **2** again adopts a 6^6-grid topology (Fig. 6.7(b)), but the *cis* configuration of the two hfa groups produces a very corrugated 2D layer. Supramolecular self-assembly of the corrugated 2D layers provides the 3D structure. The high corrugation organizes the structure with non-connected pores (8.5 % of the unit cell; vide infra).
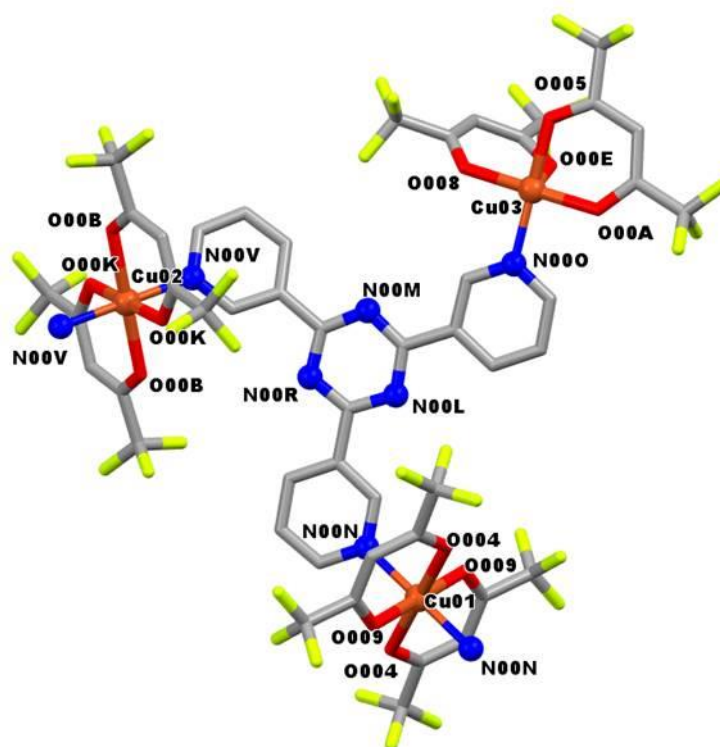
Figure 6.5. Plot of the crystal structure of **2** with a view of the 3-tpt units coordinated to Cu(II). H atoms are omitted for clarity. Color code: C grey; O red; N blue, Cu orange and F yellow.

Compound **5** *[(Cu(hfa)₂)₂(3-tpt)]ₙ* crystallizes in the triclinic space group P-1. 3-tpt depicted the symmetric conformation A and acts as a tridentate linker too (Figs. 6.1 and 6.6). The crystal structure indicates three differently coordinated Cu(II) metal atoms, two of them (Cu01 and Cu02) are hexacoordinated as in **1** and **2**, while Cu03 is pentacoordinated. Cu01 and Cu02 are coordinated by four O atoms equatorially and two N atoms axially, that is, two hfa groups coordinate each of these Cu(II) atoms with a *trans* configuration. Cu03 possess square pyramidal coordination with one N atom in the equatorial position, the other positions occupied by four O atoms from two hfa groups in *cis* conformation. The angular structural index parameter τ for the pentacoordinated geometry of Cu03 is 0.01, a value that confirms a nearly ideal square pyramidal geometry.[33] Cu–OOC and Cu–N bond lengths range from 1.910 to 2.296 Å and 2.000 to 2.051 Å, respectively. As shown in Fig. 6.7(c), the solid structure of **5** consists on 1D chains extending along the *c*-axis. The coordination polymer expands only through the Cu01 and Cu02 atoms that are octahedrically coordinated, while pentacoordinated Cu03 atoms alternate to both sides of the 1D structure. Supramolecular self-assembly of 1D chains provides a non-porous 3D structure.
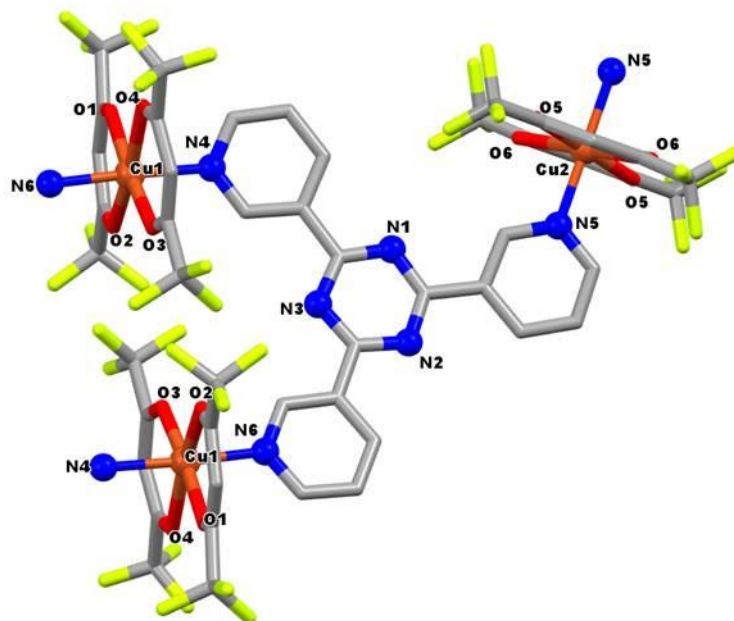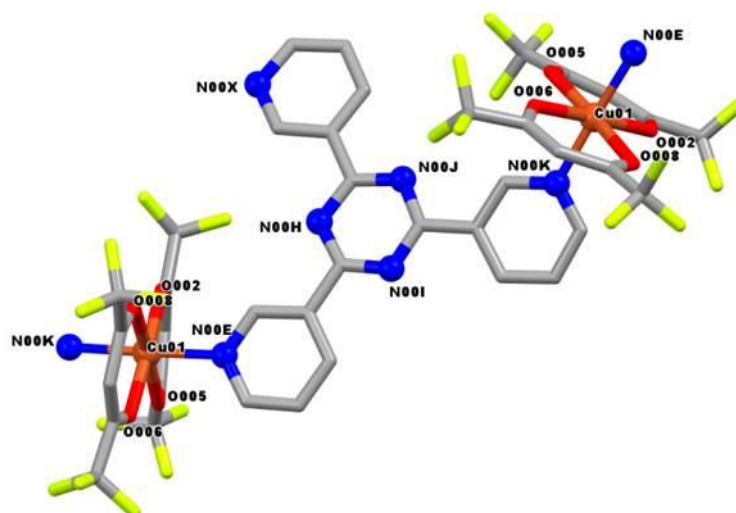
Figure 6.6. Plot of the crystal structure of **5** with a view of the 3-tpt units coordinated to Cu(II). H atoms are omitted for clarity. Color code: C grey; O red; N blue, Cu orange and F yellow.
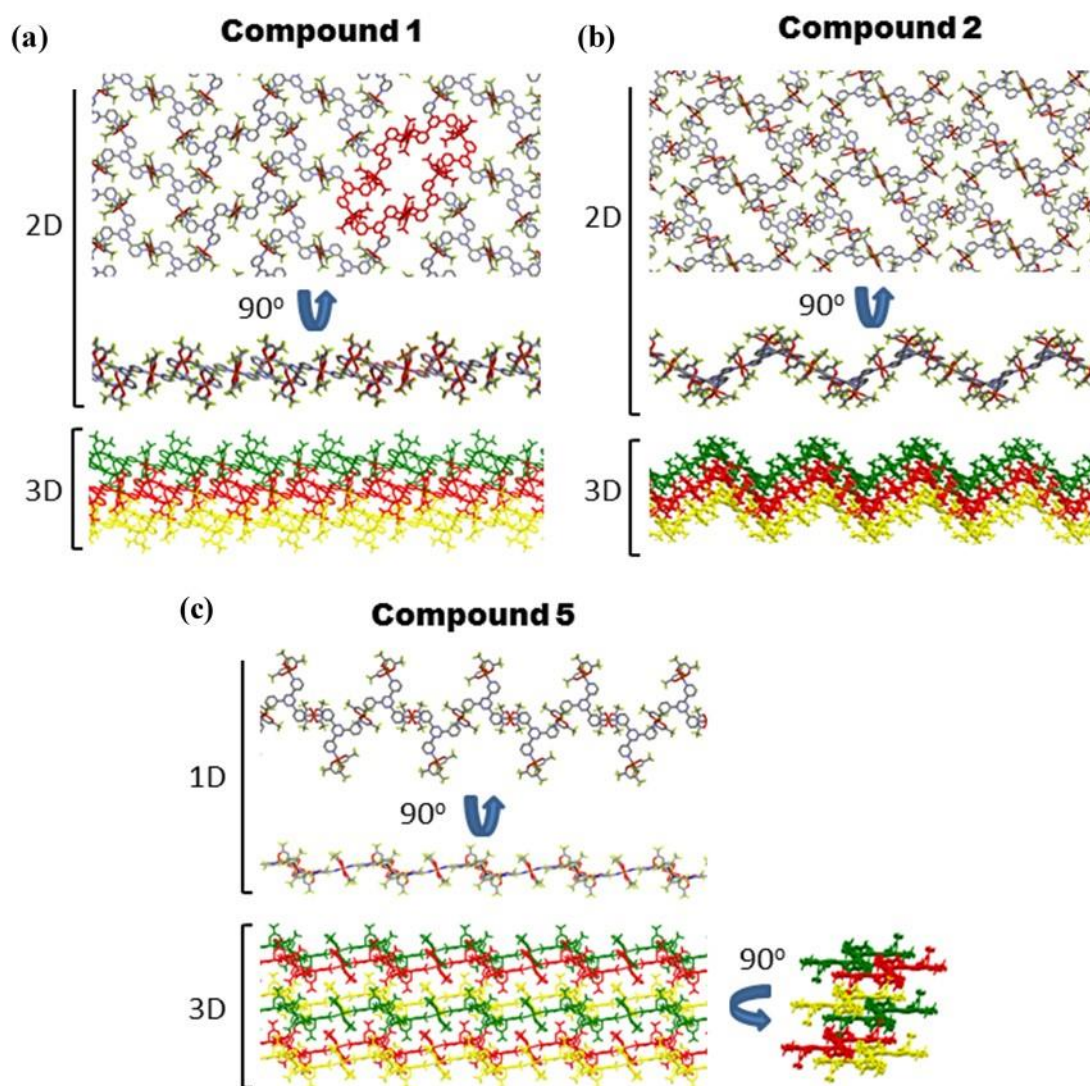
Figure 6.7. Plot of the crystal structures of compounds with 3-tpt in A conformation. The 6^6-grid topology in **1** is highlighted in red. Contiguous chains or layers are colored for clarity. Color code: C grey; O red; N blue, Cu orange and F yellow.

Compounds with 3-tpt linkers in B conformation

Compound **3** *[(Cu(hfa)$_2$)$_{1.5}$(3-tpt)]$_n$·3H$_2$O* crystallizes in the triclinic P-1 space group. Contrary to the above described compounds, the 3-tpt acts here as a tridentate linker displaying the asymmetric conformation B (Figs. 6.1 and 6.8). The hfa groups are all in *trans* configuration. Thus, each Cu(II) atom is coordinated by four O atoms equatorially and two N atoms axially to form hexacoordinated octahedral complexes. Cu–OOC and Cu–N bond lengths range from 1.960 to 2.310 Å and 2.014 to 2.041 Å, respectively. The structural analyses show that **3** forms 1D chains involving planar macrocycles of the Cu$_2$(3-tpt)$_2$ type, consisting of two Cu(hfa)$_2$ units bridged by two 3-tpt linkers through two of the pyridine N atoms, each acting as a molecular clip (flat sidewalls). The remaining N atom in each 3-tpt

linkers is connecting the macrocycles and, thus, providing the observed 1D extended structure along the *c*-axis (Fig. 6.10(a)). Supramolecular self-assembly of these chains by weak interactions forms the 3D structure. The 1D chains cannot pack efficiently in the solid state due to the awkward shape of the planar macrocycles. As a consequence, compound **3** shows some connected porosity (12 % of the unit cell; *vide infra*).

Figure 6.8. Plot of the crystal structure of **3** with a view of the 3-tpt units coordinated to Cu(II). H atoms are omitted for clarity. Color code: C grey; O red; N blue, Cu orange and F yellow.

Compound **4** *[(Cu(hfa)₂)(3-tpt)]ₙ* crystallizes in the monoclinic space group C2/c. The asymmetric unit involves one Cu(hfa)$_2$ and one 3-tpt, indicating the crystallization of a product with less content in Cu(II) than **1** to **3**. It should be noted that 3-tpt uses only two of the three available N atoms to coordinate to the metal ion (Figs. 6.1 and 6.9). The Cu(II) atoms are coordinated by four O atoms equatorially and two N atoms axially, that is, two hfa groups coordinate each metal with a *trans* configuration. Cu–OOC and Cu–N bond lengths range from 1.958 to 2.375 Å and 2.027 to 2.029 Å, respectively. The solid structure of this compound consists of 1D linear chains extended along the *c*-axis (Fig. 6.10(b)). Supramolecular self-assembly of 1D chains provides a non-porous 3D structure.

Figure 6.9. Plot of the crystal structure of **4** with a view of the 3-tpt units coordinated to Cu(II). H atoms are omitted for clarity. Color code: C grey; O red; N blue, Cu orange and F yellow.
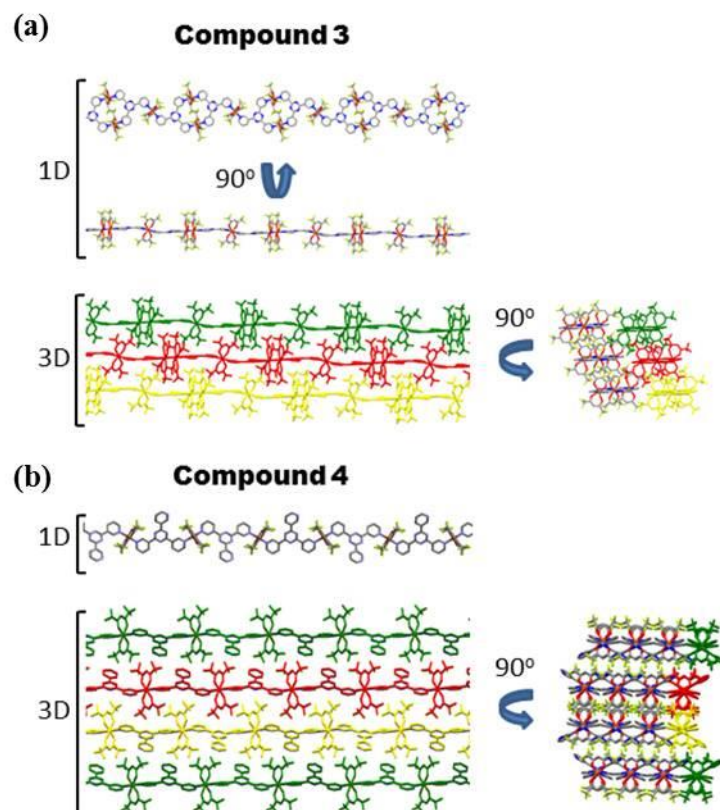
Figure 6.10. Plot of the crystal structures of compounds with 3-tpt in B conformation. Contiguous chains or layers are colored for clarity. Color code: C grey; O red; N blue, Cu orange and F yellow.

For all compounds, weak intermolecular C–F···F–C and C–F···π interactions are involved in the supramolecular construction of the observed 3D structures.

6.3.3. Thermal behavior

Characterization by TG analysis in air of **1**, **2** and **3**, crystallized in $scCO_2$, EtOH and $CHCl_3$, respectively, indicates that the thermal decomposition curves were composed of two differentiate sections, pointing to separate elimination of the subunits $Cu(hfa)_2$ and 3-tpt at 450-575 and > 650 K, respectively (Fig. 6.11). Higher thermal stability (*ca.* 100 K) of each compound component with respect to pristine reagents results from the energy needed to break the coordinative bond Cu(II)-N. For T < 450 K, a noticeable mass loss was only observed for compound **3**.
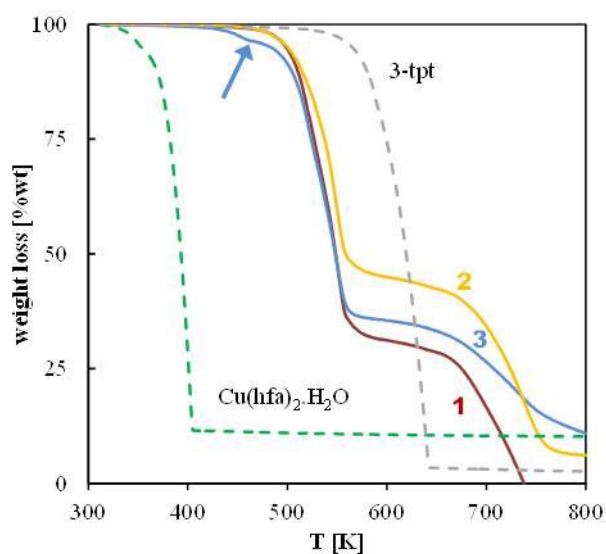
Figure 6.11. TG curves of reagents and compounds **1**, **2** and **3**. Measurements were performed in air. The arrow indicates the anomalous behavior of 3 at low temperature.

Indeed, in a series of preliminary experiments, the thermal stability of the different compounds was tested by heating samples at either 333 or 393 K during 24 h under vacuum. The studied compounds remained crystallographically stable at both temperatures, except compound **3** that modified its structural characteristics at 393 K. The structural transformation of **3** with temperature was analyzed by 2D WAXS in the 313-393 K temperature range (Fig. 6.12, left). Spectral analysis indicates that, under ambient pressure, **3** undergoes a phase transformation at temperatures close to 375 K, giving a new compound named as **6**. Microscopic analysis (Fig. 6.12, right) of crystals treated at 393 K during 24 h indicated that the molecular rearrangement needed to go from **3** to **6** does not seem to provoke a significant apparent habit modification in the crystals. However, the single crystals of **3** changed to microcrystals in **6**; thus, limiting the possibilities of structural determination of the new phase through SCXRD.
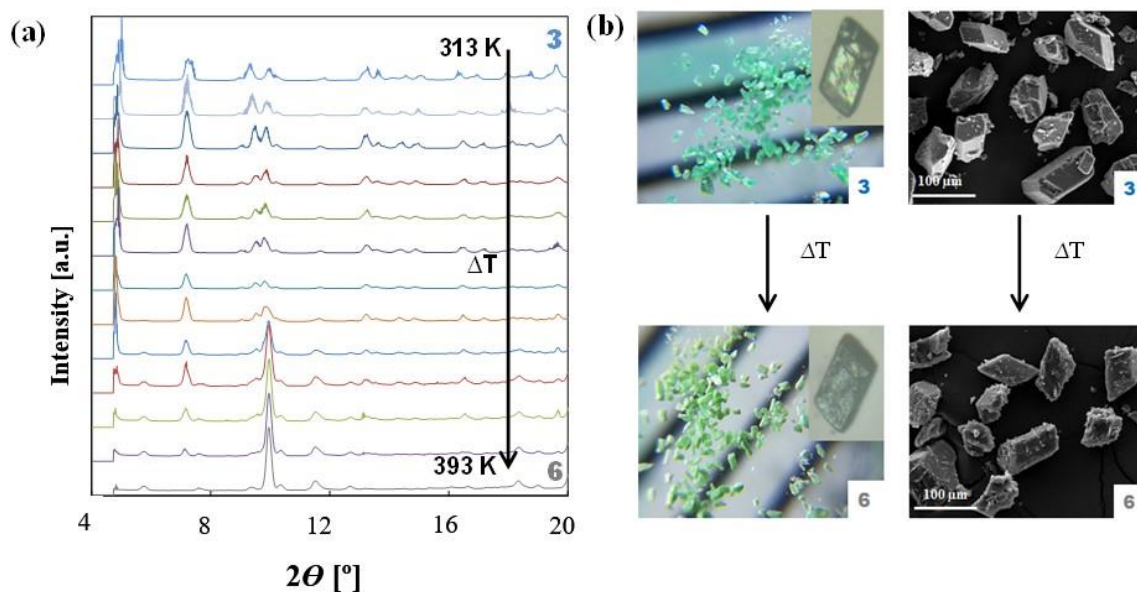
Figure 6.12. Thermal transition between 3 and **6** followed by: (a) 2D WAXS (CuKα wavelength), and (b) optical (medium) and SEM pictures (right) of the initial and end crystals after thermal treatment at 393 K during 24 h.

6.3.4. Textural properties

Low-temperature N_2 adsorption data indicates a Type II isotherm for **1**, **2** and **4**, typical of non-porous solids (Fig. 6.13). As indicated previously, **2** depicted a structural pore void of 8.4 %. However, this porosity is not measurable by physisorption due to lack of interconnected pores. Contrarily, **3**, displaying a structural porosity of 12 % of the unit cell after H_2O removal, is constituted by interconnected pores that extend in the 3D structure perpendicularly to the layers (Fig. 6.14(a)).
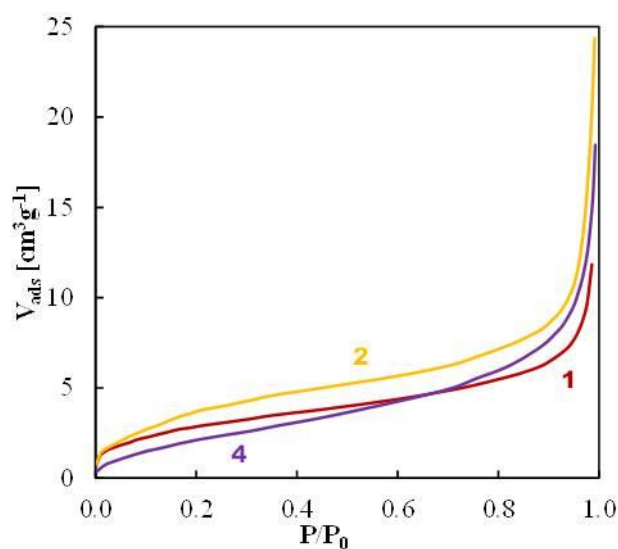
Figure 6.13. Low temperature N_2 adsorption isotherms for non-porous compounds **1**, **2** and **4**.

Structural porosity data was compared to N_2 adsorption values. In both cases, the radius assigned to the N_2 probe molecule was 1.6 Å.[34] The shape of the N_2 adsorption isotherm obtained for **3** does not correspond to any of the six types classified by IUPAC,[35] since it shows two distinct steps in the adsorbed volume and a very delayed desorption branch (Fig. 6.14(b)). The first adsorption occurs in the region of very low relative pressure (< 0.001) and it is followed by a plateau. This section of the curve can be categorized as Type I isotherm, typical of microporous solids. At plateau, the measured micropore area is 270 $m^2 \cdot g^{-1}$. The second adsorption starts at the relative pressure of 0.36 giving a new plateau at 0.50. In this section, the accessible empty void for N_2 adsorption is suddenly increased in approximately one third. This second uptake arises from a phase transition caused by a response of the flexible framework to the incremental N_2 pressure, e.g., expansion of the inter-chain distance to generate accessible free space. Hence, compound **3** can be included in the third generation of MOFs according to the classification of guest-induced structure transformation.[36] Indeed, subnetwork displacement upon molecular adsorption is a phenomenon already described for systems having 1D frameworks.[37] Finally, the adsorption and desorption paths in the isotherm differ considerably, showing a kinetic hysteresis loop that closes at the relative pressures of 0.27. A similar behavior has been described for other Cu(II) and 4-tpt based MOFs.[38,39] The advantages and potential application fields of third generation flexible MOFs are recognized in the areas of selective gas separation processes by adsorption.[40]
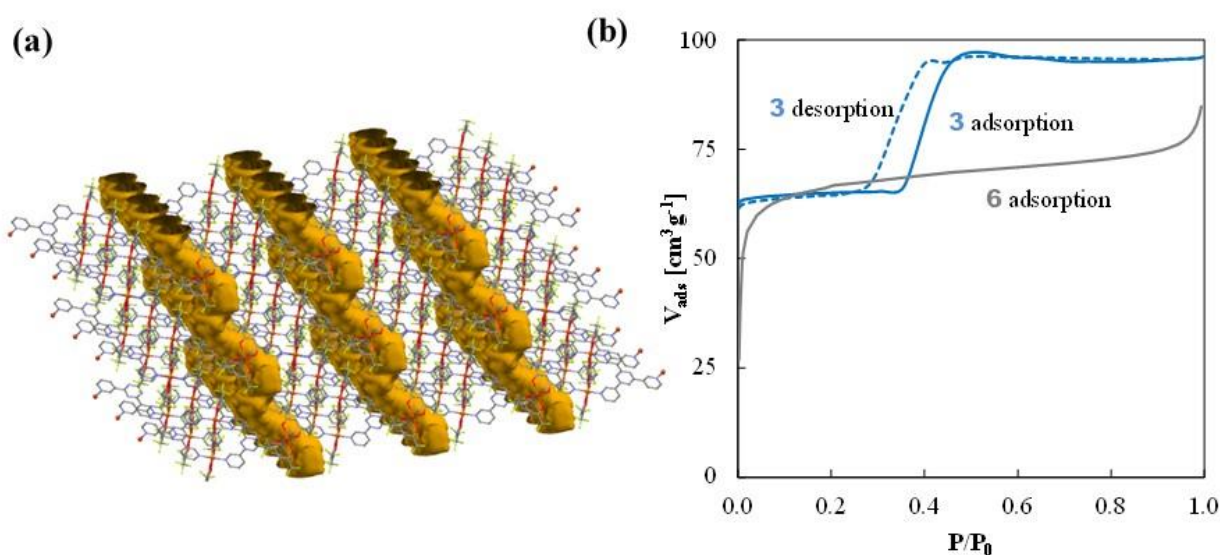

Figure 6.14. Textural properties: (a) empty void calculated for **3** with Mercury program; and (b) low temperature N_2 isotherms of **3** and **6**.

The phase obtained after processing **3** at high-temperature, i.e., **6**, displayed the generic Type I isotherm, typical of microporous solids, with a microporosity value of 260 $m^2 \cdot g^{-1}$ (Fig. 6.14(b)). Hence, the inherent microporosity of **3** was not lost during the phase transition, although the flexible character was removed in **6**.

6.3.5. Crystallization mechanism studies and phase transformation

The synthetic strategy and the used solvent have resulted critical in the formation of the structurally diverse Cu(II)/3-tpt phases. Intrigued by the possibility of controlling the isomer conformation in 3-tpt, the crystallization events in the different solvents were further studied in more detail. Quite interestingly, whereas the low polarity solvents provided MOFs with 3-tpt in the symmetric conformation A, the high polarity solvent (EtOH) afforded asymmetric 3-tpt (conformation B) related compounds (Fig. 6.1).

The solubility of the reagents in the different studied solvents guides nucleation and crystal growth kinetics, which in turn determines the crystallized phase. The organic linker 3-tpt displayed a noticeable solubility only in $CHCl_3$, while $Cu(hfa)_2 \cdot H_2O$ is highly soluble in the three studied solvents.[41] Color changes of the green-colored $Cu(hfa)_2 \cdot H_2O$ reagent give a first indication of the processes occurring in solution (Fig. 6.15).[42] Accordingly, the shift to blue-green observed in either $scCO_2$ or $CHCl_3$ indicates the presence in solution of the dehydrated complex, while in EtOH the green-grass color was retained due to the formation of a robust solvate. The solution obtained by mixing both reagents in any of the studied solvents was green-colored, thus indicating a fast reaction favored by the high affinity of $Cu(hfa)_2$ for donor linkers like 3-tpt. Taking into account reagents solubility, a direct crystallization pathway in liquid medium was observed in $CHCl_3$, i.e., both reagents were highly soluble. Contrarily, a solid-liquid reaction, progressing by "through-dissolution" steps of 3-tpt, would occur in $scCO_2$ or EtOH. In those, a significant solubility of the assembled small growing units $[(Cu(hfa)_2)_x(3\text{-tpt})_y]$, e.g., oligomers or secondary building units, would be necessary to increase the apparent reaction kinetics to practical values.
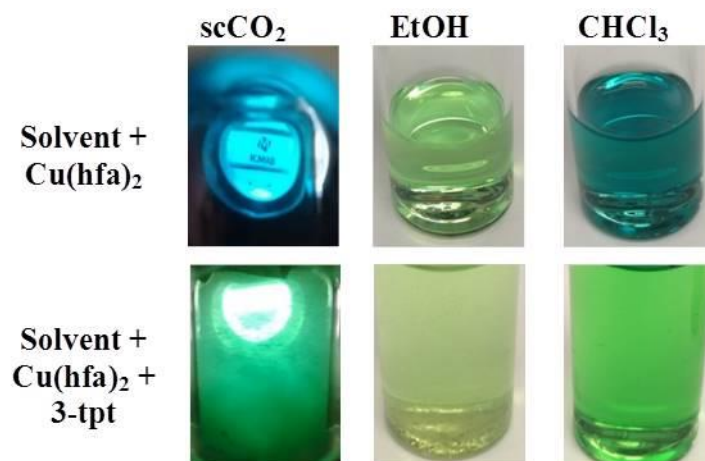
Figure 6.15. Optical pictures taken from the dissolution/dispersions obtained by adding the reagent(s) to the different studied solvents.

Fig. 6.16 shows a mechanistic resume of the crystallization behavior inferred for the $Cu(hfa)_2$/3-tpt system in the three studied solvents, as well as a SEM morphological analysis. For low polarity $scCO_2$ and $CHCl_3$ solvents, crystallization of **1** and **2**, respectively, occurs through the formation of a low-crystallinity intermediate phase. In both solvents, at short reaction times (<1 h) the precipitation of primary particles and emergent laminar structures was noticed. After 24 h, non-classical coalescent growth[1] of the laminar precursor led to the crystallization of micrometric polyhedra, either rounded in $scCO_2$ or elongated in $CHCl_3$. Compared to low polarity solvents, the induction time for nucleation was longer for polar EtOH, independently of reagents concentration, most likely due to the high solubility of the growing units. Further, the presence of solid 3-tpt in the medium during the entire crystallization process provides for a continuous supply of precursor to the solution, thus the formation of growing units can proceed constantly under near steady-state conditions.
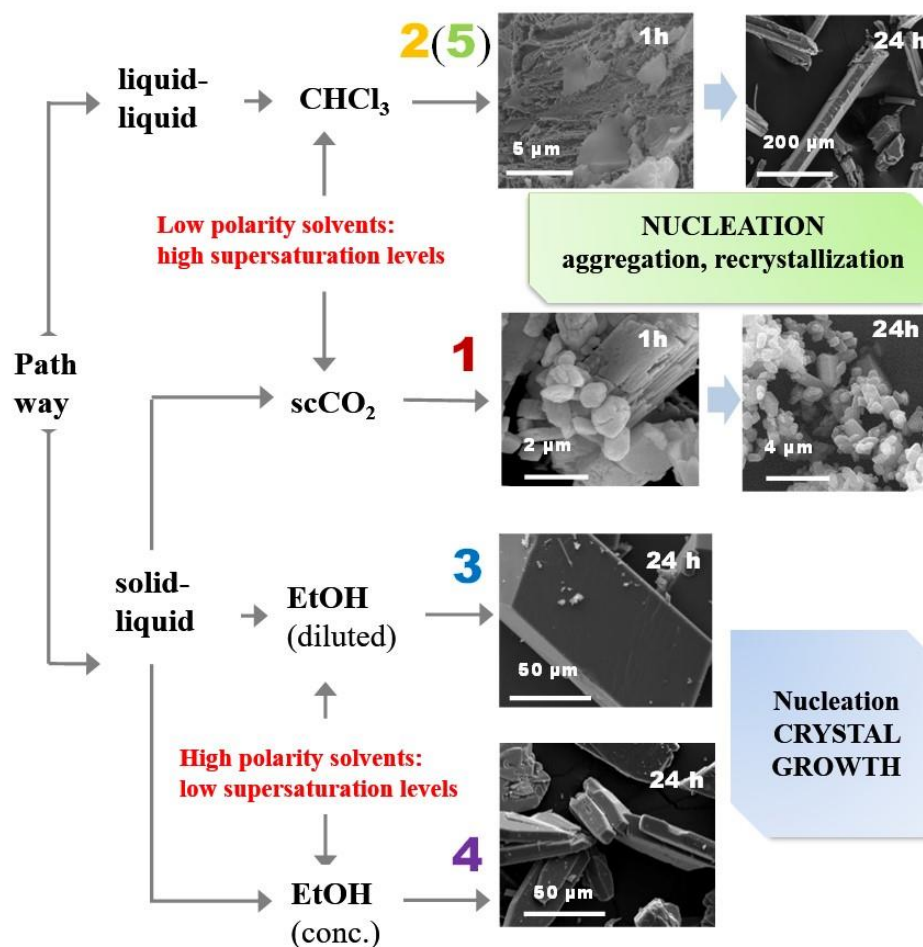
Figure 6.16. Representation of crystallization pathways proposed for each precipitated compound in the different studied solvents. SEM pictures of samples obtained at different crystallization times are also shown.

In EtOH, the most probable pathway of crystallization is, thus, diffusion controlled growth for both **3** and **4** compounds at low and high concentration levels, respectively. This crystallization pathway, together with the generation of only moderate supersaturation levels, led to the formation of well-faceted polyhedric crystals of more than 50 μm. Only in diluted EtOH, with the slowest crystallization kinetics, dynamic metal-linkers bond formation enabled the development of the porous geometry observed in **3**. Contrarily, the high nucleation rate of the kinetic phases in non-polar solvents (or in EtOH at high concentration) could explain why, instead, more dens compounds were obtained in these cases.

The key to control the isomer conformation in 3-tpt is to understand the possible structural transformations occurring among the different MOFs. The process has been studied for **1** and **3** with 3-tpt in conformations A and B, respectively. These are two end stable MOFs with the same stoichiometry: $[(Cu(hfa)_2)_{1.5}(3\text{-}tpt)]_n$ (Fig. 6.17, top). In a simple recrystallization

process, large polyhedral crystals of **3** could be obtained by soaking micrometric particles of **1** in EtOH (Fig. 6.17, bottom). What is even more surprising is that the recrystallization process is reversible. Thus, contacting **3** with scCO$_2$ provided **1**. This last process was slow due to the low solvent power of scCO$_2$. The morphological analysis indicated that the dissolution of **3** was initiated in regions of lattice defects easily attacked by scCO$_2$ (Fig. 6.17, right). The bulk crystals dissolved readily from the faces giving etch pits, which were basically inverted-pyramidal hollows. Simultaneously, the nucleation of small particles of **1** with laminar habit was observed. After 24 h, the system was constituted principally by small micrometric particles with the PXRD pattern of **1**. Some residual 3-tpt was also present in this sample, shown by a peak at $2\Theta=9.3°$.
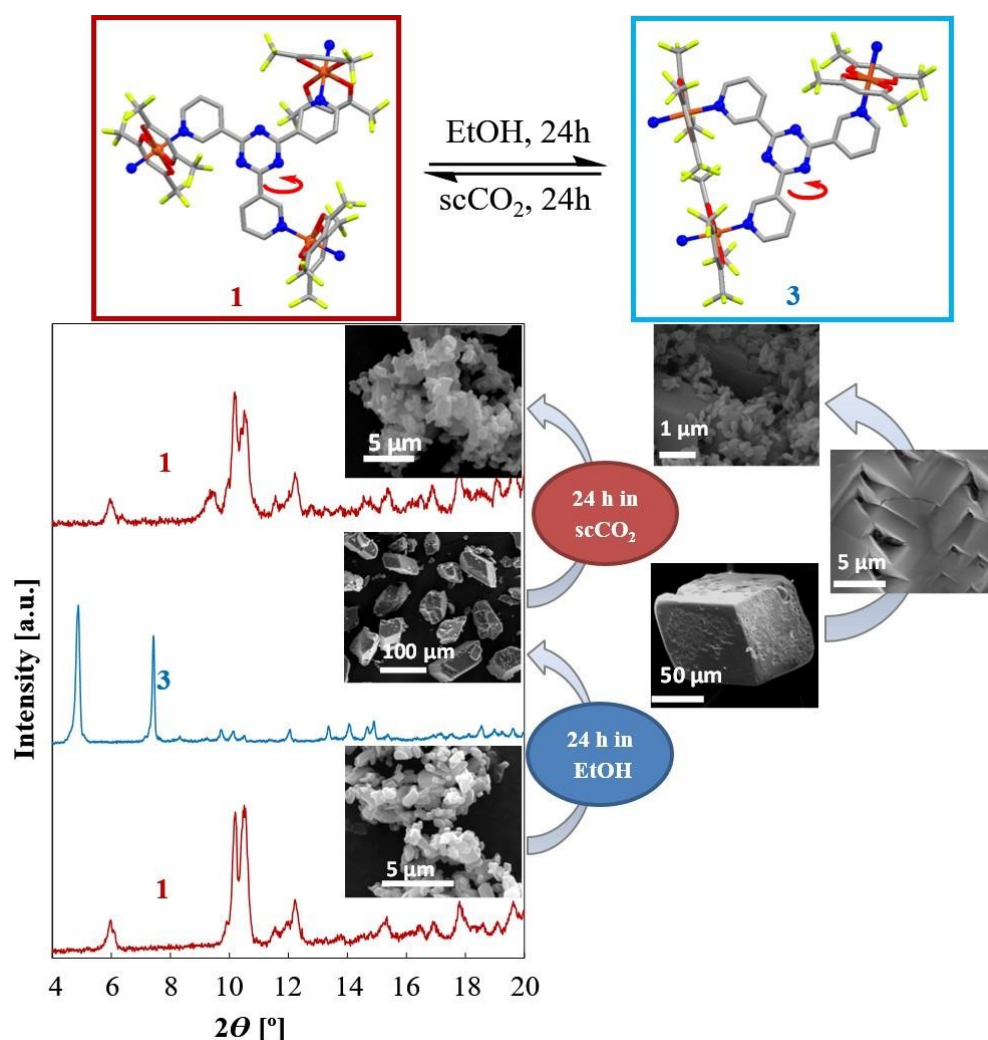

Figure 6.17. Representation of the reversible phase transformation between **1** and **3**; the red arrow indicates the rotating C-C bond in the transformation (top). PXRD structural and SEM morphological follow up of the solvent recrystallization processes occurring to compounds **1** and **3** when immersed in either EtOH or scCO$_2$ (bottom). A zoom of the SEM images corresponding to **3** to **1** transformation is shown at the right.

6.4. Conclusions

The use of three different solvents (scCO$_2$, EtOH and CHCl$_3$) afforded the synthesis of five new MOFs involving the Cu(hfa)$_2$ complex and the 3-tpt linker. 3-tpt exhibited various coordination modes, e.g., bidentate and tridentate, which result in a series of 1D or 2D polymeric structures. The primary analysis of the crystal structures of compounds **1**-**5** revealed that the 3-tpt molecule adopts the symmetric conformation A in low polar solvents (scCO$_2$ and CHCl$_3$), whereas in high polar solvents (EtOH) 3-tpt offers the asymmetric conformation B. One of these compounds (**3**) can be included in the third-generation of flexible MOFs, since it is characterized by dynamic features of their framework structure. Compound **3** shows an elastic structural deformation upon applying N$_2$ gas at low relative pressure, in which the surface area is increased in a proportion of one third. A reversible phase transition has been observed among **1** to **3** to **1**, with unprecedented control of the 3-tpt conformation. Such transformation indicates that during dissolution and recrystallization, one of the inter-ring C-C bonds in the 3-tpt molecule rotates to adjust the conformation to the characteristics of the solvent, i.e., the symmetric A isomer in non-polar scCO$_2$ and the asymmetric B isomer in polar EtOH. The present data add outstanding knowledge for constructing and controlling new organometallic architectures based on 3-tpt.
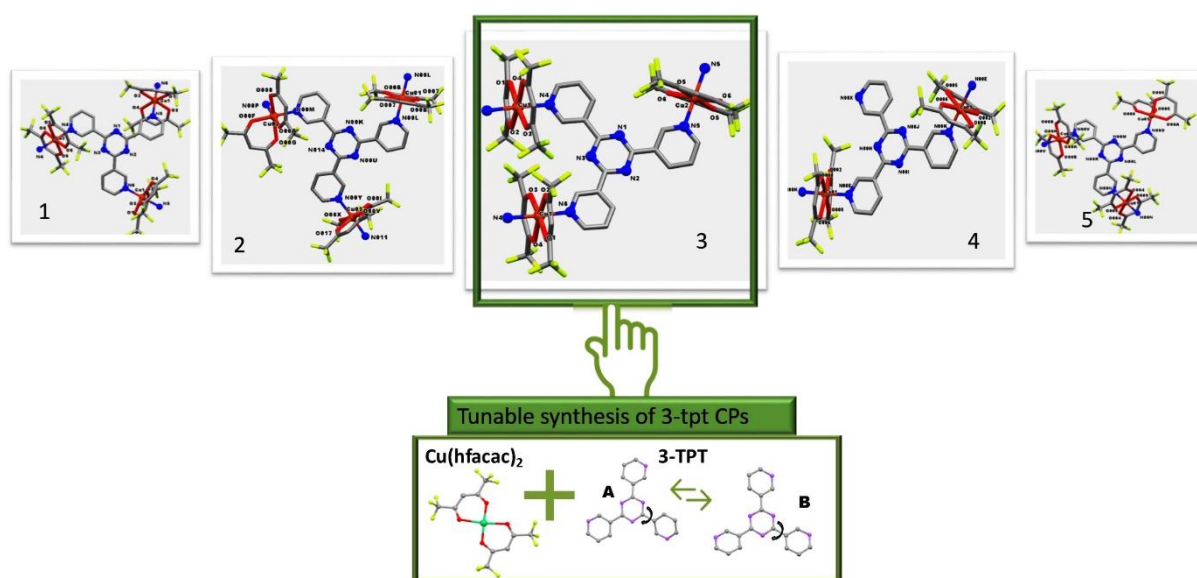

Figure 6.19. Schematic representation of the tunable synthesis of 3-tpt CPs.

6.5. References

(1) Seoane, B.; Castellanos, S.; Dikhtiarenko, A.; Kapteijn, F.; Gascon, J. Multi-scale crystal engineering of metal organic frameworks. *Coord. Chem. Rev.,* **2016**, *307*, 147-187.

(2) Férey, G. Some suggested perspectives for multifunctional hybrid porous solids. *Dalton Trans.,* **2009**, 23, 4400.

(3) López-Periago, A.; Vallcorba, O.; Frontera, C.; Domingo, C.; Ayllón, J. A. Exploring a novel preparation method of 1D metal organic frameworks based on supercritical CO_2. *Dalton Trans.,* **2015**, *44* (16), 7548-7553.

(4) Portoles-Gil, N.; Parra-Aliana, R.; Álvarez-Larena, Á.; Domingo, C.; Ayllón, J. A.; López-Periago, A. Bottom-up approach for the preparation of hybrid nanosheets based on coordination polymers made of metal-diethyloxaloacetate complexes linked by 4,4′-bipyridine. *CrystEngComm.,* **2017**, *19* (34), 4972-4982.

(5) Portolés-Gil, N.; Gowing, S.; Vallcorba, O.; Domingo, C.; López-Periago, A. M.; Ayllón, J. A. Supercritical CO_2 utilization for the crystallization of 2D metal-organic frameworks using *tert* - butylpyridine additive. *J. CO_2 Util.,* **2018**, *24*, 444-453.

(6) Therrien, B. Coordination chemistry of 2,4,6-tri(pyridyl)-1,3,5-triazine ligands. *J. Organomet. Chem.,* **2011**, *696* (3), 637-651.

(7) Li, M.-X.; Miao, Z.-X.; Shao, M.; Liang, S.-W.; Zhu, S.-R. Metal-organic frameworks constructed from 2,4,6-tris(4-pyridyl)-1,3,5-triazine. *Inorg. Chem.,* **2008**, *47* (11), 4481-4489.

(8) Drew, M. G. B.; Hudson, M. J.; Iveson, P. B.; Russell, M. L.; Madic, C. 2,4,6-tris(2-pyridyl)-1,3,5-triazine. *Acta Crystallogr. Sect. C Cryst. Struct. Commun.,* **1998**, *54* (7), 985-987.

(9) Janczak, J.; Sledz, M.; Kubiak, R. Catalytic trimerization of 2- and 4-cyanopyridine isomers to the triazine derivatives in presence of magnesium phthalocyanine. *J. Molec. Str*., 2003, 659, 71-79.

(10) Inokuma, Y.; Yoshioka, S.; Fujita, M. A molecular capsule network: guest encapsulation and control of Diels-Alder reactivity. *Angew. Chemie Int. Ed.,* **2010**, *49* (47), 8912-8914.

(11) Yu, S.-Y.; Kusukawa, T.; Biradha, K.; Fujita, M. Hydrophobic assembling of a coordination nanobowl into a dimeric capsule which can accommodate up to six large organic molecules. *J. Am. Chem. Soc.,* **2000**, *122* (11), 2665-2666.

(12) Fujita, M.; Yu, S.-Y.; Kusukawa, T.; Funaki, H.; Ogura, K.; Yamaguchi, K. Self-assembly of nanometer-sized macrotricyclic complexes from ten small component molecules. *Angew. Chemie Int. Ed.,* **1998**, *37* (15), 2082-2085.

(13) Fujita, M.; Tominaga, M.; Hori, A.; Therrien, B. Coordination assemblies from a Pd(II)-cornered square complex. *Acc. Chem. Res.,* **2005**, *38* (4), 369-378.

(14) Podesta, T. J.; Orpen, A. G. Tris(pyridinium)triazine in crystal synthesis of 3-fold symmetric structures. *Cryst. Growth Des.,* **2005**, *5* (2), 681-693.

(15) Chen, H.-L.; Li, M.-X.; He, X.; Wang, Z.-X.; Shao, M.; Zhu, S.-R. Seven organic-inorganic hybrid compounds constructed from 2,4,6-tris-(pyridyl)-1,3,5-triazine and polyoxometalates. *Inorganica Chim. Acta,* **2010**, *363* (13), 3186-3193.

(16) Zhang, N.; Li, M.-X.; Wang, Z.-X.; Shao, M.; Zhu, S.-R. Synthesis, structures and thermal stabilities of five copper(II) coordination polymers based on 2,4,6-tris(pyridyl)-1,3,5-triazine and 1,2,4,5-benzenetetracarboxylate ligands. *Inorganica Chim. Acta,* **2010**, *363* (1), 8-14.

(17) Liu, H.-B.; Yu, S.-Y.; Huang, H.; Zhang, Z.-X. Enclathrating benzene in a neutral dicopper(II) coordination framework. *Aust. J. Chem.,* **2003**, *56* (7), 671.

(18) Polunin, R. A.; Burkovskaya, N. P.; Kolotilov, S. V.; Kiskin, M. A.; Bogomyakov, A. S.; Sotnik, S. A.; Eremenko, I. L. Synthesis, structures, sorption and magnetic properties of coordination polymers based on 3d metal pivalates and polydentate pyridine-type ligands. *Russ. Chem. Bull.,* **2014**, *63* (1), 252-266.

(19) Shao, M.; Li, M.-X.; Wang, Z.-X.; He, X.; Zhang, H.-H. Structural diversity and vibrational spectra of nine Cu(I)-cyanide metal-organic frameworks with in situ generated N-heterocyclic ligands. *Cryst. Growth Des.,* **2017**, *17* (12), 6281-6290.

(20) López-Periago, A. M.; Portoles-Gil, N.; López-Domínguez, P.; Fraile, J.; Saurina, J.; Aliaga-Alcalde, N.; Tobias, G.; Ayllón, J. A.; Domingo, C. Metal-organic frameworks precipitated by reactive crystallization in supercritical CO_2. *Cryst. Growth Des.,* **2017**, *17* (5), 2864-2872.

(21) Zhang, B.; Zhang, J.; Han, B. Assembling metal-organic frameworks in ionic liquids and supercritical CO_2. *Chem. - An Asian J.,* **2016**, *11* (19), 2610-2619.

(22) Howarth, A. J.; Peters, A. W.; Vermeulen, N. A.; Wang, T. C.; Hupp, J. T.; Farha, O. K. Best Practices for the synthesis, activation, and characterization of metal-organic frameworks. *Chem. Mater.,* **2017**, *29* (1), 26-39.

(23) Avci-Camur, C.; Perez-Carvajal, J.; Imaz, I.; Maspoch, D. Metal acetylacetonates as a source of metals for aqueous synthesis of metal-organic frameworks. *ACS Sustain. Chem. Eng.,* **2018**, *6* (11), 14554-14560.

(24) Juanhuix, J.; Gil-Ortiz, F.; Cuní, G.; Colldelram, C.; Nicolás, J.; Lidón, J.; Boter, E.; Ruget, C.; Ferrer, S.; Benach, J. Developments in optics and performance at BL13-XALOC, the macromolecular crystallography beamline at the ALBA synchrotron. *J. Synchrotron Radiat.,* **2014**, *21* (4), 679-689.

(25) Kabsch, W. XDS. *Acta Crystallogr. Sect. D Biol. Crystallogr.,* **2010**, *66* (2), 125-132.

(26) Sheldrick, G. M. Crystal structure refinement with SHELXL. *Acta Crystallogr. Sect. C Struct. Chem.,* **2015**, *71* (1), 3-8.

(27) Dolomanov, O. V.; Bourhis, L. J.; Gildea, R. J.; Howard, J. A. K.; Puschmann, H. OLEX2 : A complete structure solution, refinement and analysis program. *J. Appl. Crystallogr.,* **2009**, *42* (2), 339-341.

(28) Spek, A. L. PLATON SQUEEZE: A tool for the calculation of the disordered solvent contribution to the calculated structure factors. *Acta Crystallogr. Sect. C Struct. Chem.,* **2015**, *71* (1), 9-18.

(29) Basham, M.; Filik, J.; Wharmby, M. T.; Chang, P. C. Y.; El Kassaby, B.; Gerring, M.; Aishima, J.; Levik, K.; Pulford, B. C. A.; Sikharulidze, I.; Sneddon, D.; Webber, M.; Dhesi, S. S.; Maccherozzi, F.; Svensson, O.; Brockhauser, S.; Náray, G.; Ashton, A. W. Data analysis WorkbeNch (DAWN). *J. Synchrotron Radiat.,* **2015**, *22* (3), 853-858.

(30) Liu, G.-F.; Zhang, W.-H.; Chen, Y.; Liu, D.; Lang, J.-P. Solvothermal synthesis and crystal structure of a luminescent 2D copper(I) coordination polymer with a (3,4)-connected net. *Inorg. Chem. Commun.,* **2007**, *10* (9), 1049-1053.

(31) Raveendran, P.; Ikushima, Y.; Wallen, S. L. Polar attributes of supercritical carbon dioxide. *Acc. Chem. Res.,* **2005**, *38* (6), 478-485.

(32) Reichardt, C. Solvents and Solvent Effects in Organic Chemistry. Wiley, **2002**.

(33) Addison, A. W.; Rao, T. N.; Reedijk, J.; van Rijn, J.; Verschoor, G. C. Synthesis, structure, and spectroscopic properties of copper(II) compounds containing nitrogen-sulphur donor ligands; the crystal and molecular structure of aqua[1,7-bis(N-methylbenzimidazol-2′-yl)-2,6-dithiaheptane]copper(II) perchlorate. *J. Chem. Soc., Dalton Trans.,* **1984**, 7, 1349-1356.

(34) Macrae, C. F.; Bruno, I. J.; Chisholm, J. A.; Edgington, P. R.; McCabe, P.; Pidcock, E.; Rodriguez-Monge, L.; Taylor, R.; van de Streek, J.; Wood, P. A. Mercury CSD 2.0 - new features for the visualization and investigation of crystal structures. *J. Appl. Crystallogr.,* **2008**, *41* (2), 466-470.

(35) Sing, K. S. W. Reporting physisorption data for gas/solid systems with special reference to the determination of surface area and porosity (Recommendations 1984). *Pure Appl. Chem.,* **1985**, *57* (4), 603-619.

(36) Kitagawa, S.; Kitaura, R.; Noro, S. Functional porous coordination polymers. *Angew. Chemie Int. Ed.,* **2004**, *43* (18), 2334-2375.

(37) Kondo, A.; Kajiro, H.; Noguchi, H.; Carlucci, L.; Proserpio, D. M.; Ciani, G.; Kato, K.; Takata, M.; Seki, H.; Sakamoto, M.; Hattori, Y.; Okino, F.; Maeda, K.; Ohba, T.; Kaneko, K.; Kanoh, H. Super flexibility of a 2D Cu-based porous coordination framework on gas adsorption in comparison with a 3D framework of identical composition: framework dimensionality-dependent gas adsorptivities. *J. Am. Chem. Soc.,* **2011**, *133* (27), 10512-10522.

(38) Reichenbach, C.; Kalies, G.; Lincke, J.; Lässig, D.; Krautscheid, H.; Moellmer, J.; Thommes, M. Unusual adsorption behavior of a highly flexible copper-based MOF. *Microporous Mesoporous Mater.,* **2011**, *142* (2-3), 592-600.

(39) Biradha, K.; Hongo, Y.; Fujita, M. Crystal-to-crystal sliding of 2D coordination layers triggered by guest exchange. *Angew. Chemie Int. Ed.,* **2002**, *41* (18), 3395-3398.

(40) Li, J.-R.; Kuppler, R. J.; Zhou, H.-C. Selective gas adsorption and separation in metal-organic frameworks. *Chem. Soc. Rev.,* **2009**, *38* (5), 1477.

(41) Lagalante, A. F.; Hansen, B. N.; Bruno, T. J.; Sievers, R. E. Solubilities of copper(II) and chromium(III) .beta.-diketonates in supercritical carbon dioxide. *Inorg. Chem.,* **1995**, *34* (23), 5781-5785.

(42) Maverick, A. W.; Fronczek, F. R.; Maverick, E. F.; Billodeaux, D. R.; Cygan, Z. T.; Isovitsch, R. A. structures of anhydrous and hydrated copper(II) hexafluoroacetylacetonate. *Inorg. Chem.,* **2002**, *41* (24), 6488-6492.

CHAPTER-7

Synthesis of bioMOFs in scCO₂

CHAPTER 7 focus on the extension of the scCO$_2$ green methodology for the synthesis of coordination polymers with natural bio-active molecules used as the organic linker. In particular, the synthesis of curcumin and ferulic bioMOFs has been investigated. The crystal growth mechanism of the curcumin bio-MOF in scCO$_2$ is also outlined. This Chapter is based on the published articles:

Portolés-Gil, N.; Lanza, A.; Aliaga-Alcalde, N.; Ayllón, J. A.; Gemmi, M.; Mugnaioli, E.; López-Periago, A. M.; Domingo, C. Crystalline curcumin bioMOF obtained by precipitation in supercritical CO$_2$ and structural determination by electron diffraction tomography. *ACS Sustainable Chemistry & Engineering.* **2018**, 69, 12309-12319.
DOI: 10.1021/acssuschemeng.8b02738

López-Periago, A. M.; Portoles-Gil, N.; López-Domínguez, P.; Fraile, J.; Saurina, J.; Aliaga-Alcalde, N.; Tobias, G.; Ayllón, J. A.; Domingo, C. Metal-organic frameworks precipitated by reactive crystallization in supercritical CO$_2$. *Crystal Growth & Design.* **2017**, 17 (5), 2864-2872.
DOI: 10.1021/acs.cgd.7b00378

7.1. Introduction

Metal-organic frameworks (MOFs) are typically built from transition metals and symmetric petrochemical-derived multidentate organic linkers joined by coordination bonds.[1] The structure of the MOFs is often characterized by an open framework. The attained success in controlling the structure, functionality and porosity of these materials has led to the development of numerous applications for MOFs, most notably in gas adsorption, energy conversion and storage and medicine. Medical applications would require constructions made of biocompatible building blocks, which drive on the development of the topic of metal-biomolecule frameworks or bioMOFs.[2] At present, basics to bond metal ions forming extended bioMOFs with several natural molecules, such as amino acids, peptides, proteins, nucleobases, carbohydrates, cyclodextrins, porphyrins and biological carboxylic acids, have been established.[3,4] However, the flexibility of biomolecules often leads to the generation of amorphous MOFs.[5] Additionally, bioMOFs are preferentially synthetized from nontoxic endogenous cations, such as Ca(II), Mg(II), Fe(III) or Zn(II).

Currently, phytochemicals are emerging as an important natural resource for the synthesis of compounds with biomedical applications, mainly after forming metal complexes.[6] These biomolecules are natural and abundantly available, being easily renewable. Hence, their use in synthesis is considered a sustainable initiative promoting green chemistry. Among the many possible natural products, symmetric molecules are preferred to build bioMOFs, since it has been demonstrated that the organic linker symmetry is a key parameter to prepare highly porous frameworks.[7,8] However, high degrees of symmetry are not often found in biomolecules; barely, a bilateral symmetry is present in *ca.* 7 % of natural products.[9] Some examples of symmetric biomolecules are lycopene, β-carotene and curcumin. This work focusses in the use of curcumin (CCM) and ferulic acid (FA) to synthetize bioMOFs (Fig. 7.1).
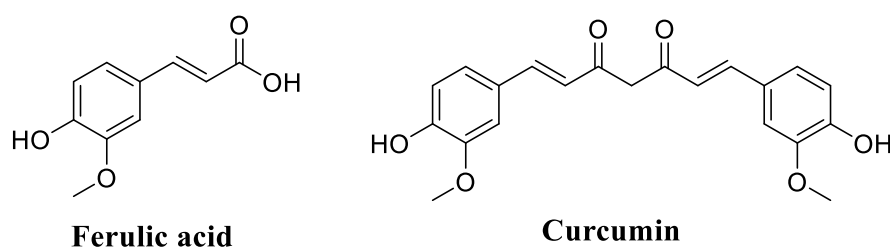

Ferulic acid   **Curcumin**

Figure 7.1. Chemical structures of ferulic acid (*trans*-4-hydroxy-3-methoxycinnamic acid) and curcumin ((1E,6E)-1,7-Bis(4-hydroxy-3-methoxyphenyl)-1,6-heptadiene-3,5-dione).

FA is an important component of widely used medicinal herbs and belongs to the family of hydroxycinnamic acid. Pure form of FA appears as yellowish powder, and it has structural resemblance to curcumin. FA is highly abundant in the leaves and seeds of many plants, especially in cereals such as brown rice, whole wheat, and oats. It has been credited with many pharmacological properties including neuronal progenitor cell proliferation, anti-inflammatory, and neuroprotective activities.[10] The molecule has antioxidant properties that may offer beneficial effects against cancer and cardiovascular diseases.[11] A MOF involving FA and Zn(II) (PhytoMOF-1) is described in the literature, showing photocatalytic activity.[12],[13] Moreover, this bioMOF can be used as a nanocarrier for drug delivery.[14]

CCM is a polyphenolic pigment presents in the turmeric root, to synthetize a bioMOF. Curcumin is one relevant example of a natural compound with C_{2v} bilateral symmetry. Moreover, it is unique in its structure for possessing three ionizable protons, two from the phenolic groups and a third one from the enolic group.[15] As a consequence, curcumin has different metal-binding sites, exhibiting multiple possible coordination modes, a feature that increases its potential structural diversity when used as a multidentate linker for reactions with metals. On this basis, several complexes of metals with curcumin or curcuminoids have been described,[16,17] together with a highly porous 3D MOF(medi-MOF-1), solvothermally synthesized in a mixture of N,N'-dimethylacetamide (DMA) and ethanol (EtOH), with empirical formula $[Zn_3(CCM)_2 \cdot 7(DMA) \cdot 3(EtOH)]_n$.[18]

The published synthesis of both bioMOFs use dimethylformamide (DMF) as a solvent, which is not considered a biocompatible solvent. Moreover, the bioMOFs required activation steps in order to eliminate the residual solvent. The use of scCO₂ in the field of MOFs has been mainly limited to the post-synthesis activation by cleansing entrapped solvents.[19] In a step forward, we have demonstrated that 1D to 3D coordination polymers can be prepared in scCO₂ through reactive crystallization by the right choice of building blocks with suitable solubility in this fluid.[20–23] In this work, our synthetic protocols in scCO₂ have been extended to the construction of a crystalline MOF phases in the CCM/Zn(II) and FA/Zn(II) systems, built exclusively from biologically friendly components and with non-toxic solvents.

The structure of the obtained phase for the FA/Zn(II) was already known. However, the CCM/Zn(II) MOF product is a structurally non-reported compound. The supercritical developed protocol provided high yields of the final material, but did not allow the growth of large crystals for standard single-crystal X-ray analysis. Despite that, the structure of this new

compound was determined *ab initio* by the recently developed electron diffraction tomography method (EDT),[24,25] which has been successfully employed for the structural solution of MOF-like materials,[26,27] and, thereafter, refined against powder X-ray diffraction (PXRD) data.

Control over particle size, crystal habit and secondary porosity in hierarchical systems become crucial for the final implementation of MOFs.[28] For instance, the crystal shape and size of a given MOF would have an important impact on the adsorption behavior, not only in terms of capacity, but especially in terms of adsorption kinetics, which are favored in hierarchical systems. Hence, the research also involves a thorough investigation of the macroscopic crystal growth-habit-size correlation performed by scanning electron microscopy (SEM) imaging. The objective here was to obtain synthetic parameters for tuning the crystal habit and size in the nanometer range and to ascertain feasible crystal growth mechanisms. The focus was on the CCM/Zn(II) phase, since it is a new compound. Beside the use of curcumin in food and cosmetics (as a yellow pigment), the molecule is also interesting from a pharmaceutical point of view for the treatment of chronic illnesses, including cancer, inflammatory and neurological diseases.[29] The main drawback for the clinical application of curcumin is its low solubility in water. This obstacle can be overcome by using different curcumin-based formulations for enhancing the bioavailability.[30] In this sense, bioMOFs find particular applications in drug delivery, as systems capable of releasing an active agent, which is carried by the material as an adsorbate or even as a building block.[31] Preliminary tests of curcumin drug delivery from the synthetized bioMOF in simulated body fluids at neutral physiological pH are presented.

7.2. Experimental

7.2.1. Materials

Curcumin, ferulic acid and zinc acetylacetonate hydrate (Zn(acac)$_2$·xH$_2$O) were purchased from Sigma Aldrich. EtOH was purchased from Panreac. Compressed CO$_2$ (99.95 v%) was supplied by Carburos Metálicos S.A. (Spain).

7.2.2. Equipment and synthesis

BioMOFs preparation in scCO$_2$ was carried out following the protocol described in Chapter 3. In each experiment, the autoclave was charged with *ca.* 100 mg of each solid reagent and 2

mL of EtOH for the experiments with curcumin. Solid reagents were added into a 10 mL Pyrex vial together with a small magnetic stir bar. Ethanol was added either into the vial mixed with the solid reagents or outside, at the bottom of the reactor, physically separated from the solids. In all cases, the vial was capped with filter paper. In a typical experiment, the autoclave was pressurized with CO_2 at 20 MPa at either 313 or 333 K. These working conditions were maintained for a period ranging from 1 to 72 h. The reactor was stirred at 500 rpm, but only during the first 20 min of the running period, although in one experiment stirring was maintained until the end of the process for comparison. Before depressurization, the product was washed off of any possible excess of starting materials with fresh CO_2 in two depressurization/pressurization stages performed from 20 MPa to 7 MPa. Finally, the reactor was depressurized to atmospheric pressure and cooled down to room temperature.

7.2.3. Characterization

The new crystallized compound was analyzed by FTIR, ATR-FTIR spectroscopy and PXRD. The thermal stability was studied by thermogravimetric analysis in N_2 flow. The textural properties were determined by N_2 adsorption/desorption at 77 K. Morphological features were examined by SEM. The used techniques were explained in Chapter 3.

A singular characterization protocol was followed for the structural analysis of the new precipitated phase CCM/Zn(II), based on EDT.[24,32] EDT data was collected by a Zeiss Libra 120 transmission electron microscope (TEM) equipped with LaB_6 electron source, in-column omega energy filter and Nanomegas Digistar P1000 for beam precession. A parallel beam of about 150 nm in diameter was obtained in Köhler illumination by the insertion of a 5 μm condenser aperture, and the crystal position was tracked in scanning-transmission electron microscopy (STEM) mode. 3D diffraction data were acquired in steps of 1° in precession-assisted nano-diffraction mode (precession angle 1°) and recorded by an ASI MEDIPIX single electron detector camera (14 bit, 512×512 pixels), after filtering out the inelastic scattering.[25,33,34] The high sensitivity of the MEDIPIX detector allows data collections under low illumination conditions (dose <0.05 el $s^{-1}Å^{-2}$) avoiding the beam damage of beam sensitive materials like MOFs. Data analysis, including 3D diffraction volume reconstruction, cell parameter determination and reflection intensity integration, was performed combining ADT3D[35] and PETS packages.[36] Data collected in this way can be treated according to the kinematical approximation $I_{hkl} \sim |F_{hkl}|^2$. Structure determination was obtained *ab initio* by direct methods implemented in the software SIR2014.[37] For Rietveld refinement, a powder

XRD pattern was collected in the range 5-70° 2θ with a step of 0.02° and a time step of 5 s, by using a Bruker-AXS (A25 D8 Discover). The solved structure corresponds to compound sc-CCMOF-1 and it is available from the CSD with deposition number CCDC 1845203.

Table 7.1. Structural and EDT experimental details of sc-CCMOF-1.

Crystallographic details		EDT data collection and structure determination	
Formula	$Zn(C_{21}H_{18}O_6)$	TEM type	Zeiss Libra 120
Formula weight, g mol⁻¹	431.74	Accelerat. voltage, kV	120
Space group	$P2_1/n$	λ, Å	0.0335
a, Å	12.0	Tilt range, °	100 + 56*
b, Å	15.6	Tilt step, °	1
c, Å	11.2	Data resolution, Å	1.0
α, °	90	Independent reflection coverage, %	94
β, °	99.6	R_{int}, %	19.33
γ, °	90	R_{SIR}, %	33.85
V, Å³	2070		
N° independent atoms (non-H)	28		

*: the intensity data set was obtained merging two EDT acquisitions obtained from two independent crystals.

Table 7.2. PXRD experimental parameters summary and Rietveld refinement results.

PXRD data collection and Rietveld refinement		Refined lattice parameters	
Diffractometer type	Bragg-Brentano	a, Å	12.0164(22)
Radiation	$CuK\alpha_{1,2}$	b, Å	15.5754(13)
Average λ, Å	1.5418	c, Å	11.2140(22)
2θ range, °	5.0 – 70.0	α, °	90
2θ step, °	0.02	β, °	99.643(9)
d-spacing resolution, Å	1.343	γ, °	90
		V, Å³	2069.17(24)
		Observations	3229
		Reflections	896
		Refined parameters	60
		R_{exp}, %	0.493
		R_p, %	3.032
		R_{wp}, %	4.129
		R_F, %	4.195
		R_{F^2}, %	10.081

The percentage of drug released from the synthetized curcumin MOF over time in physiological 0.1 M phosphate buffer at neutral pH (7.4) was followed using ultra violet-visible (UV-Vis) spectrometry. A calibration curve was first done by measuring the absorbance of curcumin solutions in this buffer at 345 nm. The range of concentrations used was between 1.4 10^{-5} and 3.6 10^{-4} M. For the release measurements, a certain amount of each sample, weighted to give *ca.* 10 mg of curcumin, was dispersed in 70 mL of phosphate buffer. The dispersion was kept under vigorous stirring for periods ranging from 24 to 168 h. Aliquots were taken at different times, filtered and measured in the spectrophotometer. A similar experiment was performed with commercial curcumin for comparison.

7.3. Results and discussion

7.3.1. Reagents behavior in scCO$_2$

A preliminary series of tests were performed to assess the behavior of the different components in the synthetic medium.

Ferulic acid

Comercial ferulic acid powder was treated in scCO$_2$ at 20 MPa and 313 K for 24 h under stirring. The structural characteristics of the recovered powder, examined by XRD (Fig. 7.2), were not affected by the supercritical treatment.
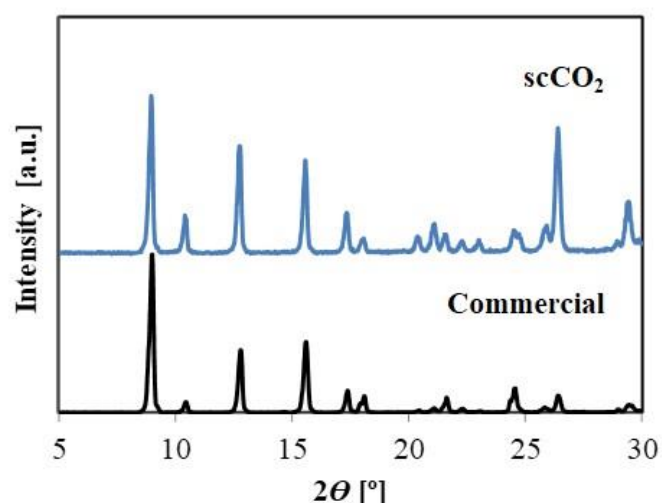
Figure 7.2. Powder XRD structural characterization of FA before and after supercritical treatment.

Similarly, the ATR-FTIR spectra (Fig. 7.3) of the raw and treated samples revealed the presence of all characteristic peaks of ferulic acid.[12] In them, the peaks in the range of 3100-

3600 cm⁻¹ are the ones corresponding to the stretching region of hydroxyl moieties. The peak at 1690 cm-1 corresponds to carboxylic acid C=O stretching. Signals at 2950, 2850, 1512, 1350 and 962 cm⁻¹ relate to C-H vibrations. The peak at 1602 cm⁻¹ is attributed to symmetric aromatic C=C stretching vibrations.
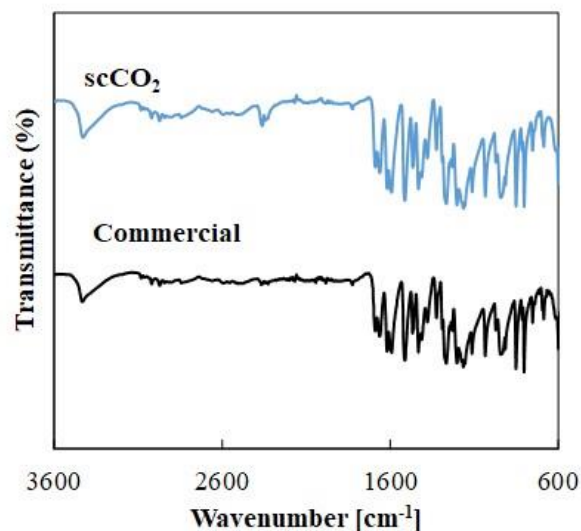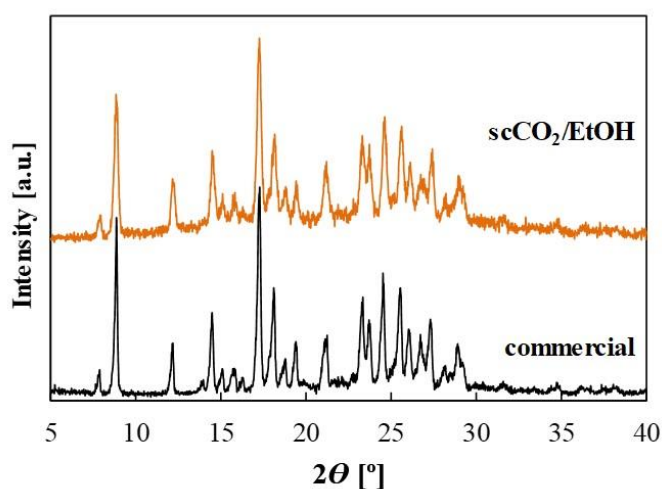

Figure 7.3. ATR-FTIR spectra characterization of FA before and after supercritical treatment.

Curcumin

Pristine curcumin powder was treated in $scCO_2$/EtOH at 20 MPa and 313 K for 24 h under stirring. The structural characteristics of the recovered powder, examined by XRD (Fig. 7.4), were not affected by the supercritical treatment.

Figure 7.4. Powder XRD structural characterization of CCM before and after supercritical treatment.

Similarly, the ATR-FTIR spectra (Fig. 7.5) of the raw and treated samples revealed the presence of all characteristic peaks of curcumin.[38] In them, the stretching region of hydroxyl moieties appears as a broad band in the range of 3100-3600 cm^{-1}. Signals at 2950, 2850, 1512, 1350 and 962 cm^{-1} relate to C-H vibrations. The strong signal at 1626 cm^{-1} is described as having a (C=C)/(C=O) mixed character. The nearby sharp peak at 1602 cm^{-1} is attributed to symmetric aromatic C=C stretching vibrations. The peak at 1506 cm^{-1} relates to C=O, while the enol C-O and the C-O-C vibrations are observed at 1280 cm^{-1} and 1026 cm^{-1}, respectively.
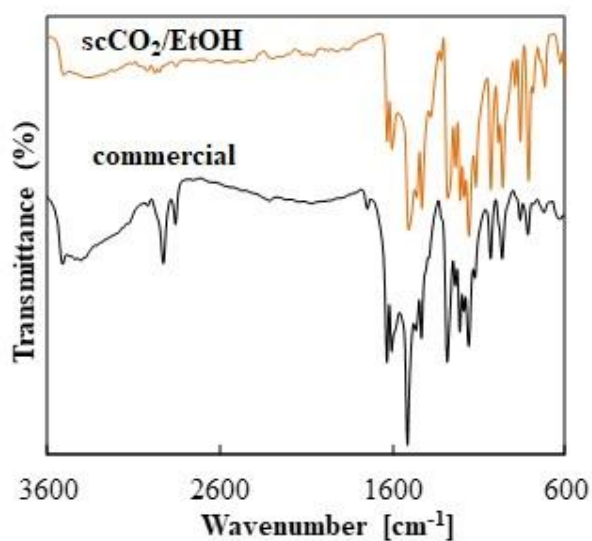
Figure 7.5. ATR-FTIR spectra characterization of CCM before and after supercritical treatment.

As observed in the SEM micrographs of Fig. 7.6(a,b) the morphology was not significantly modified by the treatment. Only a small reduction on mean particle size was appreciated, likely due to surface dissolution of curcumin crystals in the mixture scCO₂/EtOH.
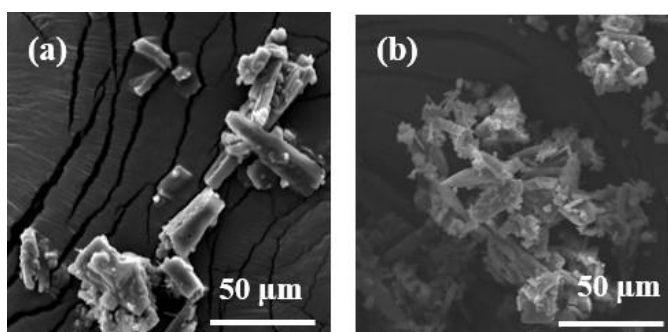
Figure 7.6. SEM micrographs of the used reagents for MOF synthesis before and after supercritical treatment: (a) raw curcumin, (b) treated curcumin.

Zn(II) acetylacetonate

A more complex behavior was observed after exposing $Zn(acac)_2 \cdot xH_2O$ reagent to $scCO_2$ and EtOH. XRD analysis indicates that the working conditions triggered the transformation of this crystalline solid into an amorphous phase (Fig. 7.7(a)). A similar XRD pattern was obtained by treating the sample exclusively with $scCO_2$ (Fig. 7.7(a)), indicating the significance of this solvent *vs.* EtOH in the amorphization process. Indeed, the micrometric acicular crystals of commercial $Zn(acac)_2$ became spherical nanoparticles of amorphous appearance in the presence of $scCO_2$ or $scCO_2$ plus EtOH (Fig. 7.7(b,c)).
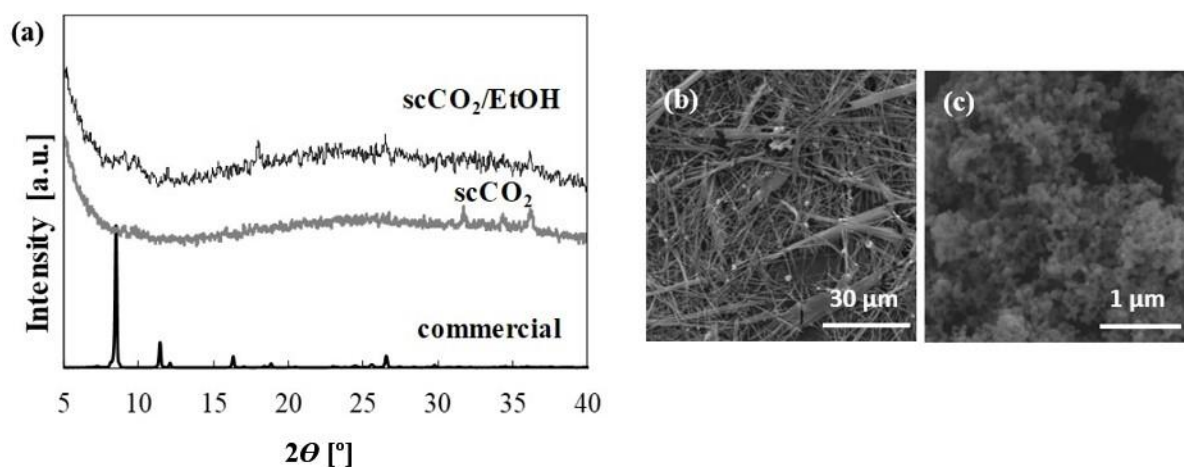
Figure 7.7. (a) Powder XRD structural characterization of $Zn(acac)_2$ before and after supercritical treatment, (b and c) SEM micrographs of curcumin used for MOF synthesis before (b) and after (c) supercritical treatment

The transformation was further studied by infrared spectroscopy. The prominent peaks in the ATR-FTIR spectrum of hydrated $Zn(acac)_2$ (Fig. 7.8) have been described as follows:[39] a broad band centered at 3190 cm^{-1}, that indicates water present in the precursor; C-H signals at 3000, 2920 and 1188 cm^{-1}; C=C and C=O peaks at 1592 cm^{-1} in addition to C=O and C-H at 1446 cm^{-1}; CH_3 at 1392, 1360 and 1017 cm^{-1}; C-C at 1258 cm^{-1}; and C-CH_3 at 932 and 655 cm^{-1}. After supercritical treatment, the intensity of the broad water band at 3190 cm^{-1} was significantly reduced, indicating dehydration of the precursor in $scCO_2$, which can be the reason of the amorphization. The anhydrous $Zn(acac)_2$ has a complex twinned trimeric structure in zinc $(Zn_3(C_5H_7O_2)_6)$,[40] responsible for the shift observed in the C=O and C=C bands with respect to the dimeric $Zn(acac)_2 \cdot xH_2O$ species (Fig. 7.8). The anhydrous derivative has been described as a more volatile product than the hydrated phase.[41]
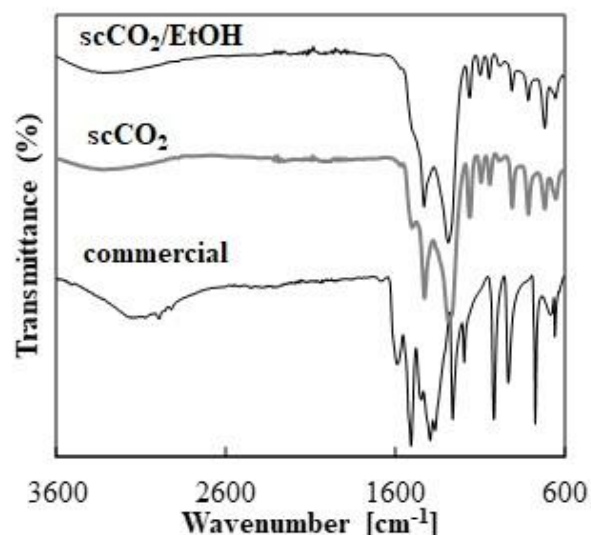
Figure 7.6. Infrared characterization of products and reagents before and after supercritical treatment: ATR-FTIR spectra of $Zn(acac)_2$.

Moreover, the decomposition of $Zn(acac)_2$ into ZnO in alcohol during solvothermal synthesis is a process widely described in the literature.[42] To check if this transformation took place in the supercritical studied system, samples from the blank test were analyzed by FT-IR spectroscopy up to 400 cm^{-1}, since ZnO is characterized by a broad band centered at *ca.* 450 cm^{-1}. In this region, The $Zn(acac)_2$ displayed a sharp band at *ca.* 430 corresponding to Zn-O stretching.[39] The broad band assigned to ZnO was only observed for the sample obtained in the presence of $scCO_2$ plus EtOH, and not for the sample processed with $scCO_2$ exclusively (Fig. 7.9). The $Zn(acac)_2$, as a reactive metal chelate, is susceptible of the attack of protic solvents. Under solvothermal conditions, the mechanism of $Zn(acac)_2$ conversion into ZnO relies on the nucleophilic attack of the alcohol to the carbonyl group of the acetylacetonate ligand, followed by the hydrolytic formation of reactive Zn-OH intermediates, which polycondensate forming ZnO.[42] This transformation did not take place in RT liquid ethanol, but could be favored in the supercritical medium due to the acidity conferred to the ethanol by the dissolved CO_2. Hence, we can conclude that amorphized $Zn(acac)_2$, likely during dehydration, is the main reagent present along the supercritical crystallization path, together with some ZnO.
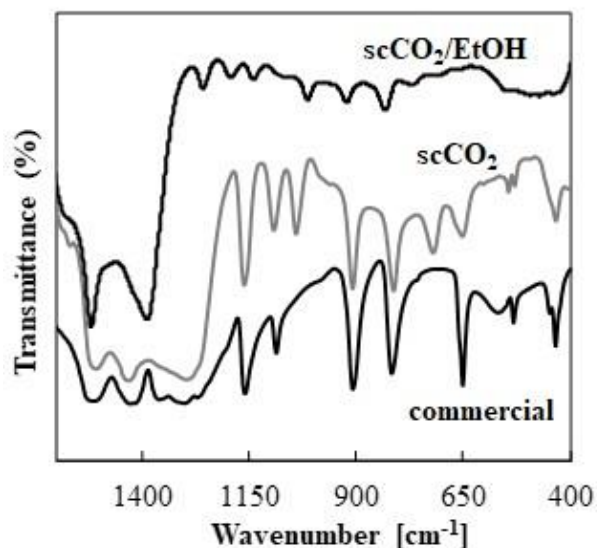
Figure 7.9. Infrared characterization (FTIR) of $Zn(acac)_2$ before and after supercritical treatment.

7.3.2. Synthesis and characterization of FA bioMOF

The synthesis of a FA bioMOF in $scCO_2$ (sample sc-$[Zn_2(F)_2]_n$) was carried out from a mixture of FA and $Zn(acac)_2$. A FA/Zn(II) bioMOF was thus obtained after 48h. PXRD indicates that the precipitated compound has the same crystalline structure than the previously described phase $[Zn_2(F)_2]_n$, named as phytoMOF-1 (Fig. 7.10).[12] PhytoMOF-1 has a 3D structure and contains channels with a considerable diameter of 15-17 Å (Fig. 7.11). Even not being a new compound, this was the only 3D MOF that could be precipitated in this thesis using the $scCO_2$ technology.
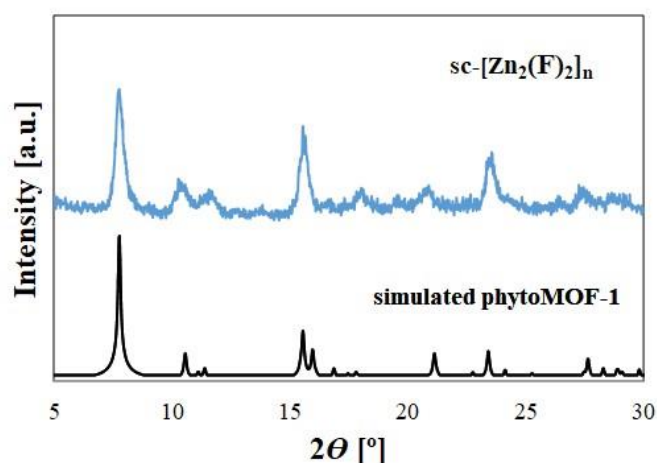
Figure 7.10. PXRD patterns of $[Zn_2(F)_2]_n$ precipitated in $scCO_2$ and simulated from phytoMOF-1 single crystal data.[12]
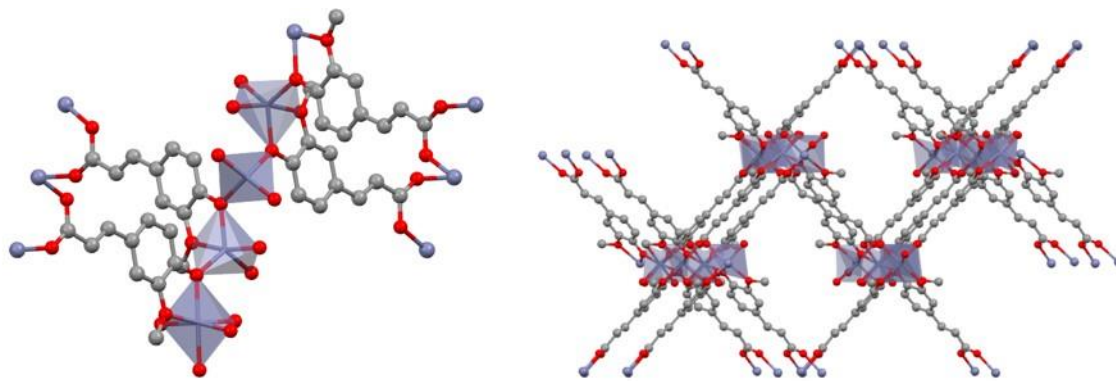
Figure 7.11. Asymmetric unit and 3D structure of the $[Zn_2(F)_2]_n$ bioMOF (taken from CCDC 1019392 deposited crystallographic data).

The theoretical total void volume of PhytoMOF-1 is calculated as 3.517 $\mathring{A}^3$/molecula. However, this high value is not reflected in the N_2 adsorption/desorption analysis. For both PhytoMOF-1, i.e., obtained in either DMF or scCO₂specific surface areas were in the order of 250 $m^2 \cdot g^{-1}$. The adsorption isotherm indicates that the precipitates are mainly microporous (Fig. 7.12).
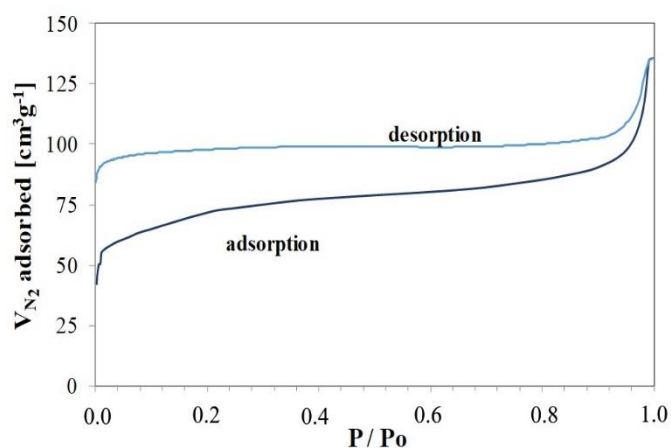

Figure 7.12. N_2 adsorption/desorption isotherm of the supercritically precipitated $[Zn_2(F)_2]_n$ bioMOF.

SEM analysis indicates that the precipitated system in scCO₂ is constituted by aggregated small particles (Fig. 7.13). This aggregates give to the sample the mesoporosity observed at high relative pressures in the N_2 adsorption/desoprtion isotherm (Fig. 7.12).
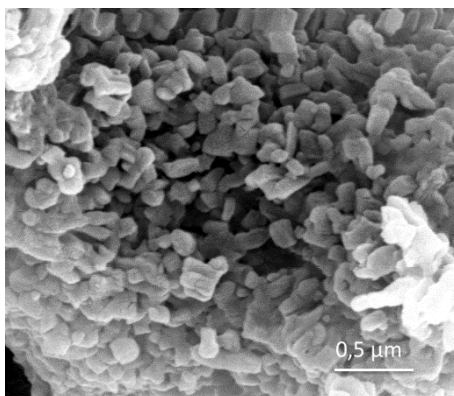
Figure 7.13. SEM micrograph of the supercritically precipitated [Zn$_2$(F)$_2$]$_n$ bioMOF.

7.3.3. Synthesis and characterization of CCM bioMOF

The synthesis of a curcumin bioMOF in scCO$_2$ (sample sc-CCMOF-1) was carried out from a mixture of CCM, Zn(acac)$_2$ and EtOH. This system was chosen because, on the one hand, the efficient extraction of curcumin pigment from turmeric rhizome by mixtures of scCO$_2$ and EtOH is a process widely described in the literature;[43,44] and, on the other, the chosen organometallic complex, Zn(acac)$_2$, has a significant solubility in scCO$_2$, with values in the order of 10^{-3} molL^{-1} at 313 K and 20 MPa.[45] In the standard supercritical experiment, 2 v% of EtOH with respect to the volume of CO$_2$ was added to the vial holding the solid reagents, and the mixture was maintained at 313 K and 20 MPa during 72 h. To favor the formation of well-shaped crystals, stirring was stopped after the first 20 min of reaction. An orange crystalline precipitate was recovered. Fig. 7.14 shows the recorded XRD pattern for the experimental sc-CCMOF-1 sample, which does not have any resemblance with the solvothermal phase previously published in ref. 18, termed by the authors as medi-MOF-1, indicating a different crystal structure. In this spectrum, the three peaks located between 2θ=30-40º corresponded to ZnO, formed by the partial decomposition of Zn(acac)$_2$. Infrared spectroscopy showed that the sc-CCMOF-1 sample mainly depicted the curcumin bands (Fig. 7.15). ATR-FTIR indicates that the sample do not contain a significant amount of water. Moreover, in the FTIR the Zn-O bond in the MOF is represented by a band at *ca.* 480 cm^{-1}. This band can also have some contribution from the side product ZnO.
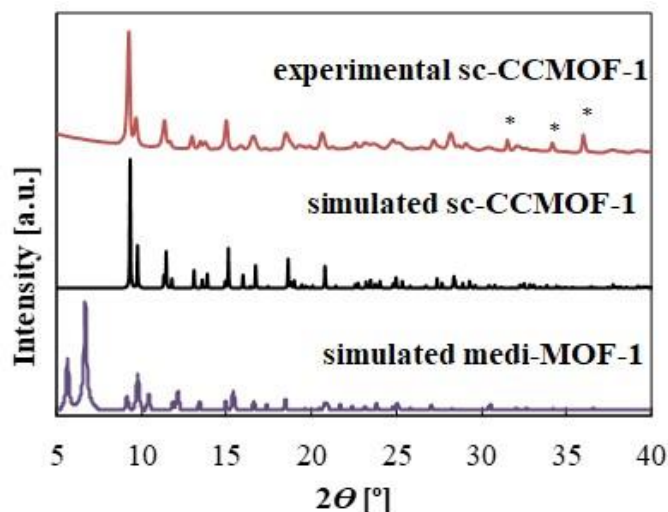
Figure 7.14. Powder XRD structural characterization of synthetized samples: (a) experimental profile of the sc-CCMOF-1 phase precipitated at running times higher than 20 h (* marks the peaks corresponding to ZnO), simulated from data obtained after crystal elucidation, and simulated pattern for medi-MOF-1 phase from ref. 18.
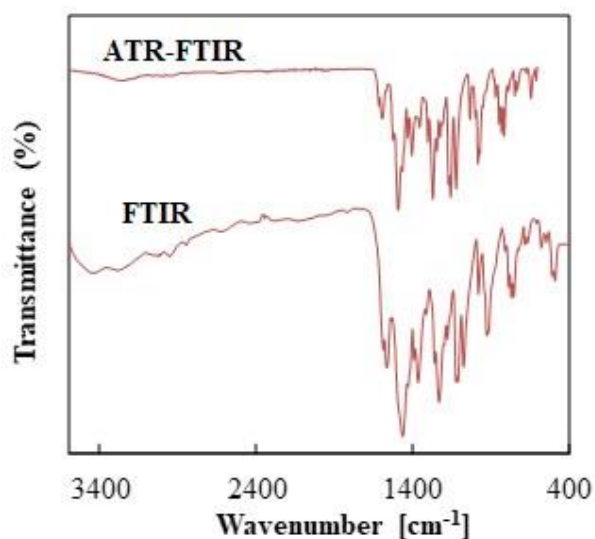

Figure 7.15. Infrared characterization, ATR-FTIR and FTIR spectra of the supercritically precipitated MOF.

The XRD pattern of the sample obtained in the 72-h stirring experiment depicted the same diffraction lines than sc-CCMOF-1. A different scenario was found in samples obtained by adding 2 v% of EtOH out of the vial containing the solid reagents. In this case, after 72 h at 313 K and 20 MPa, XRD analysis indicated that the curcumin did not reacted with $Zn(acac)_2$, and the spectrum displayed only peaks from CCM and the halo of amorphous $Zn(acac)_2$. Using the latest set-up, the temperature must be increased to 333 K to obtain a solid with the pattern found for the sc-CCMOF-1, although it was slightly contaminated with residual

curcumin. Finally, by increasing the running time to 7 days, the residual curcumin peaks disappeared from the XRD pattern.

The supercritical developed protocol provided high yields of the final material, but did not allow the growth of large crystals for standard single-crystal X-ray analysis. Therefore, classical solvothermal crystallization techniques were applied with the aim of precipitating large crystals. In this cases, the use of solvent mixtures involving ethanol and basic DMA led to the precipitation of medi-MOF-1 phase.[18] Under solvothermal conditions, the reaction between curcumin and $Zn(acac)_2$ was also tested in EtOH in the absence of $scCO_2$. The initial mixture of reagents in EtOH was prepared under ambient conditions, resulting in the immediate precipitation of an amorphous solid (Fig. 7.16, EtOH 298 K pattern), constituted by spherical nanoparticles (Fig. 7.17(a,b)). Applying solvothermal heating to this suspension, at either 333 or 353 K in 72 h runs, produced the formation of a crystalline precipitate (Fig. 7.16, EtOH 333 K pattern). The recorded diffractograms of the powders obtained at both temperatures were similar. However, this pattern did not match either the published phase medi-MOF-1 or the one described in this article as sc-CCMOF-1. Indeed, a new structure was obtained, whose solution is still pending. The solid was constituted by large (> 100 μm) spherical particles with spherulitic habit (Fig. 7.17(c,d)).
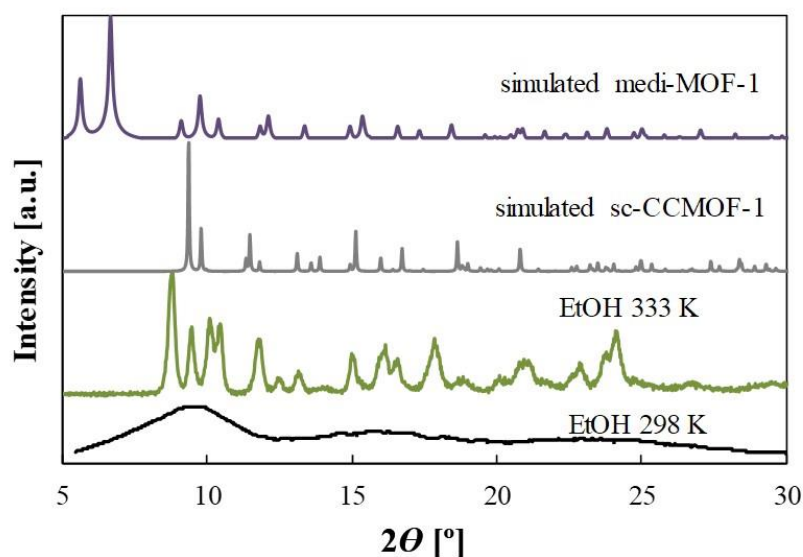

Figure 7.16. Characterization of the solids precipitated in pure EtOH at different temperatures. Patterns of described Zn/CCM phases are also included for comparison.
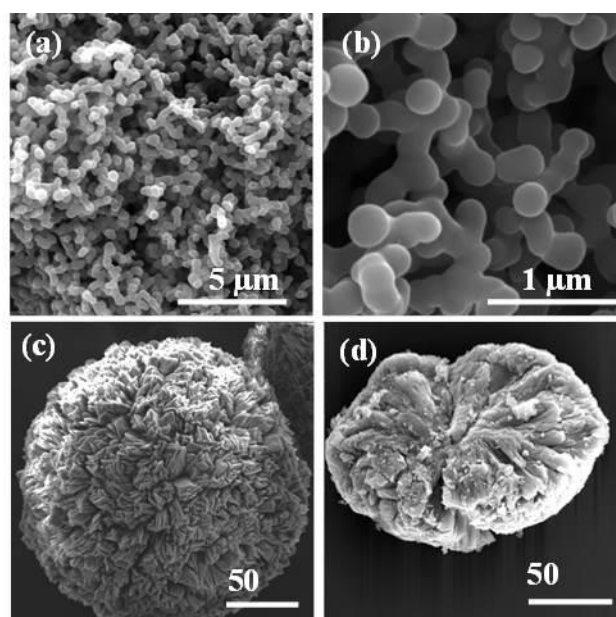
Figure 7.17. SEM images of the solid particles prepared in EtOH under different experimental conditions: (a,b) nanoparticles obtained at 298 K after 1 h run, and (c,d) microspheres precipitated at 333 K with a crystallization time of 72 h.

The structure of this new compound was determined *ab initio* by the recently developed electron diffraction tomography method (EDT). From the different set-ups used in the preparation of sc-CCMOF-1, the sample chosen for the elucidation of the crystal structure was obtained from an experiment where the ethanol was added physically separated from the rest of the reagents, in a non-stirred system. EDT data were recorded from two crystals of less than 1 μm in size, using the beam precession method for improving intensity data quality[20] and the in-column omega energy filter for cutting out most of inelastic scattering.[28] The two data sets, with tilt ranges respectively of 100° and 56°, delivered a monoclinic unit cell with approximate parameters a=11.9(2) Å, b=15.7(3) Å, c=11.1(2) Å, β=99.1(10)° (Fig. 7.18). Systematic absences were consistent with the extinction symbol '$P12_1/n1$'. Structure solution was obtained in space group $P2_1/n$ after merging the two intensity data sets, resulting in the *ab initio* localization of all non-H atoms of the MOF framework (Table 7.1).
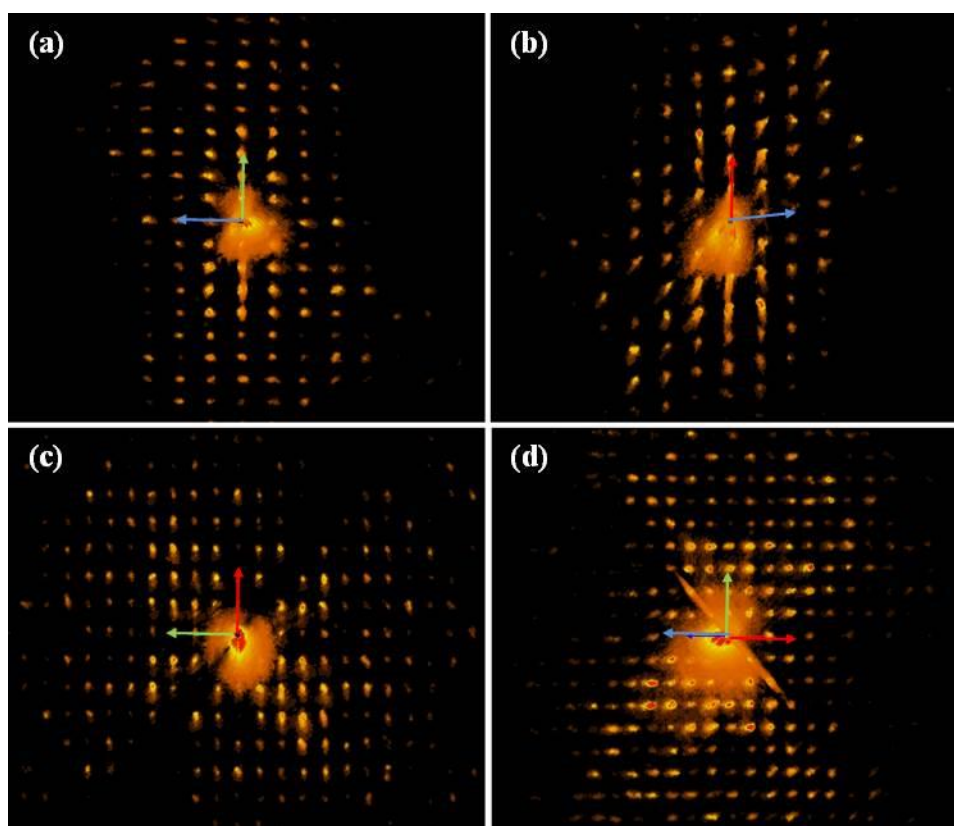
Figure 7.18. EDT reconstructed 3D diffraction volume for sc-CCMOF-1 sample: (a) view along 100*, (b) view along 010*, (c) view along 001*, and (d) view along 101*. Extinct reflections columns $h0l$: $h + l \neq 2n$ can be recognized in (d) and derive from the n-glide plane. Note that these are projections of a 3D diffraction volume and not conventional 2D electron diffraction patterns. Red arrow points along $a*$, green arrow along $b*$ and blue arrow along $c*$.

The obtained structural model was preliminarily refined with SHELXL-2016/6[41] *via* the WinGX interface.[42] The pattern showed impurity peaks due to the presence of ZnO.[43] Thanks to the much smaller unit cell parameters and high symmetry, the overlap with the phase of interest is minimal and ZnO could be included in the refinement with no detrimental effects and negligible increase in the number of parameters.

The bond distances for the linker were restrained to the values found for curcumin in similar published structures.[13,44] C-bonded hydrogen atoms were placed in calculated positions and refined with a riding model. All atoms were finally refined with isotropic thermal parameters. The obtained model was used as input for Rietveld refinement in GSAS-II (Figs. 7.19 and Table 7.2).[45] The background was described by fitting manually-picked fixed points with a 24th order Chebyschev polynomial, and it was thereafter kept fixed. Initial pseudo-Voigt profile parameters were empirically refined to obtain a good fit on the ZnO peaks, which were systematically sharper than the sc-CCMOF-1 peaks. The pre-refined single crystal model was

used as starting coordinates for the MOF phase. Moreover, a rigid body model for curcumin was created with the programs Mercury[40] and Avogadro[43] from the single-crystal coordinates. Selected torsion angles (highlighted in Fig. 7.20) were set as refineable, allowing for deviations from planarity of the molecule. Then the x, y, z coordinates and U factor were freely refined for Zn, while the position, orientation, overall U factor, and torsion angles were refined for the linker.
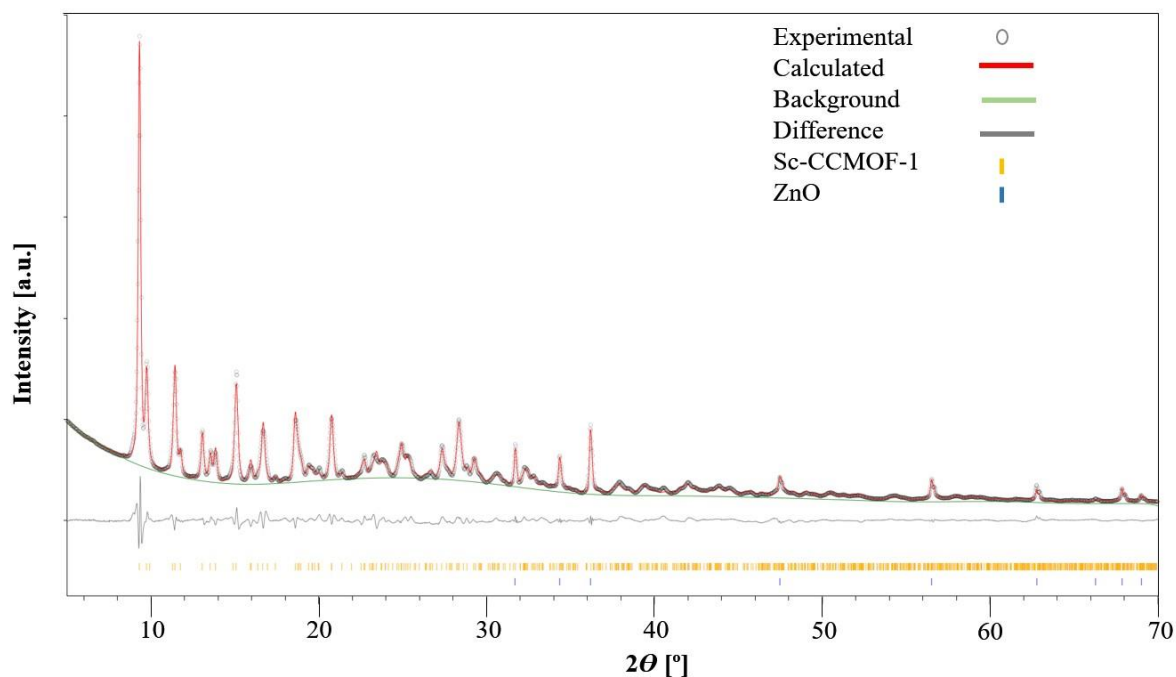

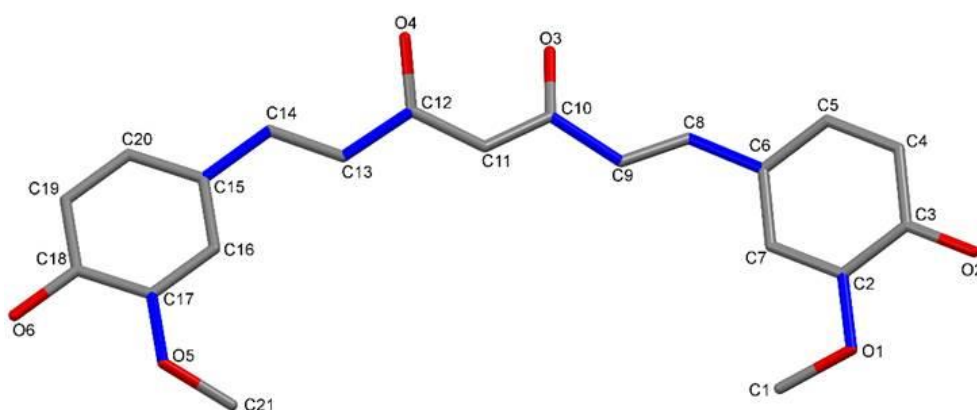**Figure 7.19.** Final Rietveld refinement.

Figure 7.20. Rigid body model of curcumin. Those torsion angles around the bonds highlighted in blue were set as refineable.

Moreover, additional parameters, including phase fraction, size and strain, and preferred orientation, were refined for both phases to improve the fitting. All variables were

alternatively refined until convergence. Finally, C-bonded H atoms were added in calculated positions and final refinement cycles were performed.

Fig. 7.21(a) shows the coordination mode of CCM. The unit cell contains four CCM molecules and four Zn atoms, thus implying one-unit formula per asymmetric unit. As an effect of symmetry, metal atoms are clustered in two edge-sharing ZnO_5 trigonal pyramids, thus building Zn_2O_8 secondary building units (SBUs) (Fig. 7.21(b)).

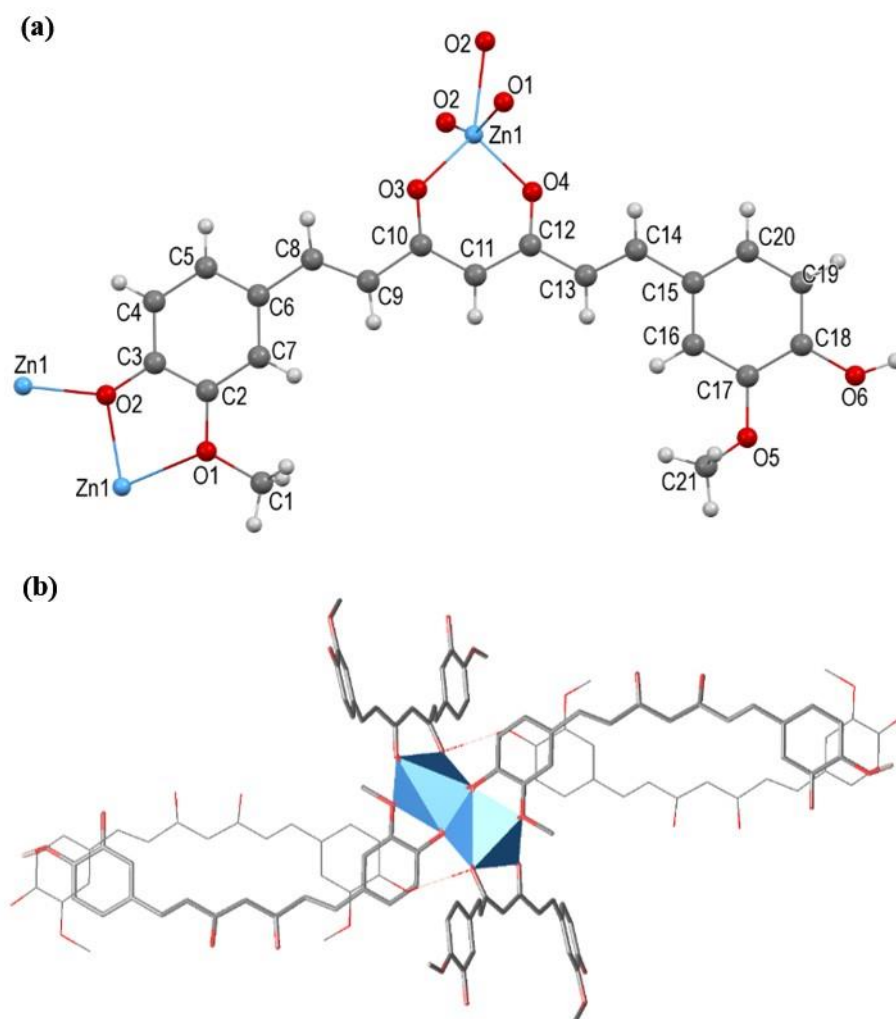**Figure 7.21.** Schematic representation of the crystal structure of the sc-CCMOF-1: (a) the coordination mode of CCM, (b) the Zn_2O_8 SBU consisting of two edge-sharing ZnO_5 trigonal pyramids. The H atom on the O6 hydroxyl oxygen is drawn at the calculated ideal coordinates that would optimize the expected H-bond with a neighboring coordinated O4. Such inferred H-bonds are represented as dashed lines in (b).
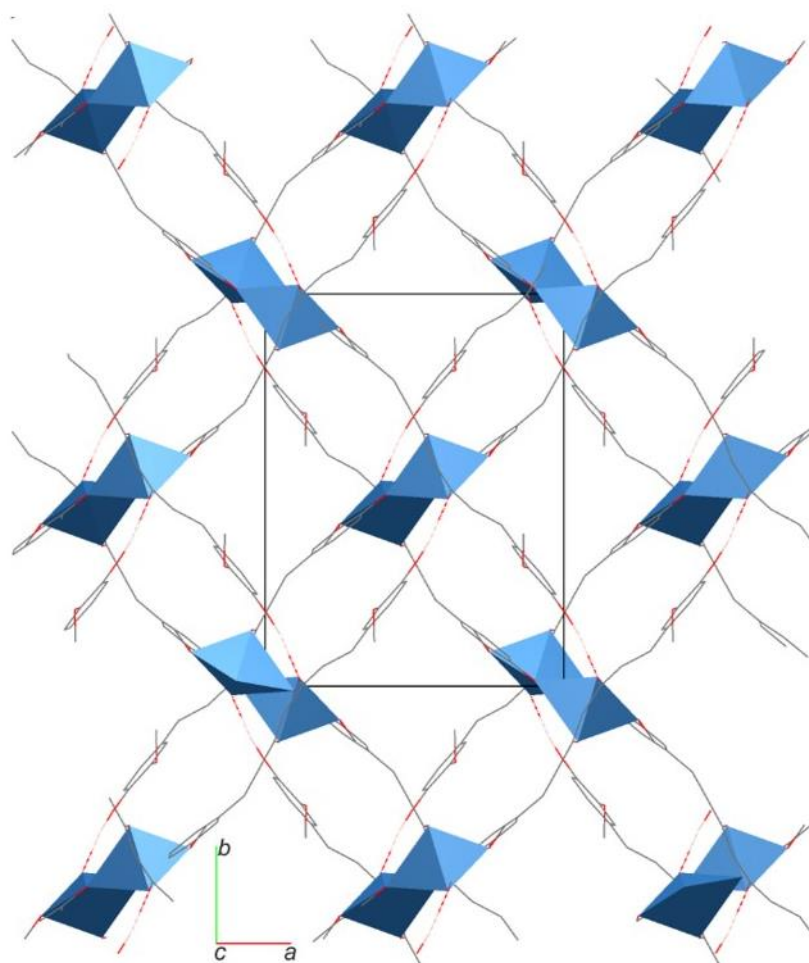
Figure 7.22. Schematic 2D framework representation of the crystal structure of the sc-CCMOF-1. The H atom on the O6 hydroxyl oxygen is drawn at the calculated ideal coordinates that would optimize the expected H-bond with a neighboring coordinated O4. Such inferred H-bonds are represented as dashed lines.

Each SBU is connected by covalent bonds to four CCM anions that act as bridges between pairs of metal clusters. CCM is doubly deprotonated, with one negative charge on the central enolic group and the other one at one terminal phenolic group. Both groups act as chelating binding sites, forming 6- and 5-membered metallocycles, respectively, with Zn ions belonging to different clusters. CCM acts, therefore, as an L-shaped bridge, and the four linkers around each Zn-cluster are oriented in two almost orthogonal directions, building an infinite 2D corrugated layer, extending along the (1 0 1) crystallographic plane. It is very likely that in the 3rd direction the layers are connected by H-bonds involving the remaining neutral phenolic groups as donors and coordinated enolic O as acceptors. As a result, the layers are closely stacked, forming a stable 3D supramolecular structure (Fig. 7.22 and Fig. 7.23).
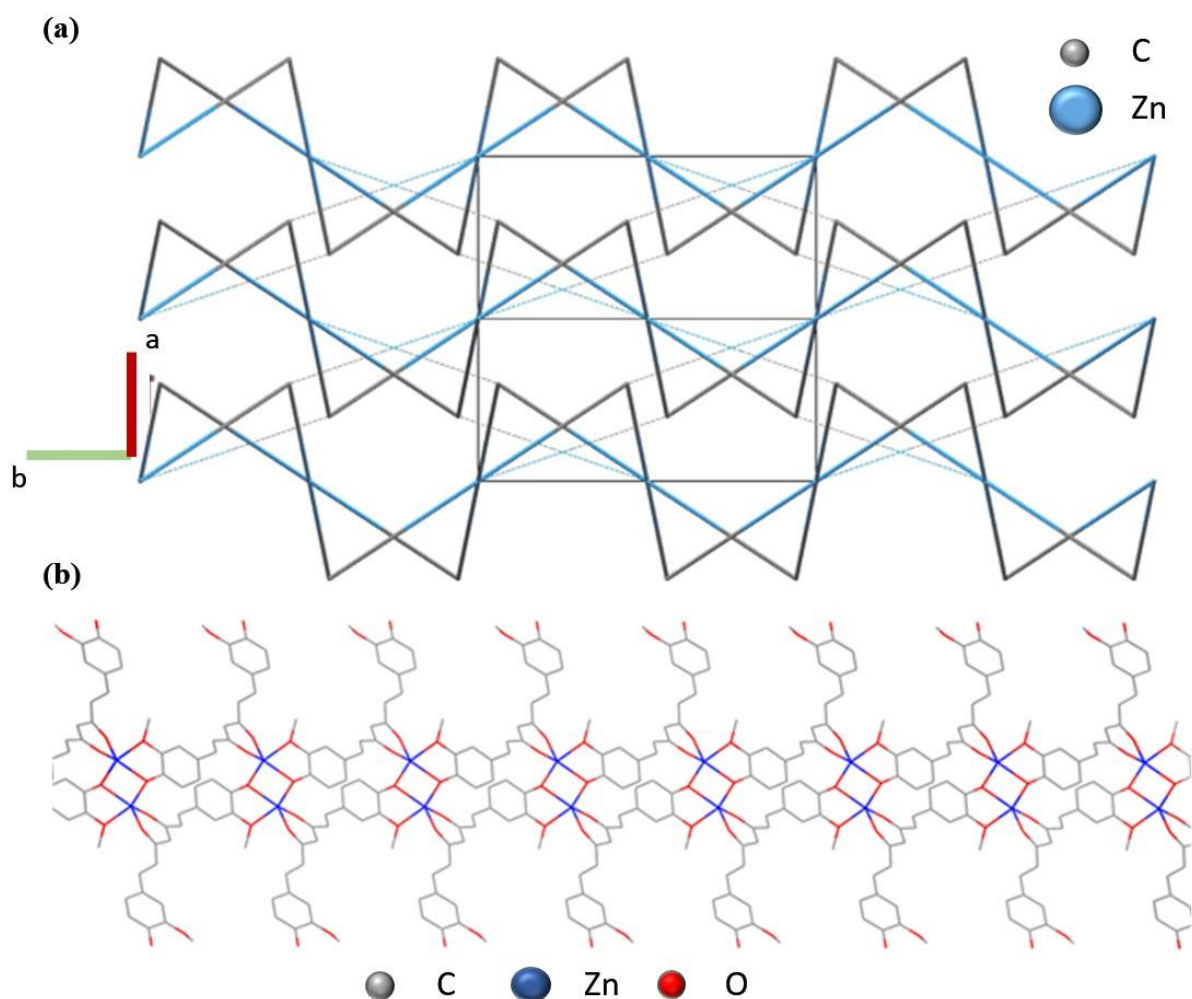
Figure 7.23. Simplified representation of the crystal structure of the sc-CCMOF-1, (a) viewed along the *b* axis. ZnO_n polyhedra are represented in blue and linkers are represented as grey linkers. By considering only covalent bonds (thick solid lines) the linker acts as a L-shaped ditopic linker bridging neighboring Zn atoms forming corrugated layers stacked along the *a* axis. Expected hydrogen bonds (thin dashed lines) cross link the layers forming a non-covalent 3D framework, in which the linkers act as T-shaped tritopic linkers; and (b) cross-section view of the layers.

A divalent negative charge and the observed di-chelating L-shaped bridging coordination geometry are unprecedented for crystal structures of metallo-curcuminoids.[51] In most of the published structures, curcumin is deprotonated at the central diketo/enolic group and acts as a monotopic chelating linker forming heterolinker molecular or 1D coordination compounds with several metals. The only reported case in which curcumin is acting as a bridging group is the case of the already mentioned medi-MOF-1 reported by Hu *et al.* in ref. 18 [CSD Ref. code CUBBEI]. In such MOF, all OH groups of curcumin are deprotonated and the resulting negative trivalent curcuminate anion acts as a T-shaped μ_3-linker, forming a highly porous 3D covalent network, with a Zn^{II}:CCM molar ratio of 3:2. In the $scCO_2$ route, despite starting from a reagents molar ratio close to 3:2, the final product has 1:1 molar ratio, depending on

the partial deprotonation of the linker. The lability of the Zn-CCM bonds combined with the lack of bulky solvents available to be incorporated to the structure in the scCO₂ reaction media and the high reaction/nucleation velocity could explain why in supercritical conditions a 2D compound is obtained instead of the solvothermally precipitated 3D product. For slow crystal growth methods, in which the MOFs self-assembly process occurs in solution, labile metal-ligand bond formation enables the development of complex coordination geometries, in which the linker is bonded through all its coordination sites.[52] On the contrary, fast nucleation attained in scCO₂ lead to the formation of sc-CCMOF-1, in which the CCM have only two chelating binding sites coordinated to the metal.

Synthetized sc-CCMOF-1 was thermally stable up to *ca.* 590 K in an inert atmosphere (Fig. 7.24(a)), which is a reasonably high value for a MOF. After this temperature, the sample sharply decomposed in two steps. The weight loss before 400 K was lower than 1 wt%, thus indicating the lack of adsorbed water in the compound.

Processed sc-CCMOF-1 samples gave consistent BET surface area values in the order of 300-350 m^2g^{-1}, from which *ca.* 250 m^2g^{-1} corresponded to micropore, with BJH pore volumes in the order of 0.1 cm^3g^{-1}. The adsorption/desorption isotherm shown in Fig. 7.24(b) indicates that the sample is essentially microporous, with only a small contribution of mesopores assigned to interparticle voids.
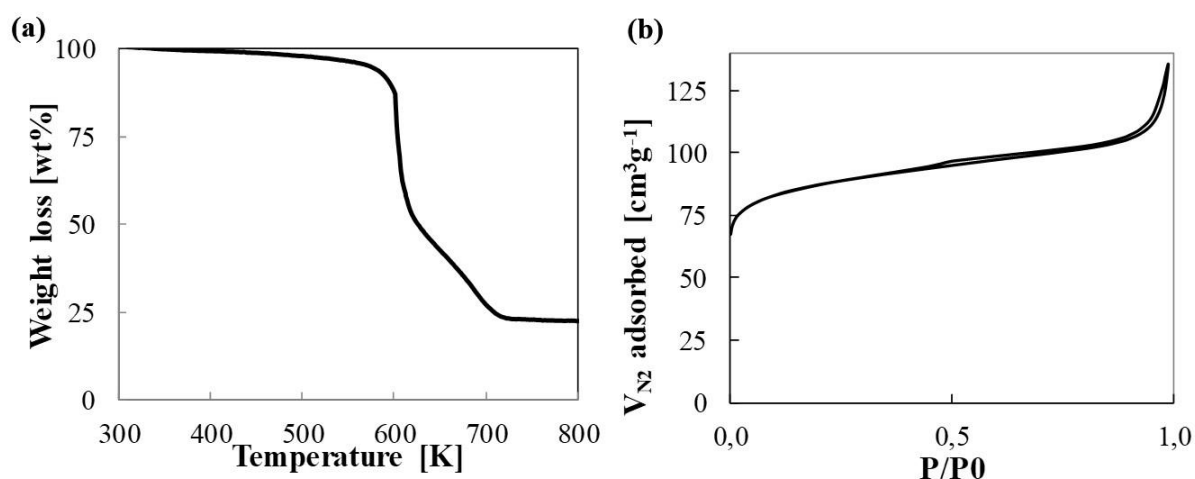

Figure 7.24. Characterization of sc-CCMOF-1 precipitated by adding EtOH in contact with the solid reagents at 313 K after a running time of 72 h: (a) TGA profile, and (b) N₂ adsorption/desorption isotherm.

Nevertheless, the structure of this sample presented a negligible N_2-accessible void, quantified with Mercury 3.10.1,[53] and calculated as 1.5 v/v% of non-interconnected pores. A diameter of 1.6 was assigned to the probe molecule for this calculation, since it is the size of the N_2 molecule used to estimate the textural properties in the adsorption experiments. Disparities between calculated and experimental porosity have previously been described for materials in the families of MOFs, covalent-organic frameworks and porous molecular crystals.[54] In some cases, the computational analysis of the static rigid framework structure gives null porosity or lower expected adsorption values than experimental. One common example is breathing or stimulus-response in flexible frameworks, in which significant crystallographic modifications of the structure lead to porosity that would be otherwise unexpected.[55] Contrarily, diffusion in solids with no apparent porosity or non-interconnected voids could be dominated by local, transient structural changes, which are not accompanied by a crystallographic phase transformation.[56] Experimental adsorption is attributed to cooperative internal motion of structural elements in the constituent molecules enabling diffusion. This porosity has been termed transient, since the modification in the crystal structure is not detectable. For the sc-CCMOF-1, the crystallographically found cavities seem to have no connection. Taking into account that all atom positions were found *ab initio* with clear electron density peaks, and the models refined with EDT (under vacuum at 10^{-5} Pa) and XRD (atmospheric pressure) gave similar conformations, the experimental adsorption values found for this compound are here reasoned on the basis of a structural dynamic transient behavior. One possibility could appear by rotating slightly the MeO groups, fact that changes the pore size and allows or blocks interconnection between cavities, facilitating gas diffusion.

7.3.3. Crystal growth mechanism in scCO₂ of the CCM MOF

The scCO₂ crystallization process described in this work is analyzed as a direct precipitation method, in which one or both reagents are in excess with respect to the solubility value. In this case, a model of continuous reagents dissolution and continuous end-product nucleation, together with crystal growth, should be considered. As the system becomes supersaturated, the crystallization process starts with an induction period; afterwards, nuclei of a critical size are formed. In the performed experiments, the induction period was reduced by stirring the system at least during the first 20 min of reaction. The nucleation process starts with the appearance of a condensed phase (primary particles), where the formation mechanism involves coordinative self-assembly between metal centers and linkers. In scCO₂, the required

size of critical nuclei is expected to be relatively small, since this is a fluid with very low solubilization power for high molecular weight entities. Additionally, solutions for MOFs crystallization usually contain a combination of inorganic and organic precursors with strong reactive interactions between them. Thus, high supersaturation ratios are rapidly attained, which lead to a fast and massive nucleation followed by crystal growth. Moreover, the significance of supercritical crystallization processes relies on the possibility of producing nucleation steps without the interference of solvent interaction.

Many MOFs have been precipitated as single crystals with highly symmetric polyhedral appearance. Hence, their growth has often been assumed to follow the classical crystal growth mechanism, i.e., through the deposition of monomeric building units. Recently, MOF crystallization mechanisms are being reviewed and described to proceed through aggregation of nanoentities followed by surface re-crystallization in a non-classical approach,[57,58] as previously described for zeolites.[59] To elucidate the crystal growth mechanisms that lead to the final habit observed for the precipitated sc-CCMOF-1 particles, crystallization was followed over time by XRD and SEM with samples obtained without continuous stirring and adding the EtOH in contact to the reagents. These techniques were used to capture intermediate stages of crystallization in samples prepared at different running times, from 1 to 72 h.

SEM pictures of the sample taken at the early growth time of 1 h show that MOF synthesis was initiated by the formation of many spherical primary particles with a gel-like morphology (Fig. 7.25(a)), obtained in a massive fast nucleation step. Close observation revealed that the primary particles form loose globular particles (Fig. 7.25(b)), which probably aggregate around CO_2/EtOH bubbles originated during stirring before the complete mixing of the two fluids. In some areas, the agglomerated particles or gel showed some micrometric holes (Fig. 7.25(c)). These macropores were likely formed during the step of expansion and evacuation of the trapped CO_2, necessary to recover the sample at the intermediate crystal growth stages. XRD characterization of those primary nanoparticles indicated a metastable amorphous phase (Fig. 7.26). In those first stages of crystallization (*ca.* 3 h), the primary particles aggregate into larger particles to reduce the surface energy (Fig. 7.25(d)). Hence, the first step on the formation of crystalline sc-CCMOF-1 seems to be random aggregation of the precursor nanoparticles in a non-classical mechanism. After 3 h, heterogeneous nucleation and early-stage surface recrystallization could be observed inside the soft agglomerates (Fig. 7.25(e,f)).

The predominant phase was the amorphous precursor as shown by XRD, although the onset of some diffraction peaks of a low crystallinity phase was already observed (Fig. 7.26).
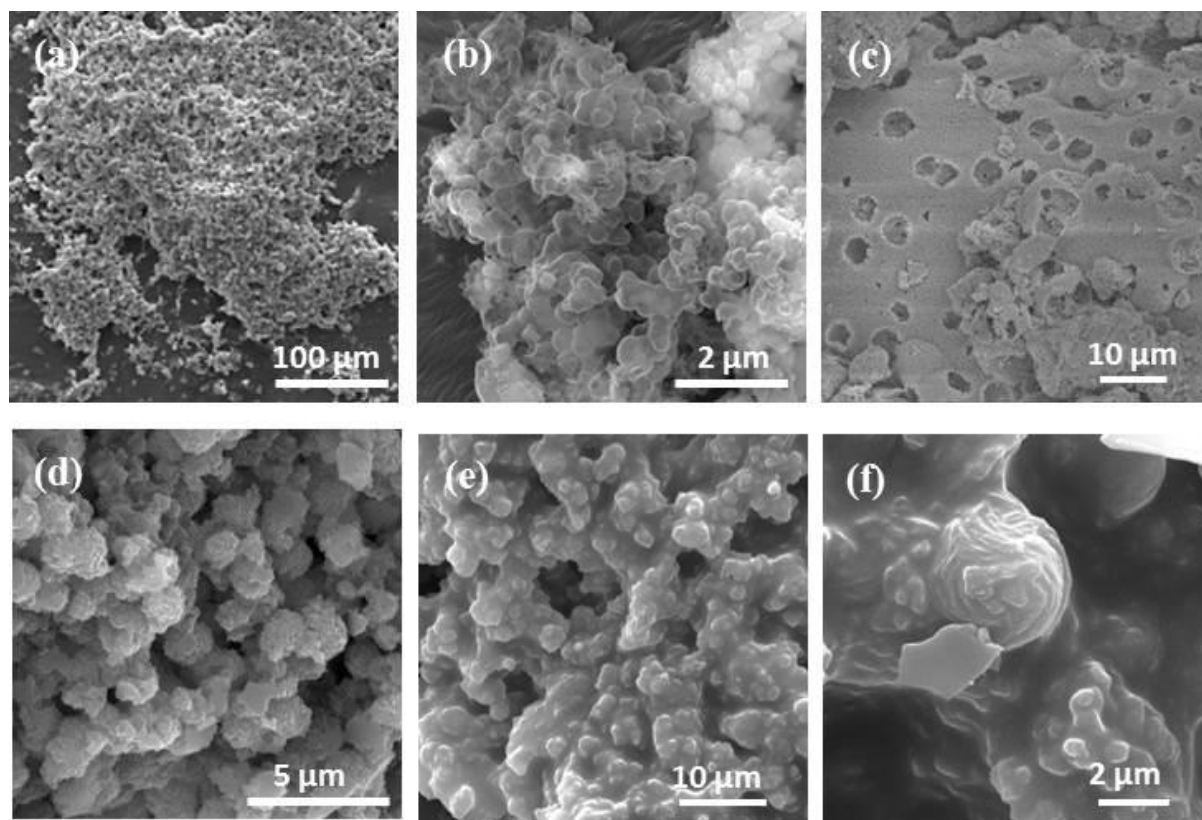

Figure 7.25. SEM micrographs taken from sc-CCMOF-1 samples prepared following the standard supercritical protocol at different running times: (a,b,c) 1 h, and (d,e,f) 3 h.
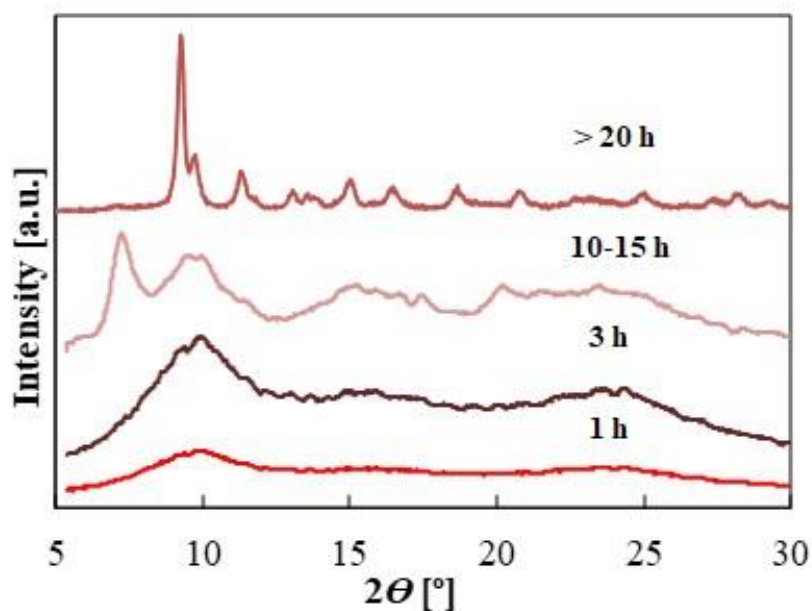

Figure 7.26. Powder XRD of sc-CCMOF-1 samples precipitated at different running times.

Subsequent SEM pictures, taken after *ca.* 10-15 h of reaction, showed that the nanocrystalite-like units have been involved in oriented attachment forming 2D nanoplates that emerged from the reservoir gel (Fig. 7.27(a,b)). A closed view of the nanoplates allowed detecting the fusing of the nanoparticulate precursor, giving a rugged surface (Fig. 7.27(c)). This observation supports the oriented attachment mechanism. This sample still showed a low degree of crystallinity in the XRD pattern (Fig. 7.26). Usually, primary crystal shape can be related to the symmetry elements of the unit cell and the internal supramolecular structure order, repeated in a symmetric manner. In the studied solid, the formation of a 2D macrostructure can be correlated to the inherent 2D crystallographic microstructure described previously. With time, the crystallinity increases slowly until the metastable phase is totally exhausted. Indeed, samples taken after 20 h showed particles with different degrees of organization and crystal growth. The semicrystalline-to-crystalline transformation takes place via Ostwald ripening involving polycrystalline intermediates. First, the rotation of adjacent nanosheets lead to the formation of incipient flower-like aggregates, in which the nanopetals extend outward from a center and also attach to the neighboring ones (Fig. 7.27(d)). In a more evolved system, the array of the nanoplates generates a curvature originating nest-like particles (Fig. 7.27(e)), which finally close by lateral engagement to give spherical superstructures (Fig. 7.27(f)). At this stage, SEM micrographs showed a microstructure consisting in monodispersed spherical particles of few microns in diameter, with a flower-like morphology (Fig. 7.27(g)). These particles are built from tens of 2D nanosheets (petals), with thickness in the nanometer range, *ca.* 50-70 nm, slightly curved, and densely interpenetrated. The fabrication of stable 3D flower-like hierarchical architectures, made by the integration of nanobuilding blocks, in this case 2D nanopetals, with some order and flexibility, is an elegant approach found in nature to increase crystals stability by reducing surface energy. One very well-known example is the formation of flower-shaped morphologies in crystallized calcium sulfate, known as desert roses. In the laboratory, these attractive architectures have been successfully fabricated for a wide variety of materials involving mainly inorganic compounds.[60,61]

For hybrid coordination polymers, several examples of this morphology have already been observed in samples obtained by solvothermal[62,63] and supercritical[64] crystallization techniques. The recovered sample at 20 h was mainly crystalline (Fig. 7.26). Progressing in time, emerging microspheres merged together forming interpenetrated superstructures (Fig. 7.27(h,i)), with a final spherical shape. Flower-like particles of a size of 8-10 μm are observed

after 72 h of reaction time. A close view of the surface shows that the aggregates are constituted by the interpenetration of several primary flower-like particles with different orientation (Fig. 7.27(j)). Crystal growth occurs again by Ostwald ripening, in which the small microspheres are integrated in large macrospheres (Fig. 7.27(k)). Spherical hierarchical superstructures of sizes as large as 20 μm can be seen after 7 days (Fig. 7.27(l)). Nanometric spherical nanoparticles were observed together with the well-formed crystals throughout the crystallization.

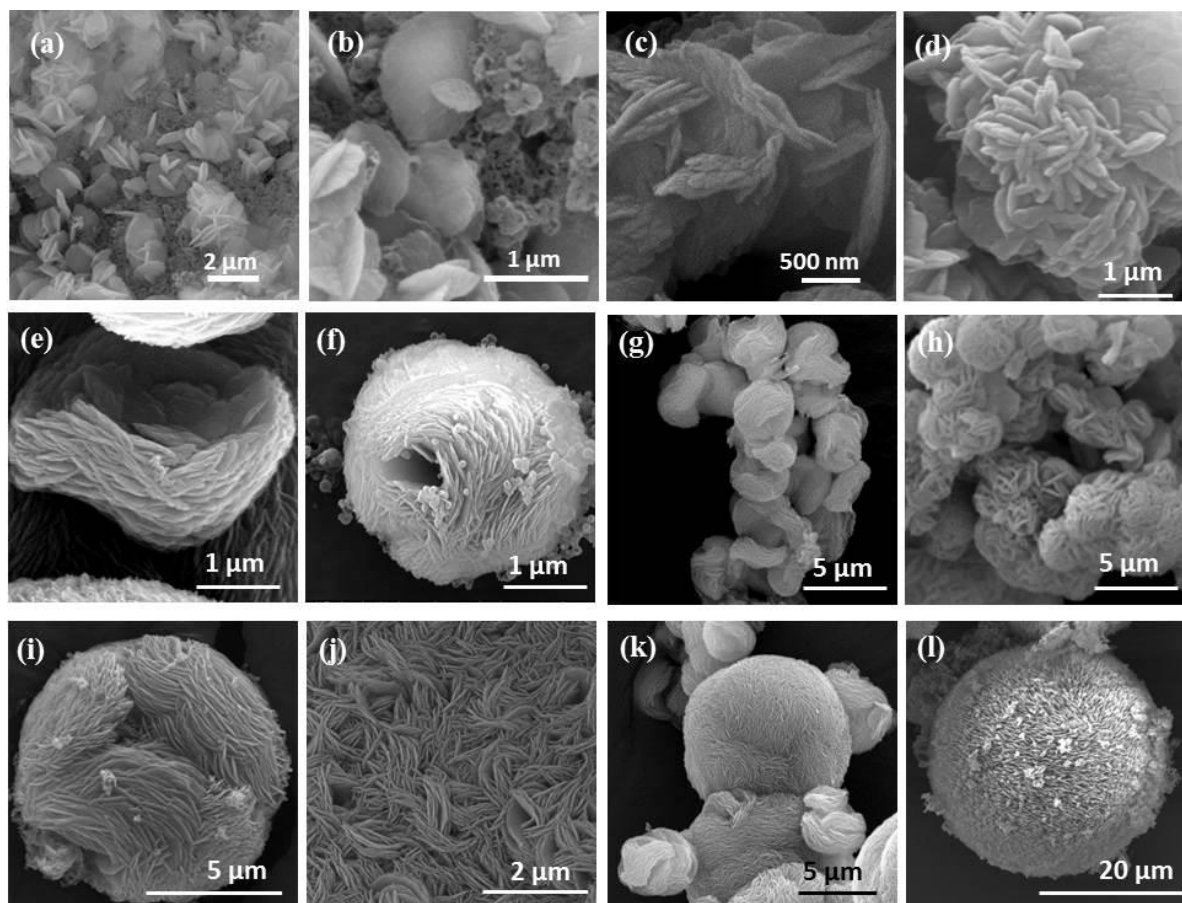**Figure 7.27.** SEM micrographs taken from sc-CCMOF-1 samples prepared following the standard supercritical protocol at different running times: (a,b,c) 10-15 h, (d,e,f) 20 h, (f,g,h,i) 20-72 h and (j,k,l) 72-168 h.

The flower-like morphology was only apparent in non-stirred media, since in a similar experiment, performed with continuous stirring, only randomly agglomerated nanoplatelets were observed (Fig. 7.28(a,b)).
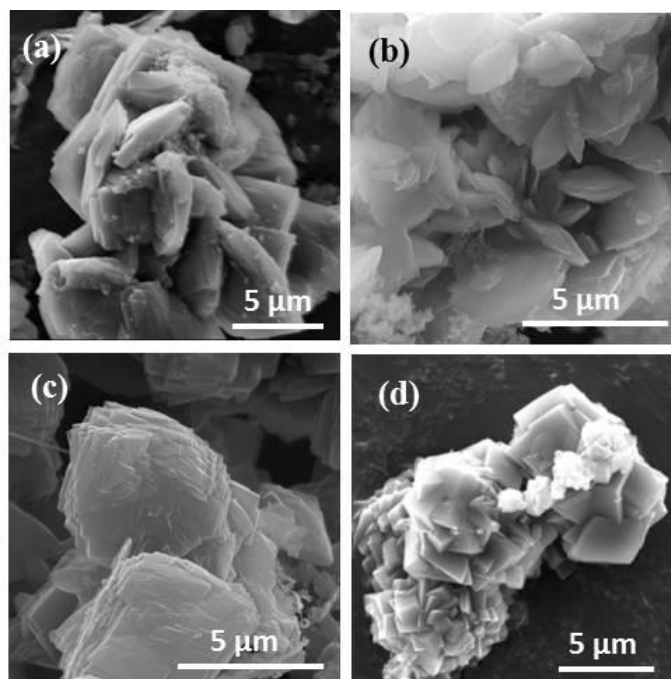
Figure 7.28. SEM micrographs taken from the different sc-CCMOF-1 samples prepared in scCO$_2$ at 20 MPa: in 72 h runs at 313 K adding the EtOH in contact with the reagents and stirring during the complete run (a,b), and in runs performed at 333 K, adding the EtOH physically separated from the reagents, lasting for: (c) 72 h, and (d) 7 days.

The primary nanoplatelets were observed in both stirred and non-stirred systems. However, when agitation was not stopped after the induction period, the aggregation of the primary particles lacks of any orientation. SEM micrographs of the sample recovered in the system in which the EtOH was added outside of the stirred vial containing the solid reagents showed the formation of incipient micrometric polyhedra (Fig. 7.28(c)). Extending the experiment to 7 days, the crystals grew to form large and well-shaped micrometric polyhedra (Fig. 7.28(d)).

7.3.4. CCMbioMOF dissolution in body fluids

Controlled drug delivery systems usually refer to formulations for transporting a therapeutic compound embedded in a composite system to improve pharmacokinetics and targeting. A different strategy has been envisaged for bioMOFs involving a therapeutic specie as the organic linker. In this case, the active component is released at the specific place where the bioMOF degrades as a function of pH. This application was previously proposed for the [Zn$_3$(curcumin)$_2$·7(DMA)·3(EtOH)]$_n$ bioMOF (medi-MOF-1) described in ref. 18. However, the as-synthetized structure occludes large amounts of DMA, which has been identified as a substance of Very High Concern (toxic for reproduction) by the European Chemical Agency. DMA is classified by the Food and Drug Administration (FDA) and European Medicines Evaluation Agency (EMEA) as Class 2 solvent with high inherent toxicity. Hence, the

medical use of the solvothermally synthetized bioMOF can be debatable, even after activation, due to technical difficulties concerning the total elimination of the high-boiling point DMA solvent. On the contrary, the supercritical synthesis of sc-CCMOF-1 performed in this work only required the use of small amounts of ethanol (Class 3 solvent with low toxicity). The lack of high porosity in this MOF precludes its use in drug delivery applications of adsorbed active agents. However, high porosity is no longer required for uses in which the released of the active agent is a building unit of the bioMOF structure. Therefore, initial experiments were performed to study the dissolution behavior of as-synthetized sc-CCMOF-1 in body fluids (phosphate buffer) at neutral pH. For comparison, the dissolution of a similar amount of curcumin was also studied. Obtained results indicate that the CCM dissolution process was faster from the synthetized MOF than from the pristine curcumin (Fig. 7.29). For instance, after three days, the amount of dissolved CCM from the MOF was three-times higher than from the pristine curcumin. Probably, the dynamic microporosity provides the advantage of speeding dissolution by facilitating water diffusion to the interior of the bioMOF, thus increasing the bioavailability.[65] These results should be taken as only preliminary, since the possible degradation of curcumin in buffer at alkaline pH was not taken into account.[66]
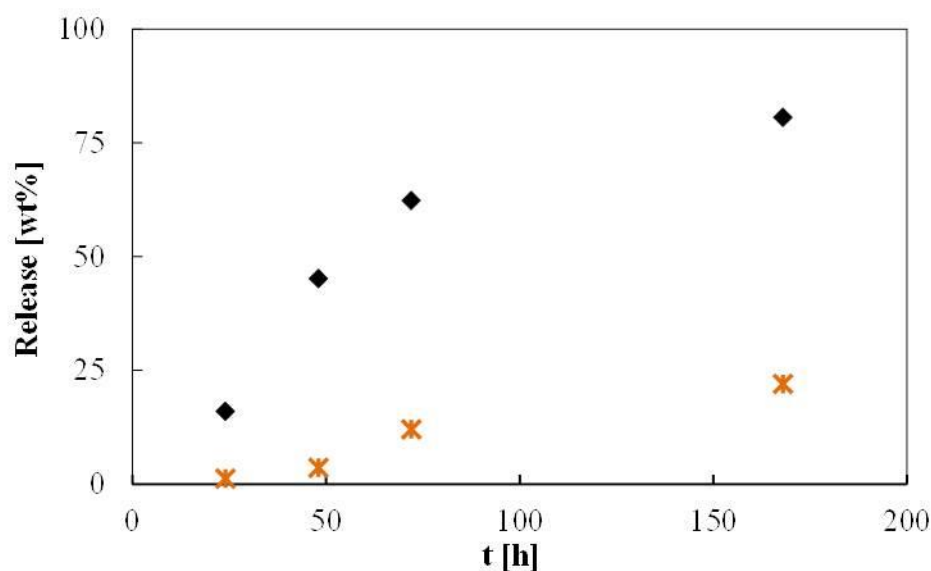

Figure 7.29. Drug dissolution profiles at neutral pH of raw curcumin (✱) and synthetized (♦) bioMOF. Depicted points are the mean values calculated from two replicates. Estimated error values are in the order of 20%.

7.4. Conclusions

This work involves a systematic study performed to synthetize new bioMOFs, containing curcumin or ferulic acid and Zn(II). They are obtained by reactive crystallization in $scCO_2$. The designed $scCO_2$ process avoids the use of toxic organic solvents, difficult to recover additives, and large excess of expensive linkers. The obtained phases are two bioMOFs with $[Zn_2(F)_2]_n$ and $[Zn(curcumin)]_n$ repeating units and 3D and 2D structure, respectively. The structure of the FA MOF was already described. On the contrary, due to the small crystal size and the complex intergrowth of the CCMbioMOF precipitated aggregates, the structural elucidation of this compound could only be achieved by using the recently developed EDT method, combined with beam precession and energy filtering. Remarkably, all non-H atoms were localized *ab initio* despite the beam sensitivity to organic-hybrid materials, demonstrating once more that the combination of EDT with a highly sensitive single electron detector extends the applicability of electron crystallography to soft matter. The structure has a non-bonded OH group per curcumin molecule, which in principle could be exploited for post-synthetic modifications, involving organic functionalization or incorporation of different metallic centers. However, sc-CCMOF-1 is highly stable, therefore post synthetic modifications would probably be challenging. The crystallization of the CCM MOF was assumed to proceed through the combination of random self-assembly of amorphous building units, heterogeneous nucleation of primary crystallites, oriented attachment and disorder-to-order rearrangement, all in a non-classical crystal growth pathway; finalized with several episodes of Ostwald ripening to give large flower-like superstructures.
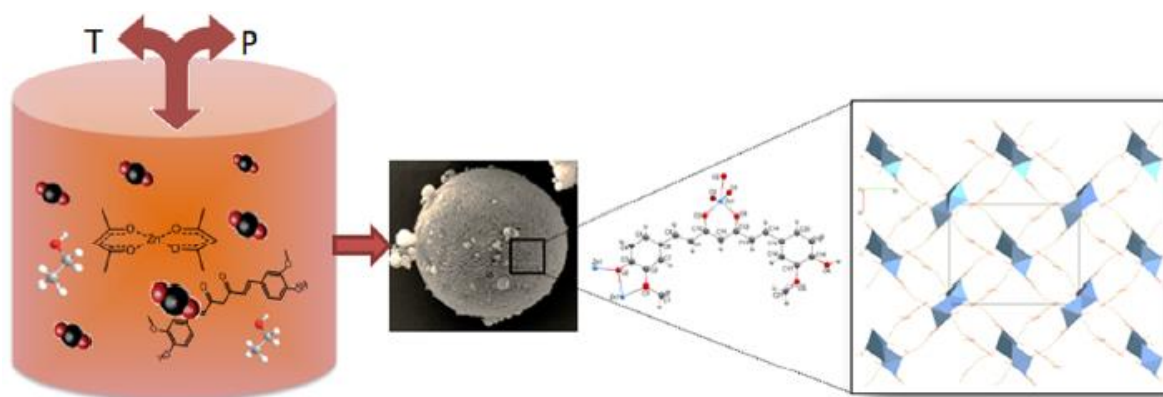

Figure 7.30. Schematic representation of the synthesis of sc-CCMOF-1.

Valuable mechanistic information for the control of the crystal size and shape can be obtained by the understanding of the crystal growth mechanism. With this information, new synthesis

protocols for the selective formation of particles with the desired characteristics can be designed. As a potential medical application for the synthetized bioMOF, it was demonstrated that the release of curcumin from the MOF was significantly faster than from pristine curcumin particles, thus increasing the bioavailability of this active agent. Moreover, preliminary studies with other natural products as organic linkers suggest the generalization of the process for this type of MOFs.

7.5. References

(1) Stock, N.; Biswas, S. Synthesis of metal-organic frameworks (MOFs): routes to various MOF topologies, morphologies, and composites. *Chem. Rev.,* **2012**, *112* (2), 933-969.

(2) Rojas, S.; Devic, T.; Horcajada, P. Metal organic frameworks based on bioactive components. *J. Mater. Chem. B,* **2017**, *5* (14), 2560-2573.

(3) Keskin, S.; Kızılel, S. Biomedical Applications of metal organic frameworks. *Ind. Eng. Chem. Res.,* **2011**, *50* (4), 1799-1812.

(4) Smaldone, R. A.; Forgan, R. S.; Furukawa, H.; Gassensmith, J. J.; Slawin, A. M. Z.; Yaghi, O. M.; Stoddart, J. F. Metal-organic frameworks from edible natural products. *Angew. Chemie Int. Ed.,* **2010**, *49* (46), 8630-8634.

(5) Imaz, I.; Rubio-Martínez, M.; An, J.; Solé-Font, I.; Rosi, N. L.; Maspoch, D. Metal-biomolecule frameworks (MBioFs). *Chem. Commun.,* **2011**, *47* (26), 7287-7302.

(6) Akram, M.; Hamid, A.; Khalil, A.; Ghaffar, A.; Tayyaba, N.; Saeed, A.; Ali, M.; Naveed, A. review on medicinal uses, pharmacological, phytochemistry and immunomodulatory activity of plants. *Int. J. Immunopathol. Pharmacol.,* **2014**, *27* (3), 313-319.

(7) Schoedel, A.; Li, M.; Li, D.; O'Keeffe, M.; Yaghi, O. M. Structures of metal-organic frameworks with rod secondary building units. *Chem. Rev.,* **2016**, *116* (19), 12466-12535.

(8) Du, M.; Wang, X.; Chen, M.; Li, C. P.; Tian, J. Y.; Wang, Z. W.; Liu, C. Sen. Ligand symmetry modulation for designing a mesoporous metal-organic framework: dual reactivity to transition and lanthanide metals for enhanced functionalization. *Chem. - A Eur. J.,* **2015**, *21* (27), 9713-9719.

(9) Voloshchuk, T.; Farina, N. S.; Wauchope, O. R.; Kiprowska, M.; Haberfield, P.; Greer, A. Molecular bilateral symmetry of natural products: prediction of selectivity of dimeric molecules by density functional theory and semiempirical calculations. *J. Nat. Prod.,* **2004**, *67* (7), 1141-1146.

(10) Yabe, T.; Hirahara, H.; Harada, N.; Ito, N.; Nagai, T.; Sanagi, T.; Yamada, H. Ferulic acid induces neural progenitor cell proliferation in vitro and in vivo. *Neuroscience,* **2010**, *165* (2), 515-524.

(11) Zhao, Z.; Moghadasian, M. H. Chemistry, natural sources, dietary intake and pharmacokinetic properties of ferulic acid: a review. *Food Chem.,* **2008**, *109* (4), 691-702.

(12) Demir, S.; Merve Çepni, H.; Topcu, Y.; Hołyńska, M.; Keskin, S. A phytochemical-containing metal-organic framework: synthesis, characterization and molecular simulations for hydrogen adsorption. *Inorganica Chim. Acta,* **2015**, *427*, 138-143.

(13) Zhou, E.-H.; Li, B.-H.; Chen, W.-X.; Luo, Z.; Liu, J.; Singh, A.; Kumar, A.; Jin, J.-C. Photocatalytic degradation of organic dyes by a stable and biocompatible Zn(II) MOF having ferulic acid: experimental findings and theoretical correlation. *J. Mol. Struct.,* **2017**, *1149*, 352-356.

(14) Li, F.; Li, B.; Wang, C.; Zeng, Y.; Liu, J.; Gu, C.-Y.; Lu, P.; Mei, L. Encapsulation of pharmaceutical ingredient linker in metal-organic framework: combined experimental and theoretical insight into the drug delivery. *RSC Adv.,* **2016**, *6* (53), 47959-47965.

(15) Shen, L.; Ji, H.-F. Theoretical study on physicochemical properties of curcumin. *Spectrochim. Acta Part A Mol. Biomol. Spectrosc.,* **2007**, *67* (3-4), 619-623.

(16) Iakovidis, I.; Delimaris, I.; Piperakis, S. M. Copper and its complexes in medicine: a biochemical approach. *Mol. Biol. Int.,* **2011**, *2011*, 594529.

(17) Aliaga-Alcalde, N.; Rodríguez, L.; Ferbinteanu, M.; Höfer, P.; Weyhermüller, T. Crystal structure, fluorescence, and nanostructuration studies of the first Zn[II] anthracene-based curcuminoid.

Inorg. Chem., **2012**, *51* (2), 864-873.

(18) Su, H.; Sun, F.; Jia, J.; He, H.; Wang, A.; Zhu, G. A highly porous medical metal-organic framework constructed from bioactive curcumin. *Chem. Commun.,* **2015**, *51* (26), 5774-5777.

(19) Nelson, A. P.; Farha, O. K.; Mulfort, K. L.; Hupp, J. T. Supercritical processing as a route to high internal surface areas and permanent microporosity in metal-organic framework materials. *J. Am. Chem. Soc.,* **2009**, *131* (2), 458-460.

(20) López-Periago, A. M.; Portoles-Gil, N.; López-Domínguez, P.; Fraile, J.; Saurina, J.; Aliaga-Alcalde, N.; Tobias, G.; Ayllón, J. A.; Domingo, C. Metal-organic frameworks precipitated by reactive crystallization in supercritical CO₂. *Cryst. Growth Des.,* **2017**, *17* (5), 2864-2872.

(21) López-Domínguez, P.; López-Periago, A. M.; Fernández-Porras, F. J.; Fraile, J.; Tobias, G.; Domingo, C. Supercritical CO₂ for the synthesis of nanometric ZIF-8 and loading with hyperbranched aminopolymers. applications in CO₂ capture. *J. CO₂ Util.,* **2017**, *18*, 147-155.

(22) López-Periago, A.; López-Domínguez, P.; Pérez Barrio, J.; Tobias, G.; Domingo, C. Binary Supercritical CO₂ solvent mixtures for the synthesis of 3D metal-organic frameworks. *Microporous Mesoporous Mater.,* **2016**, *234*, 155-161.

(23) López-Periago, A.; Vallcorba, O.; Frontera, C.; Domingo, C.; Ayllón, J. A. Exploring a novel preparation method of 1D metal organic frameworks based on supercritical CO₂. *Dalton Trans.,* **2015**, *44* (16), 7548-7553.

(24) Mugnaioli, E.; Kolb, U. Structure characterization of nanocrystalline porous materials by tomographic electron diffraction. *Zeitschrift für Krist. - Cryst. Mater.,* **2015**, *230* (4), 271-288.

(25) Mugnaioli, E.; Gorelik, T.; Kolb, U. "Ab Initio" structure solution from electron diffraction data obtained by a combination of automated diffraction tomography and precession technique. *Ultramicroscopy,* **2009**, *109* (6), 758-765.

(26) Wang, Y.; Takki, S.; Cheung, O.; Xu, H.; Wan, W.; Öhrström, L.; Inge, A. K. Elucidation of the elusive structure and formula of the active pharmaceutical ingredient bismuth subgallate by continuous rotation electron diffraction. *Chem. Commun.,* **2017**, *53* (52), 7018-7021.

(27) Yuan, S.; Qin, J. S.; Xu, H. Q.; Su, J.; Rossi, D.; Chen, Y.; Zhang, L.; Lollar, C.; Wang, Q.; Jiang, H. L.; Son, D. H.; Xu, H.; Huang, Z.; Zou, X.; Zhou, H.-C. Cluster: An Ideal inorganic building unit for photoactive metal-organic frameworks. *ACS Cent. Sci.,* **2018**, *4* (1), 105-111.

(28) Tamames-Tabar, C.; García-Márquez, A.; Blanco-Prieto, M. J.; Serre, C.; Horcajada, P. MOFs in pharmaceutical technology. in bio- and bioinspired nanomaterials; Wiley-VCH Verlag GmbH & Co. KGaA: Weinheim, Germany, **2014**; Vol. 9783527335, 83-112.

(29) Naksuriya, O.; Okonogi, S.; Schiffelers, R. M.; Hennink, W. E. Curcumin nanoformulations: a review of pharmaceutical properties and preclinical studies and clinical data related to cancer treatment. *Biomaterials,* **2014**, *35* (10), 3365-3383.

(30) Henrotin, Y.; Priem, F.; Mobasheri, A. Curcumin: a new paradigm and therapeutic opportunity for the treatment of osteoarthritis: curcumin for osteoarthritis management. *Springerplus,* **2013**, *2* (1), 56.

(31) Miller, S. R.; Heurtaux, D.; Baati, T.; Horcajada, P.; Grenèche, J.-M.; Serre, C. Biodegradable therapeutic MOFs for the delivery of bioactive molecules. *Chem. Commun.,* **2010**, *46* (25), 4526-4528.

(32) Kolb, U.; Gorelik, T.; Kübel, C.; Otten, M. T.; Hubert, D. Towards automated diffraction tomography: part I-data acquisition. *Ultramicroscopy,* **2007**, *107* (6-7), 507-513.

(33) Gemmi, M.; Oleynikov, P. Scanning reciprocal space for solving unknown structures: energy filtered diffraction tomography and rotation diffraction tomography methods. *Zeitschrift für Krist. - Cryst. Mater.,* **2013**, *228* (1), 51-58.

(34) Nederlof, I.; van Genderen, E.; Li, Y.-W.; Abrahams, J. P. A medipix quantum area detector allows rotation electron diffraction data collection from submicrometre three-dimensional protein crystals. *Acta Crystallogr. Sect. D Biol. Crystallogr.,* **2013**, *69* (7), 1223-1230.

(35) Kolb, U.; Mugnaioli, E.; Gorelik, T. E. Automated electron diffraction tomography - a new tool for nano crystal structure analysis. *Cryst. Res. Technol.,* **2011**, *46* (6), 542-554.

(36) Palatinus, L.; Petříček, V.; Corrêa, C. A. Structure refinement using precession electron diffraction tomography and dynamical diffraction: theory and implementation. *Acta Crystallogr. Sect. A Found. Adv.,* **2015**, *71* (2), 235-244.

(37) Burla, M. C.; Caliandro, R.; Carrozzini, B.; Cascarano, G. L.; Cuocci, C.; Giacovazzo, C.;

Mallamo, M.; Mazzone, A.; Polidori, G. Crystal structure determination and refinement via SIR2014. *J. Appl. Crystallogr.,* **2015**, *48* (1), 306-309.

(38) Mohan, P. R. K.; Sreelakshmi, G.; Muraleedharan, C. V.; Joseph, R. Water soluble complexes of curcumin with cyclodextrins: characterization by FT-raman spectroscopy. *Vib. Spectrosc.,* **2012**, *62*, 77-84.

(39) Nakamoto, K.; McCarthy, P. J.; Martell, A. E. Infrared spectra of metal chelate compounds. III. infrared spectra of acetylacetonates of divalent metals[1]. *J. Am. Chem. Soc.,* **1961**, *83* (6), 1272-1276.

(40) Hübner, A.; Strobusch, D.; Lerner, H.-W.; Bolte, M. The twinned crystal structure of zinc(II) acetylacetonate trimer. *J. Chem. Crystallogr.,* **2008**, *38* (12), 959-959.

(41) Rudolph, G.; Henry, M. C.; Muetterties, E. L. bis(2,4-pentanedionato) zinc. Inorganic Synthesis **2007**, 74-77.

(42) Ambrožič, G.; Škapin, S. D.; Žigon, M.; Orel, Z. C. The synthesis of zinc oxide nanoparticles from zinc acetylacetonate hydrate and 1-butanol or isobutanol. *J. Colloid Interface Sci.,* **2010**, *346* (2), 317-323.

(43) Wakte, P. S.; Sachin, B. S.; Patil, A. A.; Mohato, D. M.; Band, T. H.; Shinde, D. B. Optimization of microwave, ultra-sonic and supercritical carbon dioxide assisted extraction techniques for curcumin from curcuma longa. *Sep. Purif. Technol.,* **2011**, *79* (1), 50-55.

(44) Chassagnez-Méndez, A. L.; Machado, N. T.; Araujo, M. E.; Maia, J. G.; Meireles, M. A. A. Supercritical CO₂ extraction of curcumins and essential oil from the rhizomes of turmeric (curcuma longa L.). *Ind. Eng. Chem. Res.,* **2000**, *39* (12), 4729-4733.

(45) Teoh, W. H.; Mammucari, R.; Foster, N. R. Solubility of organometallic complexes in supercritical carbon dioxide: a review. *J. Organomet. Chem.,* **2013**, *724*, 102-116.

(46) Sheldrick, G. M. Crystal structure refinement with SHELXL. *Acta Crystallogr. Sect. C Struct. Chem.,* **2015**, *71* (1), 3-8.

(47) Farrugia, L. J. WinGX Suite for small-molecule single-crystal crystallography. *J. Appl. Crystallogr.,* **1999**, *32* (4), 837-838.

(48) Avogadro: an open-source molecular builder and visualization tool.

(49) Tønnesen, H. H.; Karlsen, J.; Mostad, A.; Samuelsson, B.; Enzell, C. R.; Berg, J.-E. Structural studies of curcuminoids. I. The crystal structure of curcumin. *Acta Chem. Scand.,* **1982**, *36b*, 475-479.

(50) Toby, B. H.; Von Dreele, R. B. GSAS-II : The genesis of a modern open-source all purpose crystallography software package. *J. Appl. Crystallogr.,* **2013**, *46* (2), 544-549.

(51) Groom, C. R.; Bruno, I. J.; Lightfoot, M. P.; Ward, S. C. The Cambridge Structural Database. *Acta Crystallogr. Sect. B Struct. Sci. Cryst. Eng. Mater.,* **2016**, *72* (2), 171-179.

(52) Morris, R. E.; Brammer, L. Coordination Change, Lability and Hemilability in Metal-Organic Frameworks. *Chem. Soc. Rev.,* **2017**, *46* (17), 5444-5462.

(53) Macrae, C. F.; Bruno, I. J.; Chisholm, J. A.; Edgington, P. R.; McCabe, P.; Pidcock, E.; Rodriguez-Monge, L.; Taylor, R.; van de Streek, J.; Wood, P. A. Mercury CSD 2.0 - new features for the visualization and investigation of crystal structures. *J. Appl. Crystallogr.,* **2008**, *41* (2), 466-470.

(54) Holden, D.; Chong, S. Y.; Chen, L.; Jelfs, K. E.; Hasell, T.; Cooper, A. I. Understanding static, dynamic and cooperative porosity in molecular materials. *Chem. Sci.,* **2016**, *7* (8), 4875-4879.

(55) Kitagawa, S.; Kitaura, R.; Noro, S. Functional porous coordination polymers. *Angew. Chemie Int. Ed.,* **2004**, *43* (18), 2334-2375.

(56) Aguilar-Granda, A.; Pérez-Estrada, S.; Sánchez-González, E.; Álvarez, J. R.; Rodríguez-Hernández, J.; Rodríguez, M.; Roa, A. E.; Hernández-Ortega, S.; Ibarra, I. A.; Rodríguez-Molina, B. Transient porosity in densely packed crystalline carbazole (*p*-diethynylphenylene) carbazole rotors: CO₂ and acetone sorption properties. *J. Am. Chem. Soc.,* **2017**, *139* (22), 7549-7557.

(57) Olafson, K. N.; Li, R.; Alamani, B. G.; Rimer, J. D. Engineering crystal modifiers: bridging classical and nonclassical crystallization. *Chem. Mater.,* **2016**, *28* (23), 8453-8465.

(58) Self, K.; Telfer, M.; Greer, H. F.; Zhou, W. Reversed crystal growth of RHO zeolitic imidazolate framework (ZIF). *Chem. - A Eur. J.,* **2015**, *21* (52), 19090-19095.

(59) Chen; Qiao; Xie; Fan; Zhou; He. Self-construction of core-shell and hollow zeolite analcime icositetrahedra: a reversed crystal growth process via oriented aggregation of nanocrystallites and recrystallization from surface to core. *J. Am. Chem. Soc.,* **2007**, *129* (43), 13305-13312.

(60) Zhang, L.; Wang, W.; Chen, Z.; Zhou, L.; Xu, H.; Zhu, W. Fabrication of flower-like Bi₂WO₆

superstructures as high performance visible-light driven photocatalysts. *J. Mater. Chem.,* **2007**, 17 (24), 2526-2532.

(61) Sun, Y.; Wang, L.; Yu, X.; Chen, K. Facile synthesis of flower-like 3D ZnO superstructures via solution route. *CrystEngComm.,* **2012**, *14* (9), 3199-3204.

(62) Yang, J.; Zheng, C.; Xiong, P.; Li, Y.; Wei, M. Zn-doped Ni-MOF material with a high supercapacitive performance. *J. Mater. Chem, A,* **2014**, *2* (44), 19005-19010.

(63) Zhang, Z.; Li, G.; Peng, H.; Chen, K. Hierarchical hollow microspheres assembled from N-doped carbon coated $Li_4Ti_5O_{12}$ nanosheets with enhanced lithium storage properties. *J. Mater. Chem. A,* **2013**, 1 (48), 15429-15434.

(64) Portoles-Gil, N.; Parra-Aliana, R.; Álvarez-Larena, Á.; Domingo, C.; Ayllón, J. A.; López-Periago, A. Bottom-up approach for the preparation of hybrid nanosheets based on coordination polymers made of metal-diethyloxaloacetate complexes linked by 4,4′-bipyridine. *CrystEngComm.,* **2017**, 19 (34), 4972-4982.

(65) McKinlay, A. C.; Morris, R. E.; Horcajada, P.; Férey, G.; Gref, R.; Couvreur, P.; Serre, C. BioMOFs: Metal-organic frameworks for biological and medical applications. *Angew. Chemie Int. Ed.,* **2010**, 49 (36), 6260-6266.

(66) Griesser, M.; Pistis, V.; Suzuki, T.; Tejera, N.; Pratt, D. A.; Schneider, C. Autoxidative and cyclooxygenase-2 catalyzed transformation of the dietary chemopreventive agent curcumin. *J. Biol. Chem.,* **2011**, 286 (2), 1114-1124.

CHAPTER-8

General conclusions

CHAPTER 8 details the general conclusions of this thesis.

8.1. General conclusions

The main objective of this doctoral thesis has been to answer some of the raised scientific questions in the synthesis of coordination polymers in $scCO_2$. When this thesis started in 2015, it was just one article published in the literature of CPs synthetized exclusively in pure $scCO_2$. This thesis is a continuation of this work by extending the number of metal nodes and linkers to expand the typology of prepared new compounds. The output of this thesis is 17 CPs from 1D to 3D crystallized in this medium.

An environmental friendly procedure to synthetize CPs has been described without the use of any toxic organic solvent, considering also post-treatment steps. It has been demonstrated that the $scCO_2$ synthetic method works as a platform for the formation of CPs involving neutral N-donor bi-/multi-dentate linkers. New 1D ($[M(deox)_2(bpy)]_n$ and $[(Cu(hfa)_2)_{1.5}(3\text{-}tpt)]_n$) and 2D ($[M(tfa)_2(dpy)_2]_n$) CPs have been crystallized and characterized. In addition, the one-pot synthesis of heterometalic CPs involving N-donor organic linkers have also been performed. The Co(II) synthetized heterometallic CPs behave as single molecular magnets.

Different approaches for the use as reagents of metal organic complexes with low solubility in $scCO_2$ have been settled. A new procedure to increase the solubility of the metal complex in $scCO_2$ has been optimized, involving the pre-modification of this precursor with *tert*-butylpirydine (*t*-bpy). Moreover, the efficiency of the use of this additive *in situ* in small quantities has been demonstrated. This new approach has been tested in two different metal complexes with negligible solubility in $scCO_2$, i.e., $[M(deox)_2 \cdot xH_2O]$ and $[M(tfa)_2]$.

The use of curcumin and ferulic acid as organic linkers has been proposed to show the possibility of using this kind of natural products, frequently extracted with $scCO_2$, as building blocks for the synthesis of biocompatible coordination polymers. This study opens a new window to test in the future different natural products for the synthesis of bioMOFs in $scCO_2$. Since these compounds are proposed for a pharmaceutical use, the main advantage of the proposed synthetic methodology relay in the lack of residual toxic solvents in the final product. The compound synthetized with ferulic acid is an example of a 3D MOF synthetized in $scCO_2$.

Non-classical crystal growth mechanism has been proposed to define CPs crystallization occurring in $scCO_2$. The crystal growth of two different CPs, i.e., $[M(deox)_2(bpy)_2]_n$ and $[Zn(CCM)]_n$, has been followed with time to demonstrate this mechanism. Crystallization has

been assumed to proceed through the combination of random self-assembly of amorphous building units, heterogeneous nucleation of primary crystallites, oriented attachment and disorder-to-order rearrangement, all in a non-classical crystal growth pathway; finalized with several episodes of Ostwald ripening to give large flower-like superstructures. This mechanistic information is important for the control of the crystal size and shape and can be used for the selective design of particles formation with the desired characteristics.

In $scCO_2$, often it has been difficult to obtain single crystals for structure elucidation of new phases. In these cases, the use of electro diffraction tomography for structure elucidation has been attempted. The phase resolution of $Zn(CCM)_2$ by this methodology open a new horizon for the elucidation of other CPs that are difficult to growth.

Further investigations in other building blocks to obtain new porous 3D MOFs in pure $scCO_2$ is still necessary in order to expand the range of CPs synthesis. Indeed, there are infinite possibilities of new CPs (known or unknown) that can be tested. Moreover, synthetic protocols can be optimized in regard of pressure and temperature and their effect in the crystallization process and the solubility of the reagents. Finally, it would be necessary to extend the analysis of the batch process to ascertain the scalability of the described methodology.

PERSONAL INFORMATION

Núria Portolés Gil
Gender Female
Date of birth 22/04/1991
Nationality Spanish
✉ nuria.portoles.gil@gmail.com
🆔 https://orcid.org/0000-0002-2580-4641

RESEARCH EXPERIENCE

2015-Present   PhD in Chemistry

Institute of Material Science of Barcelona (ICMAB-CSIC), Bellaterra, Barcelona, Spain. Autonomous University of Barcelona (UAB), Bellaterra, Barcelona, Spain.

Green synthesis of coordination polymers using supercritical carbon dioxide.

2014-2015   Scholarship/ Master project

InKemia IUCT, Mollet del Vallès, Barcelona, Spain

Collaboration of in Green Chemistry Department. Development of green solvents. Master Sustainable Chemistry UJI.

2013 -2014   Scholarship/ Erasmus exchange

University of Strathclyde, Glasgow, United Kingdom Collaboration in organic synthesis group of Dr Glenn Burley. Participation in a "click" chemistry project.

EDUCATION AND TRAINING

2015-Present   **PhD in Chemistry**
Institute of Material Science of Barcelona (ICMAB-CSIC), Bellaterra, Barcelona, Spain. Autonomous University of Barcelona (UAB), Bellaterra, Barcelona, Spain.
Green synthesis of coordination polymers using supercritical carbon dioxide.

2014-2015   **Master's Degree in Sustainable Chemistry**
School of technology and experimental science, University of Jaume I, Castellón de la Plana, Spain. Synthesis of glycerol derivatives.

2009-2014   **Bachelor's Degree in Chemistry**
Science Faculty, Autonomous University of Barcelona (UAB), Bellaterra, Barcelona.

EDUCATION AND TRINING

Techniques used during the PhD.	XRD, SEM, EDS, TGA, BET, E.A, NMR, UV-Vis, FTIR, Optical microscope
Courses	**FLUCOMP Spring School**, in the European meeting of supercritical Fluids (Ciudad real, 2019)

Introducción a la Caracterización de Adsorbentes y Catalizadores, CSIC-RRSSEE (Jarandilla, 2018)

Introduction to scanning electron microscopy for material and life science, Servei de micoscòpia UAB (Bellaterra, 2017)

Scientific School on Materials for Biomedical Applications, ICMAB-CSIC (Bellaterra, 2017)

5th International School of Crystallitzation (Granada, 2016)

Others:

Curs de Parlar en Públic, Institut de ciències de l'Educació UAB (Bellaterra, 2018)

Curs integral de seguretat, Departament de Química UAB (Bellaterra, 2017)

Curs Angles per Químics, Servei de Llengues UAB (Bellaterra, 2016)

Workshops and seminaries

II Workshop on Spectroscopy Techniques: Generalities and Applications, ICMAB-CSIC. (Bellaterra, 2019)

Workshop Intermolecular Interactions in Action. Universitat de Barcelona. (Barcelona, 2018)

SynchrotornsX: Synchrotrons and X-Ray Free Electron Lasers, L'Ecole polytechnique fédérale de Lausanne (online edX, 2018)

III Workshop on materials characterisation by diffraction method, ICMAB-CSIC. (Bellaterra, 2017)

Herramientas 2.0 para comunicar la actividad científica, Escola de doctorat UAB (Bellaterra, 2017)

Technical and Conversation English, ICMAB-CSIC. (Bellaterra 2017)

Mendeley Instotucional basic, Servei de Bibliotques UAB (Bellaterra, 2016)

IV Workshop on Sustainable Chemistry (Castellón de la Plana, 2015)

PUBLICATIONS

Portolés-Gil, N.; Vallcorba, O.; Goméz-Coca, S.; Aliaga-Alcalde, N.; Ruiz, E.; Ayllón, J. A.; López-Periago, A.; Domingo, C. One-step synthesis of new cobalt and zin homo-and heterometalic coordination polymers. *Under preparation*

Portolés-Gil, N.; López-Periago, A. M.; Borrás, A.; Fraile, J.; Solando, E.; Vallcorba, O.; Planas. J.G.; Ayllón, J.A.; Domingo, C. Tunable and scalable synthesis of five copper(II) metal-organic frameworks via linker isomerization. *Under preparation*

Portolés-Gil, N.; Lanza, A.; Aliaga-Alcalde, N.; Ayllón, J. A.; Gemmi, M.; Mugnaioli, E.; López-Periago, A. M.; Domingo, C. Crystalline curcumin bioMOF obtained by precipitation in supercritical CO_2 and structural determination by electron diffraction tomography. ACS Sustainable *Chem. Eng.,* **2018**, 69, 12309-12319. DOI: 10.1021/acssuschemeng.8b02738

Portolés-Gil, N.; Gowing, S.; Vallcorba, O.; Domingo, C.; López-Periago, A. M.; Ayllón, J. A. Supercritical CO_2 utilization for the crystallization of 2D metal-organic frameworks using *tert*-butylpyridine additive. *J. CO_2 Util.*, **2018**, 24, 444–453. DOI: 10.1016/j.jcou.2018.02.004

Portolés-Gil, N.; Parra-Aliana, R.; Álvarez-Larena, Á.; Domingo, C.; Ayllón, J. A.; López-Periago, A. Bottom-up approach for the preparation of hybrid nanosheets based on coordination polymers made of metal–diethyloxaloacetate complexes linked by 4,4′-bipyridine. *CrystEngComm*, **2017**, 19 (34), 4972–4982. DOI: 10.1039/c7ce00909g

López-Periago, A.; Portoles-Gil, N.; López-Domínguez, P.; Fraile, J.; Saurina, J.; Aliaga Alcalde, N.; Tobias, G.; Ayllon, J.A.; Domingo, C. 2017. Metal-organic frameworks precipitated by reactive crystallization in supercritical CO_2. *Crystal Growth & Design*, Vol 17, (5), 2864-2872. DOI: 10.1021/acs.cgd.7b00378

Sanchez-Sala, M.; Portolés-Gil, N.; Vallcorba, O.; Domingo, C.; López-Periago A.; Ayllón, J. A. Green synthesis of copper triflusalat and pyridine adducts. *ChemistrySelec*t, **2016**, Vol 1, Issue 21, 6692-6699. DOI: 10.1002/slct.201601836

PROJECTS

MSDP synchrotron ALBA. In situ study of the structural changes in Cu(3-tpt) flexible MOF induced by N_2 adsorption and temperatura. Proposal number 2019023285

CONFERENCES

17th European Meeting Supercritical Fluids, Ciudad Real, 2019. Oral presentation. Portolés-Gil N.; Vallcorba, O.; López-Periago A.; Ayllón J. A.; Domingo, C. Direct Synthesis of new mixed-metal coordination polymers with cobalt and zinc in supercritical carbon dioxide.

12th International Symposium in Supercritical Fluids. Niza, 2018. Poster. <u>Portolés-Gil, N</u>.; López-Periago, A.; Aliaga-Alcalde N.; Ayllón, J.A.; Domingo, C. Crystallization of nanostructured curcumin MOF in supercritical CO_2.

Jornades Doctorals Química UAB 2018. Oral presentation. <u>Portolés-Gil, N</u>.; López-Periago, A.; Ayllón, J.A.; Domingo, C. Synthesis in supercritical CO_2 of metal-organic frameworks.

XXXVI Reunión Bienal de la Sociedad Española de Química, Sitges, 2018. Flash presentation and poster. <u>Portolés-Gil, N</u>.; López-Periago, A.; Aliaga-Alcalde N.; Ayllón, J.A.; Domingo, C. Curcumin MOF crystallized in supercritical CO_2.

16th European Meeting in Supercritical Fluids, Lisbon, 2017. Oral presentation, <u>Portolés-</u>Gil, N.; Parra, R.; López-Periago, A.; Ayllón, J.A.; Domingo, C. Synthesis in supercritical CO_2 of 1D metal-organic frameworks crystallized in nanosheets with desert-rose morphology.

5th International School of Crystallization. Granada, 2016. Poster. <u>Portolés-</u>Gil, N.; López-Periago, A.; Domingo, C.; Ayllón, J. A. Supercritical CO_2 as a green solvent for the crystallization of 2D metal-organic frameworks.

HONORS AND AWARDS

IUCr Journals Student Poster Prize at ISC2016 5th International School of Crystallitzation.